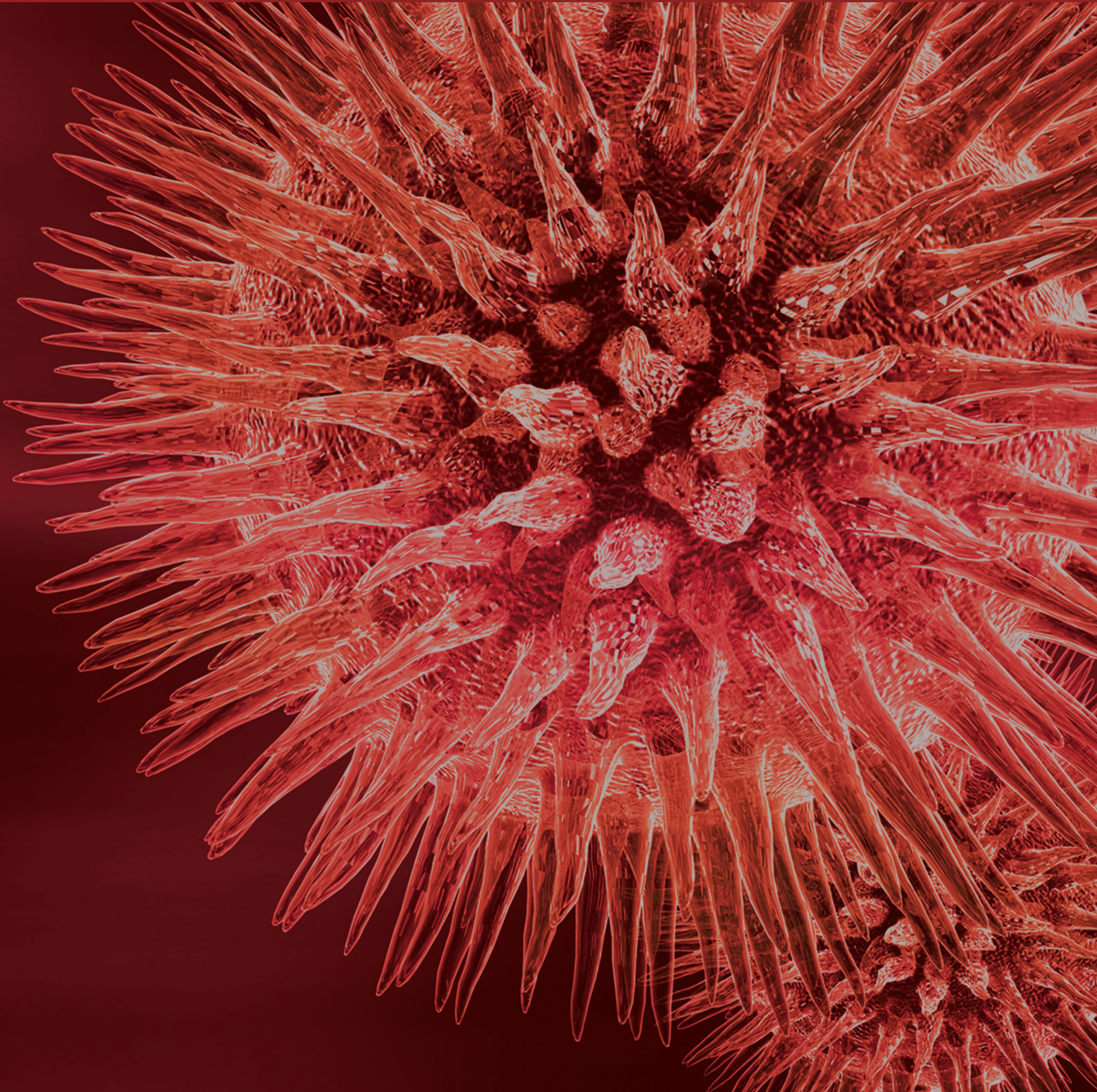


# Quantitative Anatomical Studies

Guest Editors: Ilker Ercan, Levent Sarikcioglu, Heather F. Smith,  
Juan A. Sanchis-Gimeno, Tuncay Peker, and Gulsum Ozyigit





---

# **Quantitative Anatomical Studies**

BioMed Research International

---

## **Quantitative Anatomical Studies**

Guest Editors: Ilker Ercan, Levent Sarikcioglu, Heather F. Smith,  
Juan A. Sanchis-Gimeno, Tuncay Peker, and Gulsum Ozyigit



---

Copyright © 2015 Hindawi Publishing Corporation. All rights reserved.

This is a special issue published in "BioMed Research International." All articles are open access articles distributed under the Creative Commons Attribution License, which permits unrestricted use, distribution, and reproduction in any medium, provided the original work is properly cited.

# Contents

**Quantitative Anatomical Studies**, Ilker Ercan, Levent Sarikcioglu, Heather F. Smith, Juan A. Sanchis-Gimeno, Tuncay Peker, and Gulsum Ozyigit  
Volume 2015, Article ID 781590, 2 pages

**To Compare Time-Weighted Graphs to Evaluate the Inclination of the Acetabular Component of Patients Who Had Total Hip Replacement Surgery**, Leman Tomak, Yuksel Bek, and Yilmaz Tomak  
Volume 2015, Article ID 129610, 6 pages

**Multiple Comparison of Age Groups in Bone Mineral Density under Heteroscedasticity**, Ahmet Sezer, Lale Altan, and Özer Özdemir  
Volume 2015, Article ID 426847, 7 pages

**Anthropometric Measurements Usage in Medical Sciences**, Nevin Utqualp and Ilker Ercan  
Volume 2015, Article ID 404261, 7 pages

**Three-Dimensional Assessment of Bilateral Symmetry of the Scaphoid: An Anatomic Study**, Paul W. L. ten Berg, Johannes G. G. Dobbe, Simon D. Strackee, and Geert J. Streekstra  
Volume 2015, Article ID 547250, 6 pages

**Developmental Changes in Morphology of the Middle and Posterior External Cranial Base in Modern *Homo sapiens***, Deepal H. Dalal and Heather F. Smith  
Volume 2015, Article ID 324702, 16 pages

**Using Magnetic Resonance for Predicting Femoral Strength: Added Value with respect to Bone Densitometry**, Olivia Louis, Yves Fierens, Maria Strantz, Robert Luypaert, Johan de Mey, and Erik Cattrysse  
Volume 2015, Article ID 801518, 5 pages

**Reexamination of Statistical Methods for Comparative Anatomy: Examples of Its Application and Comparisons with Other Parametric and Nonparametric Statistics**, Roqueline A. G. M. F. Aversi-Ferreira, Hisao Nishijo, and Tales Alexandre Aversi-Ferreira  
Volume 2015, Article ID 902534, 10 pages

**Association of Aortic Diameters with Coronary Artery Disease Severity and Albumin Excretion**, Bülent Özdemir, Ali Emül, Levent Özdemir, Saim Sağ, Murat Biçer, and Ali Aydınlar  
Volume 2015, Article ID 857628, 5 pages

**Automatic Tooth Segmentation of Dental Mesh Based on Harmonic Fields**, Sheng-hui Liao, Shi-jian Liu, Bei-ji Zou, Xi Ding, Ye Liang, and Jun-hui Huang  
Volume 2015, Article ID 187173, 10 pages

**Preliminary Observations on Sensitivity and Specificity of Magnetization Transfer Asymmetry for Imaging Myelin of Rat Brain at High Field**, Jae-Woong Kim, Jiye Choi, Janggeun Cho, Chulhyun Lee, Daejong Jeon, and Sung-Hong Park  
Volume 2015, Article ID 565391, 10 pages

**Volumetric Growth of the Liver in the Human Fetus: An Anatomical, Hydrostatic, and Statistical Study**, Michał Szpinda, Monika Paruszewska-Achtel, Alina Woźniak, Celestyna Mila-Kierzenkowska, Gabriela Elminowska-Wenda, Małgorzata Dombek, Anna Szpinda, and Mateusz Badura  
Volume 2015, Article ID 858162, 8 pages

**Morphometric Evaluation of Korean Femurs by Geometric Computation: Comparisons of the Sex and the Population**, Ho-Jung Cho, Dai-Soon Kwak, and In-Beom Kim  
Volume 2015, Article ID 730538, 9 pages

**Change in the Pathologic Supraspinatus: A Three-Dimensional Model of Fiber Bundle Architecture within Anterior and Posterior Regions**, Soo Y. Kim, Rohit Sachdeva, Zi Li, Dongwoon Lee, and Benjamin W. C. Rosser  
Volume 2015, Article ID 564825, 9 pages

**How to Quantify Penile Corpus Cavernosum Structures with Histomorphometry: Comparison of Two Methods**, Bruno Felix-Patricio, Diogo Benchimol De Souza, Bianca Martins Gregório, Waldemar Silva Costa, and Francisco José Sampaio  
Volume 2015, Article ID 832156, 6 pages

**Dentin Morphology of Root Canal Surface: A Quantitative Evaluation Based on a Scanning Electronic Microscopy Study**, Giuseppe Lo Giudice, Giuseppina Cutroneo, Antonio Centofanti, Alessandro Artemisia, Ennio Bramanti, Angela Militi, Giuseppina Rizzo, Angelo Favalaro, Alessia Irrera, Roberto Lo Giudice, and Marco Ciccù  
Volume 2015, Article ID 164065, 7 pages

**Functional and Structural Details about the Fabella: What the Important Stabilizer Looks Like in the Central European Population**, Nicole Helene Hauser, Sebastian Hoechel, Mireille Toranelli, Joerg Klawns, and Magdalena Müller-Gerbl  
Volume 2015, Article ID 343728, 8 pages

**Quantitative Anatomy of the Growing Lungs in the Human Fetus**, Michał Szpinda, Waldemar Siedlaczek, Anna Szpinda, Alina Woźniak, Celestyna Mila-Kierzenkowska, and Mateusz Badura  
Volume 2015, Article ID 362781, 10 pages

## Editorial

# Quantitative Anatomical Studies

**Ilker Ercan,<sup>1</sup> Levent Sarikcioglu,<sup>2</sup> Heather F. Smith,<sup>3</sup> Juan A. Sanchis-Gimeno,<sup>4</sup>  
Tuncay Peker,<sup>5</sup> and Gulsum Ozyigit<sup>6</sup>**

<sup>1</sup>*Department of Biostatistics, Medical Faculty, Uludag University, 16059 Bursa, Turkey*

<sup>2</sup>*Department of Anatomy, Medical Faculty, Akdeniz University, Antalya, Turkey*

<sup>3</sup>*Department of Anatomy, Midwestern University, Glendale, AZ 85308, USA*

<sup>4</sup>*Department of Anatomy and Human Embryology, University of Valencia, Valencia, Spain*

<sup>5</sup>*Department of Anatomy, Medical Faculty, Gazi University, Ankara, Turkey*

<sup>6</sup>*Department of Anatomy, Faculty of Veterinary Sciences, Uludag University, Bursa, Turkey*

Correspondence should be addressed to Ilker Ercan; [ercan@uludag.edu.tr](mailto:ercan@uludag.edu.tr)

Received 21 July 2015; Accepted 22 July 2015

Copyright © 2015 Ilker Ercan et al. This is an open access article distributed under the Creative Commons Attribution License, which permits unrestricted use, distribution, and reproduction in any medium, provided the original work is properly cited.

This special issue of this journal highlights new developments mainly in the field of quantification of the data of anatomical studies. In this special issue, we reviewed and edited seventeen articles from broad ranges of anatomical studies.

N. Utkualp and I. Ercan reviewed anthropometric measurement usage in medical sciences from Ancient Egyptian, Greek, and Roman civilizations to those from modern medicine. They also stressed contributions of the well-known scientists to recent diagnostic methods.

S. Liao et al. studied the fundamental problem of automatically segmenting teeth in dental mesh models into individual tooth objects and they built a novel dental-targeted harmonic field, which is able to automatically segment all teeth only once under a uniform harmonic field computation. They stressed that extensive experiments and quantitative analysis demonstrated the effectiveness of the method in terms of accuracy, robustness, and efficiency. G. Lo Giudice et al. performed a quantitative evaluation of dentin morphology in the root canal surface of premolars in paediatric-aged patients and showed that dentinal structure varied in the different root canal portions.

L. Tomak et al. developed a chart for monitoring the inclination of the acetabular component after total hip replacement surgery. They demonstrated that time-weighted quality control charts can also be used in the field of medicine and that they allow for a faster visual decision. N. Hauser et al. determined incidence and position of the fabella in a central European population and assessed how

to better estimate clinical appearances. They also described the biomechanical impact of the small sesamoid bone in its interaction with the femur, in order to determine a possible pressure distribution. O. Louis et al. compared MRI-derived bone mineral density (BMD) measured by advanced Bone Analysis Applications software and biomechanical tests. They found that MRI-derived BMD correlates with failure load to an extent, comparable to BMD estimates derived from classical bone densitometry techniques (pQCT or DXA).

H.-J. Cho et al. compared morphometric characteristics of Korean femora by geometric computation and calculated the size of the medullary canal for implant stem and intramedullary device design. They provided references for physical and forensic anthropology of a Korean population. P. W. L. ten Berg et al. studied three-dimensional assessment of bilateral symmetry of healthy bilateral scaphoid pairs in terms of three translational and three rotational parameters. They suggested that the contralateral scaphoid can serve as a reference in corrective surgery. S. Kim et al. investigated muscle architecture throughout the volume of the supraspinatus muscle by using three-dimensional model of fiber bundle architecture within the anterior and posterior regions of pathologic supraspinatus muscle. They found distinct patterns of change and suggested that their model can be incorporated with existing shoulder models to be used for biomechanical analysis in different patient populations with supraspinatus tendon pathologies. B. Felix-Patricio compared point-counting method and

*Tuncay Peker  
Gulsum Ozyigit*

color-based segmentation method in surface density data of penile corpus cavernosum trabecular smooth muscle and gave some cues in final interpretation of the results.

A. Sezer et al. performed multiple comparisons of age groups in bone mineral density under heteroscedasticity and reported their results in non-Hispanic whites, non-Hispanic blacks, and Mexican Americans. D. Dalal and H. F. Smith studied developmental changes in morphology of the middle and posterior external cranial bases in modern *Homo sapiens* and reported that the basicranium, occipital, and temporal regions reflected genetic distances among populations in childhood and adolescence.

M. Szpinda et al. assessed liver volumes in human fetuses of both sexes by using anatomical, hydrostatic, and statistical methods and proposed a formulation to calculate liver volume for evaluation of normal hepatic growth and early diagnosis of fetal microsomia and macrosomia. In another study, M. Szpinda et al. studied growing lungs in human fetuses and described relationships of lung dimensions in normative pulmonary growth and the diagnosis of pulmonary hypoplasia.

R. A. Aversi-Ferreira et al. reanalyzed previously published data in comparative anatomy statistics and suggested some cues for accurate analysis of anatomical data. J. W. Kim et al. reported their preliminary observations on sensitivity and specificity of magnetization transfer asymmetry for imaging myelin of the rat brain at high field. They found that magnetization transfer asymmetry can be a good biomarker for imaging myelination with better specificity than and similar sensitivity to magnetization transfer ratio. B. Ozdemir et al. compared the association of aortic diameters with coronary artery disease severity and albumin excretion. They found that patients with coronary artery disease had higher systolic blood pressure, pulse pressure, aortic systolic and diastolic pressure, and albumin excretion rate and had lower aortic distensibility.

We tried to summarize key points of the articles of this special issue. Readers of the special issue will have a chance to review a broad spectrum of quantification efforts of anatomical data and advances in anatomical quantification techniques. Accurate analysis in any science is a fundamental topic in study design, data collection, and drawing of interpretations from data.

As always, we wish you good reading.

## **Acknowledgments**

We hope that this special issue will be helpful for scientists and will contribute as a stimulus for further research on Quantitative Anatomical Sciences (QAS). We are very grateful to the contributing authors for their scientific contributions to this special issue. We also thank the reviewers who spend their valuable time, thoughts, and critical comments on each paper.

*Ilker Ercan  
Levent Sarikcioglu  
Heather F. Smith  
Juan A. Sanchis-Gimeno*

## Research Article

# To Compare Time-Weighted Graphs to Evaluate the Inclination of the Acetabular Component of Patients Who Had Total Hip Replacement Surgery

Leman Tomak,<sup>1</sup> Yuksel Bek,<sup>1</sup> and Yılmaz Tomak<sup>2</sup>

<sup>1</sup>Department of Biostatistics and Medical Informatics, Faculty of Medicine, Ondokuz Mayıs University, 55139 Samsun, Turkey

<sup>2</sup>Department of Orthopedics and Traumatology, Faculty of Medicine, Ondokuz Mayıs University, 55139 Samsun, Turkey

Correspondence should be addressed to Leman Tomak; [lemantomak55@gmail.com](mailto:lemantomak55@gmail.com)

Received 4 November 2014; Accepted 20 January 2015

Academic Editor: Juan A. Sanchis-Gimeno

Copyright © 2015 Leman Tomak et al. This is an open access article distributed under the Creative Commons Attribution License, which permits unrestricted use, distribution, and reproduction in any medium, provided the original work is properly cited.

Time-weighted graphs are used to detect small shifts in statistical process control. The aim of this study is to evaluate the inclination of the acetabular component with CUMulative SUM (CUSUM) chart, Moving Average (MA) chart, and Exponentially Weighted Moving Average (EWMA) chart. The data were obtained directly from thirty patients who had undergone total hip replacement surgery at Ondokuz Mayıs University, Faculty of Medicine. The inclination of the acetabular component of these people, after total hip replacement, was evaluated. CUSUM chart, Moving Average chart, and Exponentially Weighted Moving Average were used to evaluate the quality control process of acetabular component inclination. MINITAB Statistical Software 15.0 was used to generate these control charts. The assessment done with time-weighted charts revealed that the acetabular inclination angles were settled within control limits and the process was under control. It was determined that the change within the control limits had a random pattern. As a result of this study it has been obtained that time-weighted quality control charts which are used mostly in the field of industry can also be used in the field of medicine. It has provided us with a faster visual decision.

## 1. Introduction

Statistical process control (SPC) methods, utilizing the increasingly available routinely collected electronic patient records, could be used in continuous monitoring of clinical outcomes using routinely collected data [1, 2]. The “control charts” are a sequential analysis statistical tool that is particularly suited to the identification of small changes or changes in the number of cases, in one direction or another [1–3].

Control chart is an effective tool to identify specific causes of extreme variability. To distinguish the causes of variability, one of the most important visible signs is extreme observation on the control chart [1–3]. If some observations are outside the control limits, it means that the process is an out-of-control process, and the balance of the process is deteriorated. So corrective operations are needed so that the process can be controlled [2, 4]. If the process is in-control, the test results of patients are reported, but if it is out-control, the process is rejected and the results of tests are not reported [5].

The different control charts can be used for the evaluation process. While some of them are suitable for attribute data such as  $p$ -chart,  $np$ -chart,  $c$ -chart, and  $u$ -chart; some are used for continuous data such as individual, moving range,  $\bar{X}$ -bar, range, standard deviation.

There are also other control charts which are used for various purposes apart from these. The most important of them are time-weighted control charts. They are preferred in some situations where Shewhart charts did not detect the case of small shifts. There are CUMulative SUM chart, Moving Average chart, and Exponentially Weighted Moving Average (Geometric Moving Average) chart in this group [1, 4, 6, 7].

In the last decade, there has been a growing interest in the application of these techniques to the medical practice, especially evaluating and often promoting the use of control charts assessment of performance in three main areas: trainees' acquisition of competence in procedural skills [8, 9];

quality control at departmental or organizational level [10]; and performance of specialists [11, 12]. In medicine, some control chart techniques are commonly utilized.

Total hip replacement (THR) is the one of the most commonly performed adult reconstructive orthopedic procedures. However, technological advances improve successes of THR, and most of the failures of THRs are related to technical faults. Proper placement of the acetabular and femoral components in the frontal and axial plane is very important for successful THR procedures. Abnormal acetabular component inclination causes early acetabular loosening and revision surgeries. Acetabular component inclination is very important technical criteria for languidly of THR [13].

Though control charts have been well researched and developed in the last decade, it is true that many qualified practitioners do not use them, even though there may be justifiable reasons to make use of this technique. Possibly this is due to lack of instruction on control charts in many classes on SPC.

We aimed to develop and test a CUMulative SUM (CUSUM) chart, Moving Average (MA) chart and Exponentially Weighted Moving Average (EWMA) chart for monitoring the inclination of the acetabular component after total hip replacement.

## 2. Materials and Methods

The data for the time-weighted control charts were obtained by using X-rays that were obtained directly from thirty people who had had total hip replacement surgery at Ondokuz Mayıs University, Faculty of Medicine.

There are several technical criteria such as acetabular component inclination, acetabular anteversion, femoral offset, and femoral stem alignment for determination of optimal THR procedures. Standardized anteroposterior (AP) postoperative radiographs were analyzed using goniometer to measure acetabular component inclination [13].

The inclination of the acetabular component was measured using the angle between a line joining the ischial tuberosities and a line crossing the long axis of the acetabular component, determined by means of the axis of the major diameter that is formed by the apex of superior and inferior edges of the acetabular component on the radiograph (Figure 1) [13].

The data for the acetabular inclination angles was obtained from total hip replacement patients' radiographs retrospectively. Although the target value is 45° for this angle, it is considered to be normal that the angle varies from 30 degrees to 50 degrees [13].

CUSUM chart, Moving Average chart, and Exponentially Weighted Moving Average are used to evaluate quality control process of the acetabular inclination angles [1, 4, 6, 7]. MINITAB Statistical Software 15.0 was used to get variable control charts [14].

**2.1. CUMulative SUM Chart.** Control material will be monitored by control methods for at least 20 days. At the end of this process, the values of mean and standard deviation of



FIGURE 1: Measurement of the acetabular inclination angle. A. Line tangential to the ischial tuberosities. B. Line through the axis of the major diameter formed by apex of superior and inferior edges of the acetabular component on the radiograph. C. Acetabular inclination angle.

the results obtained are determined. A chart is generated using these statistics [4, 6, 15].

The values of CUMulative SUM (CUSUM) of deviations from the average are written on Y-axis. The measuring time or the number of observation is located on x-axis. Lower and upper confidence intervals are plotted as multiples of a certain standard deviation [4, 6, 15].

Given a sequence of values  $(X_i)$  generated from a process, a CUSUM statistic is formed by plotting the quantity [1, 3]

$$C_i = \sum_{j=1}^i (X_j - \mu_0) \quad \text{or} \quad (1)$$

$$C_i = \sum_{j=1}^i \frac{X_j - \mu_0}{\sigma}, \quad (2)$$

where  $\mu_0$  is the process mean or target value,  $\sigma$  is the process standard deviation,  $i$  number of the sample groups, and  $j : 1, 2, \dots, i$ . It is assumed that  $\sigma$  is known [1, 3]. When  $\sigma$  is unknown,  $\sigma$  is estimated as  $\overline{MR}/d_2$  or  $S/c_4$  [7].

Equation (2) is often known as the standardized CUSUM or scaled CUSUM. As long as the process is considered to be in-control, the average of  $C_i$  will be 0. It may be shown that the variance of  $C_i$  is  $i \cdot \sigma^2$  in (1).

Different procedures are used for CUSUM statistics, the most important of which are Tabulation S-CUSUM and the V-Mask CUSUM [1, 3, 6, 7, 16].

**2.2. Tabulation CUSUM.** CUSUM charts can be designed to detect a positive deviation or negative deviation from the average of process " $\mu_0$ ." It is assumed that the standard deviation of process does not change [3].

$C^+$  which is designed to determine the increase in the average of process and  $C^-$  which is designed to determine the reduction in the average of process are created primarily.

These are also called one-sided upper CUSUM and one-sided lower CUSUM [1, 6, 7, 17]:

$$\begin{aligned} C_i^+ &= \max \{0, (X_i - (\mu_0 + K)) + C_{i-1}^+\}, \\ C_i^- &= \max \{0, ((\mu_0 - K) - X_i) + C_{i-1}^-\}. \end{aligned} \quad (3)$$

Initial values are taken as  $C_0^+ = C_0^- = 0$ .

$K$  is called a reference value. If the shift is indicated in the form of  $\mu_1 = \mu_0 + \delta \cdot \sigma$ , the value of  $K$  is evaluated as half of the slip (the median between the two values) [1, 3]:

$$K = \frac{\delta}{2} \cdot \sigma = \frac{|\mu_1 - \mu_0|}{2}. \tag{4}$$

The value of  $k$  is the median value in the unit of one standard deviation [1, 3]:

$$k = \frac{K}{\sigma} = \frac{|\mu_1 - \mu_0|}{2\sigma}. \tag{5}$$

After the definition of the function, the control limit ( $H$ ) is determined, and this value is often referred to as the “decision interval” [1, 3, 6]:

$$H = h \cdot \sigma. \tag{6}$$

If either  $C_i^+$  or  $C_i^-$  is larger than  $H$ , the process is accepted to be out of control. The choice of the parameters “ $h$ ” and “ $k$ ” determines the performance of the CUSUM chart. Using  $h = 4$  to  $5$  and  $k = 0.5$  is generally preferred, because this provides a CUSUM chart that has good ARL properties against a shift of about  $1\sigma$  in the process mean [1, 3].

When either  $C_i^+$  or  $C_i^-$  is larger than  $H$ , in order to bring the process back to the target value  $\mu_0$  it may be helpful to have an estimate of the new process mean following the shift. The average of the new process is determined as shown below [1]:

$$\begin{aligned} C_i^+ > H &\implies \hat{\mu} = \mu_0 + K + \frac{C_i^+}{N^+}, \\ C_i^- > H &\implies \hat{\mu} = \mu_0 - K - \frac{C_i^-}{N^-}. \end{aligned} \tag{7}$$

Some researchers propose a technique of “standardized CUSUM.” To create this chart, the value of  $X_i$  must first be standardized [1, 3, 6]:

$$Y_i = \frac{X_i - \mu_0}{\sigma}. \tag{8}$$

Standardized CUSUM values are obtained as follows [1, 3]:

$$\begin{aligned} C_i^+ &= \max [0, Y_i - k + C_{i-1}^+], \\ C_i^- &= \max [0, -k - Y_i + C_{i-1}^-]. \end{aligned} \tag{9}$$

**2.3. V-Mask CUSUM.** A commonly used approach is to evaluate on the basis of the slope of the CUSUM line. This is V-Mask CUSUM.

“V” mask consists of a peak point (P), a localization point (O), and two slope lines acting as decision line (LDL and UDL lines). “V” mask consists of a peak point (P point), a localization point at the pullback distance from the peak point (O point), and 2 slope lines serving as decision lines (LDL and UDL lines). “ $w$ ” value is used to demonstrate how many observations should be shifted to get the moving average [1, 4, 6, 16].

The vertex of the V mask is placed at a certain distance in front of the most recent observation ( $C_i$ ) on the control chart. If all values placed on the table remain inside the angle formed by lines of V-Mask, the process is considered to be in control. If any of the points is located outside the angle, process is considered to be out of control [4].

V-Mask CUSUM is applied to sequential values [1]:

$$C_i = \sum_{j=1}^i Y_j = Y_i + C_{i-1}. \tag{10}$$

According to the above formula, “ $Y_i$ ” is standardized value of observation point [1]:

$$Y_i = \frac{(X_i - \mu_0)}{\sigma}. \tag{11}$$

The performance of V mask is determined by the lead distance ( $d$ ) and “ $\theta$ ” angle. If the following equations are accepted, tabular CUSUM and V-mask are equal [1]:

$$k = A \cdot \tan \theta, \quad h = A \cdot d \cdot \tan \theta = d \cdot k. \tag{12}$$

For  $A = 1$  ( $k = 1/2$  and  $h = 5$ ) these equations are [1]

$$\frac{1}{2} = 1 \cdot \tan \theta \implies \theta = 26.57, \quad 5 = d \cdot \frac{1}{2} \implies d = 10. \tag{13}$$

**2.4. Moving Average Chart.** During the creation of this chart, the individual observations are collected as  $X_1, X_2, \dots, X_i$ . The moving average value is determined as follows at the “ $w$ ” distance and the “ $i$ ” time [1]:

$$M_i = \frac{X_i + X_{i-1} + \dots + X_{i-w+1}}{w}. \tag{14}$$

The “ $w$ ” value is used to show how many observations should be slid to obtain moving average [7].

Variance of the moving average ( $M_i$ ) is as follows [1]:

$$V(M_i) = \frac{1}{w^2} \sum_{j=i-w+1}^i V(X_j) = \frac{1}{w^2} \sum_{j=i-w+1}^i \sigma^2 = \frac{\sigma^2}{w}. \tag{15}$$

Control limits for this chart are as follows [1]:

$$\begin{aligned} \text{UCL} &= \bar{X} + 3 \cdot \frac{\hat{\sigma}}{\sqrt{w}}, \\ \text{CL} &= \bar{X}, \\ \text{LCL} &= \bar{X} - 3 \cdot \frac{\hat{\sigma}}{\sqrt{w}}. \end{aligned} \tag{16}$$

The value of  $\overline{MR}/d_2$  is used to estimate  $\sigma$ . Control limits are [7]

$$\begin{aligned} \text{UCL} &= \bar{X} + 3 \cdot \frac{\overline{MR}}{d_2 \cdot \sqrt{w}}, \\ \text{CL} &= \bar{X}, \\ \text{LCL} &= \bar{X} - 3 \cdot \frac{\overline{MR}}{d_2 \cdot \sqrt{w}}. \end{aligned} \tag{17}$$

When the values of mean and standard deviation are given, the upper and lower limits would be as follows [1]:

$$\begin{aligned} \text{UCL} &= \mu_0 + \frac{3 \cdot \sigma_0}{\sqrt{w}}, \\ \text{CL} &= \mu_0, \\ \text{LCL} &= \mu_0 - \frac{3 \cdot \sigma_0}{\sqrt{w}}. \end{aligned} \quad (18)$$

The control procedure consists of the calculation of the new moving average ( $M_i$ ) value for each observation and the marking of these on the chart. If one of the values is located outside the boundaries, the process is considered to be out of control [1].

**2.5. Exponentially Weighted Moving Average Chart.** The EWMA statistic is defined for the observations of  $X_i$  with mean  $\mu$  and variance  $\sigma^2$  as follows [1, 3, 6, 7, 16, 18]:

$$Z_i = (1 - \lambda) \cdot Z_{i-1} + \lambda \cdot X_i, \quad (19)$$

where  $i = 1, 2, \dots$ ,  $\lambda$  is a parameter ( $0 < \lambda \leq 1$ ). The starting value  $Z_0$  is equal to the process mean [1, 3, 6].  $Z_i$  is a weighted average of the  $X_j$  ( $j = 1, 2, \dots, i$ ) and  $\mu$  with the weights of  $X_j$  decreasing exponentially [1, 3]:

$$Z_i = \lambda \sum_{j=0}^{i-1} [(1 - \lambda)^j X_{i-j}] + (1 - \lambda)^i Z_0. \quad (20)$$

The weight of the current observation is  $\lambda$ , and that of the previous one is  $\lambda(1 - \lambda)$ . The older the observation is, the smaller the value will be  $\lambda(1 - \lambda)^j$  with which it is weighted. The weight of the observation being studied at the moment will be  $\lambda$  and the weight of the previous observation will be  $(1 - \lambda)$ , and it will gradually decrease [3]. The sample average of the  $\lambda(1 - \lambda)^j$  weights decreases geometrically by time. When the sums of the weights are combined, the formula may be shown as follows [1]:

$$\lambda \sum_{j=0}^{i-1} (1 - \lambda)^j = \lambda \cdot \left[ \frac{1 - (1 - \lambda)^i}{1 - (1 - \lambda)} \right] = 1 - (1 - \lambda)^i. \quad (21)$$

The variance of  $Z_i$  is [1, 3]

$$\sigma_{Z_i}^2 = \left( \frac{\lambda}{2 - \lambda} \right) [1 - (1 - \lambda)^{2i}] \sigma^2. \quad (22)$$

When  $i$  is large, the variance can be shown as follows [3]:

$$\sigma_{Z_i}^2 = \left( \frac{\lambda}{2 - \lambda} \right) \sigma^2. \quad (23)$$

Control limits are [1, 3]

$$\begin{aligned} \text{UCL} &= \bar{X} + k \cdot \sigma \cdot \sqrt{\frac{\lambda}{2 - \lambda} [1 - (1 - \lambda)^{2i}]}, \\ \text{CL} &= \bar{X}, \\ \text{LCL} &= \bar{X} - k \cdot \sigma \cdot \sqrt{\frac{\lambda}{2 - \lambda} [1 - (1 - \lambda)^{2i}]}. \end{aligned} \quad (24)$$

When  $i > 10$ , the formula for the control limits can be a simplified formula, and “ $k$ ” value is considered to be typically 3 [1, 3, 6, 7, 16, 17]:

$$\begin{aligned} \text{UCL} &= \bar{X} + 3 \cdot \hat{\sigma} \cdot \sqrt{\frac{\lambda}{2 - \lambda}}, \\ \text{CL} &= \bar{X}, \\ \text{LCL} &= \bar{X} - 3 \cdot \hat{\sigma} \cdot \sqrt{\frac{\lambda}{2 - \lambda}}. \end{aligned} \quad (25)$$

If  $\sigma$  is not known,  $\sigma$  is estimated by using either  $\overline{MR}/d_2$  or  $S/c_4$  [19]. If  $\mu$  and  $\sigma$  are known, the control limits are as follows [1, 3]:

$$\begin{aligned} \text{UCL} &= \mu_0 + 3 \cdot \sigma \cdot \sqrt{\frac{\lambda}{2 - \lambda}}, \\ \text{CL} &= \mu_0, \\ \text{LCL} &= \mu_0 - 3 \cdot \sigma \cdot \sqrt{\frac{\lambda}{2 - \lambda}}. \end{aligned} \quad (26)$$

### 3. Results

Time-weighted control charts were obtained using the acetabular inclination angles of thirty patients. CUSUM chart is shown in Figure 2. It is obvious that all the observations are within the control limits and the process is stable.

All the observations are within both UCL and LCL on V-Mask CUSUM chart (Figure 3). The process is under control.

Moving Average chart is shown in Figure 4. Since all of the observations are settled within control limits, it is clear that the process is stable.

EWMA chart is given in Figure 5. There is no observation settled outside of the control bounds. Because of this random pattern, the process is stable.

### 4. Discussion

Time-weighted charts are used as an alternative to Shewhart charts in detecting small changes. Although Shewhart charts are effective in detecting changes greater than  $2\sigma$ , they are not effective enough to detect the changes between  $0.5$  and  $1.5\sigma$ . So, time-weighted charts are preferred to detect such changes [6].

CUSUM chart is a precise and quantitative chart which is used to demonstrate if this difference is random or systematic [1, 4, 6, 7].

In this study, CUSUM, EVMA, and MA charts were used to evaluate the inclination of the acetabular component in patients who underwent hip replacement surgery. The evaluation done with time-weighted charts revealed that the acetabular inclination angles were within the control limits and the process was stable. It was demonstrated that the change within the control limits had a random pattern.

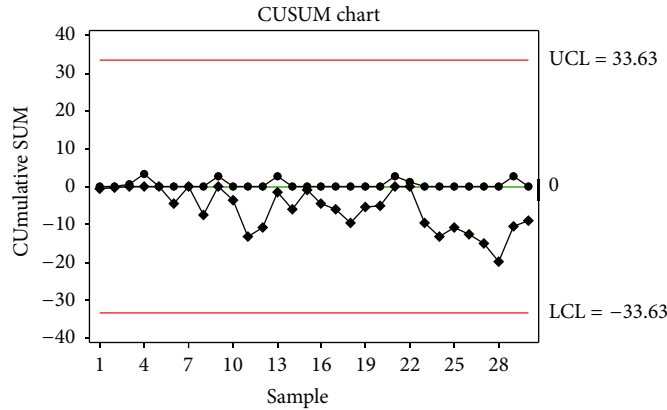


FIGURE 2: CUSUM Chart.

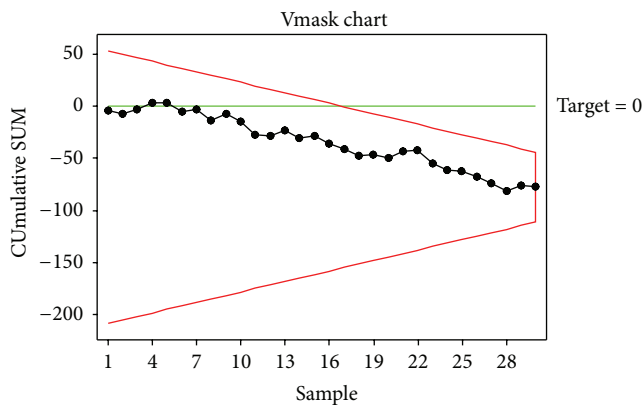


FIGURE 3: V-Mask CUSUM Chart.

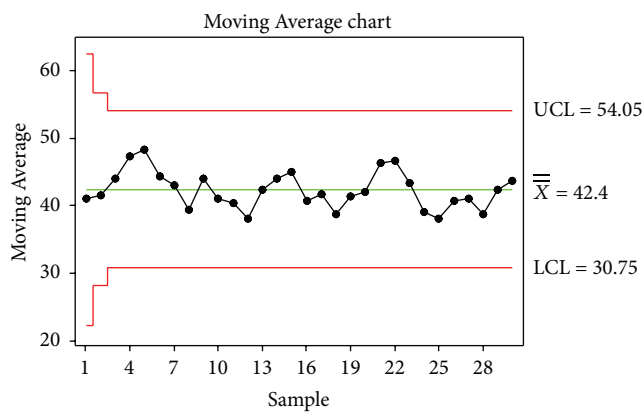


FIGURE 4: Moving Average Chart.

CUSUM statistics occur in a random pattern around zero of the variation. Random scatter around zero axis is the expected pattern, but if cumulative values display a continuous increase or decrease towards a particular direction at a certain point, then the observation values are inspected from this point on. A steep slope (gradient) indicates that there is a systematic error and that the observations are out of control [1, 4, 6].

There was no steep slope on the drawn charts for the inclination of the acetabular component in patients who underwent hip replacement surgery.

One of the advantages of charted CUSUM is the horizontal lines it has for the control limits. This allows charted CUSUM to be interpreted as Levey-Jennings chart. This type of interpretation requires less experience and evaluation. Thus, when a large number of analysts use the control process, the interpretation will be more consistent. Another advantage of this method is that it is applicable with only scaled procedures (without drawing any tables).

However, when compared with Levey-Jennings control chart limited with 3 s, CUSUM procedure is better in detecting systematic errors but less sensitive in detecting random errors. Hence, rather than being used alone, it should be used either together with Levey-Jennings procedure or as a separate table with the Levey-Jennings table. Although interpretation is easier and more objective with this technique, determining the threshold and control limits is somewhat difficult.

V-mask CUSUM technique is highly objective in interpreting data; however, it is not widely used in clinical laboratories or recommended. Instead, interpretation depends on visual inspection and evaluation of the angle of CUSUM line.

Sometimes, a special graph paper with 45-degree angle shapes is also used. The aim in using this specific graph paper is to scale the graph so that a 2 s change on y axis will be the same as the distance between the 2 points on x axis. Thus, when the observed mean is about 2 s from the expected mean, the 45-degree angle represents the expected slope/gradient [4].

Moving Average chart and EWMA chart are used in cases where Shewhart control charts are not able to detect small changes. The performance of EWMA control chart is almost equal to that of CUSUM chart, and it is an easily available and applicable chart. CUSUM, MA, and EWMA charts are ideal for the inspection of the individual observations.

The CUSUM technique has several methodological characteristics that make it perform better than the commonly used healthcare quality control tools such as incident reporting and clinical audit or indeed any other methods that report aggregate results. This graphical technique is associated with

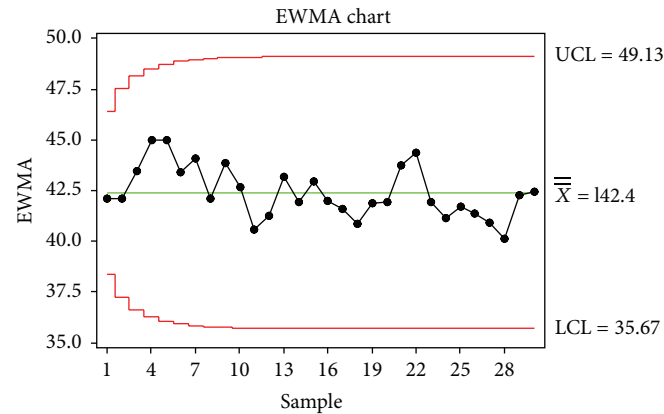


FIGURE 5: EWMA Chart.

false positive and false negative states. The choice and placement of chart limits determine which of the two states is more likely to occur, and reducing the likelihood of one increases that of the other. CUSUM methods can be used in continuous monitoring of clinical outcomes of the inclination of the acetabular component in patients who underwent hip replacement surgery. Used prospectively, they could lead to the prompt detection of periods of suboptimal standards of the hip replacement surgery.

With this study, it has been demonstrated that time-weighted quality control charts, which are used mostly in the field of industry, can also be used in the field of medicine. It has also been demonstrated that they allow a faster visual decision.

### Conflict of Interests

The authors declare no conflict of interests.

### Authors' Contribution

Leman Tomak, MD, Ph.D., Yuksel Bek, Ph.D., and Yilmaz Tomak, MD, contributed to this work.

### References

- [1] D. Montgomery, *Introduction to The Statistical Quality Control*, John Wiley & Sons, New York, NY, USA, 3rd edition, 1996.
- [2] I. Bass, *Six Sigma Statistics with Excel and Minitab*, McGraw-Hill, New York, NY, USA, 2007.
- [3] P. Winkel and N. F. Zhang, *Statistical development of Quality in Medicine*, John Wiley & Sons, Chichester, UK, 2007.
- [4] J. Westgard and G. Klee, "Quality management," in *Tietz Textbook of Clinical Chemistry and Molecular Diagnostics*, C. Burtis, E. Ashwoodve, and D. Bruns, Eds., pp. 485–523, Elsevier, New York, NY, USA, 4th edition, 2006.
- [5] J. Westgard, *Basic QC Practices*, Westgard QC, Madison, Wis, USA, 2nd edition, 2002.
- [6] H. Wadsworth, K. Stephens, and A. Godfrey, *Modern Methods for Quality Control and Improvement*, John Wiley & Sons, New York, NY, USA, 1986.
- [7] T. Ryan, *Statistical Methods for Quality Improvement*, John Wiley & Sons, New York, NY, USA, 1989.
- [8] K. R. Stringer, S. Bajenov, and S. M. Yentis, "Training in airway management," *Anaesthesia*, vol. 57, no. 10, pp. 967–983, 2002.
- [9] D. J. Biau, S. M. Williams, M. M. Schlup, R. S. Nizard, and R. Porcher, "Quantitative and individualized assessment of the learning curve using LC-CUSUM," *British Journal of Surgery*, vol. 95, no. 7, pp. 925–929, 2008.
- [10] J. E. Arrowsmith, S. J. Powell, and S. A. M. Nashef, "Local clinical quality monitoring for detection of excess operative deaths," *Anaesthesia*, vol. 61, no. 5, pp. 423–426, 2006.
- [11] C. J. Runcie, "Assessing the performance of a consultant anaesthetist by control chart methodology," *Anaesthesia*, vol. 64, no. 3, pp. 293–296, 2009.
- [12] D. J. Biau, M. Resche-Rigon, G. Godiris-Petit, R. S. Nizard, and R. Porcher, "Quality control of surgical and interventional procedures: a review of the CUSUM," *Quality and Safety in Health Care*, vol. 16, no. 3, pp. 203–207, 2007.
- [13] J. Harkess and J. Crockarell, "Arthroplasty of the hip," in *Campbell's Operative Orthopaedics*, S. Canale and J. Beaty, Eds., vol. 7, pp. 312–481, Mosby Elsevier, Philadelphia, Pa, USA, 11th edition, 2008.
- [14] Minitab, *MINITAB Statistical Software, Release 15 for Windows*, Minitab, State College, Pa, USA, 2009.
- [15] N. Goris and K. de Clercq, "Quality assurance/quality control of foot and mouth disease solid phase competition enzyme-linked immunosorbent assay. Part II. Quality control: comparison of two charting methods to monitor assay performance," *Revue Scientifique et Technique*, vol. 24, no. 3, pp. 1005–1016, 2005.
- [16] J. Oakland, *Statistical Process Control*, MPG Books Limited, London, UK, 5th edition, 2003.
- [17] J. Thompson and J. Koronacki, *Statistical Process Control*, Chapman & Hall, New York, NY, USA, 2nd edition, 2002.
- [18] M. Chandra, *Statistical Quality Control*, CRC Press, New York, NY, USA, 2001.
- [19] E. L. Grant and R. S. Leavenworth, *Statistical Quality Control*, McGraw-Hill, New York, NY, USA, 7th edition, 1996.

## Research Article

# Multiple Comparison of Age Groups in Bone Mineral Density under Heteroscedasticity

Ahmet Sezer,<sup>1</sup> Lale Altan,<sup>2</sup> and Özer Özdemir<sup>1</sup>

<sup>1</sup>Department of Statistics, Faculty of Science, Anadolu University, 26470 Eskisehir, Turkey

<sup>2</sup>Department of Physical Medicine and Rehabilitation, Medical Faculty, University of Uludag, 16059 Bursa, Turkey

Correspondence should be addressed to Ahmet Sezer; a.sezer@anadolu.edu.tr

Received 22 February 2015; Accepted 23 April 2015

Academic Editor: Heather F. Smith

Copyright © 2015 Ahmet Sezer et al. This is an open access article distributed under the Creative Commons Attribution License, which permits unrestricted use, distribution, and reproduction in any medium, provided the original work is properly cited.

Osteoporosis is a silent disease because individuals may not know that they have osteoporosis until their bones become so fragile. Bone mineral density (BMD) test helps to detect osteoporosis and determine the risk fractures. This study covers bone measurement data from total body dual energy X-ray absorptiometry scans for 28,454 persons who participated in the 1996–2006 National Health and Nutrition Examination Survey in USA Dual energy X-ray absorptiometry (DXA) method is known as the primary method for detecting osteoporosis because of its high precision and accuracy. Testing the equality of the means of normal populations when the variances are unknown and unequal is a fundamental problem in clinical trials and biomedical research. In this study we compare age groups based upon BMD in case of unequal variance being present among the groups. First we test equality of variances among the age groups by the Hartley test. And then Scott-Smith test is used to test equality of BMD means for the age groups. Finally, Tukey-Cramer confidence intervals are constructed to detect which groups start to differ from the reference group in which BMD reaches the peak level.

## 1. Introduction

Osteoporosis is a systemic skeletal disease characterized by low bone density and micro architectural deterioration of bone tissue with a consequent increase in bone fragility [1]. Measurement of BMD can be used to determine fracture risk and monitor the effects of treatment. Early detection of bone loss is essential to preventing osteoporosis. In fact, osteoporosis affects more than 75 million people in Europe, Japan, and USA and causes more than 2.3 million fractures annually in Europe and USA. The lifetime risk for hip, vertebral, and forearm (wrist) fractures has been estimated to be around 40%, very close to that for coronary heart disease. Osteoporosis does not only cause fractures, but also causes people to become bedridden and causes back pain and loss of height. Prevention of the disease and its associated fractures is important for maintaining health, quality of life, and independence among the elderly.

Early osteoporosis is not usually detected and most of the time does not become clinically evident until fractures occur.

Loss of bone density occurs with advancing age and rates of fracture increase with age, giving rise to significant morbidity and mortality. Osteoporosis is three times more common in women than in men, because women have a lower peak bone mass and hormonal changes occur at the menopause. Estrogens have an important function in preserving bone mass during adulthood, and bone loss occurs as levels decline, usually around the age of 50 years. In addition, women live longer than men [2] and therefore have greater reductions in bone mass.

Until recently, osteoporosis was considered an inevitable consequence of ageing. With Improvements in diagnostic technology and assessment facilities, now it is easier to detect the disease before fractures occur. The substantial bone loss is usually around age 65 years in men and 50 years in women [3]. Females tend to keep peak mineral content until menopause; after that it drops about 15% per decade. Fracture rates increase rapidly with age and the lifetime. Many studies show that an inadequate supply of calcium over a lifetime contributes to the development of osteoporosis.

TABLE 1: Total body mineral density (g/cm<sup>2</sup>) of Mexican-American females aged 8 years and over.

Female (Mexican-American)	Sample size	Mean	Standard deviation	Does Tukey-Kramer C. I. include zero?	
(X1) 8–11 years	471	0.820	0.091	(X5–X1)	×
(X2) 12–15 years	821	1.006	0.092	(X5–X2)	×
(X3) 16–19 years	692	1.074	0.089	(X5–X3)	×
(X4) 20–29 years	364	1.102	0.084	(X5–X4)	✓
(X5) 30–39 years	298	1.121	0.097	X5	✓
(X6) 40–49 years	372	1.121	0.092	(X5–X6)	✓
(X7) 50–59 years	194	1.059	0.125	(X5–X7)	×
(X8) 60–69 years	375	0.997	0.113	(X5–X8)	×
(X9) 70–79 years	154	0.937	0.105	(X5–X9)	×
(X10) 80 years and over	47	0.885	0.098	(X5–X10)	×

The body's demand for calcium is greater during childhood and adolescence and during pregnancy and breastfeeding. Epidemiological studies indicate that a 10% increase in peak bone mass in the Caucasian female population would decrease the risk of hip fracture by about 30%. Clearly, eliminating the risk factors might significantly reduce the burden of osteoporosis. Obvious interventions include raising levels of exercise, stopping smoking, and increasing dietary intake of calcium [4].

## 2. Materials and Methods

Testing the equality of the means of normal populations when the variances are unknown and unequal is a fundamental problem in clinical trials and biomedical research. A well known case is the Behrens-Fisher (BF) problem, which focuses on two populations. Behrens-Fisher problem is popular because there is no exact solution satisfying the classical criteria for good tests. The problem is seemingly simple, yet much effort has been made to try to solve this problem [5–7].

It is well known that there exists an analysis of variance (ANOVA)  $F$ -test for the problem of testing the equality of means from several independent samples under the assumptions of normality. It is well known that the usual  $F$ -test is not robust to the assumption of equal variances. There is, however, no standard procedure for testing this hypothesis when variances are not equal, and various approximate test procedures have been proposed in the literature. The best known procedure is the test proposed by Welch (1947) [8] and its modifications. Other tests have been proposed by James (1951) [9], Scott and Smith (1971) [10], Brown and Forsythe (1974) [11], S.-Y. Chen and H. J. Chen (1998) [12], Rice and Gaines (1989) [13], Krishnamoorthy et al. (2007) [14], Weerahandi (1995) [15], and Xu and Wang (2008) [16, 17].

**2.1. Hartley's Test for Testing Variance.** Hartley's test ( $F$ ) was developed by Hartley in 1950 [18]. This test assumes that data within each group are normally distributed and test involves computing the ratio of the largest group variance ( $\max s_i^2$ ) to the smallest ( $\min s_i^2$ ). This ratio will be compared with the critical value from a table of the sampling distribution of  $F$ . In this test null hypothesis states that all groups have equal

variances alternative to at least one group differing from the others. Consider

$$F = \frac{\max s_i^2}{\min s_i^2} \quad i = 1, \dots, k, \quad (1)$$

where  $k$  is the number of the group.

Since we have large sample sizes for the groups, we used critical value 1 from Hartley's table to make our decision. For example Hartley test is calculated for the first group, Non-Hispanic Mexican-American female group; consider

$$F = \frac{(0.125)^2}{(0.084)^2} = 2.21 > 1. \quad (2)$$

Since calculated test statistic value is bigger than 1 (critical value from the Hartley table), we reject the null hypothesis that equality of variance assumption is violated among age groups of Mexican-American females. It is evident that equal variance assumption is violated for all the cases we consider (Tables 1–6) and that leads us to check equality of means under heteroscedasticity.

**2.2. Tests for the Means.** A very common problem in applied statistics is that of comparing the means of several populations. Several methods have been proposed for handling the unequal variance among the groups: Welch test, Brown-Forsythe test, and Scott-Smith test. Since we have two classes for gender and three classes for the race, totally there are 6 tables. Each table includes sample size, sample mean, and standard deviation for the groups. In the null hypothesis we claim all age groups have the same mean of BMD. On the other hand alternative claims at least one group has different mean than the rest of the groups. Consider

$$\begin{aligned} H_0: \mu_1 = \mu_2 = \dots = \mu_k = \mu, \\ H_1: \exists \mu_i \neq \mu_j, \quad 1 \leq i \leq j \leq k. \end{aligned} \quad (3)$$

**2.2.1. The Scott-Smith Test.** In this study, because of its simplicity Scott-Smith test will be used for checking equality of BMD means for the age groups. Scott and Smith (1971)

TABLE 2: Total body mineral density (g/cm<sup>2</sup>) of Non-Hispanic White females aged 8 years and over.

Female (Non-Hispanic White)	Sample size	Mean	Standard deviation	Does Tukey-Kramer C. I. include zero?	
(X1) 8–11 years	383	0.828	0.082	(X5–X1)	×
(X2) 12–15 years	576	1.003	0.092	(X5–X2)	×
(X3) 16–19 years	543	1.087	0.084	(X5–X3)	×
(X4) 20–29 years	583	1.109	0.079	(X5–X4)	×
(X5) 30–39 years	612	1.131	0.089	X5	✓
(X6) 40–49 years	668	1.127	0.096	(X5–X6)	✓
(X7) 50–59 years	639	1.091	0.099	(X5–X7)	×
(X8) 60–69 years	644	1.040	0.107	(X5–X8)	×
(X9) 70–79 years	429	0.977	0.104	(X5–X9)	×
(X10) 80 years and over	457	0.924	0.105	(X5–X10)	×

TABLE 3: Total body mineral density (g/cm<sup>2</sup>) of Non-Hispanic Black females aged 8 years and over.

Female (Non-Hispanic Black)	Sample size	Mean	Standard deviation	Does Tukey-Kramer C. I. include zero?	
(X1) 8–11 years	490	0.871	0.090	(X5–X1)	×
(X2) 12–15 years	737	1.071	0.097	(X5–X2)	×
(X3) 16–19 years	609	1.153	0.091	(X5–X3)	×
(X4) 20–29 years	297	1.186	0.092	(X5–X4)	✓
(X5) 30–39 years	333	1.196	0.095	X5	✓
(X6) 40–49 years	398	1.191	0.098	(X5–X6)	✓
(X7) 50–59 years	250	1.136	0.114	(X5–X7)	×
(X8) 60–69 years	306	1.096	0.113	(X5–X8)	×
(X9) 70–79 years	124	1.035	0.105	(X5–X9)	×
(X10) 80 years and over	58	0.979	0.129	(X5–X10)	×

TABLE 4: Total body mineral density (g/cm<sup>2</sup>) of Mexican-American males aged 8 years and over.

Male (Mexican-American)	Sample size	Mean	Standard deviation	Does Tukey-Kramer C. I. include zero?	
(X1) 8–11 years	468	0.833	0.075	(X4–X1)	×
(X2) 12–15 years	777	0.995	0.120	(X4–X2)	×
(X3) 16–19 years	783	1.142	0.103	(X4–X3)	×
(X4) 20–29 years	444	1.173	0.096	(X4)	✓
(X5) 30–39 years	337	1.162	0.094	(X4–X5)	✓
(X6) 40–49 years	381	1.155	0.101	(X4–X6)	✓
(X7) 50–59 years	174	1.142	0.109	(X4–X7)	×
(X8) 60–69 years	348	1.136	0.104	(X4–X8)	×
(X9) 70–79 years	164	1.106	0.107	(X4–X9)	×
(X10) 80 years and over	48	1.075	0.098	(X4–X10)	×

give the following test statistics to test the means under heteroscedasticity [10]. Consider

$$F_s = \sum_{i=1}^k \frac{n_i (\bar{X}_i - \bar{X})^2}{S_i^{*2}}, \tag{4}$$

where  $S_i^{*2} = (n_i - 1)/(n_i - 3)S_i^2$ . Under the null hypothesis distribution of  $F_s$  will be  $\chi^2$  with degrees of freedom  $k$ .

2.2.2. *The Welch Test.* Welch (1951) [19] generalized the test which is proposed to handle Behrens-Fisher problem. Because of its simplicity Welch test is commonly used in practice. According to Welch, the test statistics is

$$W = \frac{\sum_{i=1}^k w_i [(\bar{X}_i - \bar{X})^2 / (k - 1)]}{1 + (2(k - 2) / (k^2 - 1)) \sum_{i=1}^k (1 / (n_i - 1)) (1 - w_i / \sum w_j)^2}, \tag{5}$$

TABLE 5: Total body mineral density (g/cm<sup>2</sup>) of Non-Hispanic White males aged 8 years and over.

Male (Non-Hispanic White)	Sample size	Mean	Standard deviation	Does Tukey-Kramer C. I. include zero?	
(X1) 8–11 years	369	0.839	0.069	(X4–X1)	×
(X2) 12–15 years	578	0.995	0.111	(X4–X2)	×
(X3) 16–19 years	591	1.171	0.107	(X4–X3)	×
(X4) 20–29 years	617	1.210	0.099	(X4)	✓
(X5) 30–39 years	647	1.213	0.106	(X4–X5)	✓
(X6) 40–49 years	700	1.206	0.102	(X4–X6)	✓
(X7) 50–59 years	683	1.181	0.110	(X4–X7)	×
(X8) 60–69 years	623	1.167	0.114	(X4–X8)	×
(X9) 70–79 years	496	1.135	0.114	(X4–X9)	×
(X10) 80 years and over	398	1.107	0.115	(X4–X10)	×

TABLE 6: Total body mineral density (g/cm<sup>2</sup>) of Non-Hispanic Black males aged 8 years and over.

Male (Non-Hispanic Black)	Sample size	Mean	Standard deviation	Does Tukey-Kramer C. I. include zero?	
(X1) 8–11 years	469	0.884	0.077	(X4–X1)	×
(X2) 12–15 years	745	1.044	0.118	(X4–X2)	×
(X3) 16–19 years	757	1.233	0.116	(X4–X3)	×
(X4) 20–29 years	325	1.304	0.120	(X4)	✓
(X5) 30–39 years	310	1.292	0.114	(X4–X5)	✓
(X6) 40–49 years	366	1.258	0.131	(X4–X6)	×
(X7) 50–59 years	240	1.256	0.122	(X4–X7)	×
(X8) 60–69 years	303	1.240	0.115	(X4–X8)	×
(X9) 70–79 years	114	1.167	0.119	(X4–X9)	×
(X10) 80 years and over	36	1.178	0.156	(X4–X10)	×

where  $w_i = n_i/S_i^2$ . Under the null hypothesis,  $W$  statistic has  $F$  distribution with  $k - 1$  and  $f$  degrees of freedom, where

$$f = \frac{1}{(3/(k^2 - 1)) \sum_{i=1}^k (1/(n_i - 1)) (1 - w_i / \sum w_j)^2}. \quad (6)$$

We reject the null hypothesis when  $P(F_{k-1,f} > w) < \alpha$ , where  $w$  is calculated test statistic from (5).

2.2.3. *The Brown-Forsythe Test.* Brown and Forsythe (1974) [11] modified classical  $F$  test. The proposed test statistic is

$$B = \frac{\sum_{i=1}^k n_i (\bar{X}_i - \bar{X})^2}{\sum_{i=1}^k (1 - n_i/n) S_i^2}. \quad (7)$$

Under the null hypothesis this test statistic has  $F$  distribution with degrees of freedom  $k - 1$  and  $\nu$ , where  $\nu$  is

$$\nu = \frac{[\sum_{i=1}^k (1 - n_i/n) S_i^2]^2}{\sum_{i=1}^k ((1 - n_i/n)^2 S_i^4 / (n_i - 1))}. \quad (8)$$

Brown-Forsythe test rejects the equality of mean hypothesis when  $P(F_{k-1,\nu} > b) < \alpha$  where  $b$  is the calculated test statistic from (7).

Finally, the Tukey-Cramer confidence intervals are constructed to determine which age groups are statistically different than the reference group. The reference group will have the highest BMD mean among the groups. If Tukey-Cramer pairwise confidence interval does contain zero, it means that there is no statistically significant difference between the considered groups with respect to their BMD. The first age group in the last column of the tables will represent the highest group with BMD mean (for females: X5, for males: X4). For example, in Table 1, the Mexican-American female group, 30–39-year (X5) group, has the highest mean with respect to BMD. Since Mexican-American females reach their BMD in 30–39-year (X5) group, this group will be our reference group and we will compare other age groups with this reference group.

### 3. Results and Discussion

Our study reveals that BMD decreases rapidly with age for both sexes and in all race groups. After 50 years old, decreasing amount of BMD speeds up for both females and males. Similar to previous studies some of the sex and race groups show significant difference in their BMD. Since heteroscedasticity is present among the age groups, different than the previous epidemiologic studies, we categorized the age groups by race and gender to investigate their BMD by

the Tukey-Cramer confidence intervals. We used the 30–39-year age group for females and 20–29-year age group for males as the reference group because in all race groups bone mineral density reaches its peak level and then it starts to decrease gradually in these age groups. As we pointed out before our goal is to detect in which age groups bone mineral density starts to differ significantly from the reference group. Knowing this will help to detect early osteoporosis in different race groups.

Peak bone density (PBD) is probably the result of interaction between endogenous (heredity, endocrine) and exogenous (nutrition, physical) factors. In fact the fastest growing and development of skeleton is between early childhood and late adolescence [20]. About 60% of the bone growth takes place during the adolescence [21]. According to [22], the earliest age to reach peak bone density is between 17 and 18 years old and latest age is around 35 years old for the females.

Increasing of bone mass is different for different skeleton parts during puberty. Bone mass reached the peak level before 20 years old at the proximal femur; however for total skeleton it takes place after 6–10 years. Although our study shows that this time is little later than 20 years old for females, this result can be considered as being consistent with the previous studies. In a recent study it is found that estimated age of peak was around age of 20 for trabecular BMD. However this study was applied only on Chinese females and measurements were made by the high resolution peripheral quantitative computed tomography (HR-pQCT). Our study reveals that in Non-Hispanic Black females in the periods of 20–29 and 30–39 years BMD is significantly higher than other race groups. This result is consistent with the other cohort-based work. For example, in a recent study [23], BMD is compared in older women across five racial/ethnic groups in four countries. Findings show substantial racial differences in BMD even within African or Asian origin individuals and highlight the contributing role of body weight and estrogen use to the geographic and racial variation in BMD.

Similar to females it is found that males start to lose their BMD with aging. Although a 60-year-old White man has a 25% lifetime risk for an osteoporotic fracture, in general osteoporosis is underdiagnosed and undertreated problem for men [24]. In this cross-sectional study [25], bone mineral density (BMD) measurements were performed in 1762 ambulatory subjects (678 men and 1084 women) aged 55 years and over from the Rotterdam Study. This study revealed that the rate of age-related bone reduction in the femoral neck appears to be approximately two times higher in women than in men. However, the 1-year mortality rate in men after hip fracture is twice that in women [26]. Diagnostic evaluation and treatment of men at high risk for fracture remain low, despite the prevalence of this condition in men. According to our figures for men, bone mass reaches the peak level during 20–29-year period and it relatively keeps that level during 30–39-year period and BMD level starts decreasing after 40 years old. Results indicate that as it is the case in females, males should be cautious for possible fractures after 40 years old. In case of serious BMD decreasing, some actions should be taken such as modification in life style, doing more exercise and having medical treatment.

Our study also indicates that Non-Hispanic Black males have significantly higher BMD than Mexican-American and Non-Hispanic White in all age groups. Black males even have higher BMD in 40–49-year age group than peak levels of Mexican-American and White males which occur between 30 and 39 years. These findings are compatible with literature that low BMD is rare among the Non-Hispanic Blacks compared to others. In [27] BMD is compared in 1,209 Black, Hispanic, and White men. Black men exhibited higher BMD than Hispanic or White men. It has been detected that BMD decreases were greatest among Hispanic.

Recently one of the epidemiologic studies showed that 21.3% of the patients are detected as low BMD in general, while this ratio is 36% among the Non-Hispanic Whites and 38% among the Mexican-Americans. Studies indicate that Non-Hispanic Black children have higher trabecular bone density and have higher bone size in appendicular skeleton than their male counterparts [28]. This conclusion is based on having high level absorbance of renal calcium and having resistant bone tissue against parathormone among the Non-Hispanic Blacks [29].

Since residual bone mineral at the age of 60–90 years is the net result of multifactors, and since there are no safe, effective ways to rebuild the osteoporotic skeleton, prevention by maximizing bone mass during skeletal growth and development and minimizing postmenopausal bone losses emerges as the crucial strategy. Consequently, knowledge of appropriate timing of peak bone mass and BMD is essential if preventive measures are to be adequately implemented [30].

In this study we grouped the BMD of individuals by their age, race, and gender. This study indicates when each group reaches its peak BMD level. It is important to increase this level to prevent future low BMD cases. Also with the result of this study we will be able to take necessary actions when BMD shows start of significant drop compared to its peak level.

#### 4. Conclusion

This report presents bone measurement data from whole body DXA scans for persons aged 8 and over who participated in the 1999–2006 NHANES. One of the limitations of the present study is that we are not able to estimate the specific prevalence of osteoporosis and low bone mass in Asian or Hispanic groups since the data we have only provide information for Non-Hispanic Whites, Non-Hispanic Blacks, and Mexican-Americans.

However interpretation of the Tukey-Cramer confidence intervals provides the following conclusions. For the Mexican-American females the peak bone density is for 30–39-year group. This group does not differ from the age groups of 20–29 years and 40–49 years. However BMD level of 30–39 years (X5) differs from the age groups of 16–19 years and 50–59 years. These results suggest that, for Mexican-American females, individual should continue to build strong bones until their early twenties and should start to be examined after 50 years old for sudden drops in their BMD.

For Non-Hispanic White females the peak time for bone density is the same as Mexican-American females, 30–39 years. However the age group of 30–39 years is different than

that of 20–29 years with respect to their BMD. That means that this group should continue to build strong bones until their late twenties.

For the Non-Hispanic Black females the peak time of BMD is 30–39 years too. And this group is not statistically different than their 40–49 years. However BMD drops dramatically for the 50–59-year age group when it is compared with the age groups of 30–39 years and 40–49 years.

Different than the females, males reach the peak BMD during their 20–29 years. And this group is different than 16–19 years in all races. Mexican-Americans male and Non-Hispanic White males intend to keep their BMD level during their 30–39 years and 40–49 years the same as their female counterparts. However Non-Hispanic Black males show statistically significant difference in their 40–49-year age group. Although osteoporosis is not common among Non-Hispanic Black community, the sudden drop in 40–49-year age group of males should be examined in more detail in the future studies.

## Conflict of Interests

The authors declare that there is no conflict of interests regarding the publication of this paper.

## References

- [1] B. Jonsson, J. Kanis, A. Dawson, A. Oden, and O. Johnell, "Effect and offset of effect of treatments for hip fracture on health outcomes," *Osteoporosis International*, vol. 10, no. 3, pp. 193–199, 1999.
- [2] J. A. Kanis and F. A. Pitt, "Epidemiology of osteoporosis," *Bone*, vol. 13, no. 1, pp. S7–S15, 1992.
- [3] A. P. Cheung and B. G. Wren, "A cost-effectiveness analysis of hormone replacement therapy in the menopause," *Medical Journal of Australia*, vol. 156, no. 5, pp. 312–316, 1992.
- [4] K. T. Khaw, "Some implications of population change," in *The Strategy of Preventive Medicine*, G. Rose, Ed., p. 88, Oxford University Press, Oxford, UK, 1992.
- [5] R. A. Fisher, "The fiducial argument in statistical inference," *The Annals of Eugenics*, vol. 6, no. 4, pp. 391–398, 1935.
- [6] H. Jeffreys, "Note on the Behrens–Fisher formula," *The Annals of Eugenics*, vol. 10, pp. 48–51, 1940.
- [7] S.-H. Kim and A. S. Cohen, "On the Behrens-Fisher problem: a review," *Journal of Educational and Behavioral Statistics*, vol. 23, no. 4, pp. 356–377, 1998.
- [8] B. L. Welch, "The generalization of student's problem when several different population variances are involved," *Biometrika*, vol. 34, pp. 28–35, 1947.
- [9] G. S. James, "The comparison of several groups of observations when the ratios of the population variances are unknown," *Biometrika*, vol. 38, pp. 324–329, 1951.
- [10] A. J. Scott and T. M. F. Smith, "Interval estimates for linear combinations of means," *Journal of the Royal Statistical Society: Series C*, vol. 20, pp. 276–285, 1971.
- [11] M. B. Brown and A. B. Forsythe, "The small sample behavior of some statistics which test the equality of several means," *Technometrics*, vol. 16, pp. 129–132, 1974.
- [12] S.-Y. Chen and H. J. Chen, "Single-stage analysis of variance under heteroscedasticity," *Communications in Statistics Part B: Simulation and Computation*, vol. 27, no. 3, pp. 641–666, 1998.
- [13] W. R. Rice and S. D. Gaines, "One-way analysis of variance with unequal variances," *Proceedings of the National Academy of Sciences of the United States of America*, vol. 86, no. 21, pp. 8183–8184, 1989.
- [14] K. Krishnamoorthy, F. Lu, and T. Mathew, "A parametric bootstrap approach for ANOVA with unequal variances: fixed and random models," *Computational Statistics & Data Analysis*, vol. 51, no. 12, pp. 5731–5742, 2007.
- [15] S. Weerahandi, "ANOVA under unequal error variances," *Biometrics*, vol. 51, no. 2, pp. 589–599, 1995.
- [16] L. W. Xu and S. G. Wang, "A new generalized p-value and its upper bound for ANOVA under unequal error variances," *Communications in Statistics—Theory and Methods*, vol. 37, no. 7, pp. 1002–1010, 2008.
- [17] L.-W. Xu and S.-G. Wang, "A new generalized P-value for ANOVA under heteroscedasticity," *Statistics & Probability Letters*, vol. 78, no. 8, pp. 963–969, 2008.
- [18] H. O. Hartley, "The use of range in analysis of variance," *Biometrika*, vol. 37, pp. 271–280, 1950.
- [19] B. L. Welch, "On the comparison of several mean values: an alternative approach," *Biometrika*, vol. 38, no. 3/4, pp. 330–336, 1951.
- [20] C. Glastre, P. Braillon, L. David, P. Cochat, P. J. Meunier, and P. D. Delmas, "Measurement of bone mineral content of the lumbar spine by dual energy x-ray absorptiometry in normal children: correlations with growth parameters," *Journal of Clinical Endocrinology and Metabolism*, vol. 70, no. 5, pp. 1330–1333, 1990.
- [21] M. O'Brien, "Exercise and osteoporosis," *Irish Journal of Medical Science*, vol. 170, no. 1, pp. 58–62, 2001.
- [22] R. R. Recker, K. M. Davies, S. M. Henders, R. P. Heaney, M. R. Stegman, and D. B. Kimmel, "Bone gain in young adult women," *The Journal of the American Medical Association*, vol. 268, no. 17, pp. 2403–2408, 1992.
- [23] H.-S. Nam, S.-S. Kweon, J. M. Zmuda et al., "Racial/ethnic differences in bone mineral density among older women," *Journal of Bone and Mineral Metabolism*, vol. 31, no. 2, pp. 190–198, 2013.
- [24] G. M. Kiebzak, G. A. Beinart, K. Perser, C. G. Ambrose, S. J. Siff, and M. H. Heggeness, "Undertreatment of osteoporosis in men with hip fracture," *Archives of Internal Medicine*, vol. 162, no. 19, pp. 2217–2222, 2002.
- [25] H. Burger, P. L. A. Van Daele, D. Algra et al., "The association between age and bone mineral density in men and women aged 55 years and over: the Rotterdam Study," *Bone and Mineral*, vol. 25, no. 1, pp. 1–13, 1994.
- [26] T. V. Nguyen, J. A. Eisman, P. J. Kelly, and P. N. Sambrook, "Risk factors for osteoporotic fractures in elderly men," *American Journal of Epidemiology*, vol. 144, no. 3, pp. 255–263, 1996.
- [27] A. B. Araujo, T. G. Travison, S. S. Harris, M. F. Holick, A. K. Turner, and J. B. McKinlay, "Race/ethnic differences in bone mineral density in men," *Osteoporosis International*, vol. 18, no. 7, pp. 943–953, 2007.
- [28] V. Gilsanz, D. L. Skaggs, A. Kovanlikaya et al., "Differential effect of race on the axial and appendicular skeletons of children," *Journal of Clinical Endocrinology and Metabolism*, vol. 83, no. 5, pp. 1420–1427, 1998.

- [29] D. E. Meier, M. M. Luckey, S. Wallenstein, T. L. Clemens, E. S. Orwoll, and C. I. Waslien, "Calcium, vitamin D, and parathyroid hormone status in young white and black women: association with racial differences in bone mass," *Journal of Clinical Endocrinology and Metabolism*, vol. 72, no. 3, pp. 703–710, 1991.
- [30] V. Matkovic, T. Jelic, G. M. Wardlaw et al., "Timing of peak bone mass in Caucasian females and its implication for the prevention of osteoporosis: inference from a cross-sectional model," *Journal of Clinical Investigation*, vol. 93, no. 2, pp. 799–808, 1994.

## Review Article

# Anthropometric Measurements Usage in Medical Sciences

Nevin Utkualp<sup>1</sup> and Ilker Ercan<sup>2</sup>

<sup>1</sup>Uludağ University School of Health, Bursa, Turkey

<sup>2</sup>Department of Biostatistics, Uludağ University Faculty of Medicine, Bursa, Turkey

Correspondence should be addressed to Nevin Utkualp; [nutkualp@uludag.edu.tr](mailto:nutkualp@uludag.edu.tr)

Received 22 January 2015; Revised 11 March 2015; Accepted 11 March 2015

Academic Editor: Juan A. Sanchis-Gimeno

Copyright © 2015 N. Utkualp and I. Ercan. This is an open access article distributed under the Creative Commons Attribution License, which permits unrestricted use, distribution, and reproduction in any medium, provided the original work is properly cited.

Morphometry is introduced as quantitative approach to seek information concerning variations and changes in the forms of organisms that described the relationship between the human body and disease. Scientists of all civilization, who existed until today, examined the human body using anthropometric methods. For these reasons, anthropometric data are used in many contexts to screen for or monitor disease. Anthropometry, a branch of morphometry, is the study of the size and shape of the components of biological forms and their variations in populations. Morphometrics can also be defined as the quantitative analysis of biological forms. The field has developed rapidly over the last two decades to the extent that we now distinguish between traditional morphometrics and the more recent geometric morphometrics. Advances in imaging technology have resulted in the protection of a greater amount of morphological information and have permitted the analysis of this information. The oldest and most commonly used of these methods is radiography. With developments in this area, CT and MRI have also been started to be used in screening of the internal organs. Morphometric measurements that are used in medicine, are widely used in the diagnosis and the follow-up and the treatment of the disease, today. In addition, in cosmetology use of these new measurements is increasing every day.

## 1. Introduction

Since ancient times, the human body has been measured for several reasons. During the ancient era, human body measurement was mostly practiced for the figurative arts. Eventually, the practice was adopted by the naturalist field and then by anthropologists to identify human basic morphological characteristics. The term anthropometria dates back to the 17th century in the naturalist field, when it first appeared in the short manual *Anthropometria* by Johann Sigismund Elsholtz [1–3]. The manual seems to be the earliest recorded material that investigated the human body for scientific and medical purposes. It introduced a quantitative approach to seek information concerning variations and changes in the forms of organisms that described the relationship between the human body and disease [4]. Elsholtz proposed that the use of anthropometry constituted a valuable measurement strategy for different fields such as medical practices, physiognomy, the arts, and ethics [3, 5]. In the second half of the century, a strong need for counting and measuring the human body arose, and the representation of the instruments

used in clinical practices became vital for the medical field. The *pulsilogium*, which was invented by Sanctorius at the University of Padua, was one of the first instruments in the field and was used to evaluate the pulse rate. During the 18th century, the well-known French anatomist Jean-Joseph Sue, Swiss physiognomist Johann Kaspar Lavater, and German naturalist Johann Friedrich Blumenbach presented valuable research on different issues concerning measurement [6]. At the prompting of these academics, “the season of measurers” began, and practitioners started to believe in the practical application of numbers. Making use of mathematics, geometry, and statistics, anthropologists presented human investigation methodologies and became “anthropometers” [1, 2]. The anthropologists’ prior object of investigation was “the skull,” which they believed represented the most important part of the body. The anthropometrical method became more popular in several fields due to the research of Adolphe Quetelet in the 19th century [2]. During this period, the new conceptualization of human diversity advanced this practice for the creation and validation of racial typologies [1].

In the West, the use of measurements and the description of the human body emerged among the artists of classical civilizations; however, more systematic body measurements and records gained importance due to the demands of early modern military organizations [2]. The measurement of the height of individuals, especially young men, became the basic procedure used to classify them as appropriate or not for military recruitment. Through the end of the 19th century, anthropometry became a new tool for clinical practices and taxonomy as public health measurements gained importance. In the 19th and 20th centuries, anthropometry manifested in the measurements of weight, circumference, stature, and skinfold thickness that were used to identify environmental influences that impacted child growth [4].

Because ancient anthropometric research was a relatively current concept, the related medical literature concerning nutrition and physical growth served as a valuable theoretical source. Hence, the biomedical literature of the World Health Organization (WHO) was regarded as one of the best sources that represented general health conditions within a society [3].

Because of its use as a measurement of physiological and developmental human growth, anthropometria appeared in several clinical practices that utilized instruments such as the manometer, sphygmograph, hemocytometer, hemoglobinometer, and spirometer [2]. The need for these measurements stemmed from the interaction between several intricately linked concepts, including nutrition and infection, psychosocial stress, food contaminants, hypoxia, and pollution [1]. Factors mostly linked to socioeconomic status and poverty indicated that body size was a signal for the quality of life. Thus, anthropometric practices could be used as a tool for social welfare, whereas factors such as culture, society, behavior, and the political economy played important but distal roles in the outcomes of growth and body size [1, 3, 5].

## 2. Historical Development of Anthropometry

Over the ages, all civilizations have been interested in the human body. Artists in particular have reflected the effects of this interest in their works.

In the ancient Egyptian, Greek, and Roman civilizations, famous artists used male figures in their artwork (i.e., pictures and statues) with the desire to represent issues such as beauty, virtue, independence, military power, and authority [6, 7].

In the ancient era, artists were interested in the depiction of body parts based on reciprocal proportions. Artists believed that the human body represented as “an ideal human figure” had specific proportions between its constituent parts. Throughout history, these proportions were considered to be canon. In practical use, any given part of the human body could be chosen for measurement and proportioned to the other parts due to the absence of standardized measurement units such as the meter, centimeter, or millimeter. Therefore, any given human body part could be described as a “unit of measurement” (module). These measurement units contained various modules such as the length of the feet, length of the hand, and height of the head [5, 8, 9].

Throughout history there have been studies related to the “human body” branches of art (i.e., sculpture and painting) as well as studies related to anatomy in the field of medicine. In the three most well-known ancient civilizations, scholars evaluated the “human body” using the concepts of canon and modules [6, 10].

## 3. Anthropometric Measurements in Ancient Civilizations

*3.1. Egyptian Civilization.* The first known dissections with the aim of learning (III century BC) were performed by scholars in Egypt [7]. In the most ancient canon, “length of feet” (LF) was used as the module. Human figures drawn on the walls of the pyramids by Egyptian artists were depicted with heights six times longer than the length of their feet; however, when the artists noticed that the proportions did not reflect reality, they adjusted the height of taller human figures to a height equivalent to seven feet. According to our present arithmetic knowledge, they proportioned the horizontal lines based on height and the vertical lines based on the width of the human body [7, 9].

*3.2. Ancient Greek Civilization.* The most famous artist of this era was Polykleitos. Polykleitos evaluated the human body and wrote the first known artistic anatomy book. The renowned scholars used the “width of hand” (WH) as a module and described the proportions he used between various body parts and the width of hand as well as the inequalities. During the period of Greek civilization, for the first time multiple equalities were used in drawings of the human body between the longitudinal, oblique, and transversal dimensions [7].

*3.3. Roman Civilization.* Roman artists and scholars further developed studies of the “human body.” Moreover, some equalities were described after a human figure in the college position was placed in a square frame. Because notables of the era such as Leonardo da Vinci found that the human figure in the college position had an equal length and width, human paintings were often performed using a square frame [7, 9, 10]. Artists during the era of the Roman Empire continued these studies by merging art with anatomy and quietly exploiting mathematics [11].

*3.4. Anthropometric Measurements during the Renaissance.* Great artists of the renaissance (Leonardo da Vinci and Albrecht Dürer) created many works based on these rules and proportions. Works related to the human body were developed according to rules that were considered to represent classical anthropometrical measurement techniques [7].

(i) The renowned renaissance artist Leonardo da Vinci was interested in both art and sciences. He performed cadaver dissections and notated his measurements, notes, and drawings with the attention to detail of a scientific investigator. For the first time in history, he investigated the human face, head, neck, and other related parts in detail, mainly following the “Polykleitan theory.” He worked on a drawing belonging to Vitruvius, and after rigorous investigation of this work he

demonstrated his success in this field. Indeed, the “Vitruvian man” became one of his most renowned works [7, 9].

(ii) Durer was a versatile artist and architect who worked in both the mathematics and anatomy fields. He was born in Germany and examined both the male and female figures from the perspective of science and art. However, in his era dissection was not allowed in Germany, so his work relied on the use of live models and examinations of the literature. He also has investigated the positions of the internal organs and depicted the projections of the spleen in his work. His most famous work titled “Adam and Eve” showed his incredibly rigorous calculations [7].

**3.5. Anthropometric Works in the “20th” Century.** After the 19th century, the concept of the “average” male figure was developed based on comprehensive measurements. In the early 20th century, the French doctor of medicine and painter-sculptor Paul Richer performed one of the most detailed and scientific studies of the postrenaissance era due to his use of anthropometric methods. He described the “average human figure” based on comprehensive measurements rather than the “ideal human figure.” He chose “height of head” as the module and depicted the front and the back view. Additionally, he explained human anatomy in the context of the medial and lateral views of the extremities [1, 5, 10].

Morphometrics, a branch of anthropometry, is the study of the size and shape of the components of biological forms and their variations in populations [11]. Morphometrics is a field concerned with studying variations and changes in forms (i.e., size and shape) of organisms; morphometrics can also be defined as the quantitative analysis of biological forms. The field has developed rapidly over the last two decades to the extent that we now distinguish between traditional morphometrics and the more recent geometric morphometrics [4].

**3.5.1. Traditional Morphometrics.** In traditional morphometrics, it is not possible to recover the shape of the original form using the usual data matrices of distance measurements, even as an abstract representation. The overall form is neither archived nor used in the analysis. For example, a researcher may know that several measurements share a common landmark, but this information is not used in the multivariate analyses. As a result, the analyses cannot be expected to be as powerful as they could be if that information were taken into account [4, 11].

Traditional morphometrics consisted of applying multivariate statistical analyses to sets of traditional measurements between points with biological and anatomical meanings to define shapes called landmarks. These measurements usually represented the lengths and widths of structures and the distances between certain landmarks, which are described as the points of correspondence on each matching object between and within populations. Sometimes angles and ratios were used [11, 12].

When multivariate morphometrics was combined with both quantitative morphology and multivariate statistics, several difficulties still remained. As an example, many ways of size correction were proposed, but there were great debates

about which method should be utilized [4, 11]. It was important due to little different results caused by different size correction methods. Second, homology of linear distances was difficult to be evaluated due to insufficiency of homologous points about defining many distances (maximum width, etc.). Thirdly, similar set of distance measures may be obtained from two different shapes because data did not include location of each distance measurement which were relative to the other distance measurements. Traditional morphometrics does not allow recovering shape of original form from usual data matrices even if it is an abstract representation. Archives and analyses did not include whole form. A researcher may know the common landmark shared by several measurements; however, this knowledge has no role in multivariate analyses. As a result, analyses will not be powerful as the condition which information were used in [4, 11–13].

**3.5.2. Geometric (Modern) Morphometrics.** In the 1960s and 1970s, biometricians began applying multivariate statistical analyses to sets of traditional measurements. Geometric morphometric methods are more valid than traditional morphometric methods in protecting morphological information and permitting the analysis of this information. For morphometrics to fulfill its promise of fusing geometry with biology there must be equal emphasis on the two components. Morphometric techniques need to be designed and applied with biology in mind, and the quantitative results must be directly interpretable using biological methods [11, 13].

In geometric morphometrics, biological shape is defined via transformation of the original shape, which is selected as a reference shape. Thompson proposed the idea in 1942, and although the method was attractive and promising for the analysis of biological shapes, the method did not have an analytical procedure. With the advent of computers, applications for morphometric analysis based on Thompson’s idea became possible. Data are recorded to represent the geometry of the structure being studied [11]. These data are in the form of two-dimensional (2D) or three-dimensional (3D) coordinates of morphological landmark-points. The estimates of the parameter of the fitted function can then be used as variables in standard univariate and multivariate statistical analyses [12]. The coordinates are much more useful than traditional measurements, and the usual distance measurements can be computed from the coordinates [11, 12, 14]. Using landmark coordinates, concise encoding of all information in any subset of distances or angles between them is possible. Analysis and visualization which is on coordinate-based approaches are called complete retention of geometric information from data collection. Within geometric morphometrics, collecting information concerning the location of different points as landmarks addresses comparisons between organic forms. Considering points as homogeneously distributed on the organism and have some biological meaning, a set of homologous points, landmarks provide information of biological life forms [11–13].

The fundamental advantages of geometric morphometrics over traditional approaches (i.e., multivariate morphometric techniques) include the development of powerful

statistical methods based on models that are used to examine the shape variation of all configurations that correspond to morphologic landmark locations. Indeed, in many biological or biomedical studies, the most efficient way to analyze the forms of whole biological organs or organisms is by registering landmarks [4]. Many studies in medicine are related to the examination of the geometrical properties of an organ or organism. In these studies, statistical analysis consists of the quantitative or qualitative measurement of given values; for example, recently a given organ or organism's appearance or shape has been used as the input data for the development of imaging techniques [13]. Commonly, quantitative or qualitative data sets used for statistical analysis consist of measurement values. In recent times, following the development of imaging techniques an organ or organism's appearance or shape began to be used as the input data [4]. In these studies, the statistical analysis consists of the quantitative or qualitative measurement of the given values.

For over 50 years, qualitative morphometric techniques have been used within limits to assess bone density. Grading systems for the spine and proximal femur were developed with the aim of characterizing the severity of bone loss. However, because the use of such systems could cause highly subjective interpretations, the inclusion of a series of reference radiographs is recommended. Quantitative morphometric techniques are repeatedly used for imaging of the spine or proximal femur with X-rays. However, some measurement parameters were required for these techniques to produce a quantitative assessment of the severity of bone loss [15–17].

#### **4. Radiological Development of Imaging Modalities**

Throughout history, many studies have focused on the human body, especially with the aim of identifying anatomical, physiological, and pathological features of the internal organs. Among these studies, those related to imaging modalities of internal organs are especially very valuable [18, 19]. During his work with cathode ray tubes in 1895, German physicist Wilhelm Conrad Röntgen noticed radiating rays when high-voltage electric current passed through a Crookes tube; Röntgen named them unknown rays (X-rays). On December 22, 1895, Röntgen obtained an image of his wife's hand following 15 minutes of irradiation. These rays were identified as very high frequency electromagnetic waves with light bursts as fluorescence. X-rays can pass through soft tissues and partially penetrate into dense tissues such as bone. This process enabled internal views to be obtained as images from living organisms. Röntgen presented his invention to the Physical Medicine Society in Germany, and two weeks later he obtained images of his own upper and lower teeth using irradiation on black paper and a glass photography plaque wrapped with plastic. These images represented the first radiography images. The first medical X-ray radiography (Röntgen graphy) in history was also obtained during these experiments, and Röntgen officially announced his important

discovery on December 28, 1895. Although potential radiation hazards due to the use of X-rays had been ignored, the dentist Frank Harrison reported skin peeling and hair loss in his patients due to the use of X-ray radiography [15, 16].

In Turkey, the usage of X-rays in the field of medicine was first performed by medical students Esat Feyzi and Osman Rifat. Both students detected bullets in wounded soldiers during the Ottoman-Greece battle using radiography [20–24]. One of the first studies concerning X-rays was performed by M. Hubert. In this study, Hubert evaluated the physiological and pathological values of kidneys collected from different species of animals. Rich et al. studied the X-ray sensitivity of human tumor cell. Both Rich et al. and Taoka and Shuloeva provided examples of roentgenological studies of pulmonary function [22, 23, 25].

#### **5. Computerized Tomography (CT)**

The first quantitative CT measurement was proposed by Johann Radon. In 1972, J. N. Hounsfield scanned a section using thin and weak X-rays and turned the result into an image after computer evaluation by reading the signals in the scintillation chamber. Using this technique, a cross-sectional image could be obtained from anywhere in the body. Investigations of the CT accessibility of tissues and body regions showed that CT is more successful in imaging bone tissue than soft tissues due to its working principles and design. This invention was an important development for the imaging of brain and malignant tumors [26, 27].

Quantitative computed tomography (CT) is used for quantifying bone mineral density (BMD) in the spine, proximal femur, forearm, and tibia as a three-dimensional non-projectional technique. It has several advantages over other densitometric techniques, including the ability to separate the cortical and trabecular bone, the fact that degenerative changes in the spine cannot affect the volumes of interest (VOI), and the ability to determine 3D geometric parameters [26, 28].

#### **6. Magnetic Resonance (MR) Imaging Technique**

The identification of spin-based physic resonance by Wolfgang Pauli in 1920 initiated the first attempts to obtain images using the MR technique. Quantitative measurements in this field were first performed by physicists Bloch and Purcell. In their experiments, they demonstrated that atoms with one nucleon in their core were affected by the magnetic field and that the orbit of the atomic cores was changed in response to the magnetic field. For a long time, this finding was applied solely to the field of physics. Then, in 1970 Paul Lauterbur obtained a clear MR image. The first diagnosis using this modality was performed by Hawkes et al. in 1980. Currently, the ability to obtain fast and quality images of internal organs using the MR technique and the relatively low risk of side effects has led to its common use both internationally and nationally [26–30].

## 7. Current Utilization of Three-Dimensional Imaging

Currently, the direct calculation of the measurements of morphometric quantitative area shapes has been made possible by utilizing various programs after the common usage of MRG. Due to its imaging capacity on multiple planes, absence of ionizing radiation, and utilization for the diagnosis of mediastinum, this method has an important place in the field of medicine [29].

Mathematical analyses are used to identify the shape of an anatomic region in the human body. These evaluations are performed using optic measuring methods with 3D imaging modalities. These methods are especially important for quantitating data in the complex anatomical structures of the human body. The assessment of the validity and safety of these data has led to improvements in human health and quality of life [31].

The most commonly used imaging modality trio today includes the PET/CT modalities. In addition to imaging structures in the human body, these modalities can also detect exact tumor locations and biological properties that are essential for diagnoses in cancer patients [28, 30].

Anthropometric measurements are important for the evaluation of morbidities of individuals in society and thus meet the requirements of that society. For human health, the field of medicine requires constant development and renewal. Throughout history, anthropometric measurements were improved as details of human anatomy were discovered, until the field reached today's standards. In recent years, the utilization of many new measurement devices for clinical use and primary studies has inevitably led to improvements in measurement parameters and techniques [6, 7].

In the eras of the Ancient Egyptian, Greek, and Roman civilizations, artists made detailed evaluations of the human body. Artists of the renaissance period created ideal ratios in their works using mathematical methods (i.e., canons and module measurement). The "golden ratio" that was used by Leonardo da Vinci in his drawings currently remains the norm for beauty. In this ratio, anthropometric data and ratios are used to compare the ratios of disproportions present on the face [7].

A tendency towards plastic surgeries has become widespread over the past several years. Interventions related with this field include corrections of congenital malformations as well as various optional modifications on individual's bodies. Anthropometries of the human body and especially the face are used for the identification of these disproportions. Therefore, more standardized and purpose-oriented measurements in the field of plastic surgery are important for a more objective evaluation of human bodies [32].

## 8. Cosmetology

The use of imaging techniques in facial cosmetics is an undesirable feature caused by extrinsic photo damage and the intrinsic aging process [33]. A decrease in wrinkle severity has become a very important evaluation criterion in aesthetic dermatology for the assessment of the success of

rejuvenating treatments. Many quantification methods have been developed to analyze wrinkles. The comparative evaluation of modern scales and 3D images can lead to a further understanding of facial wrinkles and may elucidate the connection between clinical assessment and appraisal using biophysical measuring methods. Luebberding et al. investigated facial wrinkles in a study designed to compare clinical ratings and 3D fringe projections [34]. Jiang et al. [35] used the SWIRL (Stephens wrinkle imaging raking light) method as an example. The use of this method represents a step towards better understanding of the actions and changes produced by prescription and cosmetic wrinkle treatment products and medical procedures [35]. Another branch of medicine using imaging techniques is breast cosmetics. However, the concept of breast size itself remains controversial. Breast volume and breast density must be distinguished, and the appropriate measurement, whether subjective reporting, cup size, mammographic assessment, or three-dimensional imaging, remains unclear [26]. Ultrasound and mammography are useful imaging techniques for the assessment of reconstructed breasts in symptomatic settings. Magnetic resonance imaging of the breast is another important diagnostic technique that is useful for breast cancer. Its performance is indicated in several situations, including staging of the disease and treatment planning [27]. MR imaging is the most accurate of the three preoperative imaging modalities in assessing the size and number of malignant lesions in the breast. The studies of Faermann et al. [29] were the first to assess the tumor-to-breast volume ratio measured by MRI and to correlate it to the type of surgery selected for the patient (i.e., breast conservation or mastectomy) [29]. To evaluate the comparative accuracy of magnetic resonance (MR) imaging relative to mammography and ultrasonography (US) for the assessment of the extent of breast tumors, Yılmaz et al. reviewed the findings of Boetes et al. [28] and Fischer et al. [30] and suggested that the sensitivity and specificity of US and MRI exams for detecting local recurrence were higher than clinical examinations [7, 28, 30]. Furthermore, MRI plays an important role in treatment planning and is more objective in determining the response of tumoral lesions to systemic treatment. The use of 3D imaging and computerized measurements brings a new dimension into surgical planning. Indeed, studies showed that the portrait 3D platform create in cosmetology [35].

Today, many fields, including plastic surgery, depend on photo documentation as a crucial part of both clinical practice and medical education. The most recent advancement in breast plastic surgery is ideally suited for 3D technology. The portrait 3D breast imaging system provides a highly reproducible 3D tool for measuring breast volume and simulating breast augmentation [33].

## 9. Conclusion

The main reasons for the widespread use of statistical shape analysis in medicine include the fact that geometric morphometric methods are more valid than traditional morphometric methods. Advances in imaging technology have resulted in the protection of a greater amount of morphological information and have permitted the analysis

of this information. There is hope that advances in both screening and diagnostic technology will ultimately have a positive impact on treatment. Furthermore, the use of these treatment modalities for cosmetic use has been rising.

## Conflict of Interests

The authors declare that there is no conflict of interests regarding the publication of this paper.

## References

- [1] S.-J. Ulijaszek and C. G. N. Mascie-Taylor, *Anthropometry: The Individual and the Population*, Cambridge University Press, Cambridge, UK, 2005.
- [2] A. Albrizio, "Biometry and anthropometry: from Galton to constitutional medicine," *Journal of Anthropological Sciences*, vol. 85, pp. 101–123, 2007.
- [3] T. Cuff, "Biometric method, past, present, and future," in *Historical Anthropometrics*, J. O. Irwin, Ed., pp. 363–375, Ashgate, Aldershot, UK, 1998.
- [4] I. Ercan, G. Ocakoglu, D. Sigirli, and G. Ozkaya, "Statistical shape analysis and usage in medical sciences," *Turkiye Klinikleri Journal of Biostatistics*, no. 4, pp. 27–35, 2012.
- [5] F. Vegter and J. J. Hage, "Clinical anthropometry and canons of the face in historical perspective," *Plastic and Reconstructive Surgery*, vol. 106, no. 5, pp. 1090–1096, 2000.
- [6] P. H. Smith, "Artists as scientists: nature and realism in early modern Europe," *Endeavour*, vol. 24, no. 1, pp. 13–21, 2000.
- [7] A. Yılmaz, S. Çikmaz, and R. Mesut, "Evaluation of turkish males with respect to Leonardo' scircle and upper extremity ratios," *Balkan Medical Journal*, vol. 22, pp. 137–141, 2005.
- [8] A. Özaslan, M. Y. İşcan, İ. Özaslan, H. Tuğcu, and S. Koç, "Estimation of stature from body parts," *Forensic Science International*, vol. 132, no. 1, pp. 40–45, 2003.
- [9] K. Çokanov, *Plastic Anatomy*, Nauka i İzkustvo, Sofia, Bulgaria, 1974.
- [10] M. Popov, *Anthropology of the Bulgarian Nation. Fiziçeski Oblik na Bilgarite*, BAN, Sofya, Bulgaria, 1959.
- [11] G. Ocakoglu and I. Ercan, "Traditional and modern morphometrics," *Turkiye Klinikleri Journal of Biostatistics*, vol. 5, no. 1, pp. 37–41, 2013.
- [12] D. W. Shaffer, "Learning mathematics through design: the anatomy of Escher's world," *Journal of Mathematical Behavior*, vol. 16, no. 2, pp. 95–112, 1997.
- [13] D. Sigirli and I. Ercan, "Growth and allometry in modern morphometrics," *Türkiye Klinikleri Journal of Biostatistics*, vol. 5, no. 1, pp. 42–48, 2013.
- [14] S. Lele, "Some comments on coordinate-free and scale-invariant methods in morphometrics," *American Journal of Physical Anthropology*, vol. 85, no. 4, pp. 407–417, 1991.
- [15] A. Assmus, "Early history of X rays," *Beam Line*, vol. 25, no. 2, pp. 10–24, 1995.
- [16] L. Alfred and M. D. Weber, "History of head and neck radiology: past, present and future," in *Radiology, Radiographics*, vol. 34, no. 5, chapter 26, pp. 1442–1451, 2001.
- [17] K. Engelke, J. E. Adams, G. Armbrecht et al., "Clinical use of quantitative computed tomography and peripheral quantitative computed tomography in the management of osteoporosis in adults: the 2007 ISCD Official Positions," *Journal of Clinical Densitometry*, vol. 11, no. 1, pp. 123–162, 2008.
- [18] S. L. Bonnick and L. A. Lewis, *Bone Densitometry for Technologists*, Springer, New York, NY, USA, 2013.
- [19] J. Rösch, F. S. Keller, and J. A. Kaufman, "The birth, early years, and future of interventional radiology," *Journal of Vascular and Interventional Radiology*, vol. 14, no. 7, pp. 841–853, 2003.
- [20] S. M. Weinberg, S. Naidoo, D. P. Govier, R. A. Martin, A. A. Kane, and M. L. Marazita, "Anthropometric precision and accuracy of digital three-dimensional photogrammetry: comparing the genex and 3dMD imaging systems with one another and with direct anthropometry," *Journal of Craniofacial Surgery*, vol. 17, no. 3, pp. 477–483, 2006.
- [21] M. Hubert and M. D. Turnbull, "pyelo-radiography: a clinical study: with pathological reports by Hubert M. Turnbull, M.D.; skiagrams by S. Gilbert Scott; and experimental studies by E. C. Lindsay, F.R.C.S.," *Proceedings of the Royal Society of Medicine*, vol. 7, pp. 16–40, 1914.
- [22] M. Rich, N. Delihias, and E. Mlacta, "Studies on the x-ray sensitivity of human tumor cells exposed to 5 brom odeoxyuridin," *Acta: Unio Internationalis Contra Cancrum*, no. 20, pp. 1211–1212, 1964.
- [23] T. Taoka, N. Igaku, and H. G. Zasshi, "Roentgenological studies on the pulmonary function. On the pulmonary function of the postoperative irradiation on the breast cancer," *Nippon Igaku Hoshasen Gakkai zasshi. Nippon acta radiologica*, vol. 24, no. 12, pp. 1242–1254, 1965.
- [24] M. Canger and P. Çelenk, "Development of dental radiology in the world and Turkey," *Turkiye Klinikleri Journal of Medical Ethics-Law and History*, no. 14, pp. 841–853, 2003.
- [25] Z. A. Shuloeva, "Roentgenological studies on late and remote complications after radical surgery in pulmonary tuberculosis," *Vestnik Rentgenologii i Radiologii*, vol. 40, no. 2, pp. 67–68, 1965.
- [26] L. A. Jansen, R. M. Backstein, and M. H. Brown, "Breast size and breast cancer: a systematic review," *Journal of Plastic, Reconstructive & Aesthetic Surgery*, vol. 67, no. 12, pp. 1615–1623, 2014.
- [27] Y. T. Sim and J. C. Litherland, "The use of imaging in patients post breast reconstruction," *Clinical Radiology*, vol. 67, no. 2, pp. 128–133, 2012.
- [28] C. Boetes, R. D. M. Mus, R. Holland et al., "Breast tumors: comparative accuracy of MR imaging relative to mammography and ultrasound for demonstrating extent," *Radiology*, vol. 197, no. 3, pp. 743–747, 1995.
- [29] R. Faermann, F. Sperber, S. Schneebaum, and D. Barsuk, "Tumor-to-breast volume ratio as measured on MRI: a possible predictor of breast-conserving surgery versus mastectomy," *Israel Medical Association Journal*, vol. 16, no. 2, pp. 101–105, 2014.
- [30] U. Fischer, L. Kopka, and E. Grabbe, "Breast carcinoma: effect of preoperative contrast-enhanced MR imaging on the therapeutic approach," *Radiology*, vol. 213, no. 3, pp. 881–888, 1999.
- [31] M. H. Yilmaz, G. Esen, Y. Ayarcan et al., "The role of US and MR imaging in detecting local chest wall tumor recurrence after mastectomy," *Diagnostic and Interventional Radiology*, vol. 13, no. 1, pp. 13–18, 2007.
- [32] I. L. Dryden and K. V. Mardia, *Statistical Shapeanalysis*, John Wiley & Sons, Chichester, UK, 1998.
- [33] B. Mailey, A. Freel, R. Wong, D. T. Pointer, and K. Khoobeih, "Clinical accuracy and reproducibility of Portrait 3D Surgical

Simulation Platform in breast augmentation,” *Aesthetic Surgery Journal*, vol. 33, no. 1, pp. 84–92, 2013.

- [34] S. Luebberding, N. Krueger, and M. Kerscher, “Comparison of validated assessments cales and 3D digital fringe projection method to assess life time development of wrinkles in men,” *Skin Research and Technology*, vol. 20, no. 1, pp. 30–36, 2014.
- [35] L. I. Jiang, T. J. Stephens, and R. Goodman, “SWIRL, a clinically validated, objective, and quantitative method for facial wrinkle assessment,” *Skin Research and Technology*, vol. 19, no. 4, pp. 492–498, 2013.

## Research Article

# Three-Dimensional Assessment of Bilateral Symmetry of the Scaphoid: An Anatomic Study

Paul W. L. ten Berg,<sup>1</sup> Johannes G. G. Dobbe,<sup>2</sup> Simon D. Strackee,<sup>1</sup> and Geert J. Streekstra<sup>2,3</sup>

<sup>1</sup>Department of Plastic, Reconstructive, and Hand Surgery, Academic Medical Center, University of Amsterdam, Meibergdreef 9, 1105 AZ Amsterdam, Netherlands

<sup>2</sup>Department of Biomedical Engineering and Physics, Academic Medical Center, University of Amsterdam, Meibergdreef 9, 1105 AZ Amsterdam, Netherlands

<sup>3</sup>Department of Radiology, Academic Medical Center, University of Amsterdam, Meibergdreef 9, 1105 AZ Amsterdam, Netherlands

Correspondence should be addressed to Paul W. L. ten Berg; [p.w.tenberg@amc.uva.nl](mailto:p.w.tenberg@amc.uva.nl)

Received 11 February 2015; Revised 20 March 2015; Accepted 20 March 2015

Academic Editor: Heather F. Smith

Copyright © 2015 Paul W. L. ten Berg et al. This is an open access article distributed under the Creative Commons Attribution License, which permits unrestricted use, distribution, and reproduction in any medium, provided the original work is properly cited.

Preoperative 3D CT imaging techniques provide displacement analysis of the distal scaphoid fragment in 3D space, using the matched opposite scaphoid as reference. Its accuracy depends on the presence of anatomical bilateral symmetry, which has not been investigated yet using similar techniques. Our purpose was to investigate symmetry by comparing the relative positions of distal and proximal poles between sides. We used bilateral CT scans of 19 adult healthy volunteers to obtain 3D scaphoid models. Left proximal and distal poles were matched to corresponding mirrored right sides. The left-to-right positional differences between poles were quantified in terms of three translational and three rotational parameters. The mean (SD) of ulnar, dorsal, and distal translational differences of distal poles relative to proximal poles was 0.1 (0.6); 0.4 (1.2); 0.2 (0.6) mm and that of palmar rotation, ulnar deviation, and pronation differences was  $-1.1$  (4.9);  $-1.5$  (3.3);  $1.0$  (3.7)°, respectively. These differences did not significantly differ from zero and thus were not biased to left or right side. We proved that, on average, the articular surfaces of scaphoid poles were symmetrically aligned in 3D space. This suggests that the contralateral scaphoid can serve as reference in corrective surgery. No level of evidence is available.

## 1. Introduction

A scaphoid waist fracture with displacement in which the proximal and distal poles are malaligned is seen as an indication for surgery [1]. Scaphoid fractures that failed to unite (i.e., nonunions) are associated with a flexion deformity with bone loss around fracture sites, in which the distal fragment rotates in palmar direction. Besides achieving union, the surgeon's goal is to adequately restore the normal scaphoid alignment by an adequate reduction of the fragments. In the treatment of scaphoid nonunions, the surgeon often uses an interpositional cortical bone graft between the fragments to accomplish this goal [1]. Failure of restoring alignment results in a malunited scaphoid which may lead to pain and restricted motion [2].

In current clinical practice, assessment of displacement is based on measurements using two-dimensional (2D) images (i.e., radiographs and single CT slices) which is subjective due to manual measurements, position of the wrist during imaging, and/or slice selection [3, 4]. This method of assessment has shown to be poorly reliable and is prone to inter- and intraobserver variability [5–7], making clinical decision making and surgical planning difficult. For an optimal surgical planning, a 3D approach is required to adequately restore the anatomical alignment of the articular surfaces of proximal and distal poles, since fracture displacement is a 3D problem [2].

Quantitative 3D CT imaging techniques can be applied to assess the level of scaphoid fracture displacement in 3D space,

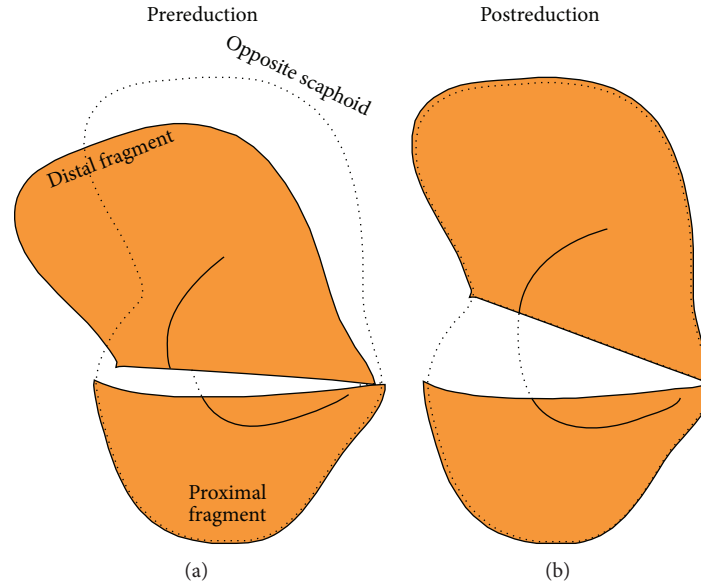


FIGURE 1: Scheme of 3D model of scaphoid fragments before virtual reduction (a) and after reduction (b). The mirrored opposite scaphoid (dotted outline) serves as guide to virtually reduce the nonunion fragments. This method enables quantifying the amount of displacement of the distal fragment in 3D space.

demonstrated by several recently published studies [2, 8, 9]. This technique is independent of imaging position of the wrist or slice selection. It is based on virtual reduction of the proximal and distal poles of the opposite mirrored healthy scaphoid as template (Figure 1). After virtual reduction, the amount of displacement of the distal scaphoid fragment can be quantified in terms of three translational parameters (ulnar, dorsal, and distal) and three rotational parameters (palmar flexion, ulnar flexion, and pronation).

A prerequisite for a reduction technique that uses the opposite scaphoid as reference is the presence of normal bilateral symmetry [10]. Asymmetry may be a limiting factor in the accuracy of this displacement analysis. Using such a potentially biased displacement analysis for surgical planning may cause an inconsistency between the achieved postreduction position and desired pretraumatic position of the distal scaphoid fragment. However, there are no reports quantifying symmetry in terms of the translational and rotational differences of scaphoid poles in 3D space. Therefore, it is unclear whether or not results of the level of fracture displacement are systematically biased in existing or future clinical scaphoid studies relying on these imaging techniques.

The purpose of this anatomic 3D CT study was to investigate the symmetry of healthy scaphoid pairs. To this end, we quantified side-to-side differences of the positions of distal poles within healthy scaphoid pairs in terms of the three translational and three rotational parameters. We hypothesize that there is no bias to the left or right side in each of these parameters, showing average difference values not significantly different from zero.

## 2. Materials and Methods

**2.1. Data Acquisition.** Nineteen healthy right-handed volunteers participated in this study (13 women and six men; average age: 26 y; range: 22–56 y). The subjects had no history of wrist injury or other musculoskeletal disorders. A high-resolution CT scan (Philips Brilliance 64 CT scanner, Cleveland, OH) was made of both wrists (i.e., bilateral CT scan) of each individual using standardized methods (voxel size  $0.45 \times 0.45 \times 0.45$  mm., 120 kV, 150 mAs, pitch 0.6, and slice thickness 0.67 mm.). The CT scans were used for subsequent 3D image analyses. To determine the methodological accuracy and reproducibility of our method, one cadaver arm was scanned multiple times (10x), using the same scan protocol. This study was approved by our Human Research Committee. Informed consent of each individual was obtained prior to participation.

**2.2. Assessment of Side-to-Side Positional Differences.** First, from each scaphoid pair, the left scaphoid is segmented from a CT scan, based on custom made software [10]. A 3D polygon mesh from the segmented data is derived which served as a virtual 3D model of the bone. To allow comparison of side-to-side differences between subjects in an unambiguous fashion, an anatomical coordinate system is defined for every scaphoid model based on its inertial properties (Figure 2) [11].

Next, we selected a proximal and a distal pole of 25% of the total length of the left scaphoid (Figure 2). The central 50% of the scaphoid, in which the fracture usually occurs [12], is therefore omitted from this analysis. Next, the left scaphoid is matched with the mirrored CT image of the right scaphoid

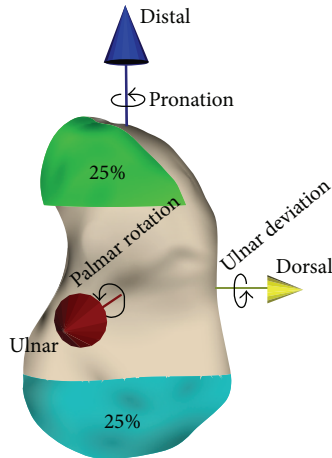


FIGURE 2: Virtual model of a left scaphoid with anatomical coordinate system, defining translational and rotational differences. After matching the proximal (blue; 25%) poles, side-to-side differences are shown as the degree in which the positions of the distal poles (green; 25%) differ between the left and right sides.

by aligning the proximal poles using intensity-based image registration [13].

For this registration process, first, a 3D double-contour polygon is automatically created based on the initial 3D polygon mesh of the left scaphoid by sampling the image intensity 0.3 mm toward the inside (high CT value) and outside (low CT value) of the bone, along the surface normal vector. The points of the double-contour polygon of the left proximal pole are registered with the reference image of the mirrored right scaphoid in a rigid point-to-image registration procedure [13]. This procedure uses the Nelder-Mead downhill simplex optimizer with a six-parameter search space (three displacements and three rotations) while the correlation coefficient was used as metric unit, which quantifies how well the gray-level points fit the reference image [14, 15]. The use of a double-contour polygon makes the registration highly discriminative [13].

Then, side-to-side differences are expressed as the degree in which the positions of the distal poles differ, relative to the proximal pole, between left and right scaphoids. The three translational differences (ulnar, dorsal, and distal translational) and three rotational differences (palmar rotation, ulnar deviation, and pronation) are derived from the  $4 \times 4$  transformation matrices that resulted from image registration [13].

Statistical analyses of the measurements included the Shapiro Wilks W test as normality test, determining the mean and standard deviation (SD) for normally distributed data. A one-sample  $t$ -test was used to investigate whether the six means of the translational and rotational differences differ significantly from zero. A post hoc power analysis for one-sample  $t$ -test was used to calculate the level of mean side-to-side differences that could have been tested on significance with sufficient power. This power analysis requires input of the sample size ( $N = 19$ ), comparison mean ( $=0$ ) and

standard deviation, while using an  $\alpha$ -level of 0.05 and a power of 0.80. A 5% significance level was used for the analyses.

**2.3. Accuracy and Reproducibility of the Method.** We assessed the accuracy and reproducibility of our method by investigating the influence of the segmentation and matching procedure on translational and rotational side-to-side differences of the distal poles. To this end, we used ten CT scans of a single cadaveric arm. For each scan, the arm was scanned at a slightly different position inside the scanner to include possible variations in the reconstructed 3D image due to different positions of the wrist. Hereafter, a single 3D model of the scaphoid was obtained from the first CT scan. The proximal pole of this scaphoid model was selected and subsequently matched to the remaining nine scans of the same cadaver arm (Figure 3). The change in relative position of the distal pole with respect to the proximal pole before and after matching yields the “side-to-side positional differences” due to methodological errors. A zero mean of these differences indicates a high level of methodological accuracy, because, in this experimental study, true symmetry is present since the scaphoid is matched to itself. The standard deviation represents the reproducibility of the method.

### 3. Results

**3.1. Accuracy and Reproducibility.** Accuracy and reproducibility of radioulnar, palmodorsal, and proximodistal translation of the distal pole relative to the proximal pole were (mean (SD))  $-0.1$  (0.1),  $0.1$  (0.1), and  $0.0$  (0.1) mm, respectively. Accuracy and reproducibility of dorsopalmar rotation, radioulnar deviation, and supination and pronation deviation of the distal pole relative to the proximal pole were (mean (SD)) equal to  $-0.1$  (0.5),  $0.1$  (0.4), and  $-0.1$  (0.3) degrees, respectively. All means did not deviate more than a tenth of a millimeter or degree from zero indicating a high level of methodological accuracy. All standard deviations were lower than a tenth of a millimeter or half a degree, indicating a relatively high reproducibility.

**3.2. Side-to-Side Positional Differences.** Values of all translational and rotational differences of the distal poles of the 19 scaphoid pairs were normally distributed. Corresponding means and standard deviations are listed in Table 1. To perform the power analysis, we calculated the average standard deviation (SD) of the 3 translational differences (mm) and of the 3 rotational differences ( $^{\circ}$ ), resulting in a SD of  $\pm 0.8$  mm and SD of  $\pm 4.0^{\circ}$ . Based on these SDs, there was sufficient power to detect a significant left-right bias if mean side-to-side differences were  $>0.5$  mm, regarding translational differences, and a significant left-right bias if mean side-to-side differences were  $>2.6^{\circ}$ , regarding rotational differences. Our reported mean side-to-side differences were smaller than these cut-offs and were not statistically different from zero (Table 1 and Figure 4). This indicated that, in our sample, differences were not biased to a left or right side. The spread in these differences due to individual left-to-right variability is much larger than the methodological errors found above.

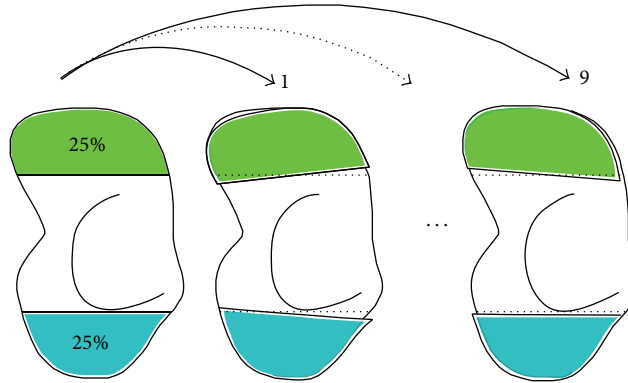


FIGURE 3: Scheme of the cadaveric experiment assessing the accuracy and reproducibility of the matching procedure. After scanning one cadaveric arm tenfold, the scaphoid from one CT scan was segmented (left model). The proximal (blue) poles were matched to the remaining 9 scans enabling displacement analysis of the distal (green) pole.

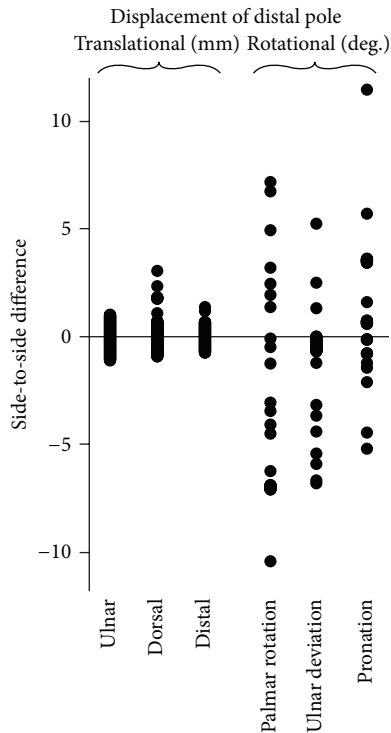


FIGURE 4: Scatterplot showing the left-to-right alignment differences of the distal poles of the 19 uninjured scaphoid pairs. Each dot represents a side-to-side difference for an individual healthy subject expressed in terms of an anatomical coordinate system (Figure 2). Negative displacement values represent opposite directions.

#### 4. Discussion

We used a quantitative 3D CT method to investigate the degree of positional differences of distal poles between healthy scaphoids sides. The proposed method of evaluation includes determination of an anatomical coordinate system that permits objectively comparing side-to-side differences of different individuals. The applied technique has proven to be accurate and highly reproducible. Overall, the translation

TABLE 1: Results of the left-to-right alignment differences of the distal poles represented by the six side-to-side differences based on the anatomical coordinate system. Negative displacement values represent opposite directions.

Displacement	Mean	Compared to 0 ( <i>p</i> value)	SD
Translational			
Ulnar (mm)	0.1	0.50	0.6
Dorsal (mm)	0.4	0.11	1.2
Distal (mm)	0.2	0.17	0.6
Rotational			
Palmar rotation (deg.)	-1.1	0.32	4.9
Ulnar deviation (deg.)	-1.5	0.07	3.3
Pronation (deg.)	-1.0	0.27	3.7

and rotation differences between sides did not significantly differ from zero. This implied that there was no bias to the left or right side, indicating anatomical bilateral symmetry of the scaphoid poles in 3D space.

A limitation of our study is that all participants were right handed, which does not provide information about the side-to-side differences in left-handed individuals. Despite being not proven in this study, we expect similar results for left-handed individuals.

In upper extremity surgery, the opposite healthy bone can be used to plan and guide reconstruction of complex fractures [16, 17]. However, the presence of bilateral asymmetry in bone shape could hamper using the opposite bone as a reference for planning. Studies have documented greater right biases in upper limb bone dimensions especially in length [18, 19]. For example, in healthy radius pairs, there is a length bias in which the dominant right side is generally longer [10]. This may cause an over- or underestimation of the pretraumatic length of an injured radius when using the opposite radius as guide.

Regarding the scaphoid, the level of bilateral symmetry has previously been investigated in several studies. Smith investigated left-to-right differences based on length,

height, and intrascaphoid angle in 2D reconstructed sagittal and coronal sections from 30 healthy scaphoid pairs [20]. Heinzelmann et al. measured cadaveric scaphoids using a caliper [21]. In three 3D CT scaphoid studies, the length of long axes, volume, and surface area were measured [22–24]. In all aforementioned studies, on average, side-to-side differences were close to zero. However, these studies did not investigate symmetry of the relative position of the articular surfaces of scaphoid poles in terms of translational and rotational differences in 3D space. Three-dimensional information of these relative positions is of utmost importance in restoring normal alignment of the proximal and distal articular surfaces. It may help the surgeon in avoiding a scaphoid malunion in which the fragments have healed in malaligned configuration.

Although, on average, we found no left or right bias, in some individual cases, side-to-side differences were as large as 2 mm or 5–10°. These differences are small compared to values reported in clinical 3D CT studies investigating scaphoid nonunion deformity [2, 8, 25, 26]. Schweizer et al. found an average proximal translation of the distal pole of 3.3 mm and palmar flexion of 23° in 11 nonunions [2]. Thus, although perfect symmetry in individual cases was not observed, the contralateral side is still clinically useful as reference in reconstruction surgery.

The best reference is obviously the native, pretraumatic scaphoid itself, but scaphoid images before injury are only rarely available by coincidence. When using alternative references such as the contralateral side, one should question what difference between the postreduction and desired pretraumatic alignment can be considered clinically acceptable. This question is difficult to answer since recent articles focusing on the consequences of scaphoid malalignment are sparse. Some relatively old clinical articles suggested an association of malunion with pain, loss of motion and weakness after fracture healing [27–29] and with an increased risk of posttraumatic osteoarthritis [30]. In 1987, Burgess used four cadaveric wrists to simulate malunion [31]. He reported that an angular malalignment (i.e., palmar flexion of the distal pole) did not restrict wrist flexion and radial and ulnar deviation. Radiocarpal extension was reduced by 24° with 5° malalignment, and all extension was lost at 15° malalignment. In contrast, other studies concluded that there was no relationship of malunion with objective clinical outcome measures including range of motion and grip strength [6] or with long-term subjective outcome, including patient satisfaction [32]. All aforementioned studies, however, used 2D measures to assess malalignment including the intrascaphoid angle which are proven to be poorly reliable [3, 7]. Therefore, new biomechanical and clinical studies are needed to investigate the consequence of certain levels of malalignment, while using more reproducible measurement techniques, preferably in 3D space.

In conclusion, we proved that, on average, the articular surfaces of left and right scaphoid poles were symmetrically aligned. This suggests that the contralateral side is a useful reference in preoperative planning in reconstruction surgery of scaphoid fractures. Three-dimensional fracture displacement analysis provides objective information which may help

the surgeon in characterizing complex fractures and surgical decision making.

## Conflict of Interests

All named authors hereby declare that they have no conflict of interests to disclose.

## Acknowledgment

Paul W. L. ten Berg received a Ph.D. grant (2014) from the Academic Medical Center (Amsterdam, Netherlands) supporting this research.

## References

- [1] K. Megerle, P. S. Harenberg, G. Germann, and S. Hellmich, “Scaphoid morphology and clinical outcomes in scaphoid reconstructions,” *Injury*, vol. 43, no. 3, pp. 306–310, 2012.
- [2] A. Schweizer, P. Fürnstahl, and L. Nagy, “Three-dimensional computed tomographic analysis of 11 scaphoid waist non-unions,” *The Journal of Hand Surgery*, vol. 37, no. 6, pp. 1151–1158, 2012.
- [3] G. I. Bain, J. D. Bennett, J. C. MacDermid, G. P. Slethaug, R. S. Richards, and J. H. Roth, “Measurement of the scaphoid humpback deformity using longitudinal computed tomography: intra- and interobserver variability using various measurement techniques,” *Journal of Hand Surgery*, vol. 23, no. 1, pp. 76–81, 1998.
- [4] M. Bhat, M. McCarthy, T. R. C. Davis, J. A. Oni, and S. Dawson, “MRI and plain radiography in the assessment of displaced fractures of the waist of the carpal scaphoid,” *The Journal of Bone and Joint Surgery—British Volume*, vol. 86, no. 5, pp. 705–713, 2004.
- [5] G. A. Buijze, P. Jørgsholm, N. O. B. Thomsen, A. Björkman, J. Besjakov, and D. Ring, “Diagnostic performance of radiographs and computed tomography for displacement and instability of acute scaphoid waist fractures,” *The Journal of Bone & Joint Surgery Series A*, vol. 94, no. 21, pp. 1967–1974, 2012.
- [6] D. P. Forward, H. P. Singg, S. Dawson, and T. R. C. Davis, “The clinical outcome of scaphoid fracture malunion at 1 year,” *Journal of Hand Surgery: European Volume*, vol. 34, no. 1, pp. 40–46, 2009.
- [7] D. Ring, J. D. Patterson, S. Levitz, C. Wang, and J. B. Jupiter, “Both scanning plane and observer affect measurements of scaphoid deformity,” *The Journal of Hand Surgery*, vol. 30, no. 4, pp. 696–701, 2005.
- [8] K. Oka, H. Moritomo, T. Murase, A. Goto, K. Sugamoto, and H. Yoshikawa, “Patterns of carpal deformity in scaphoid nonunion: a 3-dimensional and quantitative analysis,” *Journal of Hand Surgery*, vol. 30, no. 6, pp. 1136–1144, 2005.
- [9] K. Oka, T. Murase, H. Moritomo, A. Goto, K. Sugamoto, and H. Yoshikawa, “Patterns of bone defect in scaphoid nonunion: a 3-dimensional and quantitative analysis,” *The Journal of Hand Surgery*, vol. 30, no. 2, pp. 359–365, 2005.
- [10] J. C. Vroemen, J. G. G. Dobbe, R. Jonges, S. D. Strackee, and G. J. Streekstra, “Three-dimensional assessment of bilateral symmetry of the radius and ulna for planning corrective surgeries,” *Journal of Hand Surgery*, vol. 37, no. 5, pp. 982–988, 2012.

- [11] J. C. Coburn, M. A. Upal, and J. J. Crisco, "Coordinate systems for the carpal bones of the wrist," *Journal of Biomechanics*, vol. 40, no. 1, pp. 203–209, 2007.
- [12] W. B. Geissler, J. E. Adams, R. R. Bindra, W. D. Lanzinger, and D. J. Slutsky, "Scaphoid fractures: what's hot, what's not," *The Journal of Bone and Joint Surgery—American Volume*, vol. 94, no. 2, pp. 169–181, 2012.
- [13] J. G. G. Dobbe, S. D. Strackee, A. W. Schreurs et al., "Computer-assisted planning and navigation for corrective distal radius osteotomy, based on pre- and intraoperative imaging," *IEEE Transactions on Biomedical Engineering*, vol. 58, no. 1, pp. 182–190, 2011.
- [14] B. Carelsen, R. Jonges, S. D. Strackee et al., "Detection of in vivo dynamic 3-D motion patterns in the wrist joint," *IEEE Transactions on Biomedical Engineering*, vol. 56, no. 4, pp. 1236–1244, 2009.
- [15] G. J. M. Tuijthof, L. Beimers, R. Jonges, E. R. Valstar, and L. Blankevoort, "Accuracy of a CT-based bone contour registration method to measure relative bone motions in the hindfoot," *Journal of Biomechanics*, vol. 42, no. 6, pp. 686–691, 2009.
- [16] P. Frnstahl, G. Szkely, C. Gerber, J. Hodler, J. G. Snedeker, and M. Harders, "Computer assisted reconstruction of complex proximal humerus fractures for preoperative planning," *Medical Image Analysis*, vol. 16, no. 3, pp. 704–720, 2012.
- [17] J. Miyake, T. Murase, K. Oka, H. Moritomo, K. Sugamoto, and H. Yoshikawa, "Computer-assisted corrective osteotomy for malunited diaphyseal forearm fractures," *The Journal of Bone & Joint Surgery—American Volume*, vol. 94, article e150, 2012.
- [18] B. M. Auerbach and C. B. Ruff, "Limb bone bilateral asymmetry: variability and commonality among modern humans," *Journal of Human Evolution*, vol. 50, no. 2, pp. 203–218, 2006.
- [19] R. A. Lazenby, "Skeletal biology, functional asymmetry and the origins of 'handedness,'" *Journal of Theoretical Biology*, vol. 218, no. 1, pp. 129–138, 2002.
- [20] D. K. Smith, "Anatomic features of the carpal scaphoid: validation of biometric measurements and symmetry with three-dimensional MR imaging," *Radiology*, vol. 187, no. 1, pp. 187–191, 1993.
- [21] A. D. Heinzlmann, G. Archer, and R. R. Bindra, "Anthropometry of the human scaphoid," *The Journal of Hand Surgery*, vol. 32, no. 7, pp. 1005–1008, 2007.
- [22] S. Fukuda, O. Ishida, M. Kido, F. Suzumura, and Y. Ikuta, "A morphological study of the scaphoid using a mathematical technique and comparative study of the three-dimensional measurements of the scaphoid," *Hand Surgery*, vol. 8, no. 2, pp. 157–161, 2003.
- [23] Y. Guo and G. L. Tian, "The length and position of the long axis of the scaphoid measured by analysis of three-dimensional reconstructions of computed tomography images," *Journal of Hand Surgery: European Volume*, vol. 36, no. 2, pp. 98–101, 2011.
- [24] C. Letta, A. Schweizer, and P. Frnstahl, "Quantification of contralateral differences of the scaphoid: a comparison of bone geometry in three dimensions," *Anatomy Research International*, vol. 2014, Article ID 904275, 5 pages, 2014.
- [25] R. J. Belsole, D. R. Hilbelink, J. A. Llewellyn, M. Dale, T. L. Greene, and J. M. Rayhack, "Computed analyses of the pathomechanics of scaphoid waist nonunions," *Journal of Hand Surgery*, vol. 16, no. 5, pp. 899–906, 1991.
- [26] H. Moritomo, T. Murase, K. Oka, H. Tanaka, H. Yoshikawa, and K. Sugamoto, "Relationship between the fracture location and the kinematic pattern in scaphoid nonunion," *Journal of Hand Surgery*, vol. 33, no. 9, pp. 1459–1468, 2008.
- [27] P. C. Amadio, T. H. Berquist, D. K. Smith, D. M. Illstrup, W. P. Cooney III, and R. L. Linscheid, "Scaphoid malunion," *The Journal of Hand Surgery*, vol. 14, no. 4, pp. 679–687, 1989.
- [28] N. M. Lynch and R. L. Linscheid, "Corrective osteotomy for scaphoid malunion: technique and long-term follow-up evaluation," *Journal of Hand Surgery*, vol. 22, no. 1, pp. 35–43, 1997.
- [29] R. Nakamura, T. Imaeda, and T. Miura, "Scaphoid malunion," *The Journal of Bone and Joint Surgery—British Volume*, vol. 73, no. 1, pp. 134–137, 1991.
- [30] G. Lindstrom and A. Nystrom, "Incidence of post-traumatic arthrosis after primary healing of scaphoid fractures: a clinical and radiological study," *The Journal of Hand Surgery*, vol. 15, no. 1, pp. 11–13, 1990.
- [31] R. C. Burgess, "The effect of a simulated scaphoid malunion on wrist motion," *The Journal of Hand Surgery*, vol. 12, no. 5, part 1, pp. 774–776, 1987.
- [32] W. A. Jiranek, L. K. Ruby, L. B. Millender, M. S. Bankoff, and A. H. Newberg, "Long-term results after Russe bone-grafting: the effect of malunion of the scaphoid," *The Journal of Bone and Joint Surgery—American Volume*, vol. 74, no. 8, pp. 1217–1228, 1992.

## Research Article

# Developmental Changes in Morphology of the Middle and Posterior External Cranial Base in Modern *Homo sapiens*

Deepal H. Dalal<sup>1</sup> and Heather F. Smith<sup>2,3</sup>

<sup>1</sup>Department of Biomedical Sciences, Midwestern University, Glendale, AZ 85308, USA

<sup>2</sup>Department of Anatomy, Midwestern University, Glendale, AZ 85308, USA

<sup>3</sup>School of Human Evolution and Social Change, Arizona State University, USA

Correspondence should be addressed to Heather F. Smith; [heather.f.smith@asu.edu](mailto:heather.f.smith@asu.edu)

Received 27 February 2015; Revised 19 May 2015; Accepted 24 May 2015

Academic Editor: P. J. Oefner

Copyright © 2015 D. H. Dalal and H. F. Smith. This is an open access article distributed under the Creative Commons Attribution License, which permits unrestricted use, distribution, and reproduction in any medium, provided the original work is properly cited.

The basicranium has been described as phylogenetically informative, developmentally stable, and minimally affected by external factors and consequently plays an important role in cranial size and shape in subadult humans. Here basicranial variation of subadults from several modern human populations was investigated and the impact of genetic relatedness on basicranial morphological similarities was investigated. Three-dimensional landmark data were digitized from subadult basicrania from seven populations. Published molecular data on short tandem repeats were statistically compared to morphological data from three ontogenetic stages. Basicranial and temporal bone morphology both reflect genetic distances in childhood and adolescence (5–18 years), but not in infancy (<5 years). The occipital bone reflects genetic distances only in adolescence (13–18 years). The sphenoid bone does not reflect genetic distances at any ontogenetic stage but was the most diagnostic region evaluated, resulting in high rates of correct classification among populations. These results suggest that the ontogenetic processes driving basicranial development are complex and cannot be succinctly summarized across populations or basicranial regions. However, the fact that certain regions reflect genetic distances suggests that the morphology of these regions may be useful in reconstructing population history in specimens for which direct DNA evidence is unavailable, such as archaeological sites.

## 1. Introduction

Cranial morphology is frequently studied with the purpose of identifying and interpreting the extensive range of variation that exists among modern human populations and in the hominin fossil record (e.g., [1–10]). The cranium is a valuable structure for studying the genetic and ontogenetic relationships among *Homo sapiens* based on geographic provenance, population affinities, and dietary proclivities [1–7]. The vast majority of studies on the relationship between cranial morphology and genetic relatedness, however, have focused on adult crania. To date, little data exist on the ontogenetic trajectories of the developing cranium, especially the basicranium, as they relate to molecular distances among populations. Determining how basicranial shape develops in infants, juveniles, and young adults has implications for bioarchaeology and paleoanthropology, in which skeletal

specimens are often discovered that contain no DNA and thus no direct genetic evidence of ancestry. In particular, there would be great utility for future bioarchaeological studies to determine whether the basicranium can be used to classify isolated subadult specimens in populations and draw conclusions regarding the ancestry or population history from basicranial shape of a subadult specimen or group of specimens.

Previous studies have demonstrated that the basicranium is a phylogenetically informative region among human and nonhuman primate adults [11–15]. Human populations differ significantly in their adult basicranial morphology, and these differences reflect the genetic relatedness among populations [1, 3, 4, 6]. The basicranium begins to ossify early in the prenatal period, at approximately 11 to 12 weeks [16–18], experiences minimal strain [19–23], and is less susceptible to external factors, such as environment and diet, than other

regions of the cranium [2, 3, 15]. It is also developmentally stable [11, 13, 14, 24, 25], because it emerges from a cartilaginous template early in fetal life, making this region less susceptible to nongenetic forces during ontogeny than the externally sensitive intramembranous bones of the facial skeleton [19, 20]. Additionally, the osseous morphology of the basicranium experiences a lower degree of masticatory stresses than other cranial modules, such as the splanchnocranium (face). The higher strain regions are consequently more subject to biomechanical stress and therefore exhibit higher levels of variability [26]. As such, it has been argued that low strain cranial regions, such as the basicranium, should be more stable and more phylogenetically informative than higher strain regions, such as the face [26]. However, it should be noted that this prediction has not held up to empirical testing in several hominoid (ape) species [5, 26–28].

Nonetheless, since the cranium starts to develop before birth [16–18] and continues to develop until adulthood, it is fundamental to understand the ontogenetic processes, including a comparison of these processes in diverse groups of humans. This can lead to a thorough understanding of how the basicranium develops and whether it reflects among population genetic distances at various stages of subadult ontogeny.

Previous studies have compared the shape of the developing facial skeleton among groups from different geographic locations and genetic backgrounds to determine whether similar ontogenetic processes characterize divergent groups [7–10]. A wide range of variation in human craniofacial form exists and can be relatively easily altered through minor shifts in the ontogenetic process [9]. There have been a limited number of previous studies comparing cranial ontogenetic patterns among human populations, and most have been limited to the temporal bone [7, 29–31]. Thus, the morphological patterning of human cranial ontogeny is still relatively poorly understood.

To date, there have been extensive studies on the morphology of the temporal bone and its applications to phylogeny [32–34], evolution, and ontogeny [7]. The temporal bone demonstrates genetic and geographic patterning that is consistent with a predominantly neutral evolutionary history, shaped primarily by mutation, genetic drift, and gene flow [1–7, 34]. However, despite the abundance of studies on temporal bone shape, there is comparatively little information on the ontogenetic trajectories that result in morphological variation at various subadult stages of development.

Modern human populations can be readily distinguished from one another based on one particular component of the basicranium and temporal bone shape [2–4, 34]. More recently, Smith and colleagues [7] compared subadult and adult temporal bone morphologies in modern *Homo sapiens* and found that significant differences among populations originate early in ontogeny. Specifically, individuals from different populations can be differentiated based on temporal bone shape prior to the eruption of the first molar [7]. Subsequent developmental stages progress in a relatively similar manner with essentially parallel ontogenetic trajectories, however, maintaining those original differences into adulthood [7]. These findings are limited to the temporal

TABLE 1: Human population samples, their adult and subadult sample sizes, and molecular representative populations.

Population	AC1 ( <i>n</i> )	AC2 ( <i>n</i> )	AC3 ( <i>n</i> )	Total ( <i>n</i> )	Molecular representative
Alaskan	10	6	14	30	Yakut
Austrian	5	10	13	28	French
Egyptian	9	7	11	27	Mozabite
Mexican	8	7	15	30	Maya
Peruvian	3	8	19	30	Colombians
Polynesian	2	6	9	17	Solomon Islanders
Utah Native American	11	7	4	22	Pima
<b>Total</b>	<b>48</b>	<b>51</b>	<b>85</b>	<b>184</b>	

bone but encourage further analysis of other cranial regions, including other larger regions, such as the basicranium, in relation to genetics, geography, and population differences.

Several researchers have attempted to determine whether the basicranium is a more reliable region for reconstructing genetic distances than other regions of the cranium [2, 3, 32]. Smith [3] found that the basicranium was significantly more highly correlated with molecular distances than the cranial vault. Morphology of the temporal bone and the upper face were also correlated with a molecular distance matrix, demonstrating that these bones are phylogenetically informative. von Cramon-Taubadel concluded, however, that the basicranium is not significantly more congruent with genetic data than the intramembranously ossifying cranial modules (i.e., cranial vault and face) [5, 36]. In sum, the basicranium “is a good place to look for reliable characters... that describe developmental processes or events” [13, page 159], but its phylogenetic utility during various stage of development is minimally understood.

In light of the previous work and unresolved research questions outlined above, the aims of this study are to determine at what point during the ontogenetic process population-specific basicranial morphologies emerge and to compare basicranial ontogeny among human populations. Specifically, we test the following hypotheses:

- (H1) Human populations differ significantly in the shape of the basicranium and its various components irrespective of ontogenetic stage.
- (H2) Differences among human populations in basicranial morphology are significantly correlated with their genetic distances throughout ontogeny.

## 2. Methodology

**2.1. Data Collection.** Three-dimensional data on basicranial morphology were collected by one of us (DHD). The data were collected from skulls of seven modern human populations at various ontogenetic stages (Table 1) from the American Museum of Natural History, New York, NY, and The National Museum of Natural History at the Smithsonian

Institute, Washington, DC. These populations were chosen based on a single primary criterion: having sufficient cranial ontogenetic series available in museum collections. This criterion is a limiting factor, because museum collections typically consist of primarily adult skulls, since fewer individuals die as subadults and end up housed in collections. Even for individuals that die young, the smaller size and more delicate nature of their crania lead to taphonomic processes being more destructive to subadult skulls, and even those that end up in collections are more likely to be too damaged and fragmentary to measure. Thus, the populations chosen for inclusion in this study were primarily determined by the availability of well-preserved subadult cranial material. Additionally, for the sake of comparability, these populations were identical to the seven populations included in a previous study that we conducted on human temporal bone ontogeny [7].

Prior to traveling to the museums, an intraobserver error study was conducted to ensure the accuracy of the data collection. Two adult crania were digitized ten times each. To minimize the effect of investigator fatigue, the data were collected on two separate days. A paired samples *t*-test was performed, comparing the Procrustes residuals from the different trials on each skull. The paired *t*-test did not yield significant differences ( $p$  value = 0.96 to 0.99), indicating that the individual landmarks were consistently measured without significant error.

Forty-four landmarks were collected from the basi-cranium and subcategorized into temporal, occipital, and sphenoidal regions (Tables 2(a)–2(c); Figure 1). These cranial regions have been historically underrepresented in traditional craniometric studies (e.g., [37]). Thus, in order to sufficiently capture the morphology of these regions, it was necessary to include a few empirical, instrumentally determined landmarks in addition to the traditional craniometric points (Tables 2(a)–2(c)). Due to the fact that subadult specimens are more vulnerable to taphonomic processes and often fragmentary, not all subadult specimens here were complete for all cranial regions evaluated, and thus not all specimens were included in all analyses. These landmark data were collected using a MicroScribe G2 digitizer (Immersion Corp., San Jose). Following Smith et al. [7], subadult specimens were assigned a developmental age estimate based on established dental eruption standards [37]: Age category 1 (AC1) = M1s not yet erupted; Age category 2 (AC2) = M1s erupted but not M2s; Age category 3 (AC3) = M2s erupted but not M3s [33]. In humans, these stages correspond roughly to chronological ages of <5 years, 5–12 years, and 13–18 years [37–39]. A sample of adult specimens from each population was also digitized; however, since it is not possible to accurately estimate ages for adult crania, these specimens were included in only a subset of the analyses (explained in further detail below).

Data on individual genotypes for 783 short tandem repeats (STRs) were compiled from Ramachandran et al. [40, 41] and Rosenberg et al. [35, 42] for molecular population representatives matching as closely as possible the populations from which the morphological data were collected. This practice of matching morphological and molecular populations has been successfully employed by previous

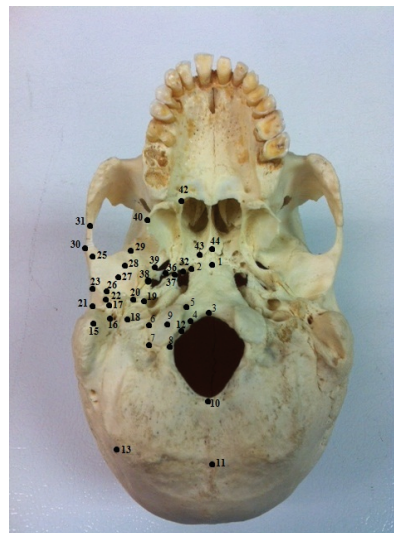


FIGURE 1: Forty-four landmarks of the basicranium digitized in the present study. Please refer to Tables 2(a)–2(c) for landmark descriptions.

studies [1–7, 34, 36]. Some of our morphological populations (i.e., the Alaskan and Egyptian samples) were not included in the Rosenberg studies from which the molecular data were derived, and thus, STR data were not available for these populations. In these cases, we attempted to choose a molecular population representative that was as similar as possible to the morphological sample. For the Alaskan sample, we chose the Yakut (a Siberian native population), and for the Egyptian sample we chose the Mozabite (an Algerian Berber group). We recognize that these imperfectly matched molecular representatives introduce a certain degree of incompatibility between the two data types; however, this mismatch renders any correlations that we obtain between the morphological and molecular distances to be a conservative, minimum estimate of the relationships between these types of data.

STRs are composed of back-to-back repeating segments of two to six nucleotides and are found at many locations within the genome [38, 39]. They are often variable in their number of repeats, and the lengths of the STRs differ among different populations, in patterns that reflect their ancestry and relatedness. STRs are appropriate for assessing human population distances because they evolve primarily neutrally and are homologous [35, 40–43]. They are also well-typed for a large number of human populations from geographically diverse locations, cultural backgrounds, and linguistic traditions [36, 37].

**2.2. Analytical Methods.** The morphological data were analyzed using a Generalized Procrustes Analysis (GPA), in which the digitized points were rotated and translated and specimens were scaled to the same size, such that the only remaining differences among them were directly attributable to shape. The GPA was followed by a Principal Components Analysis (PCA) using MorphoJ [44]. Adult specimens were

TABLE 2: (a) Definitions of occipital bone landmarks used in the present study. Refer also to Figure 1. (b) Definitions of temporal bone landmarks used in the present study. Refer also to Figure 1. (c) Definitions of sphenoid landmarks used in the present study. Refer also to Figure 1.

(a)	
Occipital	
1	Most anterior point on the basioccipital in the midline (sphenobasion, on the occipital if not connected)*
2	Most lateral point on the basioccipital*
3	Basion (anterior most point on the foramen magnum)
4	Most anterior point on the occipital condyle along the margin of the foramen magnum
5	Most anterior point on occipital condyle
6	Most lateral point on the occipital condyle (point on the middle of the lateral edge of the condyle)
7	Most posterolateral point on the occipital condyle
8	Most posterior point on the occipital condyle along the margin of the foramen magnum
9	Mid-point of the occipital condyle (inferior aspect)
10	Opisthion (posterior most point on the foramen magnum)
11	Mid-point on the median nuchal line between the external occipital protuberance and foramen magnum
12	Anteromedial point on the hypoglossal canal
13	Asterion (temporal, occipital, and parietal meet)*

\*Landmarks are repeated with regard to the overlapping cranial regions.

(b)	
Temporal	
13	Asterion (where temporal, occipital, and parietal meet)*
14	Parietal notch (not depicted)
15	Mastoidale (center of the inferior point on the mastoid process)
16	Most lateral point on the margin of the stylomastoid foramen
17	Most lateral point on the vagina of the styloid process (whether process is present or absent)
18	Most posterolateral point on the jugular fossa
19	Most posterolateral point on the margin of the carotid canal entrance
20	Point on anterior margin of tympanic element that is closest to carotid canal
21	Most posterolateral point on the external acoustic meatus
22	Most inferior point on the external acoustic meatus
23	Point on lateral margin of zygomatic process of the temporal bone at the position of the postglenoid process
24	Point of inflection where the braincase curves laterally into the supraglenoid gutter, in coronal plane of mandibular fossa (not depicted)
25	Point on the anterior of the lateral margin of the articular surface of the articular eminence
26	Most inferior point on the postglenoid process
27	Deepest point within the mandibular fossa (instrumentally determined)
28	Mid-point of the articular eminence
29	Most anterior point on the articular surface of the articular eminence
30	Auriculare (most lateral point on the temporal)
31	Suture between temporal and zygomatic bones on inferior aspect of zygomatic process
32	Most inferior point at the sphenotemporal suture closer to the midline (on the sphenoid if disconnected)
33	Most lateral point on the greater wing of the sphenoid (intersection between sphenoid, temporal, and parietal bone)* (not depicted)
34	Most frontolateral point on the greater wing of the sphenoid (intersection between sphenoid, temporal, and frontal bone)* (not depicted)
36	Most posterior, inferior point on the sphenotemporal suture*
37	Apex of the petrous part of the temporal bone

\*Landmarks are repeated with regard to the overlapping cranial regions.

(c)	
Sphenoid	
33	Most lateral point on the greater wing of the sphenoid (intersection between sphenoid, temporal, and parietal bone)* (not depicted)

(c) Continued.

Sphenoid	
35	Most anterior inferior point on the sphenozygomatic suture (sphenozygomatic) (not depicted)
36	Most posterior, inferior point on the sphenotemporal suture*
38	Most lateral point of the foramen spinosum
39	Most lateral point on the margin of foramen ovale
40	Most anterolateral point of the lateral pterygoid plate
41	Most inferior part of the pterygoid hamulus (not depicted)
42	The most anteromedial point of the sphenoidal region on the sphenovomer suture
43	Most posterior point where the vomer meets the medial pterygoid plate
44	Point on the sphenoid in the midline in contact with the vomer (vomer notch)
1	Most anterior point on the basioccipital in the midline (sphenobasion, on the occipital if not connected)*
2	Most lateral point on the basioccipital*

\*Landmarks are repeated with regard to the overlapping cranial regions.

TABLE 3: Population molecular distance matrix ( $F_{ST}$ ) based on short tandem repeat (STR) data. Data were obtained from Rosenberg et al. (2005) [35].

	Alaska	Austria	Egypt	Mexico	Peru	Polynesia	Utah Native American
Alaska	—						
Austria	0.0455	—					
Egypt	0.0530	0.1068	—				
Mexico	0.0580	0.0606	0.0731	—			
Peru	0.0951	0.0984	0.1110	0.0443	—		
Polynesia	0.0759	0.0759	0.0808	0.1028	0.1443	—	
Utah Native American	0.0984	0.1076	0.1190	0.0600	0.0973	0.1461	—

included in the PCA for the purpose of visualizing how basicranial shape varied across age categories and among populations. Procrustes distances among populations were then calculated in MorphoJ for the individual subadult age categories, while further separating the data sets into basicranial, temporal, sphenoidal, and occipital regions. Each set of resulting pairwise population distances was entered into distance matrices for each cranial dataset. The significance of these population differences was assessed using a permutation test of 1000 replicates for each region.

In order to assess the degree to which basicranial morphology can be utilized to correctly classify individuals of various ages into the population from which they derived, a discriminant function analysis (DFA) was conducted using the Principal Component (PC) scores from the PCA. The DFA was used to determine whether groups could be classified reliably or if there was excessive morphological overlap. This analysis was conducted for the morphology of the basicranium and then for each of its major components, the temporal, occipital, and sphenoidal regions. These tests were conducted with cross-validation using SPSS version 11.0.1 (SPSS, Chicago, IL). This analysis indicated how well basicranial shape discriminates among populations at the three subadult stages of ontogeny (AC1, AC2, AC3).

A matrix of Slatkin’s molecular distances among the molecular representative of these populations was calculated from the published molecular data using Arlequin 3.11 [45] (Table 3). The matrix of pairwise population Procrustes distances for each cranial region was then statistically compared

to the molecular distance matrix using Mantel tests [46] to statistically assess and quantify the correlation among matrices. This analysis indicated whether the morphology of the basicranium, and the regions contained therein, reflected genetic distances at each developmental stage.

A series of descriptive analyses were conducted to evaluate the ontogenetic trajectory in the sample. Principal Component scores were regressed against centroid size and biological age (as determined using dental eruption of each specimen, following Ubelaker [37]) to determine the PCs that were significantly correlated with size or age and therefore indicative of age-related changes in basicranial shape. The regression of centroid size and age against PC scores reveals how shape changes with age (ontogeny) and size (allometry) [8]. Finally, a wireframe was constructed by connecting points in shape-space and morphing them along each major PC axis in Morphologika 2 [47], for the PCs that were found to explain >5% of the variance. This process allowed us to visualize shape changes along these PC axes in the different populations and age categories and describe how basicranial shape changes across all populations and age categories.

### 3. Results

3.1. Differentiation and Classification of Populations. Procrustes distances based on basicranial morphology of populations sampled in this study were found to be statistically significant for all combined-age subadult samples (Table 4). When separated into age categories, the majority of the

TABLE 4: Procrustes distance matrix among populations based on subadult basicranial morphology. All pairwise population distances are significantly different at the  $p < 0.05$  level.

	Alaska	Austria	Egypt	Mexico	Peru	Polynesia	Utah
Alaska	—						
Austria	0.0361	—					
Egypt	0.0779	0.0703	—				
Mexico	0.0398	0.0444	0.0745	—			
Peru	0.0493	0.0513	0.0846	0.0411	—		
Polynesia	0.0618	0.0532	0.0809	0.0631	0.0740	—	
Utah	0.0694	0.0684	0.0998	0.0638	0.0548	0.0805	—

TABLE 5: Morphological Procrustes distance matrix among populations based on basicranial morphology in the AC1 age category. Significantly different pairwise population distances ( $p < 0.05$ ) are indicated in bold.

	Alaska	Austria	Egypt	Mexico	Peru	Polynesia	Utah
Alaska	—						
Austria	<b>0.1580</b>	—					
Egypt	0.1110	0.1611	—				
Mexico	<b>0.1341</b>	0.1518	0.0816	—			
Peru	0.1127	0.1867	<b>0.1581</b>	0.1571	—		
Polynesia	0.1045	0.1735	0.1066	0.1102	0.1519	—	
Utah	<b>0.1068</b>	0.1485	0.1040	0.0908	<b>0.1592</b>	0.1019	—

Procrustes distances were significantly different among populations. There were no consistent patterns of population differences among the age categories or regions of the basicranium. The Procrustes distances showed a higher number of pairwise significant differences among populations as the age of the individuals and sample sizes increased. Hence, at AC1, given the smaller sample size for some regions (especially the unfused occipital bone), most populations were not significantly different from each other (Table 5). In AC2, more significant differences were found (Table 6), increasing in AC3 (Table 7). Therefore, (H1)—that human populations differ in basicranial shape at every ontogenetic stage—was not supported.

DFA were performed on all regions of the basicranium: temporal, occipital, and sphenoidal. The DFA for the entire basicranium resulted in cross-validated classification rates ranging from 13.3–34.8% (Table 8). The individual cranial regions yielded higher average correct classification rates: temporal = 41.3%, occipital = 42.6%, and sphenoid = 50.0% (Tables 6–8).

The Egyptian population was one of the most correctly classified in the basicranial (33.3%), temporal bone (55%), and occipital bone (35.7%) data sets (Tables 8–11). The Egyptian population was the most correctly classified population in all regions of the basicranium except the sphenoid bone (Tables 8–11). As predicted, the three closely related Native American populations (Mexican, Utahan, and Peruvian) were frequently classified as each other. Consequently, the least correctly classified group overall was the Utah population.

3.2. Correspondence between Genetic Distances and Basicranial Morphology. The morphological Procrustes distances

based on the different age categories and regions of the basicranium were statistically compared to the molecular  $F_{ST}$  distances based on STR data using Mantel tests. In the combined subadult sample, the morphology of the basicranium and occipital bone was significantly correlated with molecular distances (Table 12). Following the analysis with all populations, populations were systemically removed from the analyses to determine whether the results were unduly influenced by the inclusion of any particular population. When the Egyptian population was excluded from the analyses, the correlations between morphology and molecular distance increased to the point of significance in several additional subgroups (Table 13). Results from both analyses are reported in further detail below.

When the subadult samples for each cranial region were divided into separate age categories, more distinct patterns emerged (Tables 12 and 13). Morphology in AC3 individuals was significantly correlated with genetic distances for the basicranium, temporal, and occipital regions (Table 13). In AC2 specimens, morphology of the basicranium and temporal bone was correlated with the genetic matrix (Table 13). There were no significant correlations between the morphology of any cranial region and genetic distances for AC1 (Table 13); however, the sample sizes of these datasets were much smaller than the other age categories, rendering these results more tenuous.

Overall, the above patterns show that the shape of the basicranium, temporal bone, and occipital bone, for all populations excluding the Egyptian population, reflects genetic distances for the combined subadult sample and AC3 (13–18 years of age), thus supporting (H2) (basicranial differences are correlated with genetic distances) for these data sets. The temporal bone and basicranium also reflect

TABLE 6: Morphological Procrustes distance matrix among populations based on basicranial morphology in the AC2 age category. Significantly different pairwise population distances ( $p < 0.05$ ) are indicated in bold.

	Alaska	Austria	Egypt	Mexico	Peru	Polynesia	Utah
Alaska	—						
Austria	<b>0.0870</b>	—					
Egypt	<b>0.1289</b>	<b>0.1337</b>	—				
Mexico	<b>0.0831</b>	<b>0.0765</b>	0.0948	—			
Peru	<b>0.1035</b>	<b>0.0867</b>	<b>0.1423</b>	0.0799	—		
Polynesia	0.0799	<b>0.0940</b>	<b>0.1016</b>	<b>0.0849</b>	<b>0.1115</b>	—	
Utah	<b>0.0888</b>	<b>0.0869</b>	<b>0.1039</b>	0.0722	<b>0.0871</b>	0.0715	—

TABLE 7: Morphological Procrustes distance matrix among populations based on basicranial morphology in the AC3 age category. Significantly different pairwise population distances ( $p < 0.05$ ) are indicated in bold.

	Alaska	Austria	Egypt	Mexico	Peru	Polynesia	Utah
Alaska	—						
Austria	<b>0.0543</b>	—					
Egypt	<b>0.0994</b>	<b>0.0921</b>	—				
Mexico	<b>0.0559</b>	<b>0.0601</b>	<b>0.0909</b>	—			
Peru	<b>0.0558</b>	<b>0.0682</b>	<b>0.1021</b>	<b>0.0506</b>	—		
Polynesia	<b>0.0659</b>	0.0620	<b>0.1031</b>	<b>0.0774</b>	<b>0.0796</b>	—	
Utah	<b>0.0953</b>	<b>0.0960</b>	0.1382	<b>0.0886</b>	0.0795	<b>0.1042</b>	—

genetic distances during AC2 (5–12 years of age) when the Egyptian population is excluded. The morphology of the sphenoid bone does not reflect genetic distances for subadults of any age category; however, its morphology can be used to discriminate among populations with slightly higher rates than the other two cranial regions. Therefore, (H2) is not supported for the sphenoid, AC1 (for any morphological region), or the occipital bone for AC2.

3.3. Ontogenetic Trajectories

3.3.1. Age. The regression of biological age with Principal Components scores (Tables 14 and 15) for the entire basicranium revealed significant correlations between age and PC1 (14.83% of the variance), PC2 (9.31% variance), and PC4 (6.53% variance) (Figures 2 and 3). While these PCs each describe a relatively low amount of variance, this pattern is typical in PCAs following a Procrustes superimposition, because the Procrustes analysis essentially removes the effect of size. PC1 was found to be correlated with age for all populations for morphology of both the entire basicranium and the isolated temporal bone (Table 15). Additionally, PC4 was correlated with biological age for sphenoid morphology in all individual populations except the Polynesians, and PC6 was correlated with age for the occipital bone in all individual populations except the Peruvian sample (Table 15).

3.3.2. Centroid Size. The regression analysis of centroid size with PC scores for the entire basicranium revealed significant correlations between size and PC1 (14.83% of the variance), PC2 (9.31% of the variance), PC3 (7.57% of the variance), and PC4 (6.53% of the variance) (Tables 14 and 16). The regression plot of PC1 scores versus log centroid size is illustrated in

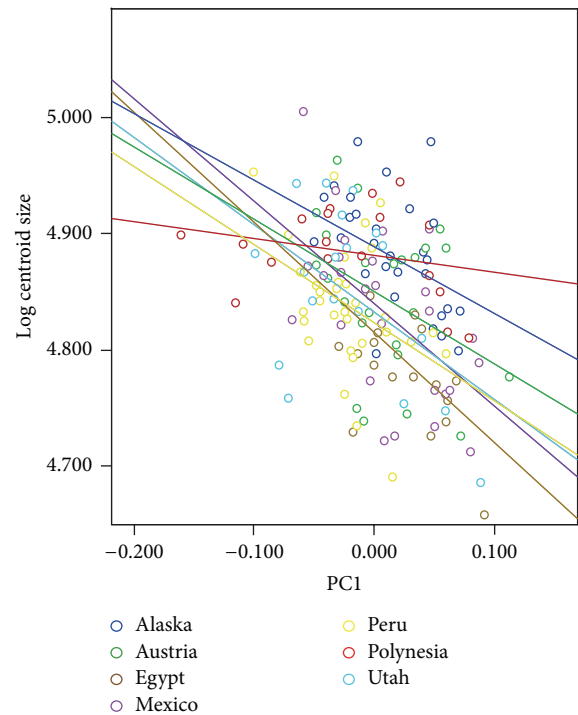


FIGURE 2: Regression plot of PC1 scores versus log centroid size for the basicranium. The individual population regression lines are indicated and their  $R^2$  values indicated.

Figure 2. PC1 was significantly correlated with centroid size for all the basicranial morphology of individual populations, except the Polynesian sample, and all individual populations for the temporal bone (Table 16), similar to the pattern

TABLE 8: Classification results from discriminant function analysis (DFA) with cross-validation for the entire basicranium.

	% Correct	Alaska	Austria	Egypt	Mexico	Peru	Polynesia	Utah	Total
Alaska	26.3	5	2	0	2	3	4	3	19
Austria	34.8	3	8	1	6	4	1	0	23
Egypt	33.3	0	0	3	1	1	3	1	9
Mexico	13.3	3	3	1	2	3	1	2	15
Peru	20.8	5	4	1	5	5	1	3	24
Polynesia	20.0	2	0	4	0	1	2	1	10
Utah	28.6	1	0	0	2	2	0	2	7

25.2% of cross-validated grouped cases correctly classified.

TABLE 9: Classification results from discriminant function analysis (DFA) with cross-validation for the temporal bone.

	% Correct	Alaska	Austria	Egypt	Mexico	Peru	Polynesia	Utah	Total
Alaska	65.4	17	2	0	3	0	0	4	26
Austria	37.0	7	10	1	4	4	0	1	27
Egypt	55.0	1	4	11	2	1	1	0	20
Mexico	23.1	2	5	2	6	6	1	4	26
Peru	48.3	2	5	1	3	14	0	4	29
Polynesia	42.9	2	2	2	1	1	6	0	14
Utah	11.1	5	1	1	4	4	1	2	18

41.3% of cross-validated grouped cases correctly classified.

TABLE 10: Classification results from discriminant function analysis (DFA) with cross-validation for the occipital bone.

	% Correct	Alaska	Austria	Egypt	Mexico	Peru	Polynesia	Utah	Total
Alaska	30	6	7	0	3	3	1	NA	20
Austria	33.3	7	8	5	2	0	2	NA	24
Egypt	35.7	1	5	5	1	1	1	NA	14
Mexico	31.3	3	2	2	5	4	0	NA	16
Peru	75	2	0	1	3	18	0	NA	24
Polynesia	40	1	2	2	1	0	4	NA	10
Utah	NA	NA	NA	NA	NA	NA	NA	NA	NA

42.6% of cross-validated grouped cases correctly classified.

TABLE 11: Classification results from discriminant function analysis (DFA) with cross-validation for sphenoid morphology.

	% Correct	Alaska	Austria	Egypt	Mexico	Peru	Polynesia	Utah	Total
Alaska	41.2	7	5	0	0	3	0	2	17
Austria	55.0	3	11	2	2	1	0	1	20
Egypt	30.0	0	3	3	1	2	0	1	10
Mexico	57.1	2	0	0	8	4	0	0	14
Peru	63.6	2	2	1	2	14	0	1	22
Polynesia	42.9	0	0	1	1	2	3	0	7
Utah	37.5	2	2	0	1	0	0	3	8

50.0% of cross-validated grouped cases correctly classified.

TABLE 12: Procrustes analyses comparing molecular distances with morphological distances based on each of the cranial data sets.

	Basicranium		Temporal		Occipital		Sphenoid	
	<i>R</i>	<i>p</i> value	<i>R</i>	<i>p</i> value	<i>R</i>	<i>p</i> value	<i>R</i>	<i>p</i> value
All subadults	<b>0.48</b>	<b>0.04*</b>	0.18	0.30	<b>0.82</b>	<b>&lt;0.001*</b>	0.33	0.14
AC1	<b>-0.58</b>	<b>&lt;0.001*</b>	-0.38	0.09	NA	NA	NA	NA
AC2	0.36	0.06	-0.18	0.28	<b>0.58</b>	<b>0.02*</b>	0.09	0.38
AC3	0.33	0.18	0.14	0.34	<b>0.84</b>	<b>&lt;0.001*</b>	-0.06	0.56

\*Statistically significant ( $p < 0.05$ ).

TABLE 13: Procrustes analyses comparing molecular distances with morphological distances based on each of the cranial data sets excluding the Egyptian population.

	Basicranium		Temporal		Occipital		Sphenoid	
	<i>R</i>	<i>p</i> value	<i>R</i>	<i>p</i> value	<i>R</i>	<i>p</i> value	<i>R</i>	<i>p</i> value
All subadults	<b>0.83</b>	<b>&lt;0.001*</b>	<b>0.79</b>	<b>&lt;0.001*</b>	<b>0.88</b>	<b>0.01*</b>	0.55	0.05
AC1	-0.45	0.17	-0.15	0.36	NA	NA	NA	NA
AC2	<b>0.57</b>	<b>&lt;0.001*</b>	<b>0.46</b>	<b>&lt;0.001*</b>	-0.01	0.50	0.09	0.38
AC3	<b>0.91</b>	<b>&lt;0.001*</b>	<b>0.81</b>	<b>0.01*</b>	<b>0.91</b>	<b>&lt;0.001*</b>	-0.26	0.22

\*Statistically significant ( $p < 0.05$ ).

TABLE 14: Principal Components of the basicranium of all populations significantly correlated with age and/or centroid size in the regression analysis.

	Age	Centroid size
PC1	$R = -0.63, p < 0.001^*$	$R = -0.50, p < 0.001^*$
PC2	$R = 0.29, p < 0.001^*$	$R = 0.26, p < 0.001^*$
PC3	$R = 0.02, p = 0.40$	$R = 0.14, p = 0.03^*$
PC4	$R = 0.12, p = 0.04^*$	$R = 0.14, p = 0.03^*$

\*Statistically significant ( $p < 0.05$ ).

revealed by the age versus PC1 comparisons (Table 15). This reflects the fact that size and age are related, as expected. PC3 was significantly correlated with centroid size for all individual populations in the occipital bone, a pattern not seen in all of the various age categories. Similar to the age comparisons, the centroid size of the sphenoid bone and PC4 were significantly correlated for all populations individually. Mean PC scores for each age group in each population are provided for comparative purposes (Tables 17 and 18).

**3.4. Shape Space Exploration.** In order to further explore how populations and age categories differed with regard to basicranial morphology, we conducted a shape space exploration in which wireframes of each cranial data set were morphed along the major PC axes to visualize how the shape varied along each PC.

In basicranial shape, subadults were commonly located on the +PC1 axis (Figure 3(a)). A positive PC1 score is associated a mediolaterally narrow basicranium, with an elongated external acoustic meatus (EAM). The external occipital protuberance (EOP) also moves relatively further away from the occipital condyle with an increasingly positive PC1 score. Given that most of the subadult values appeared on the +PC1 side, this indicates that the subadult basicranium is longer and narrower but widens into adulthood, while relatively decreasing in length. A negative PC1 score is characterized by the reverse morphological conditions (i.e., mediolaterally wider basicranial, shortened EAM, closer proximity of the EOP, and occipital condyle).

Associated with a positive PC2 score (Figure 3(a)), the EAM becomes relatively larger, but the overall basicranial length decreases. The hypoglossal canal and articular eminence move relatively further posteriorly. The length between the occipital condyle and the EOP decreases as well,

thus shortening the basicranium. The EAM length relatively increases.

## 4. Discussion

To date, extensive research has been conducted on the temporal bone and how it reflects genetic relationships in nonhuman primates (e.g., [13, 14, 31–33, 48]). In modern humans, it has been determined that the temporal bone reflects genetic relationships in both subadults and adults and that many populations significantly differ in their ontogenetic trajectories [7]. The current study focused on a larger area of the skull, the basicranium and its constituent regions, and their ontogenetic patterns.

**4.1. Hypotheses.** The hypotheses that formed the basis for the study were found to be only partially supported. In actuality, the patterns of morphological variation turned out to be more complex than the relatively simply stated hypotheses. The patterns of the individual basicranial bones differed from each other and across the various age categories. Thus, the ontogenetic processes driving basicranial development cannot be succinctly summarized across all regions of the basicranium.

(H1) Human populations differ in the shape of the basicranium and its various components irrespective of ontogenetic stage.

This hypothesis was not supported by our results. All populations were found to differ significantly in basicranial morphology in the combined subadult samples. However, in the separate age categories there was a trend toward increasing differentiation with age. In AC1, several population were not significantly different, by AC2 most populations differed, and by AC3 all populations were significantly different. Interestingly, of all the individual cranial bones, the sphenoid was revealed to be the most distinct among populations and therefore the most reliable region for population classification.

(H2) Differences among human populations in basicranial morphology are significantly correlated with their genetic distances throughout ontogeny.

This hypothesis was partially supported for several subsets of our data. Our results show that morphology of the basicranium, occipital, and temporal bones each significantly

TABLE 15: Principal Components of the basicranium and its regions significantly correlated with age in the regression analysis.

	Basicranium	Temporal	Occipital	Sphenoid
All populations	PC1, PC2, PC4	PC1, PC2, PC4	PC3, PC5, PC6	PC2, PC4
Alaska	PC1, PC2, PC4	PC1, PC4	PC2, PC3, PC4, PC6	PC1, PC2, PC4
Austria	PC1, PC3, PC4	PC1, PC2, PC3, PC6	PC1, PC2, PC6	PC4
Egypt	PC1	PC1	PC6	PC4
Mexico	PC1	PC1, PC2	PC3, PC4, PC6	PC4
Peru	PC1, PC2, PC3	PC1, PC6	PC1, PC2, PC5	PC4
Polynesia	PC1	PC1	PC3, PC5, PC6	
Utah	PC1, PC2	PC1, PC2	PC5, PC6	PC2, PC4

TABLE 16: Principal Components of the basicranium and its regions significantly correlated with centroid size in the regression analysis.

	Basicranium	Temporal	Occipital	Sphenoid
All populations	PC1, PC2, PC3, PC4	PC1, PC4, PC6	PC1, PC2, PC3, PC4, PC6	PC1, PC2, PC4
Alaska	PC1, PC2	PC1, PC4	PC2, PC3, PC4, PC6	PC1, PC4
Austria	PC1, PC3, PC4	PC1, PC2, PC4, PC6	PC3	PC2, PC4, PC5
Egypt	PC1, PC4, PC5	PC1, PC4	PC1, PC3	PC1, PC3, PC4, PC5
Mexico	PC1, PC2, PC4	PC1, PC3, PC4	PC1, PC2, PC3, PC4, PC5, PC6	PC4
Peru	PC1, PC2	PC1, PC4	PC1, PC3	PC4
Polynesia		PC1, PC2	PC2, PC3	PC2, PC4
Utah	PC1, PC2	PC1	PC1, PC3	PC1, PC4

reflects genetic distances in the combined subadult sample. The sphenoid bone, however, is not a good indicator of genetic distances in subadults in the combined subadult sample or at any ontogenetic stage. In the separate age categories for the basicranium, temporal, and occipital regions, the older the individuals, the more congruent the patterns between the genetic and morphological datasets, such that AC3 was the most highly correlated, followed by AC2 and then AC1.

*4.2. Classification among Populations.* The discriminant function analyses revealed that the Egyptian population was the most correctly classified population for the basicranium, occipital, and temporal bone in subadults. The Egyptian population was most likely classified correctly because it is the most geographically and genetically distant of the populations in this study. This finding is consistent with the previous description of Egyptian cranial morphology as unique and distinctive [49].

Unsurprisingly, the closely related Native American groups of Utah and Mexico were often classified as each other in basicranial, temporal, and occipital bone for all subadults. This trend has been supported by previous studies [6, 7] and supports the hypothesis that closely related populations should share a similar basicranial shape. Relethford [6] showed that the Peruvian population was phenotypically very similar to other Native American populations in his study (Arikara, Greenland Inuit and Santa Cruz) despite its remote geographic location compared to the other Native American populations. Consistent with the results of this study, Smith and colleagues [7] also found that the temporal bone of the subjects from Utah and Mexico was most often classified as another Native American population. In fact, the low levels of

correct classification for these populations suggest that their morphological variation overlaps considerably in the younger age categories. These findings, taken together, show that the basicranial morphology can generally be used as an indicator of genetic relatedness among children and adolescents but considerable overlap may still exist for populations which are close in genetic proximity, such as Native American populations.

Based on the findings of this research, the basicranium, temporal, and occipital bone reflect genetic distances in childhood and adolescence, but this study suggests that these differences are not seen in infancy. AC1 was not correlated with molecular distances among populations for any of the cranial regions. Two possible scenarios may explain these results in infancy. First, infant basicranial morphology may be similar among populations and the observable differences in later ontogenetic stages have not yet developed. However, an alternative explanation is that as a result of the fact that many basicranial bones are not fully fused in infants, our sample sizes in the AC1 age category may have been insufficient to reveal subtle differences among populations in infancy.

These findings contrast with some of the results found previously for the temporal bone [7, 31], which suggest that the relationships in temporal bone originate early in ontogeny and these differences reach adulthood via different ontogenetic trajectories. Terhune et al. [31] also found that subadult great apes and humans demonstrate differences in temporal bone shape early in ontogeny. Contrary to Smith et al. [7] and Terhune et al. [31] for the temporal bone, and Viðarsdóttir et al. [8] for the face, the present study did not find that early subadult morphology (i.e., AC1) reflects adult population-specific differences. This finding is surprising

TABLE 17: Mean Principal Components scores for the major PCs for each age group in each population for the entire basicranium. Note: sample size of complete basicrania of AC1 for the Polynesian population was insufficient to obtain a reasonable estimation of the mean.

Population	Age Cat.	PC1	PC2	PC3	PC4	PC5
Alaskans	AC1	0.05323	0.00302	0.00175	-0.00882	0.00855
Alaskans	AC2	0.04618	-0.01399	0.01446	-0.01085	-0.00150
Alaskans	AC3	0.02569	0.00815	-0.00014	-0.01146	0.00114
Alaskans	Adults	0.00969	0.00543	0.00499	-0.00409	0.00546
Austrians	AC1	0.07867	-0.02117	-0.03936	-0.03364	0.00580
Austrians	AC2	0.02695	0.00316	0.00068	0.02413	0.01203
Austrians	AC3	0.00584	0.02062	0.00347	0.02083	-0.00779
Austrians	Adults	-0.02377	-0.01075	0.00784	0.02859	0.00468
Egyptians	AC1	0.11390	0.02214	0.00609	-0.01172	0.00766
Egyptians	AC2	0.04530	-0.00072	-0.00789	0.00435	-0.02901
Egyptians	AC3	0.00920	0.01193	-0.00507	0.03377	-0.05306
Egyptians	Adults	0.00662	0.03986	-0.00195	0.01716	-0.01972
Mexicans	AC1	0.08308	0.02326	-0.02515	-0.01663	-0.01222
Mexicans	AC2	0.02838	-0.02994	0.01315	0.01064	0.00299
Mexicans	AC3	0.01160	-0.02266	-0.01056	0.00150	0.00459
Mexicans	Adults	-0.03151	-0.00378	0.00344	-0.00451	0.00588
Peruvians	AC1	0.00004	-0.10173	0.02027	0.01840	0.00450
Peruvians	AC2	-0.01429	-0.04447	0.00779	-0.00991	0.01923
Peruvians	AC3	-0.01735	-0.03330	0.01130	-0.01073	-0.00269
Peruvians	Adults	-0.03927	0.00426	-0.00411	-0.00933	0.00495
Polynesians	AC1	—	—	—	—	—
Polynesians	AC2	0.06510	0.02825	-0.00041	-0.00531	-0.00052
Polynesians	AC3	0.01269	0.04162	0.00118	0.00674	0.00423
Polynesians	Adults	-0.05657	0.04434	-0.01331	0.01068	0.00484
Utah	AC1	0.05701	-0.05851	-0.00487	-0.03191	0.01686
Utah	AC2	0.00952	-0.01100	-0.00275	-0.03556	-0.00031
Utah	AC3	-0.06937	-0.00900	-0.00478	-0.02770	0.00412
Utah	Adults	-0.04365	0.00478	-0.00146	-0.02958	-0.00178

given that the temporal bone has been found previously to reflect genetic distances in adult humans [2–7]. However, these seemingly contrasting results may reflect the choice of different landmarks used in the present study. Alternatively, these differences may be explained by the relatively small sample sizes necessitated by the limited subadult cranial material available in museum collections.

Interestingly, while morphology of the sphenoid was not found to reflect the molecular distance matrix at any ontogenetic stage evaluated (Table 9), it did perform quite well in the DFAs (Table 8). Thus, the morphology of this bone can be inferred to be distinct among the populations sampled here; however, those differences do not reflect genetic relatedness. In other words, more closely related populations do not share similar sphenoid morphology, but instead, each population is unique in its sphenoid shape.

**4.3. Cranial Morphology and Genetic Relationships.** Overall patterns revealed by this study show that the shape of the basicranium, the temporal bone, and occipital bone, for all populations excluding the Egyptian population, reflects

genetic distances in subadults. Removing the Egyptian population from the analyses yielded significant results in the temporal bone, occipital bone, and age categories AC2 and AC3. It cannot be definitively ascertained why the Egyptian population deviated from the patterns of the rest of the included samples, but one possibility is the relatively high degree of mismatch between the morphological Egyptian sample and its molecular population representative, the Mozabite. The Mozabite people live in Algeria and speak a Berber language. As one of the few northern Saharan populations to have been extensively studied for neutral molecular loci, they are the closest well-typed molecular representative for the Egyptians, but certainly not a perfect match.

Patterns on the basicranial PC wireframe showed that the Egyptian crania appeared on the +PC2 scale, indicating that the basicranium in the Egyptian population is relatively shorter anteroposteriorly compared to the other populations. Most of the Egyptian population clustered towards an increasingly long occipital bone (-PC2, +PC3, and -PC4) and increasing large temporal bone. It appears that the Egyptian cranium might have a relatively smaller overall basicranium

TABLE 18: Mean Principal Components scores for the major PCs for each age group in each population for the temporal bone.

Population	Age Cat.	PC1	PC2	PC3	PC4	PC5	PC6
Alaskans	AC1	0.06370	0.03778	-0.00467	0.003486	-0.01318	0.002793
Alaskans	AC2	0.05955	0.01832	-0.01152	0.012063	-0.00951	0.006615
Alaskans	AC3	0.01364	0.01492	-0.01702	-0.00626	0.01089	-0.00095
Alaskans	Adults	-0.04098	0.00911	-0.03013	-0.01553	0.003458	-0.00611
Austrians	AC1	0.06432	0.04918	0.014509	0.0147	0.004334	0.041771
Austrians	AC2	0.01920	-0.01637	-0.01942	-0.00831	-0.02196	0.000631
Austrians	AC3	-0.00658	-0.00682	-0.00317	-0.0133	-0.00137	-0.00585
Austrians	Adults	-0.04079	-0.01804	0.036348	-0.00234	-0.01313	-0.01497
Egyptians	AC1	0.09614	-0.01266	-0.00793	-0.00211	0.011929	0.021407
Egyptians	AC2	0.07456	-0.07440	0.023618	0.005589	0.039431	0.00116
Egyptians	AC3	0.03027	-0.01573	-0.01638	-0.02419	-0.01115	0.008317
Egyptians	Adults	-0.00847	-0.01948	-0.0062	-0.01665	0.009855	0.022317
Mexicans	AC1	0.07394	0.03163	-0.00879	0.015592	0.024777	0.01061
Mexicans	AC2	0.04101	0.00014	-0.0111	0.009107	0.003618	-0.02052
Mexicans	AC3	-0.00346	0.00340	-0.01835	0.013748	0.007935	-0.00232
Mexicans	Adults	-0.02252	-0.03734	0.005864	-0.02859	0.023767	0.001946
Peruvians	AC1	0.04345	-0.01427	0.00188	0.00293	0.031773	-0.00416
Peruvians	AC2	0.01024	0.00996	0.006532	0.025246	-0.00551	-0.01473
Peruvians	AC3	-0.01153	0.01216	0.011737	0.022836	-0.00735	-0.0178
Peruvians	Adults	-0.04831	-0.00314	0.015741	0.009016	-0.00291	0.010455
Polynesians	AC1	0.09089	0.03686	0.01485	-0.01808	-0.08961	-0.02056
Polynesians	AC2	0.03138	0.04798	-0.01105	-0.00197	0.01271	0.000566
Polynesians	AC3	-0.01459	-0.01922	0.003433	-0.01135	-0.00779	0.009155
Polynesians	Adults	-0.07627	-0.00224	0.001625	-0.01349	-0.00344	0.022897
Utah	AC1	0.10426	-0.00679	0.01661	0.030121	-0.0139	-0.01324
Utah	AC2	0.04445	-0.00898	0.018823	0.00818	-0.00028	0.003031
Utah	AC3	-0.05003	0.02901	0.014978	-0.01203	0.021723	-0.00859
Utah	Adults	-0.04109	0.00599	0.030287	0.003773	0.000573	-0.01027

but that the temporal and occipital bone increased in length, with the sphenoid decreasing in length to compromise.

A study by A. C. Berry and R. J. Berry [49] found that the Egyptian population was characterized by distinctive cranial morphology, which had persisted for centuries and was dissimilar to the crania of other populations in their study. Based on the current findings, the Egyptian population showed a relatively decreasing anteroposterior length but increasingly elongated temporal and occipital bones compared to other population samples in this study. Given its genetic and geographic distance and cranial stability, the Egyptian population could have likely acted as a morphological and genetic outlier, and only with its exclusion did the results begin to show significant differences among populations in various regions of the basicranium and age categories.

One potentially limiting factor of this study is the degree of mismatch between the molecular and morphological population representatives. The morphological samples were chosen based on the availability of subadult cranial material in museum collections. Thus, we were not able to include a wide geographically distribution of populations. In North American natural history collections, there is a natural bias towards Native American specimens. Consequently, the

present study included a few Native American samples. Similarly, the molecular representative for each population was not a perfect match with these morphological populations. However, there is precedent for this approach. As noted by Roseman (2004), such mismatch is not necessarily problematic, but the correlations obtained from this type of analysis should be interpreted as minimal approximations of their actual value. Thus, the significant correlations obtained here should be interpreted as minimum estimates of a real biological relationship between morphology of the cranial region and genetic relatedness.

The landmark dataset employed in the present research expands the smaller landmark sets used by previous studies. Harvati and Weaver [2] and Smith et al. [34] each used a much smaller and less anatomically distributed set of landmarks, 13 and 15, respectively, while our study included 24. There were also some differences in landmark coverage and dispersion between this and prior studies. The temporal bone landmarks in this study were widely distributed to include points that overlap with the sphenoidal and occipital regions of the basicranium, covering a large area of all components of the basicranium. We used landmarks distributed from the asterion in the occipital region and auriculare in the temporal



with rather high accuracy. This is likely because the sphenoid body of basicranium reaches adult size and shape more rapidly than other portions, presumably because vital cranial nerves (II–VI) run through the cranial base in the sphenoid region [13, 16]. This may also result in a more constrained range of variation, since the sphenoid housed these essential neurological structures.

Population relatedness can be inferred using the basicranium, temporal, and occipital bone of subadults, especially those of 13–18 years of age. The findings of this study have implications for future studies of archaeological specimens for which genetic material is not well-preserved. Given that the morphology of the temporal bone and basicranium reflect genetic distances in young subadults, the morphology of these cranial subsets can be used to sort human populations with a reasonable degree of precision (25% and 41% mean classification, resp.). This could be useful for child or adolescent cranial specimens of unknown affinity found at archaeological sites.

If future studies examine other hominoid (ape) species in a similar manner, the findings combined with those of the present study would have implications for the development of hominoid brain size, posture, and evolution. First, the angle of the midline cranial base is hypothesized to correlate with the volume of the brain relative to its basicranial length [50–52]. Thus, findings relating to how the basicranium changes during ontogeny can contribute to a more comprehensive understanding of brain development in various ape species. Second, flexion of the cranial base has been interpreted to be an adaptation for upright posture in hominins, causing the foramen magnum to position anteriorly and orient ventrally [53–55]. The basicranium therefore affects the verticality of hominin posture. Third, the basicranium likely played a role in the evolution of the overall morphology of the primate skull [14, 23]. Specifically, the cranial base develops early in ontogeny and thus influences the development of later-ossifying regions, such as the facial skeleton and neurocranium [14, 23]. Evolutionary changes in the basicranium will necessarily impact the adaptive morphology of the entire primate cranial apparatus.

## 5. Conclusion

In this study, the basicranium, occipital, and temporal regions were found to reflect genetic distances among populations in childhood and adolescence. The sphenoid bone, however, is not a good indicator of genetic distances in subadults, but its morphology may still serve as a reasonably accurate means of classifying individuals by population affinity. Unsurprisingly, the Native American populations, and especially the Utah sample, were commonly classified as another Native American population, as would be predicted if basicranial shape reflects genetic relatedness. These findings reveal valuable information on the population differences in basicranial morphology at various ontogenetic stages.

## Conflict of Interests

The authors declare that there is no conflict of interests regarding the publication of this paper.

## Acknowledgments

Funding for this study was provided by the Biomedical Sciences Department at Midwestern University (to Deepal H. Dalal) and by Midwestern University faculty start-up funds (Heather F. Smith). The authors wish to thank the museum curators, Dr. David Hunt (NMNH) and Gisselle Garcia (AMNH), for facilitating access to the collections in their care. The authors also thank Dr. Mark N. Coleman and Dr. Justin A. Georgi for providing helpful comments and guidance on this study and Brent Adrian for providing valuable insight into an earlier draft of this paper.

## References

- [1] C. C. Roseman, “Detecting interregionally diversifying natural selection on modern human cranial form by using matched molecular and morphometric data,” *Proceedings of the National Academy of Sciences of the United States of America*, vol. 101, no. 35, pp. 12824–12829, 2004.
- [2] K. Harvati and T. D. Weaver, “Human cranial anatomy and the differential preservation of population history and climate signatures,” *The Anatomical Record A*, vol. 288, no. 12, pp. 1225–1233, 2006.
- [3] H. F. Smith, “Which cranial regions reflect molecular distances reliably in humans? Evidence from three-dimensional morphology,” *The American Journal of Human Biology*, vol. 21, no. 1, pp. 36–47, 2009.
- [4] N. von Cramon-Taubadel, “Congruence of individual cranial bone morphology and neutral molecular affinity patterns in modern humans,” *American Journal of Physical Anthropology*, vol. 140, no. 2, pp. 205–215, 2009.
- [5] N. von Cramon-Taubadel, “Revisiting the homology hypothesis: the impact of phenotypic plasticity on the reconstruction of human population history from craniometric data,” *Journal of Human Evolution*, vol. 57, no. 2, pp. 179–190, 2009.
- [6] J. H. Relethford, “Population-specific deviations of global human craniometric variation from a neutral model,” *American Journal of Physical Anthropology*, vol. 142, no. 1, pp. 105–111, 2010.
- [7] H. F. Smith, T. Ritzman, E. Otárola-Castillo, and C. E. Terhune, “A 3-D geometric morphometric study of intraspecific variation in the ontogeny of the temporal bone in modern *Homo sapiens*,” *Journal of Human Evolution*, vol. 65, no. 5, pp. 479–489, 2013.
- [8] U. S. Viðarsdóttir, P. O’Higgins, and C. Stringer, “A geometric morphometric study of regional differences in the ontogeny of the modern human facial skeleton,” *Journal of Anatomy*, vol. 201, no. 3, pp. 211–229, 2002.
- [9] U. S. Vidarsdottir and P. O’Higgins, “Development variation in the facial skeleton of anatomically modern *Homo sapiens*,” in *Patterns of Growth and Development in the Genus Homo*, J. L. Thompson, G. E. Krovitz, and A. J. Nelson, Eds., pp. 114–143, Cambridge University Press, Cambridge, UK, 2003.
- [10] S. N. Cobb and P. O’Higgins, “Hominins do not share a common postnatal facial ontogenetic shape trajectory,” *Journal of Experimental Zoology, Part B: Molecular and Developmental Evolution*, vol. 302, no. 3, pp. 302–321, 2004.

- [11] T. R. Olson, "Basicranial morphology of the extant hominoids and Pliocene hominids: the new material from the Hadar Formation, Ethiopia and its significance in early human evolution and taxonomy," in *Aspects of Human Evolution*, C. B. Stringer, Ed., pp. 99–128, Taylor & Francis, London, UK, 1981.
- [12] P. Houghton, *The People of the Great Ocean: Aspects of Human Biology in the Early Pacific*, Cambridge University Press, New York, NY, USA, 1996.
- [13] D. E. Lieberman, C. F. Ross, and M. J. Ravosa, "The primate cranial base: ontogeny, function, and integration," *American Journal of Physical Anthropology*, vol. 113, supplement 31, pp. 117–169, 2000.
- [14] D. E. Lieberman, O. M. Pearson, and K. M. Mowbray, "Basicranial influence on overall cranial shape," *Journal of Human Evolution*, vol. 38, no. 2, pp. 291–315, 2000.
- [15] K. Harvati, *The Neanderthal problem: 3-D geometric morphometric models of cranial shape variation within and among species [Ph.D. thesis]*, City University of New York, New York, NY, USA, 2001.
- [16] G. H. Sperber, *Craniofacial Embryology*, Wright PSG, Boston, Mass, USA, 1981.
- [17] G. de Beer, *The Development of the Vertebrate Skull*, University of Chicago Press, Chicago, Ill, USA, 1985, Reprint of 1937 edition, Oxford University Press.
- [18] N. Jeffery and F. Spoor, "Ossification and midline shape changes of the human fetal cranial base," *American Journal of Physical Anthropology*, vol. 123, no. 1, pp. 78–90, 2004.
- [19] B. A. Wood, "Are the 'robust' australopithecines a monophyletic group?" in *Evolutionary History of the "Robust" Australopithecines*, F. E. Grine, Ed., pp. 269–284, Aldine de Gruyter, New York, NY, USA, 1988.
- [20] R. R. Skelton and M. McHenry, "Evolutionary relationships among early hominids," *Journal of Human Evolution*, vol. 23, no. 4, pp. 309–349, 1992.
- [21] A. Turner and B. A. Wood, "Comparative palaeontological context for the evolution of the early hominid masticatory system," *Journal of Human Evolution*, vol. 24, no. 4, pp. 301–318, 1993.
- [22] H. M. Mchenry, "Tempo and mode in human evolution," *Proceedings of the National Academy of Sciences of the United States of America*, vol. 91, no. 15, pp. 6780–6786, 1994.
- [23] D. E. Lieberman, B. A. Wood, and D. R. Pilbeam, "Homoplasmy and early *Homo*: an analysis of the evolutionary relationships of *H. habilis sensu stricto* and *H. rudolfensis*," *Journal of Human Evolution*, vol. 30, no. 2, pp. 97–120, 1996.
- [24] W. J. Moore and C. J. B. Lavelle, *Growth of the Facial Skeleton in the Hominoidea*, Academic Press, London, UK, 1974.
- [25] R. D. E. MacPhee and M. Cartmill, "Basicranial structures and primate systematics," in *Comparative Primate Biology, Vol. 1: Systematics, Evolution, and Anatomy*, D. R. Swindler and J. Erwin, Eds., pp. 219–275, Alan R. Liss, New York, NY, USA, 1986.
- [26] B. Wood and D. E. Lieberman, "Craniodental variation in *Paranthropus boisei*: a developmental and functional perspective," *The American Journal of Physical Anthropology*, vol. 116, no. 1, pp. 13–25, 2001.
- [27] S. J. Lycett and M. Collard, "Do homoiologies impede phylogenetic analyses of the fossil hominids? An assessment based on extant papionin craniodental morphology," *Journal of Human Evolution*, vol. 49, no. 5, pp. 618–642, 2005.
- [28] M. Collard and B. Wood, "Hominin homoiology: an assessment of the impact of phenotypic plasticity on phylogenetic analyses of humans and their fossil relatives," *Journal of Human Evolution*, vol. 52, no. 5, pp. 573–584, 2007.
- [29] T. L. Eby and J. B. Nadol Jr., "Postnatal growth of the human temporal bone. Implications for cochlear implants in children," *Annals of Otolaryngology, Rhinology, and Laryngology*, vol. 95, no. 4, pp. 356–364, 1986.
- [30] D. L. Simms and J. G. Neely, "Growth of the lateral surface of the temporal bone in children," *Laryngoscope*, vol. 99, no. 8, pp. 795–799, 1989.
- [31] C. E. Terhune, W. H. Kimbel, and C. A. Lockwood, "Postnatal temporal bone ontogeny in *Pan*, *Gorilla*, and *Homo*, and the implications for temporal bone ontogeny in *Australopithecus afarensis*," *American Journal of Physical Anthropology*, vol. 151, no. 4, pp. 630–642, 2013.
- [32] C. A. Lockwood, J. M. Lynch, and W. H. Kimbel, "Quantifying temporal bone morphology of great apes and humans: an approach using geometric morphometrics," *Journal of Anatomy*, vol. 201, no. 6, pp. 447–464, 2002.
- [33] C. A. Lockwood, W. H. Kimbel, and J. M. Lynch, "Morphometrics and hominoid phylogeny: support for a chimpanzee-human clade and differentiation among great ape subspecies," *Proceedings of the National Academy of Sciences of the United States of America*, vol. 101, no. 13, pp. 4356–4360, 2004.
- [34] H. F. Smith, C. E. Terhune, and C. A. Lockwood, "Genetic, geographic, and environmental correlates of human temporal bone variation," *American Journal of Physical Anthropology*, vol. 134, no. 3, pp. 312–322, 2007.
- [35] N. A. Rosenberg, S. Mahajan, S. Ramachandran, C. Zhao, J. K. Pritchard, and M. W. Feldman, "Clines, clusters, and the effect of study design on the inference of human population structure," *PLoS Genetics*, vol. 1, no. 6, pp. 660–671, 2005.
- [36] N. von Cramon-Taubadel, "The relative efficacy of functional and developmental cranial modules for reconstructing global human population history," *The American Journal of Physical Anthropology*, vol. 146, no. 1, pp. 83–93, 2011.
- [37] D. Ubelaker, *Human Skeletal Remains: Excavation, Analysis, Interpretation*, Smithsonian Institution Press, Washington, DC, USA, 2nd edition, 1989.
- [38] T. D. White and P. A. Folkens, *Human Osteology*, Academic Press, 2nd edition, 2000.
- [39] J. L. Weber and P. E. May, "Abundant class of human DNA polymorphisms which can be typed using the polymerase chain reaction," *American Journal of Human Genetics*, vol. 44, no. 3, pp. 388–396, 1989.
- [40] S. Ramachandran, O. Deshpande, C. C. Roseman, N. A. Rosenberg, M. W. Feldman, and L. L. Cavalli-Sforza, "Support from the relationship of genetic and geographic distance in human populations for a serial founder effect originating in Africa," *Proceedings of the National Academy of Sciences of the United States of America*, vol. 102, no. 44, pp. 15942–15947, 2005.
- [41] M. D. Shriver, L. Jin, R. Chakraborty, and E. Boerwinkle, "VNTR allele frequency distributions under the stepwise mutation model: a computer simulation approach," *Genetics*, vol. 134, no. 3, pp. 983–993, 1993.
- [42] A. M. Valdes, M. Slatkin, and N. B. Freimer, "Allele frequencies at microsatellite loci: the stepwise mutation model revisited," *Genetics*, vol. 133, no. 3, pp. 737–749, 1993.
- [43] D. B. Goldstein, A. R. Linares, L. L. Cavalli-Sforza, and M. W. Feldman, "An evaluation of genetic distances for use with microsatellite loci," *Genetics*, vol. 139, no. 1, pp. 463–471, 1995.

- [44] C. P. Klingenberg, "MorphoJ: an integrated software package for geometric morphometrics," *Molecular Ecology Resources*, vol. 11, no. 2, pp. 353–357, 2011.
- [45] L. Excoffier, G. Laval, and S. Schneider, "Arlequin (version 3.0): an integrated software package for population genetics data analysis," *Evolutionary Bioinformatics Online*, vol. 1, pp. 47–50, 2005.
- [46] N. Mantel, "The detection of disease clustering and a generalized regression approach," *Cancer Research*, vol. 27, no. 2, pp. 209–220, 1967.
- [47] P. O'Higgins and N. Jones, *Tools for Statistical Shape Analysis*, Hull York Medical School, Heslington, UK, 2006, <http://sites.google.com/site/hymsfme/resources>.
- [48] C. C. Gilbert, S. R. Frost, and D. S. Strait, "Allometry, sexual dimorphism, and phylogeny: a cladistic analysis of extant African papionins using craniodental data," *Journal of Human Evolution*, vol. 57, no. 3, pp. 298–320, 2009.
- [49] A. C. Berry and R. J. Berry, "Epigenetic variation in the human cranium," *Journal of Anatomy*, vol. 101, no. 2, pp. 361–379, 1967.
- [50] E. L. DuBrul and D. M. Laskin, "Preadaptive potentialities of the mammalian skull: an experiment in growth and form," *American Journal of Anatomy*, vol. 109, pp. 117–132, 1961.
- [51] S. J. Gould, *Ontogeny and Phylogeny*, Belknap Press, Cambridge, Mass, USA, 1977.
- [52] A. Riesenfeld, "The adaptive mandible: an experimental study," *Acta Anatomica*, vol. 72, no. 2, pp. 246–262, 1969.
- [53] E. L. DuBrul, "Early hominid feeding mechanisms," *American Journal of Physical Anthropology*, vol. 47, no. 2, pp. 305–320, 1977.
- [54] E. L. DuBrul, "Origin and adaptations of the hominid jaw joint," in *The Temporomandibular Jaw Joint*, B. G. Sarnat and D. M. Laskin, Eds., pp. 5–34, Charles C Thomas Publisher, Springfield, Ill, USA, 3rd edition, 1979.
- [55] A. H. Schultz, "Conditions for balancing the head in primates," *American Journal of Physical Anthropology*, vol. 29, no. 4, pp. 483–497, 1942.

## Research Article

# Using Magnetic Resonance for Predicting Femoral Strength: Added Value with respect to Bone Densitometry

Olivia Louis,<sup>1</sup> Yves Fierens,<sup>1</sup> Maria Strantza,<sup>2</sup> Robert Luypaert,<sup>1</sup>  
Johan de Mey,<sup>1</sup> and Erik Cattrysse<sup>3</sup>

<sup>1</sup>Department of Radiology, UZ Brussel, Vrije Universiteit Brussel, Laarbeeklaan 101, 1090 Brussels, Belgium

<sup>2</sup>Department of Mechanics of Materials and Constructions, Vrije Universiteit Brussel, Pleinlaan 2, 1040 Brussels, Belgium

<sup>3</sup>Department of Experimental Anatomy, Vrije Universiteit Brussel, Laarbeeklaan 103, 1090 Brussels, Belgium

Correspondence should be addressed to Olivia Louis; [olivia.louis@uzbrussel.be](mailto:olivia.louis@uzbrussel.be)

Received 21 January 2015; Accepted 11 March 2015

Academic Editor: Levent Sarikcioglu

Copyright © 2015 Olivia Louis et al. This is an open access article distributed under the Creative Commons Attribution License, which permits unrestricted use, distribution, and reproduction in any medium, provided the original work is properly cited.

**Background and Purpose.** To evaluate the added value of MRI with respect to peripheral quantitative computed tomography (pQCT) and dual energy X-ray absorptiometry (DXA) for predicting femoral strength. **Material and Methods.** Bone mineral density (BMD) of eighteen femur specimens was assessed with pQCT, DXA, and MRI (using ultrashort echo times (UTE) and the MicroView software). Subsequently biomechanical testing was performed to assess failure load. Simple and multiple linear regression were used with failure load as the dependent variable. **Results.** Simple linear regression allowed a prediction of failure load with either pQCT, DXA, or MRI in an  $r^2$  range of 0.41–0.48. Multiple linear regression with pQCT, DXA, and MRI yielded the best prediction ( $r^2 = 0.68$ ). **Conclusions.** The accuracy of MRI, using UTE and MicroView software, to predict femoral strength compares well with that of pQCT or DXA. Furthermore, the inclusion of MRI in a multiple-regression model yields the best prediction.

## 1. Introduction

Hip fractures represent one of the most deleterious consequences of osteoporosis. Bone strength is routinely evaluated using bone mineral density (BMD), measured either with quantitative computed tomography (QCT), as a volumetric density, or with dual-energy X-ray absorptiometry (DXA), as an areal density. These techniques provide accurate measures for BMD [1, 2], but they have the disadvantage of using X-rays. The ability of quantitative computed tomography (QCT) and/or DXA to predict femoral strength as assessed using biomechanical testing has been evaluated in some previous studies [3–6]. The conclusion was that adding some texture parameter obtained with high-resolution digital X-ray or some geometrical parameter derived from QCT or DXA improved the prediction obtained from BMD. Another technique, magnetic resonance imaging (MRI), has also been found to be suitable for assessing bone. Several groups have shown that geometrical variables can be assessed using MRI at the level of the femur or the tibia [7–9]. In a clinical

setting, MRI has the advantage of examining the patient without ionizing irradiation but also the disadvantage of not measuring BMD.

In the present study, our objective was to compare the ability of the BMD measures derived from peripheral QCT (pQCT), DXA, and MRI to predict femoral strength. In particular, we wanted to evaluate the added value of MRI with respect to classical bone densitometry techniques. For this purpose, we have examined excised femurs with pQCT, DXA, and MRI, subsequently performing biomechanical testing in order to obtain a neck fracture and to assess the failure load. The MRI consisted of an ultrashort-echo-time acquisition. After segmentation of the resulting images, BMD values were derived using the MicroView Advanced Bone Analysis Applications software (GE Healthcare, Illinois, USA).

## 2. Materials and Methods

**2.1. Specimens.** This study was performed on 18 femur specimens excised from 18 cadavers. All cadavers had been

donated through a body donation program of our university and had been preserved using the injection of a formalin solution in the vessels. Eleven of the specimens originated from women and seven from men. The age of the subjects ranged from 73 to 97 years. The main causes of death were heart failure and cerebrovascular insult. Malignancy, chronic infection, diabetes, or treatment susceptible to interfere with bone metabolism was not present in any of the cases.

**2.2. Peripheral Quantitative Computed Tomography.** Single-energy pQCT was performed using a Stratec XCT 2000 device (Stratec, Pforzheim, Germany) with a 37 keV X-ray tube as source of radiation. All the examinations were performed by the same experienced radiologist (OL). In each specimen, four slices (2 mm thick) at the level of the femoral neck and situated at, respectively, 1%, 2%, 3%, and 4% of the whole femoral length below the upper limit of the neck were studied. Trabecular and cortical bone were analyzed separately. The threshold used to define cortical bone was fixed at a linear attenuation coefficient of  $0.93 \text{ cm}^{-1}$  to minimize partial volume effect. The total bone mineral density of the first, second, third, and fourth slice (pQCT-BMD<sub>1</sub>, pQCT-BMD<sub>2</sub>, pQCT-BMD<sub>3</sub>, and pQCT-BMD<sub>4</sub>) was reported. All densities were expressed as milligrams hydroxyapatite of calcium per millilitre.

**2.3. Dual-Energy X-Ray Absorptiometry.** Dual-energy X-ray absorptiometry was performed using a Hologic Discovery apparatus (Waltham, Massachusetts, USA), with an X-ray source pulsed alternately at 100 and 140 kVp (effective beam energies 43 and 110 KV). All the examinations were performed by the same experienced radiologist (OL). The femurs were scanned while being immersed in a 16 cm water bath. Image acquisition and analysis were done following the recommendations of the manufacturer. Areal BMD ( $\text{mg}/\text{cm}^2$ ) was assessed. Here, the bone mineral density of the total hip (DXA-BMD<sub>tot</sub>), and at the level of the neck (DXA-BMD<sub>ne</sub>), the cortical thickness at the level of the neck, expressed as mm (DXA-CoT<sub>ne</sub>), and the neck shaft angle, expressed as degrees (DXA-NSA), were reported.

**2.4. Magnetic Resonance Imaging.** All femurs were scanned using a 3 Tesla Philips Achieva TX MRI system (Best, Netherlands), using a standard 8-channel knee coil, a 3D radial acquisition technique, and ultrashort echo times (UTE). All the examinations were performed by the same physicist (YF). UTE sequences allow estimation of bone  $R2^*$  and permit subsequent segmentation of the bone. This technique was previously used for attenuation correction methods in PET-MRI systems [10]. Our sequence combined two echo times (0.14 ms and 2.6 ms). Repetition time (TR) was 20 ms. Voxel size was  $0.4 \times 0.4 \times 0.4 \text{ mm}$ . The angular density of the radial profiles was 200%, in order to prevent undersampling of the boundary of k-space due to the radial acquisition trajectories. Starting from the resulting images, 2 mm thick multiplanar reconstructions corresponding to the locations of the four

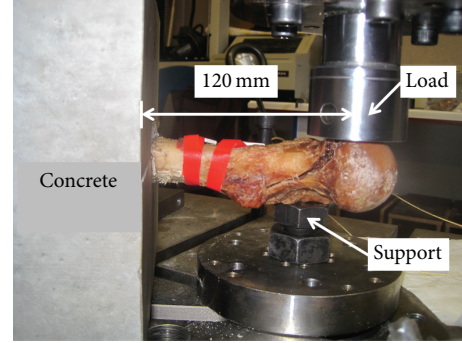


FIGURE 1: Biomechanical test of an excised femur partially encased in concrete.

pQCT slices were made using the manufacturer's software. The corresponding  $R2^*$  maps were calculated according to

$$R2^* = \frac{\ln(S_{\text{short}}) - \ln(S_{\text{long}})}{TE_{\text{long}} - TE_{\text{short}}}, \quad (1)$$

where  $TE_{\text{long}}$  and  $TE_{\text{short}}$  are the echo times and  $S_{\text{short}}$  and  $S_{\text{long}}$  are the corresponding signals.

Using thresholding, segmentation into bone, air, and tissue was obtained. Air was masked using a signal threshold on the short echo images. The threshold between tissue and bone ( $R2^*_{\text{resh}} = 0.3 \text{ MHz}$ ) was determined on the basis of a single femur and applied for all specimens. The segmented images were mapped into pseudo-computed-tomography images using standard Hounsfield units for each tissue ( $-1000$  for air,  $0$  for tissue, and  $1000$  for bone). Finally, this pseudo-computed-tomography image was analyzed using the MicroView Advanced Bone Analysis Applications (GE Healthcare, Illinois, USA) [11] to obtain BMD values for all four slice positions. The reported variables were MRI-BMD<sub>1</sub>, MRI-BMD<sub>2</sub>, MRI-BMD<sub>3</sub>, and MRI-BMD<sub>4</sub>, corresponding to the total bone mineral density assessed, respectively, at the first, second, third, and fourth slice. The densities were expressed as milligrams hydroxyapatite of calcium per milliliter.

**2.5. Biomechanical Testing.** First, an ultrasonic study was performed on some of the femur specimens in order to evaluate the elastic wave propagation in human femur tissues [12]. Next, the femur specimens were prepared for biomechanical testing by encasing the three distal quarters of the femoral diaphysis in concrete (Figure 1). The distance between the head of the femur specimen and the concrete fixation was 120 mm. In order to avoid the fracture at the fixation point and to mimic a neck fracture, a support was provided at the level of the main body using a metal bolt. The geometry of the setup resulted in a combination of bending and torsion. An Instron 5885 (Buckinghamshire, UK) machine was used, with 10 kN load cell and a constant rate of displacement of 2 mm/min. All the examinations were performed by the same experienced physicist (MS). The testing machine had been validated in our laboratory, as recommended by Turner and Burr [13], using plastics material standards, and had

TABLE 1: Descriptive statistics of 18 femur specimens.

	Unit	Mean	SD
Age	Year	83.9	6.5
pQCT-BMD <sub>1</sub>	mg/mL	250.4	58.2
pQCT-BMD <sub>2</sub>	mg/mL	230.2	53.6
pQCT-BMD <sub>3</sub>	mg/mL	228.3	45.4
pQCT-BMD <sub>4</sub>	mg/mL	241.2	51.6
DXA-BMD <sub>tot</sub>	mg/cm <sup>2</sup>	763.0	131.0
DXA-BMD <sub>ne</sub>	mg/cm <sup>2</sup>	613.0	123.0
DXA-CoT <sub>ne</sub>	mm	1.3	0.3
DXA-NSA	Degree	131.8	4.5
MRI-BMD <sub>1</sub>	mg/mL	212.4	86.5
MRI-BMD <sub>2</sub>	mg/mL	200.1	79.9
MRI-BMD <sub>3</sub>	mg/mL	199.9	76.3
MRI-BMD <sub>4</sub>	mg/mL	180.2	71.5
Load	N	2005.8	957.1

pQCT-BMD<sub>1</sub>, pQCT-BMD<sub>2</sub>, pQCT-BMD<sub>3</sub>, and pQCT-BMD<sub>4</sub>: total bone mineral density measured with pQCT, respectively, at the first, second, third, and fourth slice.

DXA-BMD<sub>tot</sub>, DXA-BMD<sub>ne</sub>, DXA-CoT<sub>ne</sub>, and DXA-NSA: bone mineral density of the total hip and at the level of the neck, cortical thickness at the level of the neck and neck shaft angle, measured with DXA.

MRI-BMD<sub>1</sub>, MRI-BMD<sub>2</sub>, MRI-BMD<sub>3</sub>, and MRI-BMD<sub>4</sub>: total bone mineral density measured with MRI, respectively, at the first, second, third, and fourth slice.

been used previously to assess the compressive strength of peripheral bone specimens [14]. Load-displacement curves were recorded during test and the failure load, expressed in Newton (N), was reported.

**2.6. Statistical Analysis.** The collected data were reported as mean (standard deviation (SD)). Linear regression analysis was performed using SPSS, version 20 (IBM Corp, Armonk, NY). Results were reported as coefficients of determination (squared correlation coefficients) and as prediction equations (load as dependent variable).

### 3. Results

Mean (SD) values of the variables obtained from pQCT, DXA, and MRI, as well as the failure load, are listed in Table 1. A specimen, partially encased in concrete, as submitted to the test, is shown in Figure 1. As expected, a neck fracture occurred in all specimens. A typical load-displacement curve is shown in Figure 2.

Simple linear regression analysis showed that the best prediction of failure load was obtained with the density measured at the level of the second slice for pQCT ( $r^2 = 0.48$ ,  $P = 0.002$ ), the total density for DXA ( $r^2 = 0.43$ ,  $P = 0.003$ ), and the total density assessed at the level of the first slice for MRI ( $r^2 = 0.41$ ,  $P = 0.004$ ). All coefficients of determination are listed in Table 2.

In a second step, we tested multiple-regression models, using the variables ranked best in the simple linear regression

TABLE 2: Simple linear regression analysis (with load as dependent variable).

Measure	$r^2$	$P$
pQCT-BMD <sub>1</sub>	0.36	0.009
pQCT-BMD <sub>2</sub>	0.48	0.002
pQCT-BMD <sub>3</sub>	0.42	0.004
pQCT-BMD <sub>4</sub>	0.15	0.110
DXA-BMD <sub>tot</sub>	0.43	0.003
DXA-BMD <sub>ne</sub>	0.41	0.004
DXA-CoT <sub>ne</sub>	0.41	0.004
DXA-NSA	0.09	0.269
MRI-BMD <sub>1</sub>	0.41	0.004
MRI-BMD <sub>2</sub>	0.32	0.015
MRI-BMD <sub>3</sub>	0.08	0.248
MRI-BMD <sub>4</sub>	0.17	0.084

The values in the table are coefficients of determination ( $r^2$ ) and significance levels ( $P$  values).

Same abbreviations as in Table 1.

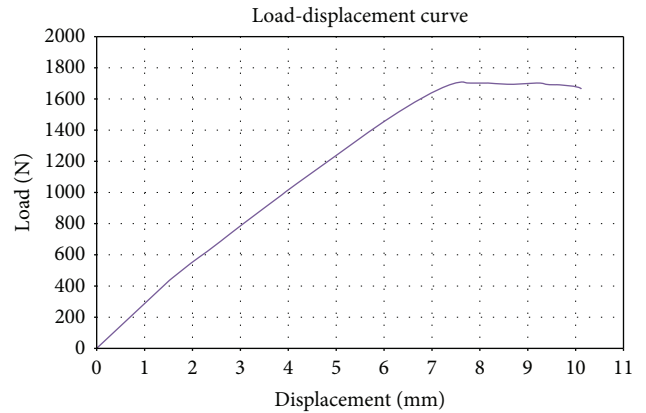


FIGURE 2: Biomechanical testing: load (N) plotted against displacement (mm).

analysis, namely, pQCT-BMD<sub>2</sub>, DXA-BMD<sub>tot</sub>, and MRI-BMD<sub>1</sub>. The stepwise and reverse-stepwise procedures yielded the same best models.

Including only pQCT and DXA, the best prediction model was

$$\begin{aligned} \text{Load} = & -1417.9 + (8.36 \times \text{pQCT-BMD}_2) \\ & + (1.96 \times \text{DXA-BMD}_{\text{tot}}) \end{aligned} \quad (2)$$

$$r^2 = 0.50, \quad P = 0.006.$$

Adding MRI improved the prediction:

$$\begin{aligned} \text{Load} = & -1674.9 + (7.03 \times \text{pQCT-BMD}_2) \\ & + (1.33 \times \text{DXA-BMD}_{\text{tot}}) \\ & + (4.96 \times \text{MRI-BMD}_1) \end{aligned} \quad (3)$$

$$r^2 = 0.68, \quad P = 0.001.$$

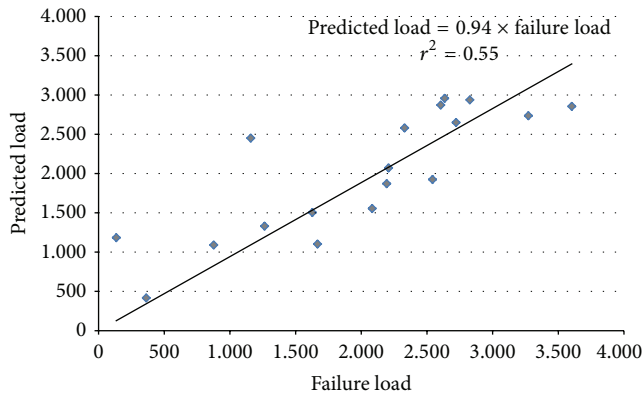


FIGURE 3: Predicted load from the multiple linear regression model plotted against the measured failure load (both expressed in N).

The agreement between the load predicted by the model and the observed failure load is illustrated in Figure 3.

#### 4. Discussion

In the present study we examined 18 excised femurs consecutively with pQCT, DXA (after immersion in a water bath), and ultrashort-echo-time MRI. Subsequently, the femurs were subjected to biochemical testing. Linear regression analysis showed that the prediction of femoral strength obtained from BMD measured using MRI compared reasonably well with that obtained from BMD measured using pQCT or DXA. Furthermore, the optimal prediction was obtained with a model including one variable from each of the three methods.

Earlier studies of the relationship between conventional bone densitometry and biomechanical properties of femur specimens have examined the potential added value of bone-imaging techniques. Several authors have found that bone texture parameters, derived from using a high-resolution digital X-ray device, are as effective as the BMD generated by DXA in predicting the maximal failure load on biomechanical testing [5, 6]. Similarly, other groups have found that combining BMD measured by DXA with texture parameters allowed a better prediction of the failure load of excised femurs than that obtained with BMD alone [15, 16]. Where bone densitometry techniques are concerned, some groups focused their study on a comparison between DXA and QCT. Cheng et al. concluded that DXA and QCT had a similar ability to predict femoral strength in vitro, the best DXA parameter being the trochanteric BMD and the best QCT parameter the cortical area [3]. On the other hand, Bousson et al. concluded that QCT was a better predictor of failure load than DXA [4] in case of cervical fracture of the proximal femur. Until now, few studies have examined the ability of MRI to predict femoral strength and all these studies have focused on geometrical parameters. Manske et al. reported that the cortical area of the femoral neck, assessed using MRI, was significantly associated with failure load, with, however, a weaker prediction than that obtained with BMD using DXA [17]. Similarly, Bae et al., studying femur cortical bone slabs and using UTE, reported significant associations between

MRI variables and mechanical properties, with, however, the best  $r^2$  being only 0.31 [18].

In the present study we chose pQCT rather than QCT because pQCT allows studying slices at different levels of the femoral neck. So doing, we obtained the best prediction of femoral strength with the density assessed at the second slice. The main originality of this study is however the segmentation of the ultrashort-echo-time MRI images and their subsequent analysis using the MicroView software, allowing us to obtain BMD values. This approach differs from that used in previous MRI bone studies, which all focused on geometrical parameters [17–19]. Using this approach we obtained a degree of prediction of failure load comparing reasonably well to that obtained with pQCT-derived or DXA-derived density. Furthermore, the addition of MRI-derived BMD to BMD derived from pQCT and DXA in a multiple linear regression model improved the coefficient of determination from 0.50 to 0.68.

Our study has strengths and limitations. To assess BMD we used DXA, the most frequently used method worldwide, but also two three-dimensional techniques, able to measure a true volumetric density. Furthermore, the specimens were obtained from subjects without any known disease interfering with bone metabolism. The main limitation of our study is the relatively small number of femurs, including both genders. In addition, we cannot exclude that the injection of a formalin solution might have some effect on the mechanical properties of the bone specimens. Finally, our results derived from the biomechanical testing cannot be extrapolated to in vivo injury characterized by complex interactions related to fall conditions, overlying soft tissue, and muscular strength.

#### 5. Conclusions

The present study performed on femur specimens suggests that MRI using UTE and a subsequent analysis with the MicroView Advanced Bone Analysis Applications software is able to measure BMD. This MRI-derived BMD correlates with failure load to an extent comparing well with BMD derived from classical bone densitometry techniques (pQCT or DXA). Furthermore, when using a multiple linear regression model, the addition of MRI improves the prediction of femoral strength.

#### Conflict of Interests

The authors declare that there is no conflict of interests regarding the publication of this paper.

#### Authors' Contribution

Louis designed the study, performed the research, and wrote the first draft. Fierens and Strantzla participated in the research. All authors participated in the interpretation of the results and in writing the subsequent drafts.

#### Acknowledgments

The authors acknowledge the people who altruistically donated their body for education and research according to

the body donation program of our university, as well as Frans Boulpaep for participating in the biomechanical testing, and Walter Rijsselaere for secretarial assistance.

## References

- [1] O. Louis, P. van den Winkel, P. Covens, A. Schoutens, and M. Osteaux, "Mineral content of vertebral trabecular bone: Accuracy of dual energy quantitative computed tomography evaluated against neutron activation analysis and flame atomic absorption spectrometry," *Bone*, vol. 15, no. 1, pp. 35–39, 1994.
- [2] O. Louis, P. van den Winkel, P. Covens, A. Schoutens, and M. Osteaux, "Dual-energy X-ray absorptiometry of lumbar vertebrae: relative contribution of body and posterior elements and accuracy in relation with neutron activation analysis," *Bone*, vol. 13, no. 4, pp. 317–320, 1992.
- [3] X. G. Cheng, G. Lowet, S. Boonen et al., "Assessment of the strength of proximal femur in vitro: relationship to femoral bone mineral density and femoral geometry," *Bone*, vol. 20, no. 3, pp. 213–218, 1997.
- [4] V. Bousson, A. le Bras, F. Roqueplan et al., "Volumetric quantitative computed tomography of the proximal femur: relationships linking geometric and densitometric variables to bone strength. Role for compact bone," *Osteoporosis International*, vol. 17, no. 6, pp. 855–864, 2006.
- [5] P. Pulkkinen, T. Jämsä, E.-M. Lochmüller, V. Kuhn, M. T. Nieminen, and F. Eckstein, "Experimental hip fracture load can be predicted from plain radiography by combined analysis of trabecular bone structure and bone geometry," *Osteoporosis International*, vol. 19, no. 4, pp. 547–558, 2008.
- [6] C. Chappard, V. Bousson, C. Bergot et al., "Prediction of femoral fracture load: cross-sectional study of texture analysis and geometric measurements on plain radiographs versus bone mineral density," *Radiology*, vol. 255, no. 2, pp. 536–543, 2010.
- [7] E. de Bisschop, R. Luypaert, S. Allein, and M. Osteaux, "Quantification of trabecular structure in the distal femur using magnetic resonance phase imaging," *Magnetic Resonance Imaging*, vol. 14, no. 1, pp. 11–20, 1996.
- [8] H. J. Woodhead, A. F. Kemp, C. J. R. Blimkie et al., "Measurement of midfemoral shaft geometry: repeatability and accuracy using magnetic resonance imaging and dual-energy X-ray absorptiometry," *Journal of Bone and Mineral Research*, vol. 16, no. 12, pp. 2251–2259, 2001.
- [9] W. Högler, C. J. R. Blimkie, C. T. Cowell et al., "A comparison of bone geometry and cortical density at the mid-femur between prepuberty and young adulthood using magnetic resonance imaging," *Bone*, vol. 33, no. 5, pp. 771–778, 2003.
- [10] V. Keereman, Y. Fierens, C. Vanhove, T. Lahoutte, and S. Vandenberghe, "Magnetic resonance-based attenuation correction for micro-single-photon emission computed tomography," *Molecular Imaging*, vol. 11, no. 2, pp. 155–165, 2012.
- [11] J. A. Meganck, K. M. Kozloff, M. M. Thornton, S. M. Broski, and S. A. Goldstein, "Beam hardening artifacts in micro-computed tomography scanning can be reduced by X-ray beam filtration and the resulting images can be used to accurately measure BMD," *Bone*, vol. 45, no. 6, pp. 1104–1116, 2009.
- [12] M. Strantza, O. Louis, D. Polyzos, F. Boulpaep, D. van Hemelrijck, and D. G. Aggelis, "Wave dispersion and attenuation on human femur tissue," *Sensors*, vol. 14, no. 8, pp. 15067–15083, 2014.
- [13] C. H. Turner and D. B. Burr, "Basic biomechanical measurements of bone: a tutorial," *Bone*, vol. 14, no. 4, pp. 595–608, 1993.
- [14] O. Louis, F. Boulpaep, J. Willnecker, P. van den Winkel, and M. Osteaux, "Cortical mineral content of the radius assessed by peripheral QCT predicts compressive strength on biomechanical testing," *Bone*, vol. 16, no. 3, pp. 375–379, 1995.
- [15] S. Kolta, S. Paratte, T. Amphoux et al., "Bone texture analysis of human femurs using a new device (BMA) improves failure load prediction," *Osteoporosis International*, vol. 23, no. 4, pp. 1311–1316, 2012.
- [16] T. le Corroller, M. Pithioux, F. Chaari et al., "Bone texture analysis is correlated with three-dimensional microarchitecture and mechanical properties of trabecular bone in osteoporotic femurs," *Journal of Bone and Mineral Metabolism*, vol. 31, no. 1, pp. 82–88, 2013.
- [17] S. L. Manske, T. Liu-Ambrose, P. M. de Bakker et al., "Femoral neck cortical geometry measured with magnetic resonance imaging is associated with proximal femur strength," *Osteoporosis International*, vol. 17, no. 10, pp. 1539–1545, 2006.
- [18] W. C. Bae, P. C. Chen, C. B. Chung, K. Masuda, D. D'Lima, and J. Du, "Quantitative ultrashort echo time (UTE) MRI of human cortical bone: correlation with porosity and biomechanical properties," *Journal of Bone and Mineral Research*, vol. 27, no. 4, pp. 848–857, 2012.
- [19] O. Louis, E. Cattrysse, A. Scafoglieri, R. Luypaert, J. P. Clarys, and J. De Mey, "Accuracy of peripheral quantitative computed tomography and magnetic resonance imaging in assessing cortical bone cross-sectional area: a cadaver study," *Journal of Computer Assisted Tomography*, vol. 34, no. 3, pp. 469–472, 2010.

## Research Article

# Reexamination of Statistical Methods for Comparative Anatomy: Examples of Its Application and Comparisons with Other Parametric and Nonparametric Statistics

Roqueline A. G. M. F. Aversi-Ferreira,<sup>1,2,3</sup> Hisao Nishijo,<sup>3</sup>  
and Tales Alexandre Aversi-Ferreira<sup>3</sup>

<sup>1</sup>Graduate School of Animal Biology, Institute of Biology, University of Brasilia, Darcy Ribeiro Campus, 70910-900 Brasilia, DF, Brazil

<sup>2</sup>Laboratory of Neuroscience and Behavior, Department of Physiology, University of Brasilia, Darcy Ribeiro Campus, 70910-900 Brasilia, DF, Brazil

<sup>3</sup>Department of System Emotional Science, Graduate School of Medicine and Pharmaceutical Sciences, University of Toyama, Toyama 930-0194, Japan

Correspondence should be addressed to Tales Alexandre Aversi-Ferreira; [aversiferreira@gmail.com](mailto:aversiferreira@gmail.com)

Received 20 February 2015; Revised 9 March 2015; Accepted 10 March 2015

Academic Editor: Ilker Ercan

Copyright © 2015 Roqueline A. G. M. F. Aversi-Ferreira et al. This is an open access article distributed under the Creative Commons Attribution License, which permits unrestricted use, distribution, and reproduction in any medium, provided the original work is properly cited.

Various statistical methods have been published for comparative anatomy. However, few studies compared parametric and nonparametric statistical methods. Moreover, some previous studies using statistical method for comparative anatomy (SMCA) proposed the formula for comparison of groups of anatomical structures (multiple structures) among different species. The present paper described the usage of SMCA and compared the results by SMCA with those by parametric test (*t*-test) and nonparametric analyses (cladistics) of anatomical data. In conclusion, the SMCA can offer a more exact and precise way to compare single and multiple anatomical structures across different species, which requires analyses of nominal features in comparative anatomy.

## 1. Introduction

Some biological sciences are dependent on subjective decision of scientists due to lack of appropriate numerical methods to determine observations. The description of biological structures, for instance, is sometimes exhaustive and depends on scientists' subjective observations. It is well known that the ancient researchers mistook analyses of the anatomical structures including their numbers, for example, the number of the cranial nerves, probably because of the scarce conditions during the works at that time [1]. Nevertheless, most structures in the body analyzed in the past were reported to contain the same number of structures nowadays.

In fact, gross anatomy requires descriptions of qualitative variables including innervation, vascularization, origin and

insertion of muscles, and arteries and nerve branches. It also requires quantitative analyses of mass, area, volume, size, and dimensional measures of such biological structures, which can be characterized by parametric statistical methods. However, parametric statistical methods can be hardly applied to description of qualitative variables in a scope of gross anatomy [2]. This is one of the reasons why the different authors with great experiences differently described structures of the same species without considering anatomical variations (for an illustrative example of confusion regarding the name and description of the tibial artery, see [3]).

Here, we propose the main methodology to characterize qualitative data in gross anatomy, which enables us to describe and compare objectively anatomical structures across different species. Specifically, there have been no

adequate quantitative methods to compare discrete-nominal variables of anatomical structures. It is desirable to quantitatively assess discrete variables [4]. Indeed, a nonparametric statistical method has been proposed for comparative anatomy [2] and actually used in some works [5, 6]. Although these studies compared their nonparametric statistical method with one of nonparametric methods (chi-square), the authors did not compare their nonparametric method with parametric ones, nor did they specify possible problems of interpretation of the data. Moreover, for statistical method for comparative anatomy (SMCA), the formula must be modified so that it accepts data of multiple structures across different species.

For objective descriptions of the anatomical structures, some authors used the chi-square comparison to analyze nominal variables [7, 8] by converting frequencies of anatomical characteristics to percentages. Thus, they calculated standard deviations of the data in percentages. However, standard deviations of nonparametric data derived from a kind of the discrete categorical variables usually generate a statistical error type I [2]. Furthermore, the basis of the chi-square statistic is causality among the data, a hypothesis that is not consistent with a theory of evolution assuming the concept of the common ancestral [9]. Anatomy of body structures such as innervation, origin, and/or insertion of muscles of the arm, for instance, seems to be not random in animals that evolved from a common ancestral animal, since the ancestral animal provided basic structures and could generate derivative features in descendant animals (for a detailed review, see [2]). Nevertheless, the chi-square statistic is an important tool among multivariate analyses of discrete variables that are considered to be independent in quantitative psychology [10]. Another nonparametric method (cladistics) was applied to comparative anatomy to analyze primitive and derivative features in evolution [11, 12] but has not yet been applied to descriptive anatomy.

In this paper we compared the nonparametric method for SMCA [5, 6] with another parametric method (*t*-test) analyzing means of the samples, using the previously published data [6]. The SMCA including Comparative Anatomy Index for groups of structures (GCAI) that enables comparison of multiple structures [5] (see Section 3.2 for details) was also compared with another nonparametric (cladistics) method.

## 2. Material

This work reanalyzed the previously published data in comparative anatomy statistic (SMCA) [5] to verify this method in detail [2] and applied the new formula (GCAI) to compare groups of structures among different species. Furthermore, using the published data [5, 6] as examples, we show the steps to calculate the SMCA and compare between the SMCA and a parametric test (*t*-test) and also between the SMCA and other nonparametric (cladistics) methods [6].

## 3. Methods

**3.1. Methods to Compare Samples from Same Species.** The first step of this statistical method for comparative anatomy

(SMCA) is to analyze the frequency based on the anatomical concept of *normality* and *variation*. “A normal structure” means that it is observed in greater than 50% of cases within the same species; therefore, the variation can be observed in less than 50% of cases [13]:

$$N = N_{ijk} = \sum_{i=1}^q (r_{v(ijk)} + n_{v(ijk)}), \quad (1)$$

where  $N$  is the total number of analyzed structures of the samples,  $n_v$  is the number of structures with variation, and  $r_v$  is the number of normal structures ( $N - n_v$ ). The subscript ( $i$ ) indicates specific species such as humans, *Cebus*, and baboon, while the subscript ( $j$ ) indicates specific structures (flexor pollicis longus, pronator quadratus, etc.), and the subscript ( $k$ ) indicates parameters of the specific structures. For muscle studies, the parameters should include at least the following 4 parameters: (1) innervation, (2) origin, (3) insertion, and (4) vascularization of muscles. For example, in case of the flexor pollicis longus muscle ( $j = 1$ ) in *Cebus* ( $i = 1$ ), the data analyses in this step should be performed in terms of the following 4 parameters: the (1) innervation ( $r_{v(111)}, n_{v(111)}$ ), (2) origin ( $r_{v(112)}, n_{v(112)}$ ), (3) insertion ( $r_{v(113)}, n_{v(113)}$ ), and (4) vascularization ( $r_{v(114)}, n_{v(114)}$ ). Furthermore, (5) number of muscles ( $r_{v(115)}, n_{v(115)}$ ) and (6) shape ( $r_{v(116)}, n_{v(116)}$ ) could be added for more detailed analyses. In addition, further detailed parameters (subscript ( $h$ )) could be added.

The relative frequency (RF =  $P_{ijk}$ ) of normal structures in each parameter against the total number of structures is defined as follows:

$$\text{RF} = P_{ijk} = \frac{r_{v(ijk)}}{N}. \quad (2)$$

When structures are pair,  $N$  will be the number of individuals multiplied by 2. It is also possible to calculate  $P_{ijk}$  in separate pieces of bodies, as well. Although any values can be used as  $N$ , smaller number of  $N$  will result in lower statistical power. Normal structure in each parameter means  $0.5 < P_{ijk} \leq 1$  in practical terms. However, in mathematical ones with normality concept,  $P_{ijk}$  can vary as follows:  $0 \leq P_{ijk} \leq 1$ .

In the same species,  $P_{ijk}$  is usually greater than 0.5. However, in comparison among different species, normality is different among the species; for instance, in the comparison of the dorsoepitrochlearis muscle among primates and modern humans, this muscle is rarely observed in humans and approximate  $P_{ijk}$  is 0.05 [14], while, in nonhuman primates, the dorsoepitrochlearis muscle is a normal feature, and the  $P_{ijk}$  is 1.00.

On the other hand, the palmaris longus could be defect in humans [15] and its prevalence is around 90% [16]; therefore,  $N$  might be 90% of total individuals. Thus, to calculate innervation, vascularization, origin, or insertion of the palmaris longus, only 90% receives attention and data from the remaining 10% are discarded. Such case is common in comparative studies, where, usually, only data in specific species are studied. Furthermore, some muscles have more than one origin or insertion, as in the triceps brachii with 3 heads, and ultimately this muscle has 4 heads of origin in

modern humans [13, 15, 16]. In this case, just 2 types of the origin are observed: type 1 with 3 heads that is the normal feature and type 2 with 4 heads that is a variation.

For a more detailed analysis, it is required to calculate  $P_{ijk}$  by including such parameters in muscle, nerves, bones, arteries, and so forth. For instance, in muscle studies, the parameters have to be chosen according to the goal of researches; parameters for muscle studies should include, at least, (1) innervation ( $P_{ij1}$ ), (2) origin ( $P_{ij2}$ ), (3) insertion ( $P_{ij3}$ ), and (4) vascularization ( $P_{ij4}$ ). Furthermore, (5) number of muscles ( $P_{ijs}$ ) and (6) shape ( $P_{ij6}$ ) could be added for more detailed analyses. It is noted that small number of parameters means that the studied structure is less characterized. For instance, in case of contrahentes muscles, the number of the muscles must be analyzed because they show variation within the same species and in different species of primates as well [14].

The calculation of  $P_{ijk}$  is the first step in the SMCA analysis, and single  $P_{ijk}$  could be compared among different species. However, what we are seeking is comparison of multiple  $P_{ijk}$  among different species. The next step is to specify pondered values for coefficients (i.e., weighted coefficients) ( $w_k$ ) that are multiplied by  $P_{ijk}$ . The coefficients must be determined based on anatomical perspective; a parameter for a specific feature with small  $P_{ijk}$  is not important when we assess similarity of a given structure. That is, since the small  $P_{ijk}$  is ascribed to greater number of variations, small  $P_{ijk}$  must accompany small weighted coefficient, while large  $P_{ijk}$  (i.e., small number of variations) must accompany greater weighted coefficients.

We gave the weighted coefficient 3 to innervation ( $k = 1, w_1 = 3$ ) in case of muscles. When the muscles are formed during the development of animals, a specific nerve terminates on a specific muscle [17]. Thus, variation in nerve innervation of muscles is small, and a variation of innervation is highly sensitive to differences among different individuals within the same species as well as among different species. Among the 4 parameters noted above (innervation ( $k = 1$ ), origin ( $k = 2$ ), insertion ( $k = 3$ ), and vascularization ( $k = 4$ )), origin and insertion usually show similar variations. Thus, the both weighted coefficients should receive the same weight coefficient 2 ( $w_2 = 2$  for origin and  $w_3 = 2$  for insertion). Finally, the parameter with greater variation, vascularization ( $k = 4$ ), received the weighted coefficient 1 ( $w_4 = 1$ ). Indeed, vascularization can be different between the same muscles in bilateral sides within the same individuals [18].

Zero cannot be accepted as weighted coefficient ( $w_k$ ). Therefore,  $w_k$  must be greater than zero; that is,  $w_k > 0$ . To make the calculation easier and to keep clear parameters, the best choice is to use only integer values; that is,  $w_k \geq 1$ . Based on the above inference, an important rule here is clear; when the weighted coefficients are defined, the values should depend on different degree of variation (highest value to the weighted coefficient for the parameter with the lowest degree of variation or the same value to weighted coefficients for the parameters with same degree of variation). The values also should be discrete since it is difficult to find proportional values that represent exact difference among nominal variables. Thus, the best way is to choose integer values according to variations of studied features.

After designation of pondered values for weighted coefficients and calculation of  $P_{ijk}$ , the next step for SMCA is to calculate the Pondered Average of Frequencies (PAF =  $P_{w(ij)}$ ), according to the following formula:

$$PAF = P_{w(ij)} = \frac{\sum_{k=1}^q w_k \cdot P_{ijk}}{\sum_{k=1}^q w_k}; \tag{3}$$

for any species ( $i = 1, 2, \dots, s$ ),

any muscles ( $j = 1, 2, \dots, m$ ),

where  $P_{ijk}$  is the relative frequency and  $w_k$  is the weighted coefficient attached to a given parameter. For example, in muscle 1 of species 1,  $P_{111}$  is relative frequency of innervation, and weighted coefficient  $w_1$  is 3;  $P_{112}$  is relative frequency of the muscle origin, and  $w_2$  is 2;  $P_{113}$  is relative frequency of muscle insertion, and  $w_3$  is 2; and  $P_{114}$  is relative frequency of vascularization, and  $w_4$  is 1 [5].

In practical terms,  $P_{w(ij)}$  must be greater than 0.5 and less than or equal to 1; that is,  $0.5 < P_{w(ij)} \leq 1$ . In fact,  $P_{w(ij)}$  could be 1 if every  $P_{w(ij)}$  has maximal value 1, and if every  $P_{w(ij)}$  is minimum ( $P_{w(ij)} > 0.5$ ), the  $P_{w(ij)}$  will be 0.5, as well. In mathematical terms, again, regardless of concept of normality,  $P_{w(ij)}$  can vary within the range of  $0 \leq P_{w(ij)} \leq 1$ , since  $P_{w(ij)}$  could be zero or less than 0.5 in case of the analyses among different species. The value of  $P_{w(ij)}$  can be used to assess quantitative difference among studied structures in that equal values indicate high similarity and large difference in the values between two species indicates dissimilarities or less similarity.

**3.2. Methods to Compare Different Structures of the Same Species and among Different Species.** To compare structures among different species or different structures in the same species,  $P_{w(ij)}$  has to be calculated in each structure in each species and the  $P_{ijk}$  must be estimated in comparison with the data of reference species (*control species*). For instance, the corachobranchialis muscle has one or two heads of origin depending on species of primates [17]. In case of this muscle,  $P_{ijk}$  (relative number of heads) could be different according to the number of heads in the *control species*. Thus, before calculating  $P_{w(ij)}$ , it is important to make sure that the  $P_{ijk}$  must be consistently calculated in comparison with *control species* (see below).

For example, the maximum number of types of origin is 2 in the corachobranchialis ( $j = 1$ ); type 1 has one origin and type 2 has two origins ( $k = 2$ ).  $P_{ijk}$  could take different values according to the number of heads in the reference species (*control species*) ( $i = 1$ ). For example, for noncontrol species to be studied ( $i = 2$ ), the  $P_{212}$  of type 1 (number of origin is 1) will be 1 in reference to the species with 1 head, and  $P_{212}$  of type 1 will be 0.5 in reference to the species with 2 heads. In case of the muscle that has 1 to 3 heads of origins across different species, the  $P_{ijk}$  value should be divided by maximum number (i.e., 3) of heads ( $1/3 = 0.333$ ), since  $P_{ijk}$  should not be greater than 1. Thus, when *control species* with 3 heads of origin is reference,  $P_{212}$  in species with 3 heads ( $i = 2$ )

is 1.000,  $P_{312}$  in species with 2 heads ( $i = 3$ ) is 0.667 (2/3), and  $P_{412}$  in species with 1 head ( $i = 4$ ) will be 0.333 (1/3).

It is also important that the values of  $P_{ijk}$  should be obtained firstly in the *control species*. If the *control species* ( $i = 1$ ) have normally two heads of origin ( $k = 2$ ) in the corachobranchialis ( $j = 1$ ) and if 100% of individuals in this species have two heads of origin,  $P_{112}$  in this species will be 1. In the case wherein 90% of individuals in this species have two heads,  $P_{112}$  will be 0.9. In other noncontrol species ( $i = 2$ ) in which the normal is one head of origin of the corachobranchialis, if 100% of individuals of the studied sample have one head, the  $P_{212}$  will be 0.5, and if 90% of the samples have one head,  $P_{212}$  will be 0.45. These values are used to estimate  $P_{w(ij)}$ , which will be applied to the CAI analyses (see below).

Although any species can be used as *control species*, the species studied in the first time or the species with much known data should be chosen as *control species*. To compare any single structure (e.g., muscle) between two different species ( $i \neq i'$ ), the data in any noncontrol species can be compared one by one with those in the *control species* using the Comparative Anatomy Index (CAI) defined by the following formula:

$$CAI_{ii'} = |P_{w(ij)} - P_{w(i'j)}|, \quad \text{where } i \neq i'. \quad (4)$$

The  $CAI_{ii'}$  represents an absolute difference of weighted averages ( $P_{w(ij)}$ ) of a single structure between the *control* ( $i$ ) and other noncontrol ( $i'$ ) species. To compare one structure ( $j = 1$ ) with one parameter ( $k = 1$ ) between the control ( $i = 1$ ) and noncontrol ( $i' = 2$ ) species, the formula can be modified as follows:

$$CAI_{12} = |P_{w(11)} - P_{w(21)}|, \quad \text{where } i = 1, i' = 2. \quad (5)$$

It is noted that the  $CAI_{ii'}$  ranges from 0 to 1; that is,  $0 \leq CAI_{ii'} \leq 1$ . This is because the maximum value of  $P_{w(ij)}$  is 1 and the minimum is 0. Note that this equation permits only comparison of just one structure between the 2 species. However, the SMCA analysis of the muscles in the forearm [5] reported necessity to compare multiple muscles among different species, for example, to compare groups of the deep flexor muscles in the forearm among different species, because these muscles work together for a common function. Comparisons of them as a group would indicate similarities in relation to functions, phylogeny, and taxonomy. Thus, the authors [5] suggested the GCAI to compare a group of the muscles among species, one by one based on the sum of the  $P_{w(ij)}$ , as follows:

$$P_{w(i)} = \frac{\sum_{j=1}^{mj} P_{w(ij)}}{m_j}; \quad (6)$$

for any species ( $i = 1, 2, \dots, s$ ),

studied structures ( $j = 1, 2, \dots, m$ ),

and  $m_j$  is the number of studied structures (e.g., muscles); indeed,  $m_j = m$  because the same number of structures is mostly studied in each species.

The GCAI, which represents difference in  $P_{w(i)}$  based on multiple muscle structures between the *control* ( $i$ ) and other noncontrol ( $i'$ ) species, is defined by the following formula:

$$GCAI_{ii'} = |P_{w(i)} - P_{w(i')}|, \quad (7)$$

or

$$GCAI_{ii'} = \left| \frac{\sum_{j=1}^{mj} P_{w(ij)}}{m_j} - \frac{\sum_{j=1}^{mj} P_{w(i'j)}}{m_j} \right|. \quad (8)$$

Based on the above inferences, using SMCA, the values close to 0.000 suggest high similarity of the structures between the species, and the value 1.000 indicates that those are completely different structures. Thus, the GCAI is the absolute difference in mean weighted averages of  $P_{w(ij)}$  for multiple muscles between the two species and is defined in Table 1.

## 4. Results

**4.1. Examples of Application and Calculation of the SMCA.** We reanalyzed the previous data of the anatomical structures in comparative anatomy by application of the SMCA. The statistic for comparative anatomy was applied to the muscle extensor pollicis brevis in the forearm to compare the muscles among primates (*Cebus* (Ce) (now *Sapajus*), baboons (Ba), chimpanzees (Ch), and modern humans (Hu)), and Ce was used as the *control species* [5]. According to the data by Aversi-Ferreira et al. [5], the characteristics of this muscle are shown in Table 2.

Firstly, the *control species* was *Cebus* (Ce), and the  $P_{ijk}$  was calculated for the muscle extensor pollicis brevis using parameters of innervation, origin, insertion, and vascularization. Eight samples of Ce were used; therefore, 16 muscles were analyzed. All specimens contained the muscle extensor pollicis brevis, and all studied muscles showed same innervation ( $P_{111}$ ) and vascularization ( $P_{114}$ ), identical origin ( $P_{112}$ ), and insertion ( $P_{113}$ ).

For the innervation of the muscle in Ce, relative frequency  $P_{111}$  is as follows:

$$RF = P_{111} = \frac{r_{v(111)}}{N} = \frac{16}{16} = 1. \quad (9)$$

The same analysis must be done for each parameter in each muscle of different species. It is noted that the parameters in primates other than Ce were obtained from previous literatures [15, 17, 18]. The insertion in Hu ( $i = 2$ ) does not match with that in Ce (Table 2). Then, the  $P_{213}$  for the parameter insertion ( $k = 3$ ) is zero. In Ba ( $i = 4$ ), every  $P_{41k}$  will be zero, because this muscle is absent in this species.

The next step is to calculate the  $P_{w(ij)}$  in each species. The  $P_{w(11)}$  of Ce is as follows:

$$P_{w(11)} = \frac{\sum_{k=1}^q w_k \cdot P_{ijk}}{\sum_{k=1}^q w_k} \quad (10)$$

$$= \frac{(1 \cdot 3) + (1 \cdot 2) + (1 \cdot 2) + (1 \cdot 1)}{8} = 1.000.$$

TABLE 1: Illustration of individual steps to compute GCAI based on multiple muscles.

Species $(i = 1, 2, \dots, s)$ $P_{ijk}$	Species 1 (control species) $(i = 1)$		Species 2 $(i = 2)$		Species $s (i = s)$	
	$M_1$	$M_2$	$M_1$	$M_2$	$M_1$	$M_2$
Investigated structures $(j = 1, 2, \dots, m)$	$M_1$	$M_2$	$M_1$	$M_2$	$M_1$	$M_2$
Innervation $(k = 1)$	$P_{111}$	$P_{121}$	$P_{211}$	$P_{221}$	$P_{s11}$	$P_{s21}$
Origin $(k = 2)$	$P_{112}$	$P_{122}$	$P_{212}$	$P_{222}$	$P_{s12}$	$P_{s22}$
Insertion $(k = 3)$	$P_{113}$	$P_{123}$	$P_{213}$	$P_{223}$	$P_{s13}$	$P_{s23}$
Vascularization $(k = 4)$	$P_{114}$	$P_{124}$	$P_{214}$	$P_{224}$	$P_{s14}$	$P_{s24}$
Weighted averages for single muscle (PAF = $P_{w(ij)}$ )	$P_{w(11)}$	$P_{w(12)}$	$P_{w(21)}$	$P_{w(22)}$	$P_{w(s1)}$	$P_{w(s2)}$
Weighted averages for multiple muscles (mean of $P_{w(ij)}$ ) $(P_{w(i)})$	$P_{w(1)}$		$P_{w(2)}$		$P_{w(s)}$	
GCAI = $\frac{P_{w(i)} - P_{w(i')}}{ P_{w(1)} - P_{w(2)} }$			$\frac{P_{w(2)} - P_{w(1)}}{ P_{w(1)} - P_{w(2)} }$			$\frac{P_{w(s)} - P_{w(1)}}{ P_{w(1)} - P_{w(s)} }$

Note.  $P_{ijk}$ : proportion of normal structured organs, where  $i$  represents individual species,  $j$  represents individual structures (i.e., muscles), and  $k$  represent individual parameters of the muscles.

TABLE 2: General features of the extensor pollicis brevis muscle based on Aversi-Ferreira et al. [5]. In primates other than Ce, only the differences in muscle parameters from Ce are indicated.

Muscle	Parameters	Ce ( $i = 1$ )	Hu ( $i = 2$ )	Ch ( $i = 3$ )	Ba ( $i = 4$ )
Extensor pollicis brevis	Origin ( $k = 2$ )	Proximal third of the radius and interosseous membrane			
	Insertion ( $k = 3$ )	Articular capsule of the trapezoid-metacarpal I articulation and the base of this last bone	Single insertion in distal phalange of the thumb	Highly similar to Ce	Absent
	Innervation ( $k = 1$ )	Posterior interosseous nerve			
	Vascularization ( $k = 4$ )	Posterior interosseous artery			

TABLE 3: CAIs for the individual flexor deep muscles in the forearm to indicate degree of difference from the control species (Ce).

	Pronator quadratus	Flexor digitorum profundus	Flexor pollicis longus
<i>Cebus</i> (Ce)	Reference	Reference	Reference
Modern human (Hu)	CAI = 0.375	CAI = 0.000	CAI = 0.125
Chimpanzee (Ch)	CAI = 0.000	CAI = 0.063	CAI = 0.000
Baboon (Ba)	CAI = 0.000	CAI = 1.000	CAI = 0.250

In Hu, the  $P_{w(213)}$  is zero, and then the  $P_{w(21)}$  is as follows:

$$P_{w(21)} = \frac{\sum_{k=1}^q \omega_k \cdot P_{ijk}}{\sum_{k=1}^q \omega_k} \quad (11)$$

$$= \frac{(1 \cdot 3) + (1 \cdot 2) + (0 \cdot 2) + (1 \cdot 1)}{8} = \frac{6}{8} = 0.750.$$

The  $P_{w(31)}$  for Ch ( $i = 3$ ) is equal to  $P_{w(11)}$ . In Ba ( $i = 4$ ), since the extensor pollicis brevis is absent,  $P_{w(41)}$  is zero. The conclusion is  $P_{w(11)} = P_{w(31)} = 1.000$ ,  $P_{w(21)} = 0.750$ , and  $P_{w(41)} = 0.000$ .

The next step is to calculate the CAI between the *control species* and others, one by one, as follows:

$$\begin{aligned} \text{CAI}_{12} &= |P_{w(11)} - P_{w(21)}| = |1.000 - 0.750| = 0.250; \\ \text{CAI}_{13} &= |P_{w(11)} - P_{w(31)}| = |1.000 - 1.000| = 0.000; \\ \text{CAI}_{14} &= |P_{w(11)} - P_{w(41)}| = |1.000 - 0.000| = 1.000. \end{aligned} \quad (12)$$

The results by the CAI calculation represent degree of difference in the extensor pollicis brevis among the species. The CAI values suggest that Ce and Ch have identical extensor pollicis brevis (high similarity), while Ce and Hu show some differences (somewhat similar), and Ce and Ba are highly different. It is because the extensor pollicis brevis does not exist in Ba or that muscle have no match between Ce and Hu. These results provide quantitative measures with previous papers that described the differences in the extensor pollicis brevis among different species.

It is also important to verify usefulness of the GCAI. We reanalyzed the previous data [5] and applied CAI to individual deep flexor muscles in the forearm (Table 3) and GCAI to the group of the deep flexor muscles in the forearm (Table 4). Although CAIs indicate the difference in individual muscles, it is unknown how the deep flexor muscles in the forearm as a group are different between the species. The

GCAI values suggest that the flexor deep muscles in the forearm of the *Cebus* (Ce) are more similar to, in order, chimpanzee, modern humans, and baboon (Table 4).

**4.2. Comparison of the SMCA with Parametrical Method (*t*-Test).** A previous study analyzed the palmaris longus among 9 nonhuman primates and humans [6] by calculating ratios of muscle length to its tendon length, and these data were submitted to *t*-test. Additionally, the characteristics of these muscles were compared among the 9 species by the SMCA (Table 5) (data from *Aotus* and modern humans were not used; for detailed analysis, see [6]). Using CAI (SMCA), nominal variables of features in the palmaris longus including (1) origin, (2) insertion, (3) innervation, (4) muscle presence, and (5) type of belly arrangement were analyzed.

The results by parametric analysis of the ratios (muscle length/tendon length) are consistent with the primate grouping (distinction of apes, old world primate, new world primates, and prosimii); within the same group, the ratios were not significantly different (Table 5). These data are further consistent with those by CAI (SMCA) analysis of the palmaris longus (Table 5). These parametric data are at least partially consistent with those by the nonparametric (CAI) comparison (Table 6).

**4.3. Comparison of the SMCA with Other Nonparametric Methods.** Another possibility to study nominal variables is to use the cladistics method. This method considers the binary characters and any other possibility could be an error, because these features are mutually excluded [11]. Indeed this characteristic limits its application to morphological analyses of structures since it considers just two parameters: 0 for absent characteristic and 1 for its presence. Nevertheless, this method is important in evolutionary studies, since this method might provide a different concept; the cladistics analysis prioritizes the primitive and derivative features [12],

TABLE 4:  $P_{ijk}$ ,  $P_{w(ij)}$  and GCAIs for the flexor deep muscles in the forearm to indicate degree of differences in this muscular group among different species in relation to the control species (Ce).

Species ( $i = 1, 2, \dots, s$ )	Cebus (Ce), control species or reference ( $i = 1$ )			Modern humans (Hu) ( $i = 2$ )			Chimpanzee (Ch) ( $i = 3$ )			Baboon (Ba) ( $i = 4$ )		
Investigated structures (flexor deep muscles of forearm)	Pronator quadratus	Flexor digitorum profundus	Flexor pollicis longus	Pronator quadratus	Flexor digitorum profundus	Flexor pollicis longus	Pronator quadratus	Flexor digitorum profundus	Flexor pollicis longus	Pronator quadratus	Flexor digitorum profundus	Flexor pollicis longus
$P_{ijk}$												
Specific weights given with respect to variation												
Innervation ( $k = 1$ )	1	1	1	0	1	1	1	1	1	1	0	1
Origin ( $k = 2$ )	1	1	1	1	1	0.5	1	1	1	1	0	1
Insertion ( $k = 3$ )	1	1	1	1	1	1	1	0.5	1	1	0	0
Vascularization ( $k = 4$ )	1	1	1	1	1	1	1	1	1	1	0	1
Weighted averages for single muscle (PAF = $P_{w(ij)}$ )	1	1	1	0.625	0	0.875	0	0.9375	0	0	1	0.750
Weighted averages for multiple muscles (mean of $P_{w(ij)}$ ) ( $P_{w(i)}$ )	1	1	1	$\frac{0.625 + 1 + 0.875}{3} = 0.833$	$\frac{0.625 + 1 + 0.875}{3} = 0.833$	$\frac{0.625 + 1 + 0.875}{3} = 0.833$	$\frac{1 + 0.9375 + 1}{3} = 0.980$	$\frac{1 + 0.9375 + 1}{3} = 0.980$	$\frac{1 + 0.9375 + 1}{3} = 0.980$	$\frac{0 + 1 + 0.750}{3} = 0.583$	$\frac{0 + 1 + 0.750}{3} = 0.583$	$\frac{0 + 1 + 0.750}{3} = 0.583$
GCAI = $ P_{w(i)} - P_{w(i')} $	Reference	Reference	Reference	$\frac{ 1 + 1 + 1 - (0.625 + 1 + 0.875) }{3} = 0.167$	$\frac{ 1 + 1 + 1 - (0.625 + 1 + 0.875) }{3} = 0.167$	$\frac{ 1 + 1 + 1 - (0.625 + 1 + 0.875) }{3} = 0.167$	$\frac{ (1 + 1 + 1) - (1 + 0.9375 + 1) }{3} = 0.020$	$\frac{ (1 + 1 + 1) - (1 + 0.9375 + 1) }{3} = 0.020$	$\frac{ (1 + 1 + 1) - (1 + 0.9375 + 1) }{3} = 0.020$	$\frac{ (1 + 1 + 1) - (0 + 1 + 0.750) }{3} = 0.417$	$\frac{ (1 + 1 + 1) - (0 + 1 + 0.750) }{3} = 0.417$	$\frac{ (1 + 1 + 1) - (0 + 1 + 0.750) }{3} = 0.417$

Note.  $P_{ijk}$ : proportion of normal structured organs, where  $i$  represents individual species,  $j$  represents individual structures (i.e., muscles), and  $k$  represent individual parameters of the muscles.

TABLE 5: Analyses of the anatomical data by parametrical *t*-test and nonparametrical SMCA (CAI) [6].

Specimens	Average ratios of length of palmaris longus to tendon length	Primate grouping	CAI (nonparametric analysis)
<i>Gorilla</i>	No data in the literature		0.133
<i>Pan</i>	1.78 ( $\pm 0.04$ )	Apes	0.082
<i>Pongo</i>	1.89 ( $\pm 0.15$ )		0.036
<i>Macaca fuscata</i>	2.37 ( $\pm 0.12$ )	Old world primate	0.036
<i>Callithrix</i> sp.	2.53 ( $\pm 0.08$ )		0
<i>Ateles</i> sp.	2.53	New world primates	0
<i>Sapajus libidinosus</i>	3.81 ( $\pm 1.07$ )		0
<i>Lemur catta</i>	4.53 ( $\pm 0.27$ )	Prosimii	0
<i>Propithecus</i> sp.	5.16 ( $\pm 0.49$ )		Reference as more primitive specimen

TABLE 6: Partial agreement between parametric and nonparametric analyses of the palmaris longus of nonhuman primates. The range of values indicates numerical definition of the groups of the primates based on the parametric and nonparametric analyses in Table 5.

Groups of the primates	Definition of groups based on parametric analysis of the ratios (muscle length/tendon length) (range of ratio)	Definition of groups based on nonparametric analysis of the features of the features (range of CAI)
Apes	1.0–2.0	0.100–0.036
Old world primates	2.0–2.5	0.036–0.000
New world primates	2.5–4.0	0.000
Prosimii	4.0–6.0	

while the morphological analysis prioritizes utmost characters observed in a structure.

To compare cladistics and SMCA methods, cladistics and CAI were applied to the same data in Table 2; the results are shown in Table 7.

CAI in Table 7 indicated that the pronator quadratus is similar among Ce, Ch, and Ba and different between Ce and Hu. The cladistics analysis also indicated the same results. For the flexor digitorum profundus, CAI indicated that this muscle is similar between Hu and Ce, somewhat similar between Ch and Ce, and completely different between Ba and Ce. The cladistics analysis also indicated the same characteristics; Hu, Ch, and Ce shared the same features of this muscle but were totally different from Ba. For the flexor pollicis longus, CAI indicated this muscle is identical in Ce and Ch, somewhat similar between Hu and Ce, and highly different between Ba and Ce. The cladistics analysis indicated that this muscle was similar between Ce and Ch and different between Hu and Ce and between Ba and Ce. Thus, the results by both methods are consistent. Nevertheless, CAI provides quantitative data to assess the features. Furthermore, GCAI provides further information demonstrating that the group of these muscles of Ce was more similar to Ch, Hu, and Ba in this order (Table 7).

### 5. Discussion

Firstly, an accurate analysis is fundamental in comparative anatomy. Photographs of structures can be used to verify the new data mainly when the new data disagree with others. However, numerical methods can help to avoid subjectivities and mistakes and make it easier to assess group similarities and to observe differences among structures and specimens. The application of numerical methods to comparison of biological structures could avoid prolix texts and ensure more exact and precise conclusions on similarities or differences among biological structures. This is especially true for gross anatomy where the nominal variables are studied and described.

Nonparametric statistics are less exact than parametric ones [19]. Numerical parametric analyses can be performed with observation of frequency of characteristics based on fundamental concepts of normality and variation in anatomy. However, the nonparametric methods take advantage when parametric methods cannot be used in situations where nominal variables are included in the analysis and the measured data do not match nonparametric one. That is, parametric statistics are preferable when continuous variables are available [19], while nonparametric methods could be applied to nominal variables. As shown in Table 5, both methods match partially when the same samples were analyzed by both methods [20].

The analyses by nonparametric methods (chi-square and cladistics) indicate that cladistics might be more applicable to anatomical analysis. However, this method cannot analyze frequency of features. Furthermore, chi-square method also has a problem in its basic premises; causality of data used in this method disagrees with evolution theory assuming a common ancestral [9], and it is not easy to obtain numerical nominal data from expected and observed data. Although the results by cladistics and CAI are consistent (Table 7), it is noted that CAI provides quantitative data to assess features. Furthermore, GCAI provides additional information of a group of multiple structures.

The objective of cladistics method is different from that of SMCA; cladistics method offers solution when data from large groups are analyzed in evolution analysis, while the

TABLE 7: Partial agreement between the two nonparametric analyses (CAI and cladistics) of the palmaris longus in human and nonhuman primates.

	Ce	Hu	Ch	Ba
Nonparametric analysis by CAI				
Pronator quadratus	<i>Control species</i>	CAI = 0.375	CAI = 0.000	CAI = 0.000
Flexor digitorum profundus	<i>Control species</i>	CAI = 0.000	CAI = 0.063	CAI = 1.000
Flexor pollicis longus	<i>Control species</i>	CAI = 0.125	CAI = 0.000	CAI = 0.250
GCAI	<i>Control species</i>	0.167	0.020	0.417
Cladistics features of the palmaris longus in features innervation (A), origin (B), insertion (C), and vascularization (D) (0 and 1 indicate absence and presence of primitive features, resp.)				
	(ABCD)	(ABCD)	(ABCD)	(ABCD)
Pronator quadratus	(1111)	(0111)	(1111)	(1111)
Flexor digitorum profundus	(0000)	(0000)	(0000)	(1111)
Flexor pollicis longus	(1101)	(1001)	(1101)	(1111)

goal of SMCA is to obtain utmost details from anatomical structures when multiple features are analyzed. The cladistics is used in evolution analysis, especially, to obtain genealogic tree. However, it can be applied to comparative anatomy, because observation of presence and absence of a specific feature provides a general idea of similarity or difference among the structures.

In conclusion, the SMCA can offer more exact and precise method to compare structures to assess same or different groups, which requires analyses of nominal features in comparative anatomy.

## Conflict of Interests

The authors declare that there is no conflict of interests regarding the publication of this paper.

## Acknowledgments

The authors thank the anonymous reviewers for their wise, detailed, and very helpful comments on previous version of this paper. R. A. G. M. F. Aversi-Ferreira was recipient of a doctoral fellowship from CAPES/Brazil and T. A. Aversi-Ferreira is recipient of Scholarship Research Productivity from National Council of Technology and Development (CNPq/Brazil). This work was supported partly by the Japan Society for the Promotion of Science Asian Core Program and the Ministry of Education, Science, Sports and Culture, Grant-in-Aid for Scientific Research (B) (25290005). The authors declare no competing financial interests.

## References

- [1] G. D. A. Pfrimer, T. de Abreu, V. S. Vieira et al., "Historic and teaching aspects of anatomy and cebus genus role in contemporary anatomy," *International Journal of Morphology*, vol. 30, no. 2, pp. 607–612, 2012.
- [2] T. A. Aversi-Ferreira, "A new statistical method for comparative anatomy," *International Journal of Morphology*, vol. 27, no. 4, pp. 1051–1058, 2009.
- [3] R. A. G. M. F. Aversi-Ferreira, T. de Abreu, G. A. Pfrimer et al., "Comparative anatomy of the hind limb vessels of the bearded capuchins (*Sapajus libidinosus*) with apes, baboons, and *Cebus capucinus*: with comments on the vessels' role in bipedalism," *BioMed Research International*, vol. 2013, Article ID 737358, 15 pages, 2013.
- [4] W. Thomson, "Electrical units of measurement," in *The Practical Applications of Electricity*, The Institution of Civil Engineers, London, UK, 1884.
- [5] T. A. Aversi-Ferreira, R. S. Maior, F. O. Carneiro-e-Silva et al., "Comparative anatomical analyses of the forearm muscles of *Cebus libidinosus* (Rylands et al. 2000): manipulatory behavior and tool use," *PLoS ONE*, vol. 6, no. 7, Article ID e22165, 8 pages, 2011.
- [6] R. A. G. M. F. Aversi-Ferreira, R. V. Bretas, R. S. Maior et al., "Morphometric and statistical analysis of the palmaris longus muscle in human and non-human primates," *BioMed Research International*, vol. 2014, Article ID 178906, 6 pages, 2014.
- [7] R. A. C. Barros, I. L. S. Prada, Z. Silva, A. R. Ribeiro, and D. C. O. Silva, "Constituição do plexo lombar do macaco *Cebus apella*," *Brazilian Journal of Veterinary Research and Animal Science*, vol. 40, no. 5, pp. 373–381, 2003.
- [8] A. R. Ribeiro, I. L. S. Prada, Z. Silva, R. A. C. Barros, and D. C. O. Silva, "Origem do plexo braquial do macaco *Cebus apella*," *Brazilian Journal of Veterinary Research and Animal Science*, vol. 42, no. 2, pp. 143–149, 2005.
- [9] C. Darwin, "Afinidades mútuas dos seres vivos; morfologia; embriologia; órgãos rudimentares," in *The Origin of Species*, John Murray, London, UK, 6th edition, 1876.
- [10] Y. Takane and L. Zhou, "Anatomy of Pearson's Chi-square statistic in three-way contingency tables," in *New Developments in Quantitative Psychology*, vol. 66 of *Springer Proceedings in Mathematics & Statistics*, pp. 41–57, Springer, New York, NY, USA, 2013.
- [11] R. A. Pimentel and R. Riggins, "The nature of cladistic data," *Cladistics*, vol. 3, no. 3, pp. 201–209, 1987.
- [12] J. A. Hawkins, C. E. Hughes, and R. W. Scotland, "Scotland primary homology assessment, characters and character states," *Cladistics*, vol. 13, no. 3, pp. 275–283, 1997.
- [13] K. L. Moore, A. F. Dalley II, and A. M. R. Agur, "Introduction to clinically oriented anatomy," in *Clinically Oriented Anatomy*, Wolters Kluwer Health, Lippincott Williams & Wilkins, Philadelphia, Pa, USA, 7th edition, 2014.

- [14] S. Gibbs, *Comparative soft tissue morphology of the extant Hominoidea, including man [Ph.D. thesis]*, The University of Liverpool, Liverpool, UK, 1999.
- [15] S. Standring, "Pelvis girdle and lower limb," in *Gray's Anatomy: The Anatomical Basis of Clinical Practice*, Churchill Livingstone, London, UK, 2008.
- [16] H. Gray, "Miology," in *Anatomy of the Human Body*, Lea & Febiger, Philadelphia, Pa, USA, 1918.
- [17] K. L. Moore, T. V. N. Persaud, and M. G. Torchia, *Muscular System in the Developing Human: Clinically Oriented Embryology*, Saunders, Philadelphia, Pa, USA, 9th edition, 2013.
- [18] D. R. Swindler and C. D. Wood, *In an Atlas of Primates Gross Anatomy: Baboon, Chimpanzee and Man*, University of Washington Press, Seattle, Wash, USA, 1973.
- [19] C. R. Kitchen, "Nonparametric versus parametric tests of location in biomedical research," *American Journal of Ophthalmology*, vol. 147, no. 4, pp. 571–572, 2009.
- [20] D. J. Sheskin, *Handbook of Parametric and Nonparametric Statistical Procedures*, Chapman & Hall/CRC, Boca Raton, Fla, USA, 3rd edition, 2004.

## Research Article

# Association of Aortic Diameters with Coronary Artery Disease Severity and Albumin Excretion

Bülent Özdemir,<sup>1</sup> Ali Emül,<sup>2</sup> Levent Özdemir,<sup>3</sup> Saim Sağ,<sup>1</sup> Murat Biçer,<sup>4</sup> and Ali Aydınlar<sup>1</sup>

<sup>1</sup>Department of Cardiology, Uludağ University, Bursa, Turkey

<sup>2</sup>Şevket Yılmaz Government Research and Training Hospital, Bursa, Turkey

<sup>3</sup>Department of Public Health, Cumhuriyet University, Sivas, Turkey

<sup>4</sup>Tıp Fakültesi Kalp, Damar Cerrahisi Anabilim Dalı, Uludağ Üniversitesi, Görükle Kampüsü, Nilüfer, 16059 Bursa, Turkey

Correspondence should be addressed to Murat Biçer; mbicer23@yahoo.com

Received 17 February 2015; Revised 7 April 2015; Accepted 8 April 2015

Academic Editor: Juan A. Sanchis-Gimeno

Copyright © 2015 Bülent Özdemir et al. This is an open access article distributed under the Creative Commons Attribution License, which permits unrestricted use, distribution, and reproduction in any medium, provided the original work is properly cited.

**Introduction.** Aortic diameters, aortic distensibility, microalbuminuria, coronary artery disease which are all together related to vascular aging are investigated in this paper. **Methods.** Eighty consecutive nondiabetic patients undergoing elective coronary angiography were enrolled into the study. Systolic and diastolic aortic diameters, aortic distensibility, CAD severity by angiogram with the use of Gensini scoring, and albumin excretion rates were determined. **Results.** Cases with CAD had significantly larger systolic ( $30,72 \pm 3,21$  mm versus  $34,19 \pm 4,03$  mm for cases without and with CAD, resp.) and diastolic aortic diameters measured 3 cm above aortic valve compared to patients without CAD ( $33,56 \pm 4,07$  mm versus  $29,75 \pm 3,12$  mm). The systolic and diastolic diameters were significantly higher in albuminuria positive patients compared to albuminuria negative patients ( $p = 0.017$  and  $0.008$ , resp., for systolic and diastolic diameters). **Conclusion.** In conclusion aortic diameters are increased in patients with coronary artery disease and in patients with microalbuminuria. In CAD patients, systolic blood pressure, pulse pressure, aortic systolic and diastolic pressure, and albumin excretion rate were higher and aortic distensibility was lower.

## 1. Introduction

Aortic diameters are related to coronary artery disease. In a recent study, ascending aorta, aortic arch, distal thoracic aorta, and abdominal aorta diameters measured during autopsies of subjects that died of cardiovascular disease were significantly bigger than those of the subjects who died from other causes [1]. Aortic distensibility is a characteristic of the vessel wall and is related somewhat to contraction and dilation of the aorta. The definition can be equated as maximum change in area/(minimum area  $\times$  pulse pressure). It can be measured anywhere through the course of the aorta. Many studies reported these changes during the cardiac cycle in both the ascending aorta and the descending aorta [2].

Coronary artery disease severity and extent determined by modified Gensini score were predicted by distal descending atheroma burden, ascending aorta distensibility, carotid flow mediated dilatation, and atheroma class in a magnetic resonance imaging study [3].

Association of aortic stiffness and microalbuminuria has been the focus of many studies [4–7]. In patients with hypertension, microalbuminuria and mildly reduced creatinine clearance were independently related to aortic stiffness which was calculated with carotid and femoral pulse [8]. Aortic distensibility is related to coronary flow reserve and coronary flow restoration with percutaneous coronary interventions improves aortic distensibility and coronary flow velocity reserve [9, 10].

The rate of having coronary heart disease among renal failure patients is quite high [11]. The same risk factors may affect both renal and cardiac functions and vasculature. End stage renal disease patients' coronary artery disease risk is 10 times higher compared to high-risk patients of Framingham's study [12]. Microalbuminuria was used as a marker for diabetic nephropathy and lately for cardiovascular morbidity and mortality [13, 14]. Also the association of the severity of coronary artery disease with microalbuminuria presence

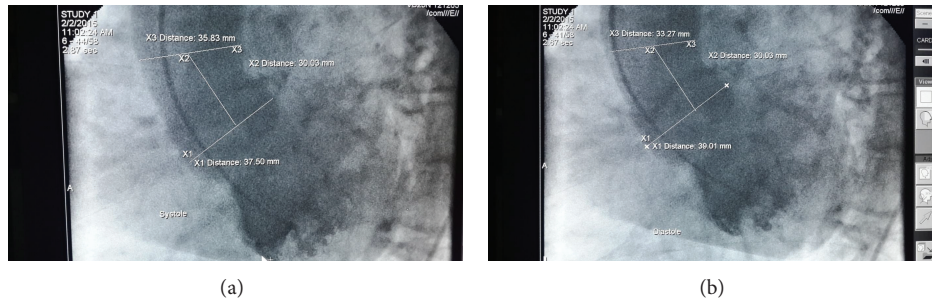


FIGURE 1: Aortic diameters are measured 3 cm above the aortic orifice. The illustrations cover systole (a) and diastole (b).

was reported in another study by Khan et al. [15]. In a study that utilised coronary computed tomography angiography, association of presence, extent, and severity of coronary artery disease in asymptomatic patients with type 2 DM with microalbuminuria was investigated. In that study patients with microalbuminuria had more severe coronary lesions. Microalbuminuria clearly predicted high coronary artery disease risk and worse clinical outcomes [16].

## 2. Materials and Methods

Eighty consecutive patients undergoing elective coronary angiography in the Cardiology Department of the Applied Research Centre for Health of Uludağ University were enrolled into the study. The angiograms were performed with use of Siemens cardiac catheterization unit in the Hemodynamics Laboratory of the Cardiology Department. This was a prospective study in which the aortic diameters and aortic elasticity were determined along with the Gensini score that allowed assessing the severity of CAD [17]. A Gensini score greater than 20 was defined as a high Gensini score.

Systolic and diastolic diameters were measured 3 cm above the aortic valve (in cm) (Figures 1(a) and 1(b)). Aortic distensibility was calculated as follows:  $2 \times (\text{change in aortic diameter}) / (\text{diastolic aortic diameter}) \times (\text{change in aortic pressure})$ , where change in aortic diameter equals systolic minus diastolic aortic diameter, and change in aortic pressure equals systolic minus diastolic aortic pressure [18, 19]. Aortic pulse pressure was calculated as systolic aortic pressure minus diastolic aortic pressure. Hypertension was defined as having blood pressure greater than or equal to 140/90 mmHg or being on treatment.

The coronary angiograms were evaluated. Chi-Square Test was used for classified variables and Mann-Whitney *U* test was used for comparison of two groups. The statistical analyses were performed by use of SPSS data Manager Software system. Statistical significance was assumed in case of a *p* value <0.05. The results are expressed as mean  $\pm$  standard deviation.

The patients were evaluated by dividing into two groups according to having CAD and also having albuminuria. The comparisons were made by categorising the cases as having no CAD, mild CAD, and severe coronary artery diseases. Also

TABLE 1: Characteristics of the patients.

	Male	%	Female	%	Total
Gender	49	61,3	31	38,7	80
	Present	%	Absent	%	
Obesity	21	26,3	59	73,7	80
Smoking	38	47,5	42	52,5	80
Hypertension	48	60,0	32	40,0	80
Dyslipidemia	37	46,3	43	53,8	80
Age (years)	59,9 $\pm$ 10,0				
Height (cm)	165,8 $\pm$ 6,9				
Weight (kg)	75,9 $\pm$ 9,5				
BMI (kg/m <sup>2</sup> )	27,6 $\pm$ 3,9				
Serum levels of biochemical markers					
Total cholesterol (mg/dL)	183,4 $\pm$ 47,9				
LDL cholesterol (mg/dL)	113,5 $\pm$ 38,3				
HDL cholesterol (mg/dL)	44,0 $\pm$ 13,6				
Triglyceride (mg/dL)	140,7 $\pm$ 68,6				
Urea (mg/dL)	36,9 $\pm$ 12,8				
Creatinine (mg/dL)	0,98 $\pm$ 0,23				
Uric acid (mg/dL)	5,58 $\pm$ 1,82				
Haemoglobin (g/dL)	12,84 $\pm$ 1,96				
Aortic measurements					
Systolic blood pressure (mmHg)	124,7 $\pm$ 14,6				
Diastolic blood pressure (mmHg)	74,9 $\pm$ 8,9				
Pulse pressure (mmHg)	49,8 $\pm$ 10,8				
Mean aortic pressure (mmHg)	100,1 $\pm$ 14,0				
Aortic distensibility	2,88 $\pm$ 2,21				
Aortic systolic diameter (mm)	33,2 $\pm$ 4,11				
Aortic diastolic diameter (mm)	32,5 $\pm$ 4,1				

comparisons were made according to having no, moderate, and severe albumin excretion rates.

## 3. Results and Discussion

The characteristics of the patients are given in Table 1. When the cases were divided into two according to having CAD

TABLE 2: Aortic measurement and albuminuria levels according to CAD presence.

	Coronary artery disease negative ( <i>n</i> = 21)			Coronary artery disease positive ( <i>n</i> = 59)			<i>p</i> value
	Median	(min-max)	IQR	Median	(min-max)	IQR	
*Systolic blood pressure	117	95-135	19	127	97-184	19	0,003
*Diastolic blood pressure	75	64-94	11,50	74	57-98	12	0,45
*Pulse pressure	43	26-65	13	52	32-78	13	0,003
*Mean aortic pressure	100	70-120	12	100	73-133	17	0,12
Aortic distensibility	3,02	0,99-14,40	3,80	2,27	0,32-11,20	1,60	0,013
Aortic systolic diameter (mm)	30,61	25,81-38,10	5,41	33,52	27,32-48,16	6,30	<0,001
Aortic diastolic diameter (mm)	29,47	25,46-36,83	5,62	33,02	26,73-47,06	6,46	<0,001
Proteinuria level	12	4-256	125	170	5-1931	161	<0,001

\*mmHg; IQR: interquartile range.

TABLE 3: Comparison of the groups according to presence of albuminuria.

	Proteinuria negative ( <i>n</i> = 13)			Proteinuria positive ( <i>n</i> = 67)			<i>p</i> value
	Median	(min-max)	IQR	Median	(min-max)	IQR	
*Systolic blood pressure	117	103-136	20	126	95-184	16	0,11
*Diastolic blood pressure	77	64-94	10	74	57-98	10	0,13
*Pulse pressure	41	26-51	9	52	32-78	13	0,01
*Mean aortic pressure	100	73-120	13,5	100	70-133	17	0,24
Aortic distensibility	2,93	1,56-14,40	3,70	2,44	0,32-11,20	1,98	0,14
Aortic systolic diameter (mm)	30,61	26,55-38,31	5,60	33,11	25,81-48,16	6,30	0,01
Aortic diastolic diameter (mm)	29,18	26,10-37,71	5,84	32,78	25,46-47,06	6,62	0,008

\*mmHg; IQR: interquartile range.

or not having CAD, aortic dimensions both in systole and diastole were significantly different. When systolic aortic diameter was compared, cases with CAD had significantly larger systolic aortic diameter ( $30,72 \pm 3,21$  mm versus  $34,19 \pm 4,03$  mm for cases without and with CAD, resp.). Also the same was true for the aortic diastolic diameters measured 3 cm above aortic valve with significantly bigger aortic diameter for the CAD patients compared to patients without CAD ( $33,56 \pm 4,07$  mm versus  $29,75 \pm 3,12$  mm). The aortic distensibility showing the elastic properties of the aorta was significantly smaller in CAD patients ( $p = 0.013$ ) (Table 2). Also in CAD patients the systolic blood pressure was significantly higher compared to cases without CAD ( $127,4 \pm 14,7$  mmHg versus  $117,1 \pm 11,9$  mmHg;  $p = 0.03$ ). However the diastolic blood pressure failed to show a significant difference. Pulse pressure and proteinuria level also were significantly higher in CAD patients (Table 2).

In Table 3 the comparison of the albuminuria positive and albuminuria negative groups is given. Systolic pressure and diastolic pressure were indifferent in albuminuria positive and albuminuria negative patients. Pulse pressure was significantly higher in albuminuria positive patients. Albuminuria presence did not cause significant difference in aortic distensibility among groups. But both the systolic and diastolic diameters were significantly higher in albuminuria positive patients compared to albuminuria negative patients ( $p = 0.017$  and  $0.008$ , resp., for systolic and diastolic diameters).

Grouping the cases by <50 years of age and  $\geq 50$  years of age showed that rate of presence of hypertension was significantly higher in the cases belonging to the latter group (25% versus 66.2%, resp., with a  $p$  value <0.05). However, rate of presence of albuminuria was not significantly different between the groups of cases with <50 and  $\geq 50$  years of age. Also grouping of cases according to a cut-off of age of 50 years showed that rate of having CAD in the cases with age of 50 years or older was significantly higher compared to others. Also only 3,1% of cases with significant coronary artery disease according to Gensini scoring were younger than 50 years of age. A cut-off value of 50 mmHg for pulse pressure significantly showed that a higher level of albumin excretion was the case for cases which had a pulse pressure of 50 mmHg or higher compared to others ( $p < 0.05$ ).

When cases with CAD were compared to cases without CAD the mean albumin excretion rate was significantly lower ( $p < 0.05$ ). However, albumin excretion rate did not differ between cases with mild CAD and cases with severe CAD patients ( $p > 0.05$ ). When patients were grouped into having microalbuminuria or having CAD and compared accordingly, presence of albuminuria predicted presence of CAD (Figure 2).

Presence of CAD is significantly related to aortic diameters [1]. In the study by Milan et al. all the studied segments of aorta were significantly larger in the group with cardiovascular disease. A tendency to decrease in the size of aorta from ascending to abdominal aorta segments was

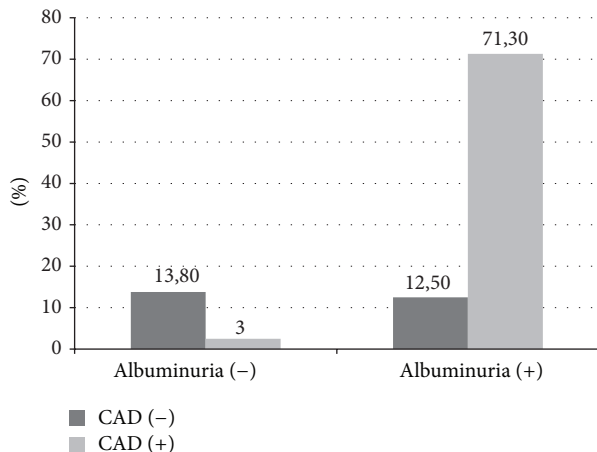


FIGURE 2: Percent distribution of all the cases ( $n = 80$ ) according to presence of CAD and albuminuria. Albuminuria presence was significantly associated with presence of coronary artery disease ( $p < 0,001$ ).

also noted in the study that involved autopsy subjects. These results were consistent with the results in this paper. In cases with hypertension dilatation of the ascending aorta is more common [20]. In a study by Giannattasio et al., arterial distensibility in patients with type I (insulin-dependent) diabetes mellitus without macrovascular complication was evaluated. In their study arterial distensibility was lower in a consistent manner compared to the control group. Noting increased radial and carotid artery thicknesses, they stated that the changes were more pronounced in patients with microalbuminuria, retinopathy, or neuropathy. Interestingly, the arterial wall stiffening and thickening was seen in the absence of diabetic complications, suggesting those being an early marker of vascular damage [21]. Arterial stiffness also is associated with premature coronary artery disease occurrence [22]. Being consistent with the result of our study there are reports saying that in CAD patients the aortic distensibility is markedly reduced. Ascending aorta stiffness index is associated with coronary artery disease in hypertensive patients [23].

In our study albuminuria did not affect aortic distensibility but aortic diameters were significantly higher in the albuminuria positive patients. However, in a study by Cuspidi et al. microalbuminuria was not associated with abdominal aortic diameter [24]. Also endothelial dysfunction is associated with microalbuminuria as reported 2 decades ago by Pedrinelli et al. In their study von Willebrand Factor antigen concentrations that showed presence of endothelial dysfunction were higher in hypertensive patients with microalbuminuria compared to other groups [25]. Coronary artery disease is considered as an important complication of type 2 diabetes mellitus. Guo et al. evaluated the correlation of urinary albumin excretion rate with the coronary heart disease severity and incidence, in patients with type 2 diabetes mellitus, aged 60 years or older. They reported that urinary albumin excretion rate was independently correlated with coronary artery disease in patients with type 2 diabetes

mellitus. Also the severity of coronary artery disease determined with Gensini scoring was independently associated with urinary albumin excretion rate [26]. However in our study the microalbuminuria did not differ between mild and severe coronary artery disease patients according to Gensini scoring. That makes us think that microalbuminuria helps us to detect presence of CAD but fails to show the extent of the disease. But we have to admit that these subjects need further investigation.

#### 4. Conclusion

In conclusion aortic diameters are increased in patients with coronary artery disease and in patients with microalbuminuria. In CAD patients, systolic blood pressure, pulse pressure, aortic systolic and diastolic pressure, and albumin excretion rate were higher and aortic distensibility was lower.

#### Conflict of Interests

No conflict of interests is declared by the authors.

#### References

- [1] O. C. Mirea, A. A. Ancuța, M. S. Șerbănescu et al., "Analysis of aortic size in subjects died due to cardiovascular and non-cardiovascular events: a necropsy study," *Romanian Journal of Morphology and Embryology*, vol. 55, no. 3, supplement, pp. 1105–1109, 2014.
- [2] M. Ganten, U. Krautter, W. Hosch et al., "Age related changes of human aortic distensibility: evaluation with ECG-gated CT," *European Radiology*, vol. 17, no. 3, pp. 701–708, 2007.
- [3] I. Kylintireas, C. Shirodaria, J. M. S. Lee et al., "Multimodal cardiovascular magnetic resonance quantifies regional variation in vascular structure and function in patients with coronary artery disease: relationships with coronary disease severity," *Journal of Cardiovascular Magnetic Resonance*, vol. 13, article 61, 2011.
- [4] G. Mulè, S. Cottone, A. Vadalà et al., "Relationship between albumin excretion rate and aortic stiffness in untreated essential hypertensive patients," *Journal of Internal Medicine*, vol. 256, no. 1, pp. 22–29, 2004.
- [5] E. Ishimura, H. Taniwaki, T. Tsuchida et al., "Urinary albumin excretion associated with arterial wall stiffness rather than thickness in type 2 diabetic patients," *Journal of Nephrology*, vol. 20, no. 2, pp. 204–211, 2007.
- [6] D. I. Shin, K.-B. Seung, H. E. Yoon et al., "Microalbuminuria is independently associated with arterial stiffness and vascular inflammation but not with carotid intima-media thickness in patients with newly diagnosed type 2 diabetes or essential hypertension," *Journal of Korean Medical Science*, vol. 28, no. 2, pp. 252–260, 2013.
- [7] M. M. H. Hermans, R. Henry, J. M. Dekker et al., "Estimated glomerular filtration rate and urinary albumin excretion are independently associated with greater arterial stiffness: the Hoorn study," *Journal of the American Society of Nephrology*, vol. 18, no. 6, pp. 1942–1952, 2007.
- [8] G. Mulè, S. Cottone, P. Cusimano et al., "Unfavourable interaction of microalbuminuria and mildly reduced creatinine clearance on aortic stiffness in essential hypertension," *International Journal of Cardiology*, vol. 145, no. 2, pp. 372–375, 2010.

- [9] A. Nemes, M. Csanády, and T. Forster, "Does increased aortic stiffness predict reduced coronary flow velocity reserve in patients with suspected coronary artery disease?" *Acta Physiologica Hungarica*, vol. 99, no. 3, pp. 271–278, 2012.
- [10] A. Nemes, I. Ungi, M. Csanády, and T. Forster, "Simultaneous improvement in aortic distensibility and coronary flow velocity reserve after successful coronary interventions," *Echocardiography*, vol. 27, no. 3, pp. 311–316, 2010.
- [11] P. A. McCullough, "Coronary artery disease," *Clinical Journal of the American Society of Nephrology*, vol. 2, no. 3, pp. 611–616, 2007.
- [12] P. A. McCullough, "Cardiorenal risk: an important clinical intersection," *Reviews in Cardiovascular Medicine*, vol. 3, no. 2, pp. 71–76, 2002.
- [13] C. E. Mogensen, "Microalbuminuria predicts clinical proteinuria and early mortality in maturity-onset diabetes," *The New England Journal of Medicine*, vol. 310, no. 6, pp. 356–360, 1984.
- [14] G. Mancia, G. de Backer, A. Dominiczak et al., "ESH/ESC 2007 Guidelines for the management of arterial hypertension," *Revista Española de Cardiología*, vol. 60, no. 9, pp. 968.e1–994.e1, 2007.
- [15] K. N. Khan, M. H. Khan, and M. Z. Haque, "Correlation between microalbuminuria with complexity of coronary artery disease in diabetic patients," *Mymensingh Medical Journal*, vol. 22, no. 2, pp. 353–357, 2013.
- [16] J. Kim, B.-H. Hwang, I. J. Choi et al., "A prospective two-center study on the associations between microalbuminuria, coronary atherosclerosis and long-term clinical outcome in asymptomatic patients with type 2 diabetes mellitus: evaluation by coronary CT angiography," *The International Journal of Cardiovascular Imaging*, vol. 31, no. 1, pp. 193–203, 2015.
- [17] G. G. Gensini, "A more meaningful scoring system for determining the severity of coronary heart disease," *The American Journal of Cardiology*, vol. 51, no. 3, article 606, 1983.
- [18] B. Özdemir, M. Biçer, L. Özdemir et al., "Aortic distensibility and coronary artery bypass graft patency," *Journal of Cardiothoracic Surgery*, vol. 4, no. 1, article 14, 2009.
- [19] C. Stefanadis, C. Stratos, H. Boudoulas, C. Kourouklis, and P. Toutouzas, "Distensibility of the ascending aorta: comparison of invasive and non-invasive techniques in healthy men and in men with coronary artery disease," *European Heart Journal*, vol. 11, no. 11, pp. 990–996, 1990.
- [20] A. Milan, F. Tosello, D. Naso et al., "Ascending aortic dilatation, arterial stiffness and cardiac organ damage in essential hypertension," *Journal of Hypertension*, vol. 31, no. 1, pp. 109–116, 2013.
- [21] C. Giannattasio, M. Failla, A. Piperno et al., "Early impairment of large artery structure and function in Type I diabetes mellitus," *Diabetologia*, vol. 42, no. 8, pp. 987–994, 1999.
- [22] B. Güngör, H. Yilmaz, A. Ekmekçi et al., "Aortic stiffness is increased in patients with premature coronary artery disease: a tissue Doppler imaging study," *Journal of Cardiology*, vol. 63, no. 3, pp. 223–229, 2014.
- [23] Q. Lu and H. Liu, "Correlation of ascending aorta elasticity and the severity of coronary artery stenosis in hypertensive patients with coronary heart disease assessed by M-mode and tissue doppler echocardiography," *Cell Biochemistry and Biophysics*, vol. 71, no. 2, pp. 785–788, 2015.
- [24] C. Cuspidi, S. Meani, F. Negri, C. Sala, and G. Mancia, "Left ventricular hypertrophy and abdominal aorta size in essential hypertension," *Journal of Hypertension*, vol. 29, no. 6, pp. 1213–1219, 2011.
- [25] R. Pedrinelli, O. Giampietro, F. Carmassi et al., "Microalbuminuria and endothelial dysfunction in essential hypertension," *The Lancet*, vol. 344, no. 8914, pp. 14–18, 1994.
- [26] L.-X. Guo, J. Ma, Y. Cheng, L.-N. Zhang, and M. Li, "Urinary albumin excretion rate is correlated with severity of coronary artery disease in elderly type 2 diabetic patients," *Chinese Medical Journal*, vol. 125, no. 23, pp. 4181–4184, 2012.

## Research Article

# Automatic Tooth Segmentation of Dental Mesh Based on Harmonic Fields

Sheng-hui Liao,<sup>1</sup> Shi-jian Liu,<sup>1</sup> Bei-ji Zou,<sup>1</sup> Xi Ding,<sup>2</sup> Ye Liang,<sup>3</sup> and Jun-hui Huang<sup>4</sup>

<sup>1</sup>*School of Information Science and Engineering, Central South University, Changsha 410083, China*

<sup>2</sup>*Department of Stomatology, First Affiliated Hospital of Wenzhou Medical University, Wenzhou 325000, China*

<sup>3</sup>*Department of Stomatology, Xiangya Hospital of Central South University, Changsha 410008, China*

<sup>4</sup>*Xiangya Stomatological Hospital of Central South University, Changsha 410008, China*

Correspondence should be addressed to Bei-ji Zou; [bjzou@vip.163.com](mailto:bjzou@vip.163.com)

Received 27 September 2014; Accepted 6 January 2015

Academic Editor: Ilker Ercan

Copyright © 2015 Sheng-hui Liao et al. This is an open access article distributed under the Creative Commons Attribution License, which permits unrestricted use, distribution, and reproduction in any medium, provided the original work is properly cited.

An important preprocess in computer-aided orthodontics is to segment teeth from the dental models accurately, which should involve manual interactions as few as possible. But fully automatic partition of all teeth is not a trivial task, since teeth occur in different shapes and their arrangements vary substantially from one individual to another. The difficulty is exacerbated when severe teeth malocclusion and crowding problems occur, which is a common occurrence in clinical cases. Most published methods in this area either are inaccurate or require lots of manual interactions. Motivated by the state-of-the-art general mesh segmentation methods that adopted the theory of harmonic field to detect partition boundaries, this paper proposes a novel, dental-targeted segmentation framework for dental meshes. With a specially designed weighting scheme and a strategy of a priori knowledge to guide the assignment of harmonic constraints, this method can identify teeth partition boundaries effectively. Extensive experiments and quantitative analysis demonstrate that the proposed method is able to partition high-quality teeth automatically with robustness and efficiency.

## 1. Introduction

In recent years, much effort has been spent in developing computerized systems for clinical and research applications in dentistry. Most computerized algorithms for orthodontic diagnosis and treatment require 3D dental mesh models, which are often needed to extract, move, and rearrange teeth for simulation of the treatment outcome. Thus, teeth segmentation is an important step in many automated and semiautomated, computer-based dental software packages.

However, tooth segmentation on dental meshes remains a difficult task [1]. Dental meshes from patients often have teeth crowding problems when adjacent teeth are misaligned, thus making the interstices between them irregular and difficult to distinguish. Various tooth shapes make outlining tooth contours difficult. Artifacts resulting from scanning or

model-making errors on commonly obtained clinical meshes make teeth segmentation more challenging.

General mesh segmentation approaches are not directly suited for segmenting dental meshes because they lack adjustments to handle complex tooth shapes and teeth arrangements. Other segmentation approaches proposed to handle dental meshes have shortcomings, such as being either labor-intensive or not sufficiently accurate [2]. Although several commercial products in this field are available, such as “3Shape,” their user interactions are intensive and significantly influence the accuracy of results.

Many tooth segmentation methods prefer to use surface curvature when identifying potential tooth boundaries, as they follow the most widely cited mesh segmentation criterion, the minima rule, which states that human perception usually divides a surface into parts along the concave discontinuity of the tangent plane [3, 4]. However, surface

curvature estimation is typically error-prone for real-world noisy models; for example, curvature distribution on clinical dental models is generally complicated and irregular (see Section 2 for further description).

This paper aims to develop an automatic and robust method for segmentation of digital dental models. Motivated by state-of-the-art general interactive mesh segmentation methods [5–8], we developed a convenient and efficient dental segmentation framework, which identifies tooth boundaries by a dental-targeted, harmonic field. This approach has three major benefits.

- (1) The dental-targeted harmonic field is robust to various tooth shapes, complex malocclusion, and crowding problems and is insensitive to noise with minimum parameter considerations.
- (2) The dental-targeted harmonic field can guarantee closed tooth boundary extraction from dental mesh, unlike curvature-based methods needing complex connectivity and morphologic operations in most cases.
- (3) The whole dental segmentation procedure is automatic, which requires no user interaction to generate teeth with accurate and high-quality cutting boundaries.

## 2. Related Work

This paper focuses on dental mesh segmentation. We introduce general mesh segmentation methods before dental specific methods. The theory of harmonic field will be given at the end of the section.

*2.1. General Segmentation Method.* Numerous mesh segmentation approaches have been proposed in computer graphics. Some of these algorithms are automated, like clustering [9], random walk [10], shape diameter function [11], fitting primitives [12], and fast marching watershed [13]. Most of these methods aim to partition different regions based on similarity measures [14], but defining a semantic subarea of tooth with various shapes remains a challenging task and none of these methods is directly suitable for our specific application.

Recently, sketch-based interactive mesh segmentation methods have become very popular [5–8]. Most of these methods employ harmonic field theory and similar user interfaces, but they are different in computational weighting scheme and constraint styles. Interested readers should refer to literature such as surveys of comparisons between these sketch-based methods [15]. These methods have good performance in general mesh segmentation but require time-consuming and error-prone user interaction when dealing with special and complicated tooth shapes and arrangements. Furthermore, they cannot produce high-quality cutting boundaries in cases where no obvious concave regions are near the location of interaction.

While our method also employs the harmonic field for segmentation, it fully exploits the dental characteristics

(see Section 3.3), which makes the proposed method smart, accurate, and more robust in tooth partition.

*2.2. Dental-Targeted Segmentation Method.* A large group of dental segmentation approaches prefer to use surface curvature to identify tooth boundaries. The typical routine can be summarized as follows.

(1) Curvature estimation: principal curvatures, including minimum principal curvature [16–19] and mean principal curvature [1], are used to measure the surface property quantitatively. (2) Teeth-part rough locating: though not always necessary, this is a plane-estimating technique, based on PCA that produces a cutting plane to separate gingiva and teeth part, introduced in previous works [1, 20]. We also involve this step in our framework, but the method we used is more convenient and effective (see Section 3.2). (3) Thresholding: a curvature threshold value is inevitably needed to separate potential tooth boundary regions from the rest when using curvature fields for boundary identification. That value can be obtained either interactively, such as when using an intuitive slider [16], or by taking a result of an experiential equation or even plugging in a constant preset number [19, 20]. In fact, a global threshold value used in this mandatory step is one of the major drawbacks; it can significantly influence this entire solution, because the thresholding generally cannot appropriately distinguish target objects from the rest of the region, leading to either over- or undersegmentation. (4) Potential boundary region refining: because the curvature field introduces lots of useless features in tooth crown regions and is sensitive to noise in identifying tooth boundary methods [1, 17, 19], using a morphologic operation will further refine the region obtained by thresholding. For some complicated dental models, however (e.g., in cases of adjacent teeth crowding when the interstices in between are irregular and difficult to distinguish), the potential tooth boundary region may still be incomplete even after morphologic operation. (5) Boundary locating and refining: as proposed in previous works [1, 16, 17, 19], a skeleton operation is used to extract boundaries from potential regions. However, teeth with such boundaries are unacceptable for precise clinical treatment planning. Refinements should be carried out to make sure the boundary of each tooth is both smooth and precise [1]. More seriously, the extracted boundaries could be incomplete (e.g., opened) so special refinement should be taken to close the opened boundaries before attempting smooth and precise operations. All such procedures make the entire framework tedious and complicated.

Kondo et al. introduced a fully automatic algorithm to segment tooth from dental models using two range images [20]. However, they used a rectangular inspection spoke to cut the model, which will introduce inaccurate cuts for severe malocclusions. Kronfeld et al. proposed a snake-based approach that starts with an initial contour on the gingiva and evolves through a feature attraction field [21]. The cusps of each tooth are then selected to start a local tooth contour and evolve until each tooth bottom is reached. The approach is automatic but may not produce good results when the model has boundary noises that interrupt a feature field defined by the curvature information.

As another option, interactive dental partition methods [22, 23] allow users to select several boundary points interactively for segmentation. Geodesics are then generally used to connect two adjacent control points. The interactive partition procedures are intuitive and capable of segmenting complicated dental models, but the shortcomings are also quite obvious; for example, users would have to rotate or translate multiple times to carefully specify particular mark points to generate one accurate tooth boundary. Such tedious and time-consuming experiences certainly are undesirable and impracticable for clinical application.

Recently, Zou et al. proposed an interactive tooth partition method based on harmonic field [24]. The method has great flexibilities which benefit from their specially designed user interfaces. But the employed harmonic field is only “tooth-target”; in other words, only one tooth could be identified manually one time, and the whole dental mesh has to be processed multiple times to finish the whole segmentation. In contrast, our novel segmentation framework is able to segment all teeth only once under a uniform harmonic field automatically, which greatly improves the partition efficiency.

**2.3. Harmonic Field.** In mathematics, a harmonic field on 3D mesh,  $M = (V, E, F)$ , is a scalar field attached to each mesh vertex and satisfies  $\Delta\Phi = 0$ , where  $V$ ,  $E$ , and  $F$  denote vertex, edge, and face set of  $M$ , respectively. The symbol,  $\Delta$ , is the Laplacian operator, subject to particular Dirichlet boundary constraint conditions. For example, 0 and 1 are used as minimum and maximum constraints in most harmonic field computations. The standard definition of Laplacian operator on a piecewise linear mesh,  $M$ , is the operator:

$$\Delta\Phi_i = \sum_{(i,j) \in E} w_{ij} (\Phi_i - \Phi_j), \quad (1)$$

where  $w_{ij}$  is a scalar weight assigned to the edge,  $E_{ij}$ . This Poisson equation,  $\Delta\Phi = 0$ , can be solved by the least-squares sense, which leads to

$$\begin{aligned} A\Phi &= b, \\ A &= \begin{bmatrix} L \\ C \end{bmatrix}, \\ b &= \begin{bmatrix} 0 \\ b' \end{bmatrix}, \end{aligned} \quad (2)$$

where  $L$  is the Laplacian matrix given by

$$L_{ij} = \begin{cases} \sum_{k \in N_1(i)} w_{ik}, & \text{if } i = j, \\ -w_{ij}, & \text{if } (i, j) \in E, \\ 0, & \text{otherwise,} \end{cases} \quad (3)$$

where  $N_1(i)$  is the 1-ring neighbor set of vertex,  $i$ .  $C$  and  $b'$  are matrix and vector, respectively, standing for the constraints in the harmonic field. Different weighting scheme and constraints will lead to a different kind of harmonic field. For example, let  $\alpha_{ij}$  and  $\beta_{ij}$  denote angles opposite to  $E_{ij}$ ,

respectively; the standard cotangent-weighting scheme will be given by

$$w_{ij} = \frac{\cot\alpha_{ij} + \cot\beta_{ij}}{2}, \quad (4)$$

leading to a smooth, transiting harmonic field, suited to applications like mesh deformation [25] and direction field design [26]. However, the standard weighting scheme cannot identify the local shape variation; this drawback makes it no longer suitable for segmentation purposes.

Our method utilizes a novel, dental-targeted weighting scheme, which preserves the nice property of classic cotangent-weighting scheme, while having the ability to sense the concave feature for each tooth boundary. A special constraint assigning strategy is also proposed accordingly.

### 3. Materials and Methods

Since human teeth occur in different shapes and their arrangements vary substantially from one individual to another, careful selection of test datasets is necessary in tooth segmentation studies. We evaluate 60 sets of dental models including both low and up jaw of varying complexity and precision. For instance, teeth on some of the dental meshes have severe malocclusion and crowding problem, while others may be absent from the jaw. These datasets were accumulated in the years between 2010 and 2014, at Xiangya Hospital of Central South University and the First Affiliated Hospital of Wenzhou Medical University, from patients who need medical treatments such as orthodontics or dental implantation. These models are acquired by a 3D dental scanner or intraoral scanner with accuracy of 0.01 mm–0.1 mm. Each of the dental meshes is guaranteed to be manifold and nondegenerate as preprocessed by the software supplied by the scanner manufacturers.

These dental mesh models are taken as input of the proposed framework as demonstrated in Figure 1, and the output results are segmented individual teeth.

As illustrated in the block diagram, teeth anatomical feature points and the occlusal plane, employed as the prior knowledge of following computation, are firstly identified (Section 3.1). Secondly, a rough locating procedure for teeth parts is performed and a cut plane is found to automatically remove the gingival region of the dental model (Section 3.2). Then, dental-targeted constraint points can be initialized to prepare for the harmonic field calculation. Once a harmonic field is generated, an optimal isoloop for each tooth can be extracted as a tooth boundary (Section 3.3).

**3.1. Dental Features Identification.** We use a priori knowledge of feature points on human teeth and occlusal plane in our method. The feature points consist of cusps on the canines, premolars, and molars and point to the end of the incisal edge on incisors. Identification of these points and the occlusal plane is a fundamental dental process. A robust, computer-aided, automatic identification method [27] is used in our framework to identify them, as demonstrated by white spheres and a blue plane in Figure 2.

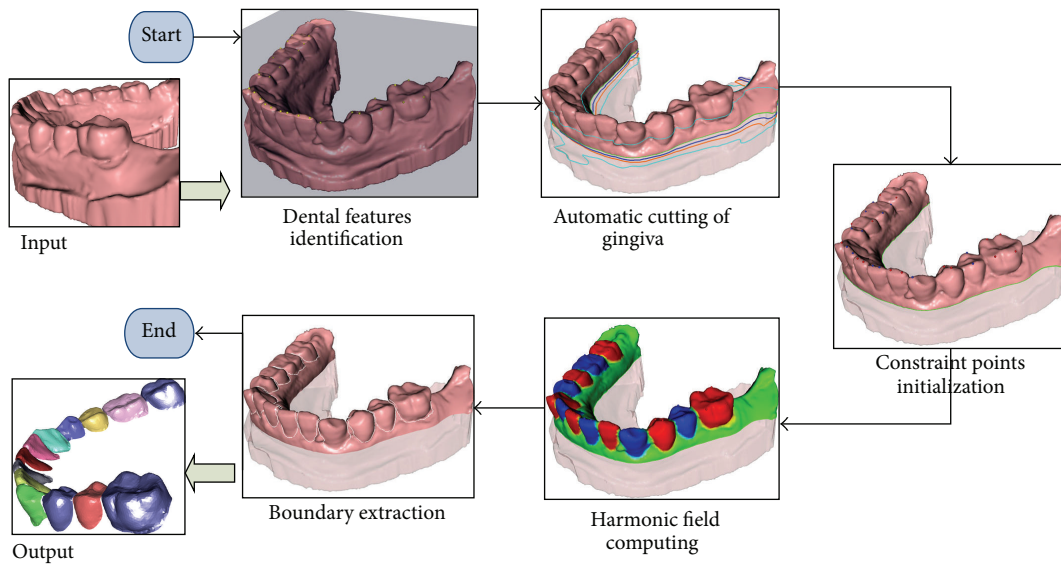


FIGURE 1: Block diagram of our proposed framework.

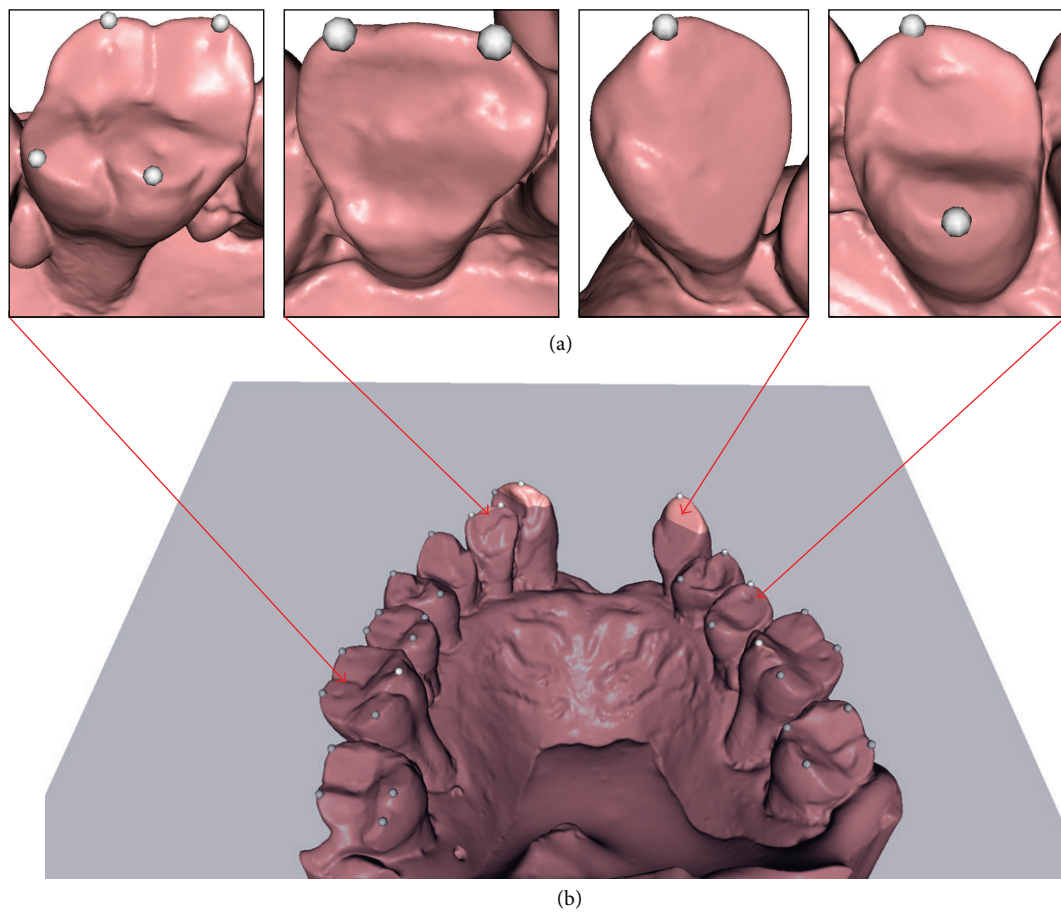


FIGURE 2: Automatically identified features of a dental model. Top row from left to right indicates anatomical feature points on molar, incisor, canine, and premolar; bottom row illustrates the occlusal plane.

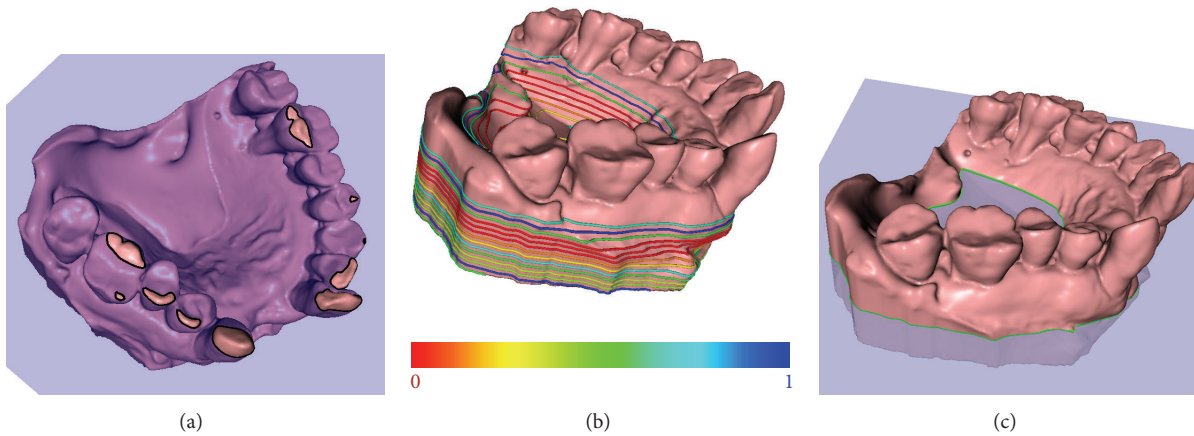


FIGURE 3: Steps of gingiva cutting. Images from left to right illustrate (a) the inappropriate cutting when multiple intersection loops are acquired; (b) the acquisition of only one intersection loop; (c) the desirable cutting attained when the variance energy stops decreasing.

The inspection spoke-based strategy [20] is then employed to automatically separate these teeth feature points into different groups. This approach first fits a curve of the tooth-based dental arch and then detects inspection spokes along the dental arch. Instead of using the inspection spokes to do tooth segmentation, which may lead to unsatisfactory cut results, we utilize them to separate those feature points into different groups (each group corresponding to one tooth).

In addition, these feature point groups are arranged in order along the direction of the dental arch. And we further classify them into two bigger point sets, that is, one feature points set,  $\Omega_1$ , consisting of groups with odd indexes of 1, 3, 5, ... and the other set,  $\Omega_2$ , consisting of alternating groups with even indexes of 2, 4, 6, ... These two feature point sets will be employed as part of constraints in the computation of the dental-targeted harmonic field.

**3.2. Automatic Cutting of Gingiva.** We seek a cutting plane to roughly separate the teeth parts from the gingiva region to accelerate following harmonic field computation. The basic idea is similar to earlier methods [1], but we have made it more efficient. Initially, the plane is located at the position of the occlusal plane and then moved iteratively towards the bottom of the dental model along the normal direction. The distance moved in each step is a small constant value,  $d$  (we noticed that  $d = 1$  mm meets the requirement of almost all dental models in our experiments). During the movement, each plane  $P_i$  ( $1 \leq i \leq N$ ,  $N$  is the count of move steps) will intersect with dental mesh and generate one or more intersecting loops.

At the beginning, a multiple-loop intersection will be detected as shown in Figure 3(a), which implies that the plane is intersecting with the teeth parts or outliers. The iteration is continued until only one-loop intersection is acquired, as the first meaningful loop shown in Figure 3(b). Afterwards, for

each  $P_i$ , the variance energy of minimum principal curvature,  $\phi_i$ , is used to evaluate the intersection:

$$\phi_i = \frac{1}{n-1} \sum_{k=1}^n (c_{\min,k} - c_{\min,\text{avg}})^2, \quad (5)$$

where  $n$  is the number of mesh points on the intersection loop,  $c_{\min,k}$  denotes the minimum principal curvature of point  $k$ , and  $c_{\min,\text{avg}}$  indicates the average minimum principal curvature of all points.

When all one-loop intersections are found, their corresponding variance energies are linearly mapped to axes 0, 1. The results are shown as colors ranging from red to blue in Figure 3(b). The normalized variance energy of each,  $P_i$ , is utilized to select the best cutting plane because we notice that the energy is high at the teeth parts (larger than 0.5 generally) and decreases towards the gingiva region. Based on this observation, we select the cutting plane by checking the normalized variance, which is less than 0.5 in each step, until it stops decreasing. In the extreme situation, the movement stops when there is no intersection of the plane with the dental model; in this case, we use the last one-loop intersection plane as the cutting plane.

Finally, useless dental parts (e.g., the transparent gingiva region in Figure 3(c)) are clipped out using the cutting plane. In addition, the mesh points on the loop are recorded as part of constraints in the following harmonic field computation (see Section 3.3).

Procedures described in this section are valuable for high-precision dental meshes because large percentages of useless mesh can be removed to relieve the burden of harmonic field computation. Although general mesh decimation processes can be also used to reduce complexity of mesh, along with the global decimation quality of teeth surfaces will receive damage as well.

**3.3. Harmonic Field Calculation.** We adopted the basic idea of utilizing harmonic field for tooth boundary identification

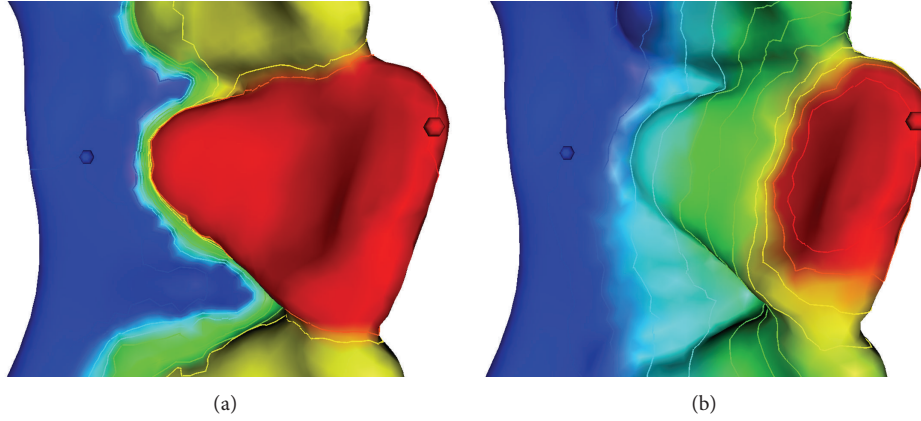


FIGURE 4: Harmonic fields under different weighting schemes. The images demonstrate harmonic field under (a) the special weighting scheme and (b) cotangent-weighting scheme, respectively.

[24], which makes use of a special weighting scheme, given by

$$w_{ij}^* = \frac{\gamma_{ij} (\cot\alpha_{ij} + \cot\beta_{ij})}{2}. \quad (6)$$

The properties of this kind of harmonic field can be summarized as follows, which is the reason we chose it for the tooth partition.

(i) *Smoothness*. As a method derived from classic cotangent-weighting scheme, the harmonic field successfully inherits the smooth transition property. That is, the transitions of vertex scalars from minimum to maximum Dirichlet boundary values are stable and smooth in both concave and nonconcave regions.

(ii) *Shape-Awareness*. The harmonic field has strong awareness of concave creases and seams. Therefore, the uniformly sampled isolines, which are dense at concave regions, can naturally form the candidates of partition boundaries.

Figure 4 demonstrates differences between two harmonic fields by mapping field scalars, whose values range from 0 to 1 and the colors range from red to blue. Figure 4(a) shows the harmonic field using the special weighting scheme, while Figure 4(b) shows the harmonic field with the same constraints but uses the standard cotangent-weighting scheme. Uniformly sampled isolines on mesh are also extracted and colored to indicate field variance.

Our new dental-targeted segmentation framework is different from previous tooth-targeted study [24] in two major aspects. The first one is that the constraints of dental harmonic field are automatically identified as proposed above. And the second one is our special designed assignment of constraints for dental teeth segmentation, as introduced in the following, which is the key to segment all teeth only once under a uniform harmonic field computation automatically.

For Dirichlet constraints of the dental-targeted harmonic field, there are two major considerations: (1) the method for choosing constraint points on dental meshes and (2) the value of constraint points assigned in harmonic field computation.

For the first issue, we choose constraint points by taking a priori knowledge of human teeth into consideration. In other words, the teeth feature points sets,  $\Omega_1$  and  $\Omega_2$ , and the mesh points set,  $\Omega_3$ , on the gingiva cutting plane are used as constraints.

For the second issue, the maximum and minimum constraint values 1 and 0 are assigned to the teeth feature points sets,  $\Omega_1$  and  $\Omega_2$ , separately. That is, feature points on the same tooth will have the same constraint value, either 0 or 1, but feature points on the neighbor teeth will have different constraint value, either 1 or 0, as demonstrated by red and blue spheres in Figure 5(a), respectively.

In addition, a middle constraint value of 0.5 is assigned to the mesh points set,  $\Omega_3$ , on the gingiva cutting plane (as green contour and points depicted in Figure 5(a)).

As demonstrated by Figures 5(b) and 5(c), the resulting harmonic field, using our assignment strategy of a priori knowledge guided constraints, has much better distinguishing tooth partition patterns for all teeth, compared to one without such middle constraint value, which is a conventional case in many other harmonic field-based methods.

According to the constraints assignment, entities of matrix  $C$  and vector  $b'$  introduced above can be set solving (2). Specifically, if we denote points assigned with constraint values 0, 0.5, and 1 by  $p_{\min}$ ,  $p_{\text{mid}}$ , and  $p_{\max}$  on mesh  $M$ , respectively, and put them into a list  $S$ , then  $c_{ij} \in C$  ( $1 \leq i \leq n$ ,  $1 \leq j \leq m$ ) and  $b_i \in b'$  ( $1 \leq i \leq n$ ) can be given by the following equations, respectively:

$$c_{ij} = \begin{cases} w, & \text{for } \{(i, j) \mid M(p_i) = j\}, \\ 0, & \text{otherwise,} \end{cases} \quad (7)$$

$$b_i = \begin{cases} w, & \text{for } \{i \mid \text{Type}(p_i) = p_{\max}\}, \\ 0.5w, & \text{for } \{i \mid \text{Type}(p_i) = p_{\text{mid}}\}, \\ 0, & \text{for } \{i \mid \text{Type}(p_i) = p_{\min}\}, \end{cases} \quad (8)$$

where  $w$  is a large constant value (1000 in our experiments),  $n$  and  $m$  denote number of vertexes in  $S$  and  $M$ , respectively, and  $p_i$  ( $0 \leq i \leq n-1$ ) is an element of  $S$ , whose index is  $i$ .

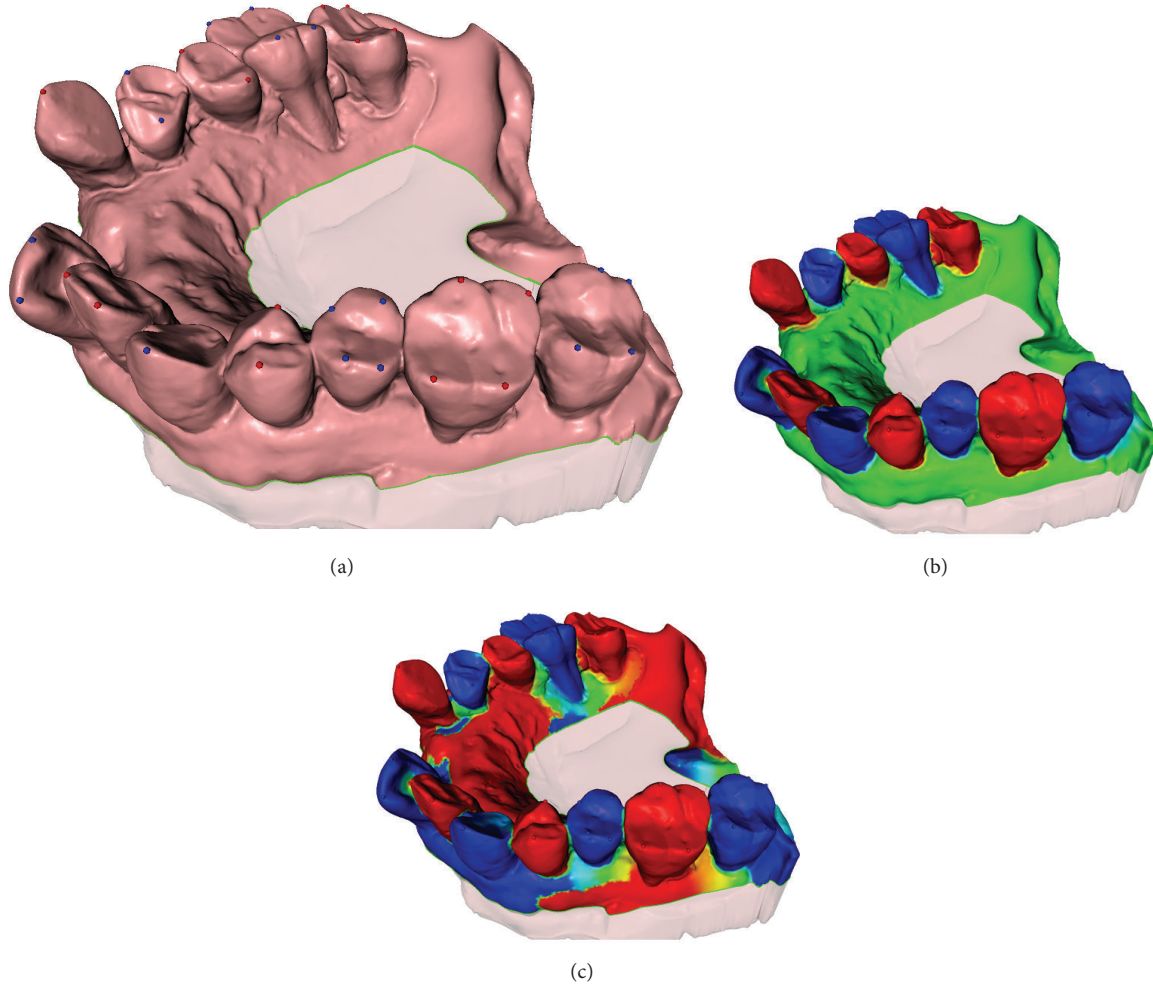


FIGURE 5: Assignment of constraint points on dental mesh for harmonic field computation. (a) Constraints assigned in our proposed method. (b) Resulting harmonic field with intersecting contour mesh points as constraints. (c) Resulting field without intersecting contour mesh points as constraints.

$M(p_i)$  denotes the index of  $p_i$  in  $M$ ,  $Type(p_i)$ , and returns the type of  $p_i$ .

Modern sparse Cholesky factorization and modification software package [28, 29] are used to solve the linear system (i.e., (2)) efficiently, which results in the dental-targeted harmonic field showed in Figure 5(b).

With our objective almost accomplished, all that is left to sample and uniformly extract is a number of isolines from the harmonic field, as shown by colored loops in Figure 6(a), and select optimal isoloops as the tooth boundaries (e.g., white loops in Figures 6(b) and 6(c)). And we use the voting strategy proposed in previous work [5] to automatically select the best isoloop.

#### 4. Experiments and Results

We have tested our approach on 60 dental mesh models (low and up jaw) of varying complexity. The datasets included laser scans of plaster models obtained from different commercial

scanners. Our approach was performed with reasonable accuracy on almost all of these models. Figure 7 illustrates 12 of these dental models, some of which show teeth with severe crowding problems, while others may be absent from the jaw. For each of the 12 models in Figure 7, three images are used to illustrate states during the partition, namely, (1) the input original mesh, (2) the clipped dental mesh attached with dental-targeted harmonic field, and (3) the segmented nontooth part (colored with red) and individual teeth (with other colors) as output.

To provide a “ground truth” dental segmentation benchmark for quantitative evaluation, we asked two dentists, each with the necessary training and sufficient practice time, to identify the boundary of each tooth manually on all experimental models. For each tooth, all marked contours from the two dentists were averaged to produce a ground truth. The boundaries of our segmented teeth were then compared with the ground truth results using mean errors, as shown in Figure 8. The average mean error of our approach

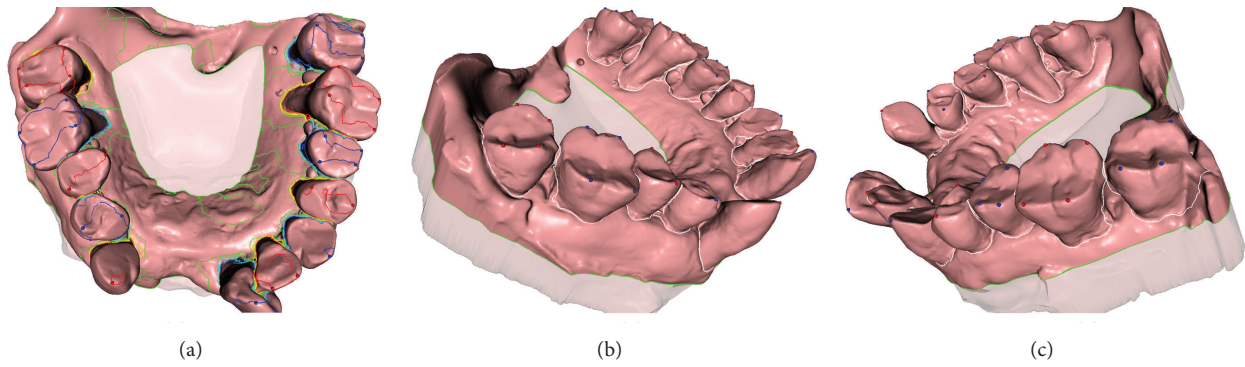


FIGURE 6: Tooth boundaries identification: (a) iso-loops evenly extracted from generated harmonic field; (b and c) two perspectives of the extracted optimal iso-loops as the tooth boundaries.

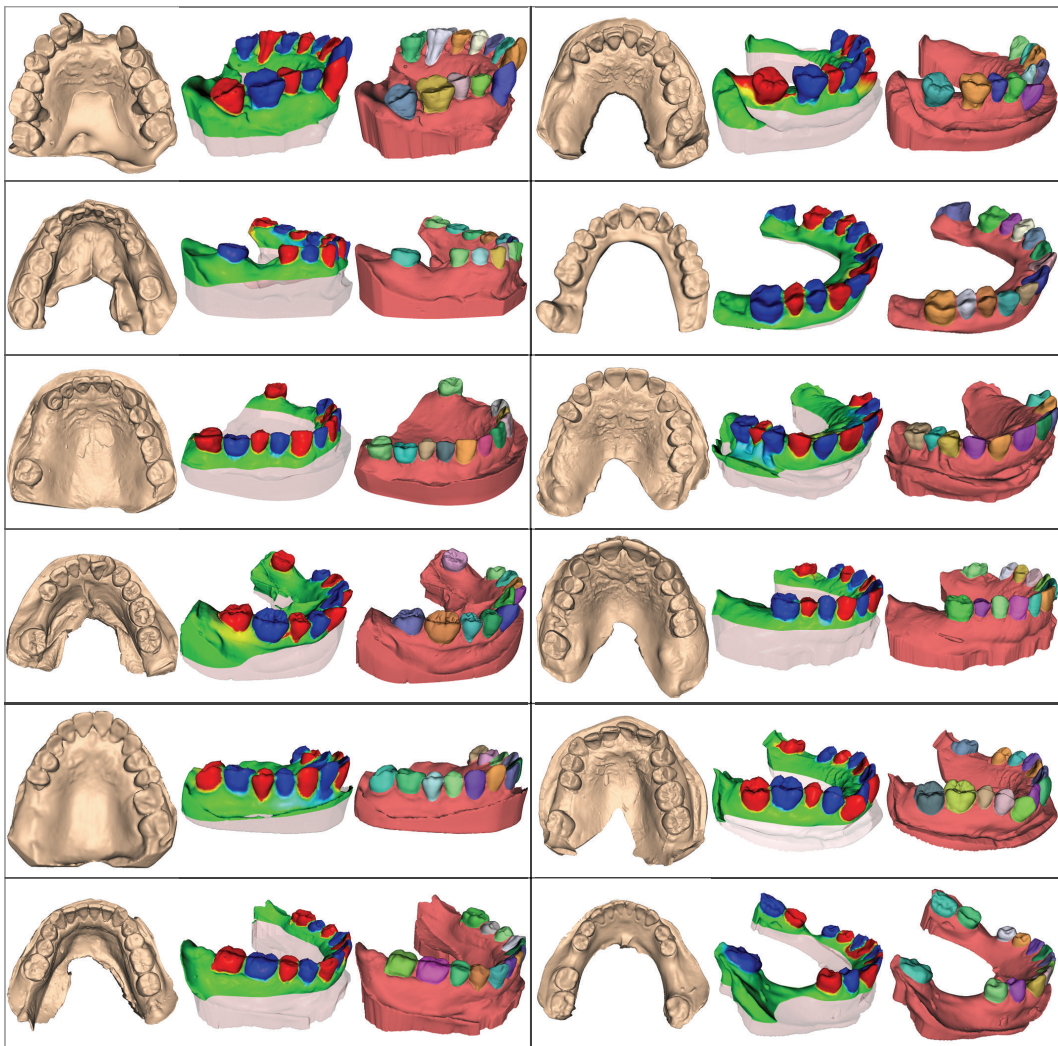


FIGURE 7: The segmentation results of our approach on various dental meshes with crowding problems.

within the 60 models is about 0.1 mm, which was approved by the dentists.

We also recorded the time consumed by our approach on different scales of dental models (measured with a

number of mesh points and faces) during experiments, as shown in Figure 9, including the time for (a) dental base cutting, (b) harmonic field precomputing, (c) harmonic field updating, (d) boundary extraction, and (e) total time for

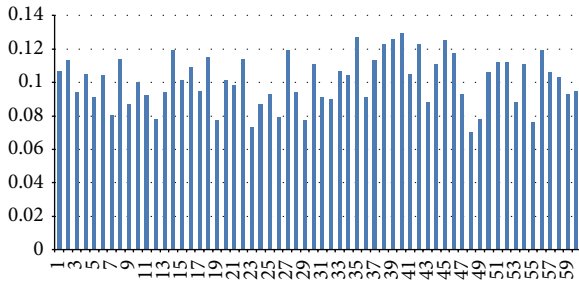


FIGURE 8: The mean errors of our tooth segmentation results compared to manually labeled ground truth of all 60 models. The horizontal axis denotes 60 cases in our experiments and the vertical axis denotes the mean errors, correspondingly.

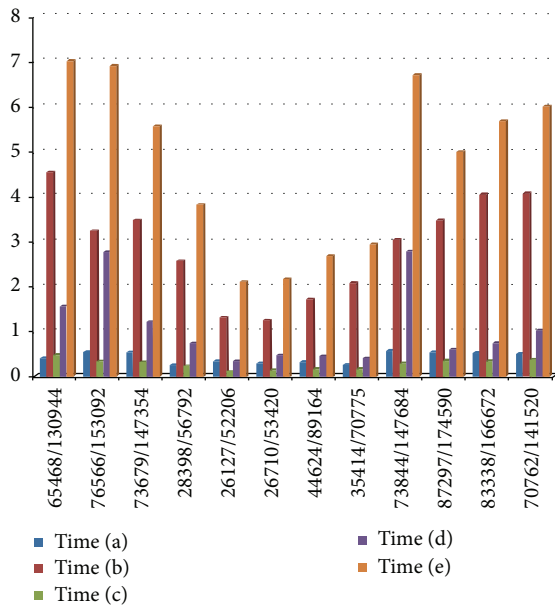


FIGURE 9: Time statistics of our dental mesh segmentation. The timing is recorded in seconds for (a) dental base cutting, (b) harmonic field precomputing, (c) harmonic field updating, (d) boundary extraction, and (e) total time of dental segmentation. The horizontal axis illustrates different mesh model scales by number of mesh points and faces. The vertical axis illustrates the time consumption for procedures in the segmentation framework.

dental segmentation. All experiments were carried out on a common PC with Intel Core Quad-Core Processor 2.67 GHz with 4 GB memory. The total segmentation time of one dental model in our experiments is usually less than 7 seconds. By contrast, the popular commercial software, “3Shape,” often takes many minutes of interaction to segment one model; the accompanying method [1] often takes 1 or 2 minutes.

**5. Conclusions**

For this paper, we studied the fundamental problem of automatically segmenting teeth in dental mesh models into individual tooth objects. With a specially designed weighting scheme and a strategy of a priori knowledge to guide the

assignment of constraints, we built a novel dental-targeted harmonic field, which is able to segment all teeth only once under a uniform harmonic field computation automatically. This harmonic field is robust to various tooth shapes, complex malocclusion, and crowding problems and can guarantee closed tooth boundary extraction from dental mesh, unlike curvature-based methods needing complex connectivity and morphologic operations, in most cases.

Extensive experiments and quantitative analysis demonstrated the effectiveness of the method in terms of accuracy, robustness, and efficiency. We plan to integrate this convenient, dental segmenting algorithm in a computer-aided, 3D-orthodontic system that is suitable for deployment in clinical settings.

**Conflict of Interests**

The authors declare that there is no conflict of interests regarding the publication of this paper.

**Authors’ Contribution**

Sheng-hui Liao and Shi-jian Liu are co-first authors; they contributed equally to the work.

**Acknowledgments**

This study was supported by the National Natural Science Foundation of China (no. 60903136, no. 61173122, and no. 81000461), the Doctoral Fund of Ministry of Education of China (no. 20130162130001), and the Cultivate Strategic Emerging Industries Special Foundation of Changsha City (no. K1406035\_11).

**References**

- [1] K. Wu, L. Chen, J. Li, and Y. Zhou, “Tooth segmentation on dental meshes using morphologic skeleton,” *Computers and Graphics*, vol. 38, no. 1, pp. 199–211, 2014.
- [2] L. Fan, L. Liu, and K. Liu, “Paint mesh cutting,” *Computer Graphics Forum*, vol. 30, no. 2, pp. 603–611, 2011.
- [3] Y. Lee, S. Lee, A. Shamir, D. Cohen-Or, and H.-P. Seidel, “Mesh scissoring with minima rule and part salience,” *Computer Aided Geometric Design*, vol. 22, no. 5, pp. 444–465, 2005.
- [4] Z. Ji, L. Liu, and Z. Chen, “Easy mesh cutting,” in *Computer Graphics Forum*, vol. 25, pp. 283–291, Blackwell, London, UK, 2006.
- [5] Y. Zheng, C.-L. Tai, and O. K.-C. Au, “Dot scissor: a single-click interface for mesh segmentation,” *IEEE Transactions on Visualization and Computer Graphics*, vol. 18, no. 8, pp. 1304–1312, 2012.
- [6] M. Meng, L. Fan, and L. Liu, “ICutter: a direct cut-out tool for 3D shapes,” *Computer Animation and Virtual Worlds*, vol. 22, no. 4, pp. 335–342, 2011.
- [7] Y. Zheng and C.-L. Tai, “Mesh decomposition with cross-boundary brushes,” *Computer Graphics Forum*, vol. 29, no. 2, pp. 527–535, 2010.
- [8] O. Kin-Chung Au, Y. Zheng, M. Chen, P. Xu, and C.-L. Tai, “Mesh segmentation with concavity-aware fields,” *IEEE*

- Transactions on Visualization and Computer Graphics*, vol. 18, no. 7, pp. 1125–1134, 2012.
- [9] S. Katz and A. Tal, “Hierarchical mesh decomposition using fuzzy clustering and cuts,” *ACM Transactions on Graphics*, vol. 22, no. 3, pp. 954–961, 2003.
- [10] Y.-K. Lai, S.-M. Hu, R. R. Martin, and P. L. Rosin, “Rapid and effective segmentation of 3D models using random walks,” *Computer Aided Geometric Design*, vol. 26, no. 6, pp. 665–679, 2009.
- [11] L. Shapira, A. Shamir, and D. Cohen-Or, “Consistent mesh partitioning and skeletonisation using the shape diameter function,” *Visual Computer*, vol. 24, no. 4, pp. 249–259, 2008.
- [12] M. Attene, B. Falcidieno, and M. Spagnuolo, “Hierarchical mesh segmentation based on fitting primitives,” *Visual Computer*, vol. 22, no. 3, pp. 181–193, 2006.
- [13] A. F. Koschan, “Perception-based 3D triangle mesh segmentation using fast marching watersheds,” in *Proceedings of the IEEE Computer Society Conference on Computer Vision and Pattern Recognition*, vol. 2, pp. II-27–II-32, IEEE, June 2003.
- [14] A. Shamir, “A survey on mesh segmentation techniques,” *Computer Graphics Forum*, vol. 27, no. 6, pp. 1539–1556, 2008.
- [15] L. Fan, M. Meng, and L. Liu, “Sketch-based mesh cutting: a comparative study,” *Graphical Models*, vol. 74, no. 6, pp. 292–301, 2012.
- [16] Y. Kumar, R. Janardan, B. Larson, and J. Moon, “Improved segmentation of teeth in dental models,” *Computer-Aided Design and Applications*, vol. 8, no. 2, pp. 211–224, 2011.
- [17] T. Yuan, W. Liao, N. Dai, X. Cheng, and Q. Yu, “Single-tooth modeling for 3D dental model,” *International Journal of Biomedical Imaging*, vol. 2010, Article ID 535329, 14 pages, 2010.
- [18] Z. Li, X. Ning, and Z. B. Wang, “A fast segmentation method for STL teeth model,” in *Proceedings of the IEEE/ICME International Conference on Complex Medical Engineering (CME '07)*, pp. 163–166, IEEE, May 2007.
- [19] M. Zhao, L. Ma, W. Tan, and D. Nie, “Interactive tooth segmentation of dental models,” in *Proceedings of the 27th Annual International Conference on Engineering in Medicine and Biology Society (IEEE-EMBS '05)*, pp. 654–657, IEEE, Shanghai, China, January 2006.
- [20] T. Kondo, S. H. Ong, and K. W. C. Foong, “Tooth segmentation of dental study models using range images,” *IEEE Transactions on Medical Imaging*, vol. 23, no. 3, pp. 350–362, 2004.
- [21] T. Kronfeld, D. Brunner, and G. Brunnett, “Snake-based segmentation of teeth from virtual dental casts,” *Computer-Aided Design and Applications*, vol. 7, no. 2, pp. 221–233, 2010.
- [22] Y. Q. Ma and Z. K. Li, “Computer aided orthodontics treatment by virtual segmentation and adjustment,” in *Proceedings of the International Conference on Image Analysis and Signal Processing*, pp. 336–339, IEEE, 2010.
- [23] C. Sinthanayothin and W. Tharanont, “Orthodontics treatment simulation by teeth segmentation and setup,” in *Proceedings of the 5th International Conference on Electrical Engineering/Electronics, Computer, Telecommunications and Information Technology*, vol. 1, pp. 81–84, IEEE, May 2008.
- [24] B.-J. Zou, S.-J. Liu, S.-H. Liao, X. Ding, and Y. Liang, “Interactive tooth partition of dental mesh base on tooth-target harmonic field,” *Computers in Biology and Medicine*, vol. 56, pp. 132–144, 2014.
- [25] M.-F. Li, S.-H. Liao, and R.-F. Tong, “Facial hexahedral mesh transferring by volumetric mapping based on harmonic fields,” *Computers & Graphics*, vol. 35, no. 1, pp. 92–98, 2011.
- [26] S.-H. Liao, B.-J. Zou, J.-P. Geng, J.-X. Wang, and X. Ding, “Physical modeling with orthotropic material based on harmonic fields,” *Computer Methods and Programs in Biomedicine*, vol. 108, no. 2, pp. 536–547, 2012.
- [27] Y. Kumar, R. Janardan, and B. Larson, “Automatic feature identification in dental meshes,” *Computer-Aided Design and Applications*, vol. 9, no. 6, pp. 747–769, 2012.
- [28] Y. Chen, T. A. Davis, W. W. Hager, and S. Rajamanickam, “Algorithm 887: CHOLMOD, supernodal sparse Cholesky factorization and update/downdate,” *ACM Transactions on Mathematical Software*, vol. 35, no. 3, article 22, 2008.
- [29] T. A. Davis, *User Guide for CHOLMOD: A Sparse Cholesky Factorization and Modification Package*, Department of Computer, Information Science and Engineering, University of Florida, Gainesville, Fla, USA, 2014.

## Research Article

# Preliminary Observations on Sensitivity and Specificity of Magnetization Transfer Asymmetry for Imaging Myelin of Rat Brain at High Field

Jae-Woong Kim,<sup>1,2</sup> Jiye Choi,<sup>1</sup> Janggeun Cho,<sup>2,3</sup> Chulhyun Lee,<sup>2</sup>  
Daejong Jeon,<sup>1</sup> and Sung-Hong Park<sup>1</sup>

<sup>1</sup>Department of Bio and Brain Engineering, Korea Advanced Institute of Science and Technology, Daejeon 305-701, Republic of Korea

<sup>2</sup>Division of Magnetic Resonance Research, Korea Basic Science Institute, Ochang-eup, Cheongwon-gun, Chungcheongbuk-do 363-883, Republic of Korea

<sup>3</sup>Department of Chemistry, Chung-Ang University, Seoul 156-756, Republic of Korea

Correspondence should be addressed to Sung-Hong Park; [sunghongpark@kaist.ac.kr](mailto:sunghongpark@kaist.ac.kr)

Received 26 February 2015; Revised 15 June 2015; Accepted 8 July 2015

Academic Editor: Gulsum Ozyigit

Copyright © 2015 Jae-Woong Kim et al. This is an open access article distributed under the Creative Commons Attribution License, which permits unrestricted use, distribution, and reproduction in any medium, provided the original work is properly cited.

Magnetization transfer ratio (MTR) has been often used for imaging myelination. Despite its high sensitivity, the specificity of MTR to myelination is not high because tissues with no myelin such as muscle can also show high MTR. In this study, we propose a new magnetization transfer (MT) indicator, MT asymmetry (MTA), as a new method of myelin imaging. The experiments were performed on rat brain at 9.4 T. MTA revealed high signals in white matter and significantly low signals in gray matter and muscle, indicating that MTA has higher specificity than MTR. Demyelination and remyelination studies demonstrated that the sensitivity of MTA to myelination was as high as that of MTR. These experimental results indicate that MTA can be a good biomarker for imaging myelination. In addition, MTA images can be efficiently acquired with an interslice MTA method, which may accelerate clinical application of myelin imaging.

## 1. Introduction

Myelin is an essential microstructure component for normal brain function. It is a type of glial cells that wraps around axons, forming dielectric myelin sheath structure. Myelin induces saltatory conduction enabling nerve impulse to propagate more than 200 times faster. Moreover, myelin accounts for 50% of the dry weight of central nervous system [1]. For these reasons, imaging and observing myelination state are important to understand neurological state and diagnose neural diseases. The gold standard to image myelination is direct observation using staining [2]. Various histochemistry methods have been developed and verified by comparing normal and impaired brains. However, the methods are not applicable to clinical studies due to invasiveness. Medical imaging devices, therefore, have drawn neurological and

neuropathological interests for noninvasive clinical diagnosis of myelin-related diseases such as multiple sclerosis (MS) [3–7] and schizophrenia [8–11].

Magnetic resonance imaging (MRI) provides apparent soft tissue contrast and various approaches have been developed for imaging myelin distribution using MRI. Myelin water imaging is an approach that utilizes short  $T_2$  decay of water in myelin sheath [12, 13]. The method assumes the measured decay curve to be weighted sum of multiexponential functions. A nonnegative least square algorithm plays a crucial role in converting the decay curves to  $T_2$  distribution and thus clearly separating myelin water signal from the other tissue water signals [5, 12–17]. However, long scan time per slice and long data processing time hinder its clinical applications. Other approaches for separation of myelin from other components based on faster decay of

myelin are  $T_2^*$ -based methods [7, 18] and a double inversion recovery method [19].

Another fast and efficient MRI approach for myelin imaging is magnetization transfer (MT). MT is a phenomenon of magnetization exchange between free water and proton bound to macromolecules. The exchange enables an RF pulse of off-resonance saturation to decrease signals in free water typically used in MR imaging, thereby indirectly providing information of proton bound to macromolecules. MT ratio (MTR) is typically measured for the MT techniques and has been used for appraising abnormality of brain structures, especially those related to myelination. MTR imaging offers noticeable sensitivity on white matter (WM), showing decreased signal on the myelinated regions in multiple sclerosis (MS) patients [4, 6, 20–22] and demyelinated animals [23–26]. The MTR method has advantages of shorter scan time and shorter postprocessing time than myelin water imaging. However, the MTR signal is not exclusively high in myelinated tissue, indicating low specificity. In other words, MTR can be generated by various pathophysiological components. The water concentration in multiple sclerosis lesions is induced by inflammatory activity and affects the MTR signal [24, 27]. Also, densely packed structure of biological tissue (i.e., skeletal muscle) has plenty of macromolecular bound protons resulting in high MTR signal [28].

In previous studies, the asymmetric MT effects around the water-resonance frequency have been reported [29–31]. Recently, a study proposed a possibility of imaging myelination by using asymmetric chemical exchange saturation transfer effect in the domain of Nuclear Overhauser Effects [32]. Another previous study directly measured extracted myelin in  $^1\text{H}$  NMR system and reported that myelin exhibits main peak at 3.5 ppm upfield from water-resonance frequency due to the chemical shift [33]. From these results, it is anticipated that taking advantage of the chemical shift as well as the MT strength (rather than the MT strength alone) would be beneficial to image myelination. This notion indicates that MT asymmetry (MTA) may be a better choice than the conventional MTR approach for improving the specificity of the myelin signals, by suppressing the MT signals from the nonmyelin tissues.

The goal of this study is to assess the sensitivity and specificity of the MTA approach for imaging myelination. We hypothesized that MTA imaging would provide better specificity to myelin than conventional MTR. For the MTA and MTR imaging, we used a new method, alternate ascending/descending directional navigation (ALADDIN), which enables us to acquire interslice perfusion-weighted and MTA images simultaneously [34–37], and MTR imaging was also performed through ALADDIN by additionally acquiring MT free images [38]. We investigated the contrast between WM and other brain tissues on various flip angles and compared the results of MTA to those of MTR. We also examined MTA and MTR in normal rats and demyelinated rats through the histogram analysis, which is typically used in the MTR studies [3, 4, 39, 40], in order to investigate the effects of the myelination state on the two MT measures of MTA and MTR.

## 2. Materials and Methods

**2.1. Animal Preparation.** Total 6 male Sprague-Dawley rats with 8–9 weeks of age were scanned in this study approved by the Institutional Animal Care and Use Committee at the Korea Basic Science Institute. Before MRI scan, rats were initially anesthetized by 5% isoflurane mixed with a 3:7 mixture of pure oxygen and nitrous oxide in a plastic box. The animals were then fixed in a cradle to minimize motion and the isoflurane level was decreased at 1.5% for anesthesia with a breath mask. The body temperature was maintained at around 37°C. After being placed inside the MRI system, the animals were monitored for the breath rate to be kept at 50–70 per minute by adjusting the isoflurane level at around 1.5%. To examine demyelination effects, 4 rats (2 control and 2 demyelinated rats) with 8 weeks of age were used for the MRI scans. For the 2 rats of demyelination, 0.2% (w/w) cuprizone (bis-cyclohexanone oxaldihydrazone, Sigma-Aldrich Inc., St. Louis, MO, USA) mixed into a ground standard rodent chow from 4 weeks to 8 weeks of age [41]. In order to study remyelination effects, the cuprizone administration was stopped for the demyelinated rats from 8 weeks of age (the first MRI study) to 9 weeks of age (for one week) and then the second MRI study was performed for the remyelinated rats.

**2.2. Data Acquisition.** All experiments were conducted on a 9.4 T Varian animal MRI system (Palo Alto, CA, USA) with a volume RF coil (a diameter of 72 mm) for both transmission and reception of the signals. All the MTA and MTR acquisitions were performed using ALADDIN based on balanced steady state free precession (bSSFP) readout, as described previously at low fields [34–36, 38]. Briefly, 4 different types of data were acquired by alternating the slice acquisition order (i.e., ascending and descending) and the slice-select gradient polarity (denoted as PosAsc, NegAsc, PosDes, and NegDes in Figure 1). The MTA was acquired by combining the 4 datasets to separate interslice MTA out of the interslice blood flow effects, as described in Figure 1 and also in the references [34, 36]. The readout gradient polarity was also alternated for averaging to suppress the effects of gradient imperfections, and thus eventually total 8 different types of data were acquired [34, 36].

**2.2.1. Flip Angle-Dependent Study.** To investigate the specificity of magnetization transfer signals of WM relative to the other brain tissues, 2 healthy male rats with 8–9 weeks of age were scanned using ALADDIN at various flip angles of 30°, 45°, and 60°. The imaging parameters were TR = 3.8 ms, TE = 1.9 ms, matrix size = 128 × 128, field of view = 30 × 30 mm<sup>2</sup>, number of slices = 21, phase cycle angle = 180°, slice thickness = 1 mm, phase over sampling = 0%–100%, and total scan time = 8.2–13.6 min. A large interslice gap (100% of the slice thickness) was used to avoid the crosstalk effects. The interslice offset frequency for the first prior slice was 6700 Hz corresponding to 16.7 ppm at 9.4 T. For MTR imaging, MT free acquisition was performed with interslice delay of 6

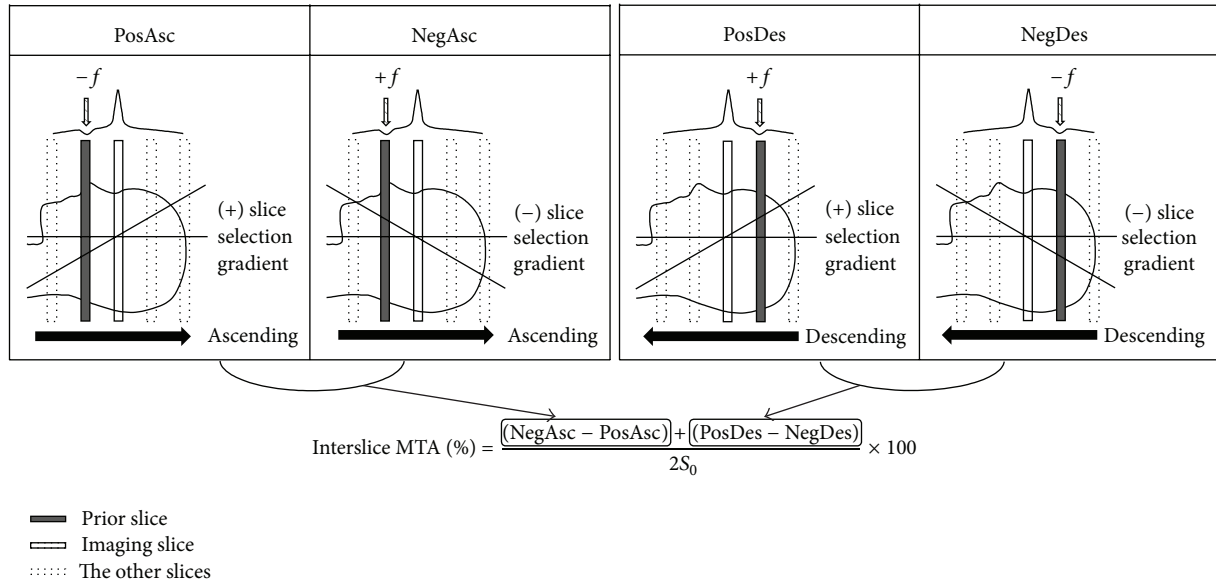


FIGURE 1: Alternate ascending/descending directional navigation (ALADDIN) data acquisition and reconstruction schemes used in this study. Four different types of data acquisition were sequentially performed by alternating the slice acquisition order (ascending and descending, “Asc” and “Des”) and the slice-selection gradient polarity (positive and negative, “Pos” and “Neg”). The on-resonance RF pulses for imaging the prior slices simultaneously act as off-resonance saturation pulses for the present imaging slice.  $f$  indicates the saturation offset frequency induced by the first prior slice. The four types of images (PosAsc, NegAsc, PosDes, and NegDes) are combined to generate an interslice MT asymmetry (MTA) image.  $S_0$  represents the average of the four types of images.

seconds for longitudinal magnetizations to recover back to the equilibrium state. The MT free scan was averaged once. MTR images were calculated using the formula:  $MTR (\%) = (S_0 - S_{MT})/S_0 \times 100$ , where  $S_0$  and  $S_{MT}$  stand for MT free and MT weighted images.  $S_{MT}$  was obtained by averaging the images from both positive and negative offset frequencies.

**2.2.2. Demyelination and Remyelination Effects on MT Signals.** The two demyelinated rats and the two control rats were scanned at 8 weeks of age. The remyelinated rats were scanned one week after the first MRI scan (i.e., 9 weeks of age). The scan parameters were similar to the above flip angle-dependent study except TR = 3.8–4.4 ms, TE = 1.9–2.2 ms, bandwidth = 64–100 kHz, matrix size = 128 × 128, flip angle = 60°, phase oversampling = 0%, and scan time per dataset = 31.1–37.8 min. The ALADDIN acquisitions were averaged 24 times, resulting in the number of repeated acquisitions of volume to be 192. Because of the long scan time, the water-resonance frequency was recalibrated every 3 repeated volume acquisitions to minimize  $B_0$  drift effects. MT free scan was averaged 4 times with interslice delay of 5 s.

**2.3. Data Processing and Analysis.** For each rat, we selected a slice of interest that included both corpus callosum (CC) and internal capsule (IC). The regions of interest (ROIs) were manually defined in CC, IC, GM, and muscle areas from each hemisphere using MATLAB, avoiding regions of banding artifacts ( $N = 4$  hemispheres for each group). Figure 2 presents the exemplary ROIs and slice of interest in a rat brain. All statistical analyses were performed based

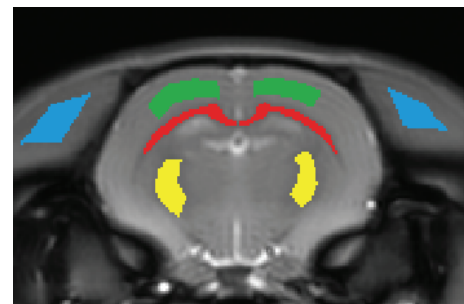


FIGURE 2: Regions of interest (ROIs) manually defined in each hemisphere from a baseline image. Red: corpus callosum (CC), yellow: internal capsule (IC), green: gray matter (GM), and blue: muscle. White matter (WM) ROI is combination of CC and IC.

on the average intensities within the ROIs by using one-tailed nonparametric tests at the significance level of  $\alpha = 0.1$  because of the small sample size.

In the flip angle-dependent study, average intensities were calculated within WM (CC + IC), GM, and muscle ROIs and then plotted as a function of flip angle. Subsequently, specificity was evaluated based on the definition that specificity is the proportion of negatives that are correctly measured. If a technique is prominently sensitive only to WM but not to tissues with no myelination (e.g., muscle), then it is considered having high specificity to myelination. The statistical significance was assessed between WM and GM as well as between WM and muscle on each flip angle by using the Wilcoxon signed rank test.

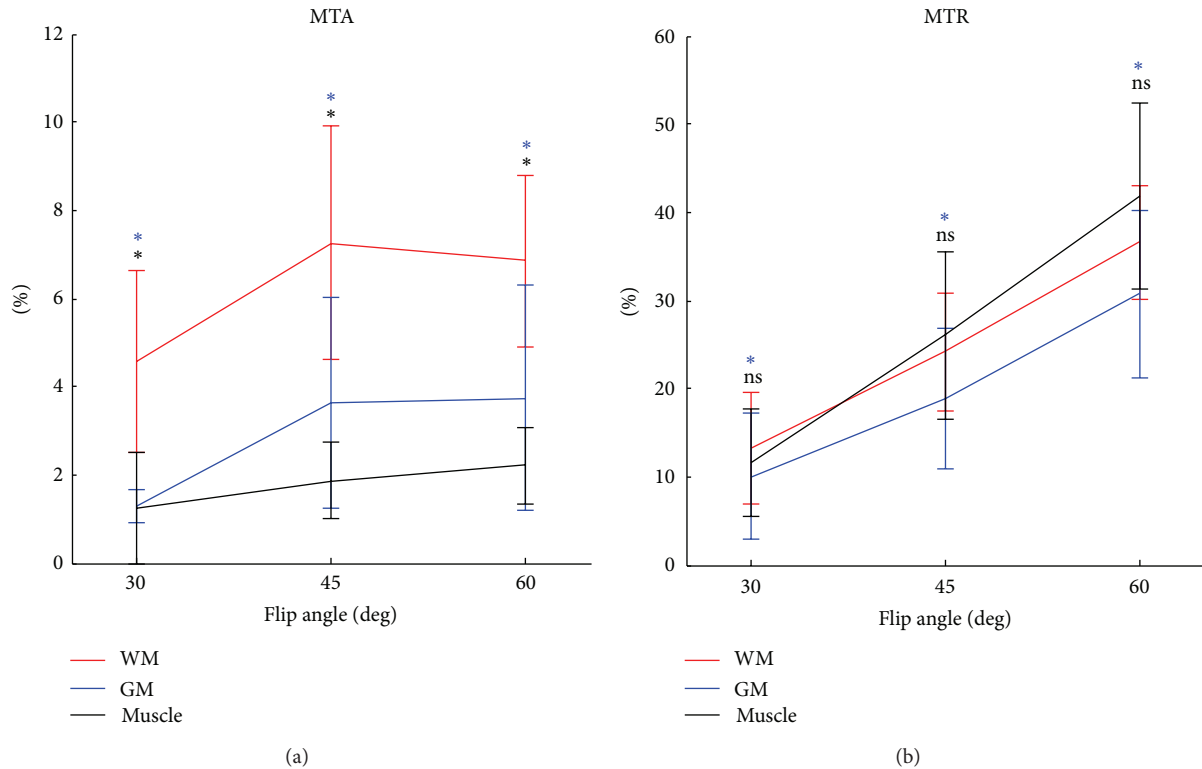


FIGURE 3: MT asymmetry (MTA) and MT ratio (MTR) plots as a function of flip angle. The error bars represent the range of one standard deviation. The blue and black asterisks (upper and lower rows, resp.) represent the significant differences between WM and GM and between WM and muscle, respectively. \*:  $p < 0.1$ , ns:  $p \geq 0.1$ .

In the study of demyelination and remyelination effects on the MT signals, histograms were obtained from the ROIs and normalized by the number of pixels within the ROI. Subsequently, the histograms of MTA and MTR from demyelinated rats and control rats were compared in regard to histogram shape, mean value, and standard deviation within the ROIs. Because most of the MTA and MTR signals were less than 15% and 45%, respectively, MTA and MTR histograms were plotted within ranges of 0%–15% and 0%–45%, respectively, with the same number of bins. Sensitivity was assessed for the demyelination and remyelination study. Sensitivity is the proportion of positives that are correctly measured. If changes in the myelin contents through demyelination and remyelination can be detected, the technique is considered having high sensitivity to myelination. Therefore, the statistical significance was assessed between demyelinated and control rats and between remyelinated and control rats in both WM and GM by using the Wilcoxon rank-sum test.

### 3. Results

**3.1. Flip Angle-Dependent Study.** Figure 3 shows the MTA and MTR signal intensities, which generally increased with flip angle in most cases. However, there were differences in the results of the ROI analysis between MTA and MTR. The MTA signals showed plateau or even decreased at 60°, whereas the MTR signals continuously increased with flip

angle. MTA showed much higher WM signals than GM and muscle, while MTR showed WM signals as high as muscle signals. The statistical tests showed that MTA discriminated WM from the other tissues, but MTR showed difference only between WM and GM (Figure 3), indicating that MTA is more specific to myelinated tissue than MTR. The visual inspection of the MTA and MTR images showed similar results (Figure 4). In the MTR images (the first row in Figure 4), WM signals were strong; however, GM and muscle signals were also not negligible. The MTA images (the second row of Figure 4) also showed higher intensities in WM but noticeably suppressed signals in the other tissue regions.

#### 3.2. Demyelination and Remyelination Effects on MT Signals.

Figures 5 and 6, respectively, show histograms from tissue regions of demyelinated and remyelinated rats in comparison with those of control rats. For both MTA and MTR, the histograms of demyelinated rats shifted left compared to those of the control rats, indicating signal decrease due to demyelination effects. In contrast to the results of demyelinated rat brains, the histograms from the remyelinated rats showed almost no difference from those of the control rats in both MTA and MTR (Figure 6), indicating signal recovery due to the remyelination effects.

The quantitative MTA and MTR values for the demyelinated, remyelinated, and control rats (Figure 7) were roughly in agreement with the histogram analysis. Both MTA and

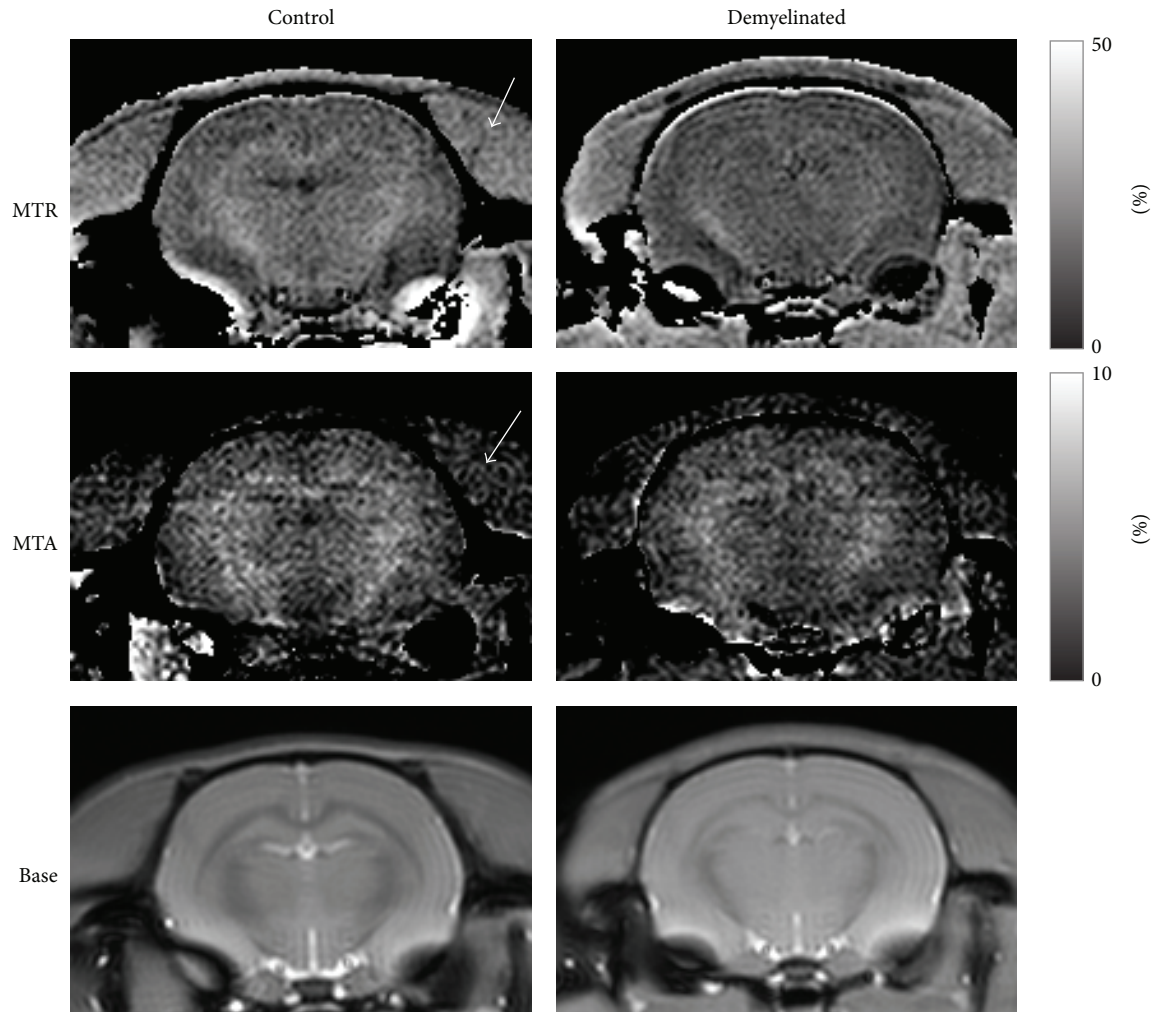


FIGURE 4: Representative MT asymmetry (MTA), MT ratio (MTR), and baseline (Base) images. Left and right columns correspond to images of control rats and demyelinated rats, respectively. The white arrow indicates the muscle region, where MTA and MTR signals are suppressed and enhanced, respectively.

MTR commonly show signal decrease from demyelination and signal increase from remyelination. However, the statistical results showed that MTA signal changes were significant only for WM whereas MTR signal changes were significant for both WM and GM except GM in the remyelinated rat brain (Figure 7).

#### 4. Discussion

The ROI analysis of the flip angle-dependent study and the visual inspection of the representative images indicate that MTA provides better WM specificity than MTR (Figures 3 and 4). Also, the demyelination and remyelination studies indicate that MTA has sensitivity to myelination as high as MTR (Figures 5–7). The MTA signal is derived from asymmetric MT spectrum, indicating that the strength of MT saturation effect is not symmetric around the water-resonance frequency. According to the previous studies, the saturation is stronger at the negative offset frequency

( $-f$ ) than the positive offset frequency ( $+f$ ), because of the negatively shifted MT spectrum of macromolecular proton pool in the central nervous system [11, 29–31].

High MTA can be achieved when the two conditions are satisfied: (i) the shift in the center of bound proton pool MT spectrum compared to free proton pool and (ii) strong MT saturation which depends on the tissue type. As shown in the result part, MTA exhibited noticeably high signals in WM and low signals in the other brain tissues. We can postulate that the distinction of WM in MTA method is due to a certain component prevalent in WM, but rare in GM and muscle. In the brain, myelin is a leading candidate for the main signal source of MTA, because myelin satisfies the two conditions above. First, myelin is mostly made up of lipid which forms a main peak centered at about 3.5 ppm upfield from water-resonance frequency in  $^1\text{H}$  NMR system due to the chemical shift [33]. About 80% of myelin is lipid and ~20% is protein [42]. The lipid composition is much higher in WM (49–66%) than in GM (36–40%). Therefore, the

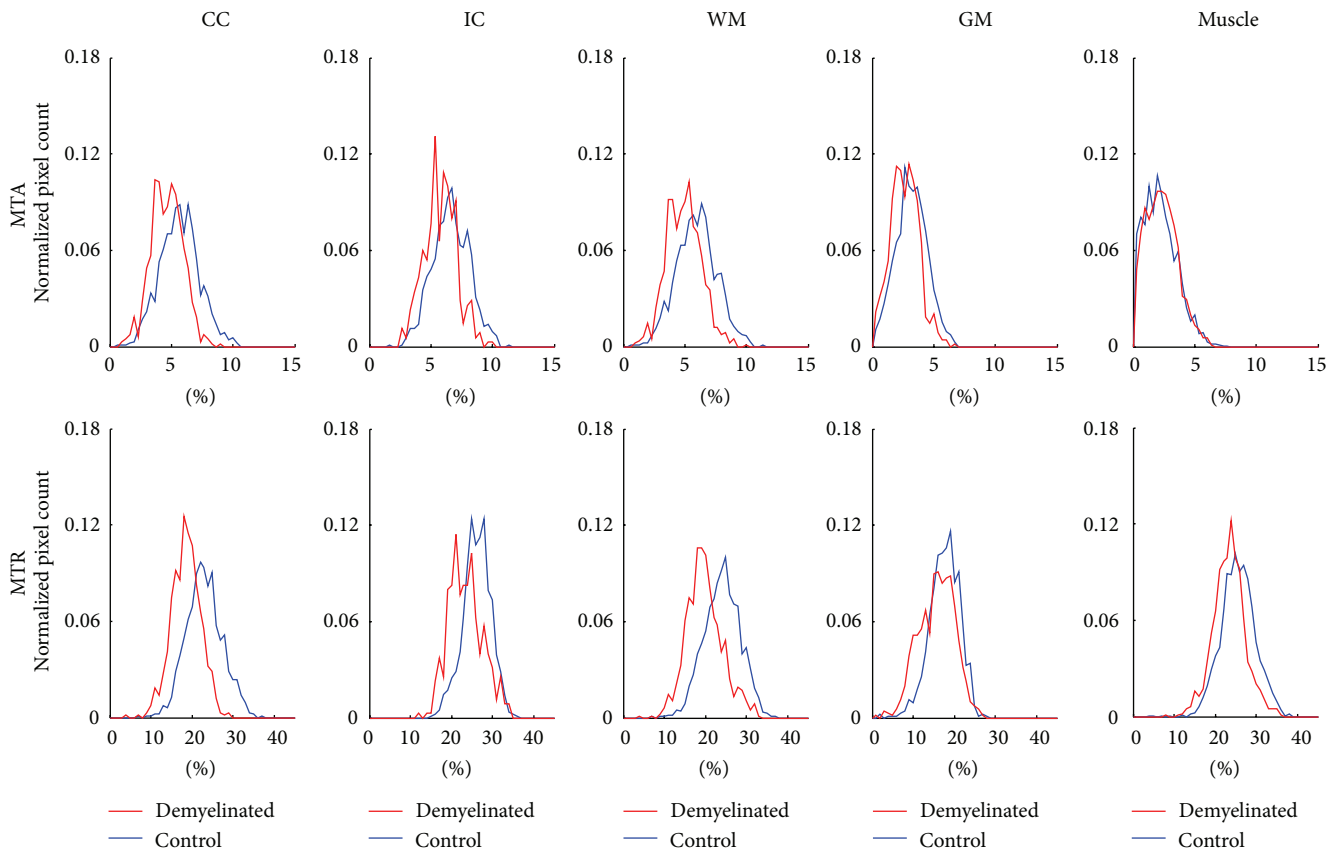


FIGURE 5: Normalized histogram results from demyelinated rats and control rats showing demyelination effects. CC: corpus callosum, IC: internal capsule, WM: white matter (CC + IC), and GM: gray matter.

exchange of magnetizations takes place mostly between water protons and lipid-bound aliphatic protons which compose the side chains of myelin. The interaction between free proton pool and aliphatic proton pool relates to Nuclear Overhauser Effects and provides broad contribution to the MT spectrum around  $-3.5$  ppm [32, 43]. Second, from previous studies about MTR, myelin is known to be sensitive to MT-related imaging techniques indicating that myelin has MT effects as high as or even stronger than those in the other brain tissues [39, 44, 45]. As a result, it is plausible that myelin property of the high lipid composition induces not only shift in MT spectrum of bound proton pool but also vast contribution of MT saturation, resulting in high MTA signal.

Sensitivity of MTA to myelination was demonstrated to be similar to that of MTR through the demyelination and remyelination studies (Figures 5–7). MTA successfully detected the change of myelination state caused by the cuprizone administration (Figure 5) and one week interval of no cuprizone administration (Figure 6) in the same manner as MTR, which is in agreement with the other MTR studies [25, 26, 46]. In this study, the MTR signal loss from cuprizone-induced demyelination was lower than that in other studies [25, 46, 47] and the MTR recovery from remyelination was relatively faster compared to the results of other studies [25,

26, 46]. It could be due to the fact that the dose of cuprizone in this study (0.2%), which has been typically adopted for demyelination of mice rather than rats [25, 26, 46, 48–50], was relatively lower than the dose used in the other studies for demyelination of rats [51, 52]. The remyelination effects observed in this study after one week of no cuprizone administration were generally in agreement with the previous studies, which reported significant remyelination shortly after the termination of cuprizone diet [48, 49, 53, 54].

Small signal changes in GM were observed with demyelination and remyelination for MTR (Figure 7). Similar signal changes in GM were also observed for MTA in the histogram analysis, despite being statistically not significant (Figure 7). This could be ascribed to the recovery of small amount of myelin in GM [55]. The oral administration of cuprizone might induce a global demyelination regardless of tissue types. The cuprizone-induced demyelination in cerebral cortex is found in another animal study with decrease of immunodetection [52]. Decreased MTR signal in GM was also reported in previous studies about MS patients [40, 56–58]. In a previous study with demyelinated and remyelinated mice [26], the MTR signal changes in deep GM reached statistical significance but those in the cerebral cortex (similar to GM in this study) were not significant, an observation

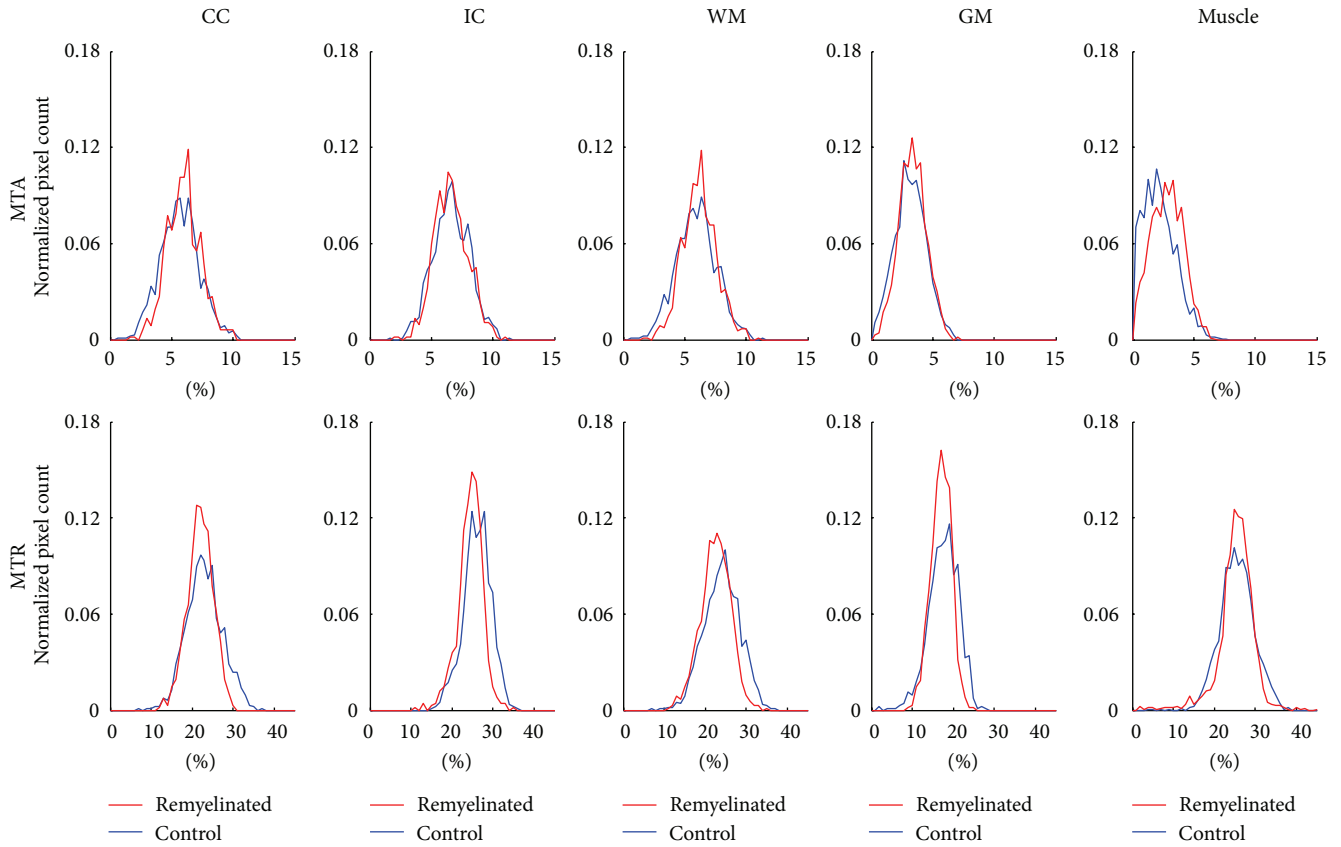


FIGURE 6: Normalized histogram results from remyelinated rats and control rats showing remyelination effects. CC: corpus callosum, IC: internal capsule, WM: white matter (CC + IC), and GM: gray matter.

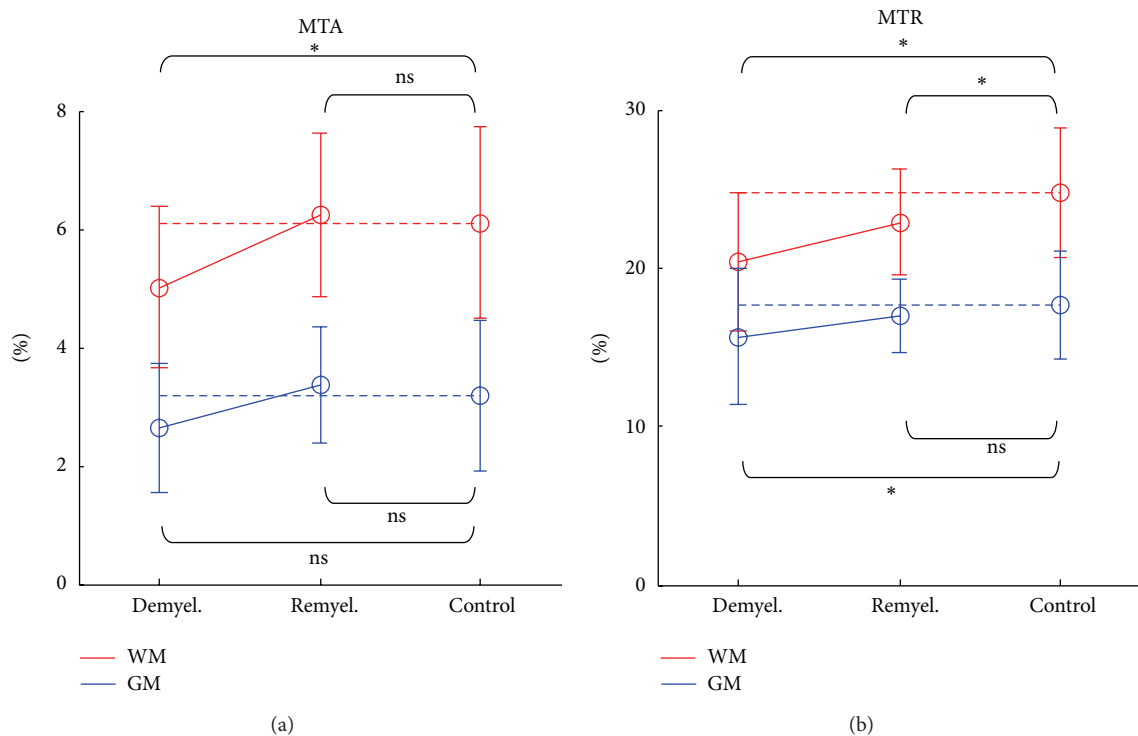


FIGURE 7: MT asymmetry (MTA) (a) and MT ratio (MTR) (b) values for demyelinated (Demyel.), remyelinated (Remyel.), and control rats. MTA and MTR are plotted in different intensity scales. WM: white matter, GM: gray matter. \*:  $p < 0.1$ , ns:  $p \geq 0.1$ .

slightly different from this study. Therefore, further studies are necessary to assess the significance of signal changes in GM associated with demyelination and remyelination.

The high MTR signal from muscle may be attributed to the unique structure of the muscle tissue. Muscle has numerous micromuscle fibers aligned in parallel that are surrounded by electrolyte, providing a suitable environment for transfer of magnetization. However, unlike the case of myelin, the MT effect does not mainly occur between lipid proton pool and free proton pool, resulting in mostly symmetric MT spectrum and thus low MTA signals.

When bSSFP readout is combined to interslice imaging method based on ALADDIN, the scan time can be effectively reduced because of the absence of MT presaturation period, which was already demonstrated in the clinical scanner [34, 36]. This advantage of ALADDIN may potentially facilitate clinical application of MTA in a reasonable scan time.

## 5. Conclusion

In this study, MTA was compared to conventional myelin imaging technique, MTR, in terms of imaging myelination. MTA imaging revealed high signal in WM and significantly low signals in GM and muscle, indicating better specificity than MTR. The demyelinated rats revealed apparent decrease of MTA and MTR signals, whereas remyelinated rats showed enhanced MTA and MTR signals comparable to those of normal rats. The main signal source of MTA in WM is presumed to be the MT effects occurring between free proton pool and lipid-bound proton pool associated with myelination. The experimental results indicate that MTA can be a good biomarker for imaging myelination with better specificity than and similar sensitivity to MTR. In addition, MTA images can be efficiently acquired with ALADDIN, which may accelerate clinical application of myelination imaging.

## Conflict of Interests

The authors declare that there is no conflict of interests regarding the publication of this paper.

## Acknowledgments

This work was supported by National Research Foundation of Korea (NRF-2013R1A1A1061759) and the Basic Science Research Program Grant (NRF-2014R1A2A2A01002608) funded by Ministry of Science, ICT and Future Planning.

## References

- [1] N. Baumann and D. Pham-Dinh, "Biology of oligodendrocyte and myelin in the mammalian central nervous system," *Physiological Reviews*, vol. 81, no. 2, pp. 871–927, 2001.
- [2] H. Klüver and E. Barrera, "A method for the combined staining of cells and fibers in the nervous system," *Journal of Neuro-pathology & Experimental Neurology*, vol. 12, no. 4, pp. 400–403, 1953.
- [3] J. L. Ostuni, N. D. Richert, B. K. Lewis, and J. A. Frank, "Characterization of differences between multiple sclerosis and normal brain: a global magnetization transfer application," *American Journal of Neuroradiology*, vol. 20, no. 3, pp. 501–507, 1999.
- [4] I. Catalaa, R. I. Grossman, D. L. Kolson et al., "Multiple sclerosis: magnetization transfer histogram analysis of segmented normal-appearing white matter," *Radiology*, vol. 216, no. 2, pp. 351–355, 2000.
- [5] C. Laule, I. M. Vavasour, G. R. Moore et al., "Water content and myelin water fraction in multiple sclerosis. A T2 relaxation study," *Journal of Neurology*, vol. 251, no. 3, pp. 284–293, 2004.
- [6] K. Schmierer, F. Scaravilli, D. R. Altmann, G. J. Barker, and D. H. Miller, "Magnetization transfer ratio and myelin in postmortem multiple sclerosis brain," *Annals of Neurology*, vol. 56, no. 3, pp. 407–415, 2004.
- [7] Y. P. Du, R. Chu, D. Hwang et al., "Fast multislice mapping of the myelin water fraction using multicompartiment analysis of T2\* decay at 3T: a preliminary postmortem study," *Magnetic Resonance in Medicine*, vol. 58, no. 5, pp. 865–870, 2007.
- [8] K. O. Lim, M. Hedehus, M. Moseley, A. de Crespigny, E. V. Sullivan, and A. Pfefferbaum, "Compromised white matter tract integrity in schizophrenia inferred from diffusion tensor imaging," *Archives of General Psychiatry*, vol. 56, no. 4, pp. 367–374, 1999.
- [9] J. Foong, M. Maier, G. J. Barker, S. Brocklehurst, D. H. Miller, and M. A. Ron, "In vivo investigation of white matter pathology in schizophrenia with magnetisation transfer imaging," *Journal of Neurology Neurosurgery & Psychiatry*, vol. 68, no. 1, pp. 70–74, 2000.
- [10] S. W. Flynn, D. J. Lang, A. L. Mackay et al., "Abnormalities of myelination in schizophrenia detected in vivo with MRI, and post-mortem with analysis of oligodendrocyte proteins," *Molecular Psychiatry*, vol. 8, no. 9, pp. 811–820, 2003.
- [11] F. Du, A. J. Cooper, T. Thida, A. K. Shinn, B. M. Cohen, and D. Öngür, "Myelin and axon abnormalities in schizophrenia measured with magnetic resonance imaging techniques," *Biological Psychiatry*, vol. 74, no. 6, pp. 451–457, 2013.
- [12] A. MacKay, K. Whittall, J. Adler, D. Li, D. Paty, and D. Graeb, "In vivo visualization of myelin water in brain by magnetic resonance," *Magnetic Resonance in Medicine*, vol. 31, no. 6, pp. 673–677, 1994.
- [13] K. P. Whittall, A. L. MacKay, D. A. Graeb, R. A. Nugent, D. K. B. Li, and D. W. Paty, "In vivo measurement of T2 distributions and water contents in normal human brain," *Magnetic Resonance in Medicine*, vol. 37, no. 1, pp. 34–43, 1997.
- [14] S. D. Wolff and R. S. Balaban, "Magnetization transfer contrast (MTC) and tissue water proton relaxation in vivo," *Magnetic Resonance in Medicine*, vol. 10, no. 1, pp. 135–144, 1989.
- [15] A. MacKay, C. Laule, I. Vavasour, T. Bjarnason, S. Kolind, and B. Mädler, "Insights into brain microstructure from the T2 distribution," *Magnetic Resonance Imaging*, vol. 24, no. 4, pp. 515–525, 2006.
- [16] C. Laule, P. Kozlowski, E. Leung, D. K. B. Li, A. L. MacKay, and G. R. W. Moore, "Myelin water imaging of multiple sclerosis at 7 T: correlations with histopathology," *NeuroImage*, vol. 40, no. 4, pp. 1575–1580, 2008.
- [17] S. H. Kolind, B. Mädler, S. Fischer, D. K. B. Li, and A. L. MacKay, "Myelin water imaging: implementation and development at 3.0T and comparison to 1.5T measurements," *Magnetic Resonance in Medicine*, vol. 62, no. 1, pp. 106–115, 2009.

- [18] D. Hwang, D.-H. Kim, and Y. P. Du, "In vivo multi-slice mapping of myelin water content using T2' decay," *NeuroImage*, vol. 52, no. 1, pp. 198–204, 2010.
- [19] S.-H. Oh, M. Bilello, M. Schindler, C. E. Markowitz, J. A. Detre, and J. Lee, "Direct visualization of short transverse relaxation time component (ViSTa)," *NeuroImage*, vol. 83, pp. 485–492, 2013.
- [20] L. A. Loevner, R. I. Grossman, J. A. Cohen, F. J. Lexa, D. Kessler, and D. L. Kolson, "Microscopic disease in normal-appearing white matter on conventional MR images in patients with multiple sclerosis: assessment with magnetization-transfer measurements," *Radiology*, vol. 196, no. 2, pp. 511–515, 1995.
- [21] G. B. Pike, N. De Stefano, S. Narayanan et al., "Multiple sclerosis: magnetization transfer MR imaging of white matter before lesion appearance on T2-weighted images," *Radiology*, vol. 215, no. 3, pp. 824–830, 2000.
- [22] S. Ropele, S. Strasser-Fuchs, M. Augustin et al., "A comparison of magnetization transfer ratio, magnetization transfer rate, and the native relaxation time of water protons related to relapsing-remitting multiple sclerosis," *The American Journal of Neuroradiology*, vol. 21, no. 10, pp. 1885–1891, 2000.
- [23] M. S. A. Deloire-Grassin, B. Brochet, B. Quesson et al., "In vivo evaluation of remyelination in rat brain by magnetization transfer imaging," *Journal of the Neurological Sciences*, vol. 178, no. 1, pp. 10–16, 2000.
- [24] P. J. Gareau, B. K. Rutt, S. J. Karlik, and J. R. Mitchell, "Magnetization transfer and multicomponent T2 relaxation measurements with histopathologic correlation in an experimental model of MS," *Journal of Magnetic Resonance Imaging*, vol. 11, no. 6, pp. 586–595, 2000.
- [25] W. Zaaraoui, M. Deloire, M. Merle et al., "Monitoring demyelination and remyelination by magnetization transfer imaging in the mouse brain at 9.4 T," *Magnetic Resonance Materials in Physics, Biology and Medicine*, vol. 21, no. 5, pp. 357–362, 2008.
- [26] S. Fjær, L. Bø, A. Lundervold et al., "Deep gray matter demyelination detected by magnetization transfer ratio in the cuprizone model," *PLoS ONE*, vol. 8, no. 12, Article ID e84162, 2013.
- [27] I. M. Vavasour, C. Laule, D. K. B. Li, A. L. Traboulsee, and A. L. MacKay, "Is the magnetization transfer ratio a marker for myelin in multiple sclerosis?" *Journal of Magnetic Resonance Imaging*, vol. 33, no. 3, pp. 710–718, 2011.
- [28] D. M. Yousem, M. D. Schnall, L. Dougherty, G. S. Weinstein, and R. E. Hayden, "Magnetization transfer imaging of the head and neck: normative data," *American Journal of Neuroradiology*, vol. 15, no. 6, pp. 1117–1121, 1994.
- [29] J. Pekar, P. Jezzard, D. A. Roberts, J. S. Leigh Jr., J. A. Frank, and A. G. McLaughlin, "Perfusion imaging with compensation for asymmetric magnetization transfer effects," *Magnetic Resonance in Medicine*, vol. 35, no. 1, pp. 70–79, 1996.
- [30] J. Hua, C. K. Jones, J. Blakeley, S. A. Smith, P. C. M. van Zijl, and J. Zhou, "Quantitative description of the asymmetry in magnetization transfer effects around the water resonance in the human brain," *Magnetic Resonance in Medicine*, vol. 58, no. 4, pp. 786–793, 2007.
- [31] M.-C. Ng, J. Hua, Y. Hu, K. D. Luk, and E. Y. Lam, "Magnetization transfer (MT) asymmetry around the water resonance in human cervical spinal cord," *Journal of Magnetic Resonance Imaging*, vol. 29, no. 3, pp. 523–528, 2009.
- [32] O. Mougin, M. Clemence, A. Peters, A. Pitiot, and P. Gowland, "High-resolution imaging of magnetisation transfer and nuclear Overhauser effect in the human visual cortex at 7 T," *NMR in Biomedicine*, vol. 26, no. 11, pp. 1508–1517, 2013.
- [33] M. J. Wilhelm, H. H. Ong, S. L. Wehrli et al., "Direct magnetic resonance detection of myelin and prospects for quantitative imaging of myelin density," *Proceedings of the National Academy of Sciences of the United States of America*, vol. 109, no. 24, pp. 9605–9610, 2012.
- [34] S.-H. Park and T. Q. Duong, "Alternate ascending/descending directional navigation approach for imaging magnetization transfer asymmetry," *Magnetic Resonance in Medicine*, vol. 65, no. 6, pp. 1702–1710, 2011.
- [35] S.-H. Park and T. Q. Duong, "Brain MR perfusion-weighted imaging with alternate ascending/descending directional navigation," *Magnetic Resonance in Medicine*, vol. 65, no. 6, pp. 1578–1591, 2011.
- [36] S.-H. Park, T. Zhao, J.-H. Kim, F. E. Boada, and K. T. Bae, "Suppression of effects of gradient imperfections on imaging with alternate ascending/descending directional navigation," *Magnetic Resonance in Medicine*, vol. 68, no. 5, pp. 1600–1606, 2012.
- [37] S. H. Park, P. K. Han, and S. H. Choi, "Physiological and functional magnetic resonance imaging using balanced steady-state free precession," *Korean Journal of Radiology*, vol. 16, no. 3, pp. 550–559, 2015.
- [38] J. W. Barker, P. K. Han, S. H. Choi, K. T. Bae, and S.-H. Park, "Investigation of inter-slice magnetization transfer effects as a new method for MTR imaging of the human brain," *PLoS ONE*, vol. 10, no. 2, Article ID e0117101, 2015.
- [39] M. A. van Buchem, J. C. McGowan, D. L. Kolson, M. Polansky, and R. I. Grossman, "Quantitative volumetric magnetization transfer analysis in multiple sclerosis: estimation of macroscopic and microscopic disease burden," *Magnetic Resonance in Medicine*, vol. 36, no. 4, pp. 632–636, 1996.
- [40] L. K. Fisniku, D. R. Altmann, M. Cercignani et al., "Magnetization transfer ratio abnormalities reflect clinically relevant grey matter damage in multiple sclerosis," *Multiple Sclerosis*, vol. 15, no. 6, pp. 668–677, 2009.
- [41] J. R. Gregg, N. R. Herring, A. V. Naydenov, R. P. Hanlin, and C. Konradi, "Downregulation of oligodendrocyte transcripts is associated with impaired prefrontal cortex function in rats," *Schizophrenia Research*, vol. 113, no. 2-3, pp. 277–287, 2009.
- [42] J. S. O'Brien and E. L. Sampson, "Lipid composition of the normal human brain: gray matter, white matter, and myelin," *Journal of Lipid Research*, vol. 6, no. 4, pp. 537–544, 1965.
- [43] D. Liu, J. Zhou, R. Xue, Z. Zuo, J. An, and D. J. J. Wang, "Quantitative characterization of nuclear overhauser enhancement and amide proton transfer effects in the human brain at 7 tesla," *Magnetic Resonance in Medicine*, vol. 70, no. 4, pp. 1070–1081, 2013.
- [44] R. I. Grossman, "Magnetization transfer in multiple sclerosis," *Annals of Neurology*, vol. 36, supplement 1, pp. S97–S99, 1994.
- [45] M. A. Van Buchem, S. C. A. Steens, H. A. Vrooman et al., "Global estimation of myelination in the developing brain on the basis of magnetization transfer imaging: a preliminary study," *American Journal of Neuroradiology*, vol. 22, no. 4, pp. 762–766, 2001.
- [46] D. Merkler, S. Boretius, C. Stadelmann et al., "Multicontrast MRI of remyelination in the central nervous system," *NMR in Biomedicine*, vol. 18, no. 6, pp. 395–403, 2005.
- [47] J. D. Thiessen, Y. Zhang, H. Zhang et al., "Quantitative MRI and ultrastructural examination of the cuprizone mouse model of demyelination," *NMR in Biomedicine*, vol. 26, no. 11, pp. 1562–1581, 2013.
- [48] M. Lindner, J. Fokuhl, F. Linsmeier, C. Trebst, and M. Stangel, "Chronic toxic demyelination in the central nervous system

- leads to axonal damage despite remyelination,” *Neuroscience Letters*, vol. 453, no. 2, pp. 120–125, 2009.
- [49] P. Morell, C. V. Barrett, J. L. Mason et al., “Gene expression in brain during cuprizone-induced demyelination and remyelination,” *Molecular and Cellular Neurosciences*, vol. 12, no. 4-5, pp. 220–227, 1998.
- [50] Ø. Torkildsen, L. A. Brunborg, K.-M. Myhr, and L. Bø, “The cuprizone model for demyelination,” *Acta Neurologica Scandinavica*, vol. 117, no. 188, pp. 72–76, 2008.
- [51] P. G. Franco, L. Silvestroff, E. F. Soto, and J. M. Pasquini, “Thyroid hormones promote differentiation of oligodendrocyte progenitor cells and improve remyelination after cuprizone-induced demyelination,” *Experimental Neurology*, vol. 212, no. 2, pp. 458–467, 2008.
- [52] L. Silvestroff, S. Bartucci, J. Pasquini, and P. Franco, “Cuprizone-induced demyelination in the rat cerebral cortex and thyroid hormone effects on cortical remyelination,” *Experimental Neurology*, vol. 235, no. 1, pp. 357–367, 2012.
- [53] A. M. Adamo, P. M. Paez, O. E. Escobar Cabrera et al., “Remyelination after cuprizone-induced demyelination in the rat is stimulated by apotransferrin,” *Experimental Neurology*, vol. 198, no. 2, pp. 519–529, 2006.
- [54] G. K. Matsushima and P. Morell, “The neurotoxicant, cuprizone, as a model to study demyelination and remyelination in the central nervous system,” *Brain Pathology*, vol. 11, no. 1, pp. 107–116, 2001.
- [55] K. Suzuki, J. F. Poduslo, and S. E. Poduslo, “Further evidence for a specific ganglioside fraction closely associated with myelin,” *Biochimica et Biophysica Acta—Lipids and Lipid Metabolism*, vol. 152, no. 3, pp. 576–586, 1968.
- [56] B. Audoin, G. Davies, W. Rashid, L. Fisniku, A. J. Thompson, and D. H. Miller, “Voxel-based analysis of grey matter magnetization transfer ratio maps in early relapsing remitting multiple sclerosis,” *Multiple Sclerosis*, vol. 13, no. 4, pp. 483–489, 2007.
- [57] Y. Ge, R. I. Grossman, J. K. Udupa, J. S. Babb, D. L. Kolson, and J. C. McGowan, “Magnetization transfer ratio histogram analysis of gray matter in relapsing-remitting multiple sclerosis,” *American Journal of Neuroradiology*, vol. 22, no. 3, pp. 470–475, 2001.
- [58] Y. Ge, R. I. Grossman, J. K. Udupa, J. S. Babb, L. J. Mannon, and J. C. McGowan, “Magnetization transfer ratio histogram analysis of normal-appearing gray matter and normal-appearing white matter in multiple sclerosis,” *Journal of Computer Assisted Tomography*, vol. 26, no. 1, pp. 62–68, 2002.

## Research Article

# Volumetric Growth of the Liver in the Human Fetus: An Anatomical, Hydrostatic, and Statistical Study

Michał Szpinda,<sup>1</sup> Monika Paruszevska-Achtel,<sup>1</sup>  
Alina Woźniak,<sup>2</sup> Celestyna Mila-Kierzenkowska,<sup>2</sup> Gabriela Elminowska-Wenda,<sup>1</sup>  
Małgorzata Dombek,<sup>1</sup> Anna Szpinda,<sup>1</sup> and Mateusz Badura<sup>1</sup>

<sup>1</sup>Department of Normal Anatomy, Collegium Medicum of Nicolaus Copernicus University, Łukasiewicza 1 Street, 85-821 Bydgoszcz, Poland

<sup>2</sup>Department of Medical Biology, Collegium Medicum of Nicolaus Copernicus University, Karłowicza 24 Street, 85-092 Bydgoszcz, Poland

Correspondence should be addressed to Michał Szpinda; kizanat@cm.umk.pl

Received 12 February 2015; Revised 30 March 2015; Accepted 6 April 2015

Academic Editor: Tuncay Peker

Copyright © 2015 Michał Szpinda et al. This is an open access article distributed under the Creative Commons Attribution License, which permits unrestricted use, distribution, and reproduction in any medium, provided the original work is properly cited.

Using anatomical, hydrostatic, and statistical methods, liver volumes were assessed in 69 human fetuses of both sexes aged 18–30 weeks. No sex differences were found. The median of liver volume achieved by hydrostatic measurements increased from 6.57 cm<sup>3</sup> at 18–21 weeks through 14.36 cm<sup>3</sup> at 22–25 weeks to 20.77 cm<sup>3</sup> at 26–30 weeks, according to the following regression:  $y = -26.95 + 1.74 \times \text{age} \pm Z \times (-3.15 + 0.27 \times \text{age})$ . The median of liver volume calculated indirectly according to the formula liver volume = 0.55 × liver length × liver transverse diameter × liver sagittal diameter increased from 12.41 cm<sup>3</sup> at 18–21 weeks through 28.21 cm<sup>3</sup> at 22–25 weeks to 49.69 cm<sup>3</sup> at 26–30 weeks. There was a strong relationship ( $r = 0.91$ ,  $p < 0.001$ ) between the liver volumes achieved by hydrostatic ( $x$ ) and indirect ( $y$ ) methods, expressed by  $y = -0.05 + 2.16x \pm 7.26$ . The liver volume should be calculated as follows liver volume = 0.26 × liver length × liver transverse diameter × liver sagittal diameter. The age-specific liver volumes are of great relevance in the evaluation of the normal hepatic growth and the early diagnosis of fetal micro- and macrosomias.

## 1. Introduction

Since the fetal liver is a pivotal organ involved in fetoplacental metabolism, the assessment of liver volume is indispensable to satisfactory understanding of fetal physiology and the status of fetal growth and nutrition [1]. Aberrant fetal growth directly results in disparate alterations of fetal liver volume [2]. In pregnancy complicated by maternal insulin-dependent diabetes mellitus, the fetal liver volume accelerates by approximately 20% at every week of gestation when compared with normal controls [2]. In fetuses at 11 to 13 weeks with trisomy 21, the liver volume is considerably increased [3, 4]. On the other hand, significantly decreased liver volumes are typical of fetuses with growth restriction [5–8]. Determination of fetal liver volume *in utero* can mainly be achieved by preferable three-dimensional ultrasound, including either multiplanar or VOCAL (Virtual Organ Computer-Aided

Analysis) techniques [3, 9], and sporadically by MRI, a costly method of low acceptability in pregnant women [10, 11]. To date, the liver volume of normal fetuses measured by 3D ultrasound has been found to increase disparately, from a linear function with age [12], through a log linear relationship [2] or a third-order polynomial regression with age [1] to an exponential model with crown-rump length [3] and with gestational age [13].

The current paper caps the morphometric investigation of the fetal liver, some outcomes of which concerning liver length and transverse and sagittal diameters have recently been published in the Surgical and Radiologic Anatomy [14]. To date, however, no nomograms have been computed by means of detailed direct measurements of liver volume in the human fetus. A limited number of articles focused on the liver volume accomplished indirectly by measurements of liver length and

transverse and sagittal diameters in accordance with the two empirical formulae: liver volume =  $0.45 \times \text{length} \times \text{transverse diameter} \times \text{sagittal diameter}$  [15] or liver volume =  $0.55 \times \text{length} \times \text{transverse diameter} \times \text{sagittal diameter}$  [16]. In the light of the recently published INTERGROWTH-21st Project [17], in this study we aimed to concentrate on

- (i) age-specific references for liver volume at varying gestational ages,
- (ii) possible sex differences in liver volume,
- (iii) the 3rd, 10th, 50th, 90th, and 97th smoothed centile curves for the liver volume over time (optimal growth curve),
- (iv) the relationship between liver volumes for the 50th centile measured directly and those calculated indirectly on the base of liver length and transverse and sagittal diameters.

## 2. Materials and Methods

The examinations were executed in the Department of Anatomy of the Ludwik Rydygier Collegium Medicum in Bydgoszcz. The current study was carried out on 69 autopsied formalin-fixed human fetuses of both sexes (32 male, 37 female) aged 18–30 ( $23.35 \pm 3.39$ ) weeks of Caucasian ethnic origin (Table 1), gathered in the years 1989–1999 from spontaneous miscarriages or stillbirths. First of all, fetuses from diabetic or manifold gravidities and fetuses affected by innate and chromosomal abnormalities or intrauterine growth restriction were omitted from the study. So, the sample included fetuses that could be considered as normal. Legitimate and moral dilemmas were granted by the Collegium Medicum Research Ethics Committee (KB 161/2013). According to the INTERGROWTH-21st Project, the fetal ages in weeks were precisely elaborated owing to the three subsequent criteria: (1) the fetal crown-rump length, (2) identified date of the start of the last motherly menstrual period, and (3) a combination of known values of the five fetal anthropometric measurements: head circumference, biparietal diameter, occipitofrontal diameter, abdominal circumference, and femur length assessed by early second-trimester ultrasound scan (ultrasound age) [14, 17]. The crown-rump length was measured with the use of a flexible caliper from the top of the head (crown) to the bottom of the buttocks (rump) of the fetus in its natural C-shaped position [18].

**2.1. Anatomical Method.** After having been immersed for 12–24 months in 10% neutral buffered formalin solution, the fetuses were subjected to anatomical dissection by both median and transverse laparotomies under 10-fold magnification with the use of a stereoscope with Huygens ocular. By cutting off peritoneal ligaments, diaphragm, inferior vena cava, and structures at the porta hepatis, the liver was freed and removed out of the abdominal cavity.

**2.2. Hydrostatic Method.** Subsequently, every isolated liver as an object of multifaceted form was subjected to direct volumetric analysis, with the use of a hydrostatic method,

TABLE 1: Distribution of the fetuses examined.

Fetal age [weeks]	Crown-rump length [mm]			<i>n</i>	Sex	
	Median	Minimum	Maximum		Males	Females
18	139.5	131.0	143.0	4	3	1
19	152.5	145.0	155.0	6	4	2
20	161.0	159.0	167.0	7	3	4
21	175.0	170.0	180.0	7	5	2
22	185.5	181.0	190.0	6	1	5
23	199.5	195.0	204.0	6	4	2
24	212.0	205.0	214.0	10	2	8
25	215.0	215.0	220.0	5	2	3
26	233.0	225.0	233.0	3	1	2
27	240.5	235.0	242.0	4	2	2
28	253.0	247.0	253.0	7	1	6
30	264.0	263.0	265.0	4	4	0

Note: for anatomists dealing with fetuses, the most objective information for establishing fetal ages is the crown-rump length, when compared to the known data of the beginning of the last maternal menstrual period or to ultrasonic measurements of head circumference, biparietal diameter, occipitofrontal diameter, abdominal circumference, and femur length.

grounded in Archimedes' principle [19]. Therefore, the liver submerged in water loses weight quantitatively tantamount to the weight of the water displaced by the liver. Consequently, a dual weighing method (Figure 1) was then used to acquire the weight (in g) of the liver in air ( $W_A$ ) and in distillate water ( $W_W$ ), taking into account the specific gravity (in  $\text{g}/\text{cm}^3$ ) of water ( $G_W$ ) and air ( $G_A$ ) in the range of temperature between 14 and 20°C [19]. Thus, for every fetus, the liver volume in  $\text{cm}^3$  ( $V$ ) was accurately calculated by the succeeding formula:  $V = W_A - W_W / G_W - G_A$ . Of note, notwithstanding that both  $W_A$  and  $W_W$  are considerably influenced by formalin fixation, the difference between these two expressed in the nominator ( $W_A - W_W$ ) is utterly unfettered by the weight gain of formalin-fixed structures. Furthermore, we calculated the liver volume, extrapolated through a series of indirect, previously achieved measurements [14], according to the following formula: liver volume =  $0.55 \times \text{liver length} \times \text{liver transverse diameter} \times \text{liver sagittal diameter}$ .

**2.3. Statistical Analysis.** In an unceasing attempt at minimizing measurement and observer bias, all the measurements were performed by one investigator (Monika Paruszevska-Achtel). Each measurement was executed three times ( $V_1, V_2, V_3$ ) under the same circumstances but at different times, and the average was involved in individual numerical data. In the current study, the statistical program *Statistica 10* was used. The intraobserver variation between the reiterated measurements was evaluated by ANOVA for repeated measurements and post hoc RIR Tukey test. The numerical data were verified for normality of distribution (Shapiro-Wilk's test) and for homogeneity of variance (Levene's test). As the first step of the statistical analysis, the Mann-Whitney  $U$  test for unpaired variables was preferred to evaluate the likelihood of appearance of statistically significant differences

TABLE 2: Liver volumes in both sexes measured directly by a hydrostatic method.

Fetal age [weeks]	n	Liver volume [cm <sup>3</sup> ]						p value
		Males			Females			
		Median	Minimum	Maximum	Median	Minimum	Maximum	
18–21	24	6.46	2.23	12.14	10.31	4.94	13.24	0.128
22–25	27	15.41	6.58	25.93	14.21	7.46	26.30	0.758
26–30	18	21.48	17.36	32.10	20.77	14.95	29.54	0.477
18–30	69	11.60	2.23	32.10	14.36	4.94	29.54	0.166

TABLE 3: Liver volumes measured directly by a hydrostatic method and calculated indirectly through a series of indirect, previously achieved measurements, according to the following formula: liver volume = 0.55 × length × transverse diameter × sagittal diameter.

Fetal age [weeks]	n	Liver volume [cm <sup>3</sup> ]					
		Measured directly by a hydrostatic method based on Archimedes' patent			Calculated indirectly according to the following formula: liver volume = 0.55 × length × transverse diameter × sagittal diameter		
		Median	Minimum	Maximum	Median	Minimum	Maximum
18–21	24	6.57 <sup>(1)</sup>	2.23	13.24	12.41 <sup>(a)</sup>	4.02	28.51
22–25	27	14.36 <sup>(2)</sup>	6.58	26.30	28.21 <sup>(b)</sup>	16.17	49.60
26–30	18	20.77 <sup>(3)</sup>	14.95	32.10	49.69 <sup>(c)</sup>	31.68	80.96

Note: liver volumes measured directly differ significantly in columns as follows: for (1) versus (2),  $p < 0.001$ ; for (1) versus (3),  $p < 0.001$ ; and for (2) versus (3),  $p = 0.007$ .

Liver volumes calculated indirectly differ significantly in columns as follows: for (a) versus (b),  $p < 0.001$ ; for (a) versus (c),  $p < 0.001$ ; and for (b) versus (c),  $p = 0.003$ .

Liver volumes measured directly and calculated indirectly differ significantly in rows: for (1) versus (a), (2) versus (b), and (3) versus (c),  $p < 0.001$ .



FIGURE 1: A double weighing procedure to obtain the weight of the liver in air (a) and distillate water (b).

in values with relation to sex. Since the fetuses studied were collected into 12 one-week intervals inadequately dispersed with fetal age, the first four intervals (18–21 weeks), the consecutive four intervals (22–25 weeks), and the last four intervals (26–30 weeks) were aggregated. At first, we tested sex differences between the three forenamed age groups, 18–21 ( $n = 24$ ), 22–25 ( $n = 27$ ), and 26–30 ( $n = 18$ ) weeks, and later for the whole sample. Having considered the sample size of the groups, the Kruskal Wallis test for unpaired data proved

to be more appropriate for comparisons to check whether significant differences in liver volume occurred with fetal age. The algebraic volumetric data were correlated to fetal age, and linear and nonlinear regression analysis were used to achieve the specific best-fit growth curve for liver volume against fetal age. The creation of charts of the liver volume followed the Altman-Chitty method [14, 18]. In such a way, we established the mean, standard deviation, and the five centiles (3rd, 10th, 50th, 90th, and 97th) for liver volume at each gestational age. After that, the 3rd, 10th, 50th, 90th, and 97th smoothed centile curves for the liver volume *versus* gestational age were computed. Linear regression analysis was used to examine the relationship between the liver volumes obtained directly and indirectly. Typically, statistically significant differences were deliberated at  $p < 0.05$ .

### 3. Results

No statistically significant difference ( $p = 0.291$ ) was found in evaluating intraobserver reproducibility of three liver volume measurements that in the fetuses aged 18–30 weeks averaged  $V_1 = 14.20 \pm 7.09 \text{ cm}^3$ ,  $V_2 = 14.00 \pm 6.86 \text{ cm}^3$ , and  $V_3 = 14.01 \pm 6.91 \text{ cm}^3$ , respectively. Since no significant sex difference was observed in liver volume (Table 2), no attempt was made to further separate the results obtained according to males and females. Therefore, both its direct measurements and its indirect calculations have been collectively summarized for both sexes in Table 3. Obviously, having previously been published, the three aforementioned morphometric parameters of the liver [14], namely, its length

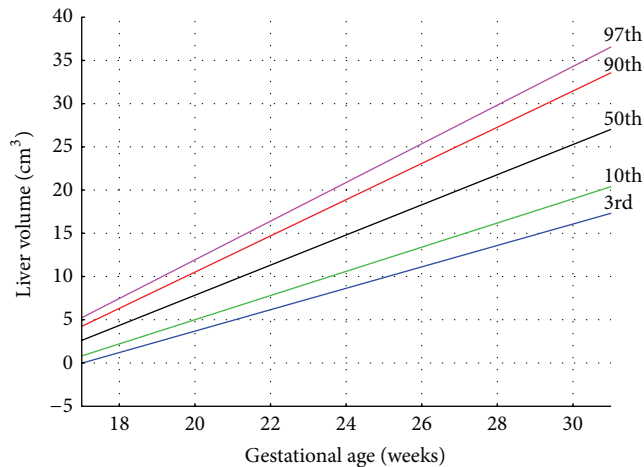


FIGURE 2: The 3rd, 10th, 50th, 90th, and 97th smoothed centiles for liver volume versus gestational age.

and transverse and sagittal diameters, were excluded from Table 3. On the contrary, a statistically significant increase in liver volume was found in fetuses aged 18–21, 22–25, and 26–30 weeks.

The median value of liver volume achieved by direct hydrostatic measurements was found to increase from  $6.57 \text{ cm}^3$  at the age of 18–21 weeks through  $14.36 \text{ cm}^3$  in fetuses aged 22–25 weeks to  $20.77 \text{ cm}^3$  at 26–30 weeks of gestation. The best suitable curves for the liver volume were presented in the following five cutoff points: 3rd, 10th, 50th, 90th, and 97th centiles (Figure 2). The two corresponding formulae for the estimation of the mean and SD (in  $\text{cm}^3$ ) of liver volume in accordance with gestational age (in weeks) were displayed as follows: “ $-26.95 + 1.74 \times \text{age}$ ” and “ $-3.15 + 0.27 \times \text{age}$ ,” respectively. The specific centiles were calculated as “ $\text{mean} \pm Z \times \text{SD}$ .” From a statistical point of view, the value of  $Z$  depends on a particular centile and constantly equals  $-1.88$  for the 3rd centile,  $-1.28$  for the 10th centile,  $0$  for the 50th centile,  $+1.28$  for the 90th centile, and  $+1.88$  for the 97th centile [17]. Thus, the values of liver volume for particular centiles in relation to gestational age in weeks were calculated by the following linear regressions:  $y = -26.95 + 1.74 \times \text{age} \pm Z \times (-3.15 + 0.27 \times \text{age})$ . It is noteworthy that the whole model (statistics  $F$ ) and its parameters were statistically significant ( $p < 0.001$ ). According to this formula, for the 50th centile ( $Z$  equals 0), the fetal liver volume grew proportionately during the study period at a rate of  $1.74 \text{ cm}^3$  per week. Of note, the coefficient of determination ( $r^2$ ) for the 50th centile reached the value of 0.79.

On the other hand, during the study period, the median value of liver volume (equivalent to the 50th centile) calculated indirectly according to the formula  $\text{liver volume} = 0.55 \times \text{liver length} \times \text{liver transverse diameter} \times \text{liver sagittal diameter}$  increased from  $12.41 \text{ cm}^3$  at 18–21 weeks through  $28.21 \text{ cm}^3$  at 22–25 weeks to  $49.69 \text{ cm}^3$  at 26–30 weeks. The calculated liver volume considerably predominated over the measured 50-centile liver volume. The measured-to-calculated liver volume ratio for the 50th centile attained the

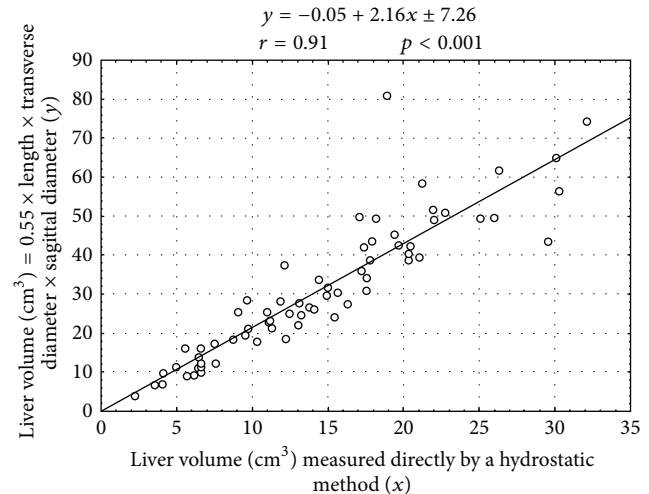


FIGURE 3: Linear relationship between the liver volumes for the 50th centile achieved by the two methods.

value of  $0.48 \pm 0.08$  throughout the analyzed period. There was a strong relationship ( $r = 0.91$ ,  $p < 0.001$ ) between the liver volumes for the 50th centile (Figure 3), achieved by hydrostatic ( $x$ ) and indirect ( $y$ ) methods, expressed by the following linear function:  $y = -0.05 + 2.16x \pm 7.26$ , where “ $\pm 7.26$ ” meant the standard error of the estimate. In order to obtain equal values of liver volume in both methods, a constant of 0.55 should be substituted with 0.26 (in brief,  $0.55 \times 0.48 = 0.26$ ).

#### 4. Discussion

The present study is no veracious representation of growth in itself but comprises a cross-sectional design of the longitudinal growth of liver volume supported by the numerical evidence obtained from a relatively numerous sample ( $n = 69$ ) of normal autopsied formalin-fixed fetuses aged 18–30 weeks. Of note, the 12–24-month formalin preservation substantially alters the weight and density of fixed organs. The weight gain of formalin-fixed organs may even fluctuate from 10–12% for the encephalon to 20–25% for the heart and liver, when compared to their initial weight [20]. As a consequence of tissue shrinkage, formalin preservation may additionally influence volume of organs in question, predominantly with relation to isolated organs [14, 20]. On the contrary, with relation to organs preserved *in situ* in the sealed abdominal cavity, formalin fixation influences little (0.5–1.0%) their volumes [18, 19]. This has been supported by the fact that the liver length and transverse and sagittal diameters in the material under examination are harmonious with those in *in utero* fetuses of the same age assessed by 3D ultrasound [14]. Therefore, from the clinical perspective, visceral measurements and growth curves obtained anatomically are comparable with particular ultrasonic measurements [14, 21]. As stated by Breeze et al. [21], conventional autopsy still remains the gold reference standard in the quantitative evaluation of fetal organs. As a result, the findings obtained

in this study can both aggregately be discussed and straightly be adapted *in vivo* to the fetus.

The precise estimation of fetal ages in the material under examination has been compatible with the Fetal Growth Longitudinal Study, part of the International Fetal and Newborn Growth Consortium for the 21st Century (INTERGROWTH-21st) Project [17]. In this study, the fetuses could not suffer from intrauterine growth retardation since their gestational, amenorrhea, and ultrasound ages proved to be highly ( $r = 0.99$ ,  $p < 0.001$ ) correlated [14]. It should be emphasized that we performed liver volume determination by a direct and clearly precise method based on Archimedes' principle [19]. Since both the material studied and the method used have been apposite, our findings can be considered factual.

In the material under examination, we found no statistically significant male-female differences in liver volume. These findings are in line with previous reports in which anatomical [22], 3D ultrasound [7, 16, 23], and MRI [11, 21, 24] methods were used.

The anatomical research by Albay et al. [22] found the liver volume to grow from  $18.0 \pm 0.6 \text{ cm}^3$  in the first trimester through  $14.8 \pm 12.5 \text{ cm}^3$  in the second trimester and  $45.7 \pm 21.0 \text{ cm}^3$  in the third trimester to  $71.8 \pm 19.9 \text{ cm}^3$  in full term fetuses. Guihard-Costa et al. [20] evaluated liver weight in 640 autopsied formalin-fixed human fetuses aged 13–42 weeks. The liver weight increased from  $3.09 \pm 0.27 \text{ g}$  in fetuses aged 12–13 weeks to  $161.94 \pm 37.78 \text{ g}$  in fetuses aged 41–42 weeks. It is noteworthy that for the 5th and 95th centiles the liver volume averaged  $2.64 \text{ cm}^3$  and  $3.54 \text{ cm}^3$  at 13–14 weeks and  $99.80 \text{ cm}^3$  and  $224.08 \text{ cm}^3$  at 41–42 weeks of gestation. Since the density of the fetal liver did not change throughout the gestation, the weight growth dynamics of the fetal liver precisely revealed its volumetric growth [8]. This was also confirmed by Breeze et al. [21], who reported both liver volume ( $y$ ) and liver weight ( $x$ ) to increase parabolically, with a reciprocal relationship, best modelled by the following linear function:  $y = 2.93 + 0.87x$ . In the material under examination, the median value of liver volume achieved by direct hydrostatic measurements grew from  $6.57 \text{ cm}^3$  at 18–21 weeks through  $14.36 \text{ cm}^3$  at 22–25 weeks to  $20.77 \text{ cm}^3$  at 26–30 weeks.

For the growing fetal liver, we tested three regression models, namely, third-degree polynomial, natural logarithmic, and linear functions. The choice of the best-fit model encountered the following criteria: the greatest  $r^2$  value, all coefficients different from 0, and the lowest SD of regression. Regrettably, in the estimated third-degree polynomial model, its parameters proved to be statistically insignificant ( $p = 0.254$ ). The linear and logarithmic models displayed approximated  $r^2$  values: 0.794 and 0.791, respectively. However, the linear model was characterized by the lowest values of both standard deviation for parameters and the standard error of the estimate for the whole model. Of note, residual value analysis showed normality of distribution for both linear and logarithmic models. In the linear and logarithmic models, there were three and four extremal values, respectively, for which standardized residuals were beyond the range of  $(-2, +2)$ .

Finally, the linear model was of best-fit for our empirical data throughout the analyzed fetal period. In this study, the algebraic data have been presented in an analogous manner as the INTERGROWTH-21st Project data [17], comprising the fitted 3rd, 10th, 50th, 90th, and 97th smoothed centile curves. Therefore, the best-fit growth dynamics was expressed by the linear function  $y = -26.95 + 1.74 \times \text{age} \pm Z \times (-3.15 + 0.27 \times \text{age})$ . According to such a growth pattern for the 50th centile ( $Z = 0$ ), the rate of hepatic volumetric growth averaged  $1.74 \text{ cm}^3$  per week.

With the use of 2D ultrasound, Gimondo et al. [15] indirectly estimated liver volume by measuring the length and transverse and sagittal diameters of the fetal liver and multiplying them by a constant of 0.42. Chang et al. [16] tested hypothesis whether the liver volume obtained by 2D ultrasound from Gimondo's formula [15], that is, liver volume =  $0.45 \times \text{length} \times \text{transverse diameter} \times \text{sagittal diameter}$ , is tantamount to that determined directly by 3D ultrasound. As it turned out, a volume constant of 0.42 tenuously reflected direct volumetric determination because of its underestimation of the fetal liver volume. Therefore, the new reference volume constant of 0.55 was substituted for the old one to obtain the formula: liver volume =  $0.55 \times \text{liver length} \times \text{liver transverse diameter} \times \text{liver sagittal diameter}$ , of practical meaning if only 2D ultrasound is available. The new formula yielded a more accurate estimation of liver volume, because it proved to be closer to and displayed no difference when compared to the actual liver volume evaluated with 3D ultrasound [16].

The introduction of 3D ultrasound has considerably enhanced diagnostic power in maternal fetal medicine. This method allows determination of hepatic volume by slicing through collected images and recording a truncated pyramidal volume [5]. The superior outline of the liver referring to the diaphragm is easy to delineate, while its inferior outline fades away. Volume determination is possible in only technically satisfactory ultrasonic liver recordings by multiplanar stepping through the liver and then by building the total liver volume equal to the sum of all individual volumes of parallel slices as follows [5]. Firstly, a reference plane (mostly a frontal cross section of the liver, prior to the stomach) has to be selected and fixed as an anchor. Secondly, in a concurrently obtainable sagittal cross section, the contour of the liver is manually traced and the liver surface area is measured slice by slice in some 10 sagittal projections flanked by the most lateral left and right points of the diaphragm in the frontal plane. Thirdly, the system integrates and calculates the total liver volume automatically. Chang et al. [16] showed that with respect to fetal liver volume 3D ultrasound is superior to 2D ultrasound and should be used for reaching its accurate determination. Ioannou et al. [25] identified six 3D ultrasound studies reporting normal volumes of the fetal liver at 32 weeks of gestation [1, 5, 8, 12, 16, 25]. However, because of poor standardization of volumetric methodology, there were wide discrepancies, even by 30% in reported normal hepatic volumes. The reference group was considered the most numerous one ( $n = 226$ ) presented by Chang et al. [1] with the liver volume of  $54.57 \text{ cm}^3$  that

turned out to be the least of all. The remaining liver volumes in the 32-week fetus averaged  $62.02 \text{ cm}^3$  by Chang et al. [16],  $63.3 \text{ cm}^3$  by Kuno et al. [8],  $66.42 \text{ cm}^3$  by Boito et al. [5],  $72.02 \text{ cm}^3$  by Laudy et al. [12], and  $74 \text{ cm}^3$  by Rizzi et al. [26]. Chang et al. [16] demonstrated the liver volumetric growth in 55 fetuses aged 20–31 weeks that followed proportionately:  $y = -78.29 + 4.38 \times \text{age}$  ( $r = 0.85$ ,  $p < 0.001$ ). In another study by Chang et al. [1] carried out on 226 fetuses at the age of 20–40 weeks, the liver volume increased from  $11.73 \pm 1.39$  to  $131.59 \pm 16.71 \text{ cm}^3$ , in accordance with the following cubic function:  $y = -398.26 + 46.20 \times \text{age} - 1.76 \times (\text{age})^2 + 0.02 \times (\text{age})^3$  ( $r = 0.97$ ,  $p < 0.001$ ). Furthermore, these authors presented differentiated regression lines of fetal liver volume with relations to biparietal and occipitofrontal diameters, head and abdominal circumferences, femur length, and estimated fetal weight. The linear relationship ( $y = 0.04x - 7.52$ ;  $r = 0.93$ ,  $p < 0.001$ ) between liver volume and estimated fetal weight was noted. The second-degree polynomial growth of liver volume was found in relation to both occipitofrontal diameter ( $y = 3.23x^2 - 40.98x + 146.5$ ;  $r = 0.85$ ,  $p < 0.001$ ) and abdominal circumference ( $y = 0.24x^2 - 6.53x + 60.05$ ;  $r = 0.93$ ,  $p < 0.001$ ). The third-degree polynomial growth in liver volume occurred relative to biparietal diameter ( $y = 1.74x^3 - 31.38x^2 + 195.8x - 396.53$ ;  $r = 0.90$ ,  $p < 0.001$ ), head circumference ( $y = 0.04x^3 - 2.80x^2 + 61.81x - 444.77$ ;  $r = 0.90$ ,  $p < 0.001$ ), and femur length ( $y = 2.50x^3 - 30.99x^2 + 138.22x - 195.1$ ;  $r = 0.92$ ,  $p < 0.001$ ). Laudy et al. [12] found the liver volume to increase proportionately in 25 fetuses, including small-, appropriate-, and large-for-gestational-age subjects. Because the fetuses did not constitute a homogenous sample, such a growth pattern could be doubtful for estimating the growth of liver volume during normal pregnancy. Kuno et al. [8] measured liver volume every 2 weeks in 14 appropriate-for-gestational-age fetuses from 20 weeks of gestation until delivery. The growth dynamics for liver volume was found to follow curvilinearly (parabolically). According to Boito et al. [2], after a logarithmic transformation of volumes in  $\text{cm}^3$ , the  $\log_{10}$  linear regression for fetal liver volume against gestational age in weeks was calculated as follows:  $\log_{10}$  liver volume =  $0.14 \times \text{age} - 0.31$  in the normal group. Gielchinsky et al. [3] used an improved 3D ultrasound method, that is, the VOCAL technique for measuring liver volumes. This method allows liver volume determination by rotating the organ around a fixed axis through a number of sequential steps [10]. These authors found that the liver volume of 200 normal fetuses aged 11–13 weeks as a function of crown-rump length (CRL) grew exponentially from  $0.5 \text{ cm}^3$  at 11 weeks (CRL 45 mm) to  $2.5 \text{ cm}^3$  at 13 weeks (CRL 84 mm) according to the following formula:  $\log_{10}$  liver volume =  $-1.20 + 0.02 \times \text{CRL}$  ( $r^2 = 0.86$ ,  $p < 0.001$ ). This was consistent with the autopsy findings by Archie et al. [13], who confirmed that liver weight grew exponentially with gestation from 1 g at 12 weeks through 5 g at 16 weeks to 30 g at 30 weeks.

In the material under examination, we compared the liver volume directly achieved by a hydrostatic method based on Archimedes' patent with the liver volume indirectly

calculated due to the following formula: liver volume =  $0.55 \times$  liver length  $\times$  liver transverse diameter  $\times$  liver sagittal diameter, using the three aforementioned numerical parameters of the fetal liver recently published by us [14]. In doing so, the median value of liver volume calculated indirectly in accordance with the formula liver volume =  $0.55 \times$  liver length  $\times$  liver transverse diameter  $\times$  liver sagittal diameter revealed an increase from  $12.41 \text{ cm}^3$  at 18–21 weeks through  $28.21 \text{ cm}^3$  at 22–25 weeks to  $49.69 \text{ cm}^3$  at 26–30 weeks of gestation. Independently of fetal age, the calculated liver volume substantially predominated over the measured liver volume. We confirmed a strong relationship ( $r = 0.91$ ,  $p < 0.001$ ) between the liver volumes obtained by hydrostatic ( $x$ ) and indirect ( $y$ ) methods, expressed by the linear model:  $y = -0.05 + 2.16x \pm 7.26$ . The measured-to-calculated liver volume ratio attained the value of  $0.48 \pm 0.08$  throughout the analyzed period. However, our volumetric comparisons have accentuated that the calculation of fetal liver volume essentially overestimates the results obtained by a hydrostatic method. Because calculated liver volumes are well-suited with those achieved by 3D ultrasonic measurements [1, 16], we opine that liver volume determination provided by 3D ultrasonography does not reveal factual results. Supportive evidence for this concept is the finding that in the material under examination the liver length and transverse and sagittal diameters were harmonious with those assessed by 3D ultrasound in *in utero* fetuses matched for gestational age [14]. According to our calculations, the best-fit constant should be 0.26 in the following formula: liver volume =  $0.26 \times$  liver length  $\times$  liver transverse diameter  $\times$  liver sagittal diameter.

Having discussed the quantitative growth of fetal liver volume, we would like to highlight some germaneness of liver volume determination in the fetus. Owing to the best-fit growth models for the mean and SD for liver volume, readers can readily calculate any chosen centiles according to gestational age. It is essential to know the value of  $Z$  that constantly equals  $-1.88$  for the 3rd centile,  $-1.28$  for the 10th centile,  $0$  for the 50th centile,  $+1.28$  for the 90th centile, and  $+1.88$  for the 97th centile [17]. As reported by Boito et al. [2], liver volume was found to be greater by 20% in 32 fetuses of diabetic women ( $45.9 \pm 34.0 \text{ cm}^3$ ) when compared to 32 normal controls ( $38.3 \pm 28.7 \text{ cm}^3$ ) at the age of 18–36 weeks of gestation. The  $\log_{10}$  linear regression for fetal liver volume against gestational age in weeks was expressed by the following relationship:  $\log_{10}$  liver volume =  $0.14 \times \text{age} - 0.04$  in the diabetic group. Furthermore, liver volume was positively related to maternal glycosylated hemoglobin concentrations (HbA1c), in accordance with the following regression:  $\log_{10}$  liver volume =  $0.14 \times \text{age} + 0.08 \times \text{HbA1c} - 0.48$ . This means that the liver volume was increased by 8% for each unit increase in maternal HbA1c and by 14% per week of gestational age. Astonishingly enough, using the VOCAL technique, Dubé et al. [9] exposed no difference in fetal liver volume during the third trimester in 10 women with normal glucose tolerance and in 17 women with gestational diabetes mellitus. In the diabetic group, the fetal liver volume increased from  $52 \pm 24 \text{ cm}^3$  at 24–28 weeks through  $90 \pm 16 \text{ cm}^3$  at 32 weeks to  $124 \pm 23 \text{ cm}^3$  at 36 weeks of gestation.

The fetal liver volumes in the control group were characterized by the following values:  $54 \pm 16 \text{ cm}^3$ ,  $89 \pm 17 \text{ cm}^3$ , and  $128 \pm 31 \text{ cm}^3$ , respectively. Moreover, differences in liver volume between 28 and 32 weeks ( $35 \pm 17 \text{ cm}^3$  versus  $36 \pm 26 \text{ cm}^3$ ), 32 and 36 weeks ( $39 \pm 25 \text{ cm}^3$  versus  $29 \pm 22 \text{ cm}^3$ ), and 28 and 36 weeks ( $75 \pm 37 \text{ cm}^3$  versus  $70 \pm 35 \text{ cm}^3$ ) proved to be statistically insignificant. Of note, as reported by Archie et al. [13] in 73% of fetuses with trisomy 21, the liver was enlarged over the 95th percentile, as a consequence of the disturbed hematopoiesis with intrahepatic expansion of the “leukemia-initiating” progenitor population. On the contrary, in fetal growth restriction, reduction is more expressed for hepatic volume than for head or upper abdominal circumference [5]. According to Kuno et al. [8], in 10 small-for-gestational-age fetuses from 20 weeks of gestation until delivery, liver volume was decreased and followed in accordance with the following formula: liver volume =  $167 - 14.6 \times \text{menstrual age} + 0.36 \times \text{menstrual age}^2$  ( $r^2 = 0.88$ ,  $p < 0.001$ ). Due to the brain-sparing effect in the small-for-gestational-age fetus, a decrease in liver volume is much more conspicuous than that in brain weight, and the former may thus contribute to the early recognition of fetal growth restriction [5, 23, 27].

To the best of our knowledge, this research paper is the first autopsy study to endow us with direct hepatic volume measurements. Consequently, our results are not affected by many ultrasound disadvantages attributable to the difficulty in outlining the whole contour of the liver because of inherent ultrasonic artifacts (image speckle, signal attenuation, and acoustic shadowing), unclear reference planes and anatomical landmarks, heterogeneity of 3D ultrasound system platforms and methods, fetal movement artifacts, the fetal back in the anterior position, and reduced amniotic fluid volume [5, 25]. It is noteworthy that, in 3D volumetry, errors in caliper placement will be multiplied over the volume [25]. The main limitations of this study appear to be (1) a lack of fetuses younger than 18 weeks and older than 30 weeks of gestation, (2) retrospective analysis without prospective ultrasound quality control, (3) measurements conducted by a single observer in a blind fashion, and (4) a lack of interobserver variability.

In summary, both the numerical data and computed nomograms for liver volume obtained in this study improve our information of hepatic quantitative anatomy in human fetuses. This may serve as a suitable reference in monitoring normal fetal development and screening for disturbances in fetal growth.

## 5. Conclusions

The fetal liver volume does not reveal sex differences. The growth of fetal liver volume follows a linear function. The regression equations for the estimation of the mean and standard deviation of liver volume allow for calculating any desired centiles according to gestational age. 3D ultrasound techniques considerably overestimate liver volumes relative to an accurate hydrostatic method. The liver volume should be calculated by the following formula: liver volume =  $0.26 \times$

liver length  $\times$  liver transverse diameter  $\times$  liver sagittal diameter. The age-specific references for liver volume at varying gestational ages are of great relevance in the evaluation of the normal hepatic growth and the early diagnosis of fetal micro- and macrosomias.

## Conflict of Interests

The authors declare they have no conflict of interests.

## References

- [1] C. H. Chang, C. H. Yu, F. M. Chang, H. C. Ko, and H. Y. Chen, “The assessment of normal fetal liver volume by three-dimensional ultrasound,” *Ultrasound in Medicine and Biology*, vol. 29, no. 8, pp. 1123–1129, 2003.
- [2] S. M. Boito, P. C. Struijk, N. T. C. Ursem, T. Stijnen, and J. W. Wladimiroff, “Assessment of fetal liver volume and umbilical venous volume flow in pregnancies complicated by insulin-dependent diabetes mellitus,” *BJOG*, vol. 110, no. 11, pp. 1007–1013, 2003.
- [3] Y. Gielchinsky, M. Zvanca, R. Minekawa, N. Persico, and K. H. Nicolaides, “Liver volume in trisomy 21 and euploid fetuses at 11 to 13 weeks,” *Prenatal Diagnosis*, vol. 31, no. 1, pp. 28–32, 2011.
- [4] S. Hojo, K. Tsukimori, S. Kitade et al., “Prenatal sonographic findings and hematological abnormalities in fetuses with transient abnormal myelopoiesis with Down syndrome,” *Prenatal Diagnosis*, vol. 27, no. 6, pp. 507–511, 2007.
- [5] S. M. E. Boito, J. A. M. Laudy, P. C. Struijk, T. Stijnen, and J. W. Wladimiroff, “Three-dimensional US assessment of hepatic volume, head circumference, and abdominal circumference in healthy and growth-restricted fetuses,” *Radiology*, vol. 223, no. 3, pp. 661–665, 2002.
- [6] S. Boito, P. C. Struijk, N. T. C. Ursem, T. Stijnen, and J. W. Wladimiroff, “Umbilical venous volume flow in the normally developing and growth-restricted human fetus,” *Ultrasound in Obstetrics & Gynecology*, vol. 19, no. 4, pp. 344–349, 2002.
- [7] C. H. Chang, C. H. Yu, H. C. Ko, C. L. Chen, and F. M. Chang, “Predicting fetal growth restriction with liver volume by three-dimensional ultrasound: efficacy evaluation,” *Ultrasound in Medicine & Biology*, vol. 32, no. 1, pp. 13–17, 2006.
- [8] A. Kuno, Y. Hayashi, M. Akiyama et al., “Three-dimensional sonographic measurement of liver volume in the small-for-gestational-age fetus,” *Journal of Ultrasound in Medicine*, vol. 21, no. 4, pp. 361–366, 2002.
- [9] M. C. Dubé, M. Girard, A. S. Morisset, A. Tchernof, S. J. Weisnagel, and E. Bujold, “Evaluation of fetal liver volume by tridimensional ultrasound in women with gestational diabetes mellitus,” *Journal of Obstetrics and Gynaecology Canada*, vol. 33, no. 11, pp. 1095–1098, 2011.
- [10] K. R. Duncan, “Fetal and placental volumetric and functional analysis using echo-planar imaging,” *Topics in Magnetic Resonance Imaging*, vol. 12, no. 1, pp. 52–66, 2001.
- [11] K. R. Duncan, B. Issa, R. Moore, P. N. Baker, I. R. Johnson, and P. A. Gowland, “A comparison of fetal organ measurements by echo-planar magnetic resonance imaging and ultrasound,” *BJOG: An International Journal of Obstetrics and Gynaecology*, vol. 112, no. 1, pp. 43–49, 2005.
- [12] J. A. M. Laudy, M. M. M. Janssen, P. C. Struyk, T. Stijnen, H. C. S. Wallenburg, and J. W. Wladimiroff, “Fetal liver volume measurement by three-dimensional ultrasonography:

- a preliminary study," *Ultrasound in Obstetrics and Gynecology*, vol. 12, no. 2, pp. 93–96, 1998.
- [13] J. G. Archie, J. S. Collins, and R. R. Lebel, "Quantitative standards for fetal and neonatal autopsy," *The American Journal of Clinical Pathology*, vol. 126, no. 2, pp. 255–265, 2006.
- [14] M. Szpinda, M. Paruszevska-Achtel, A. Woźniak, M. Badura, C. Mila-Kierzenkowska, and M. Wiśniewski, "Three-dimensional growth dynamics of the liver in the human fetus," *Surgical and Radiologic Anatomy*, 2015.
- [15] P. Gimondo, P. Mirk, A. La Bella, G. Messina, and C. Pizzi, "Sonographic estimation of fetal liver weight: an additional biometric parameter for assessment of fetal growth," *Journal of Ultrasound in Medicine*, vol. 14, no. 5, pp. 327–333, 1995.
- [16] F. M. Chang, K. F. U. Hsu, H. C. Ko et al., "Three-dimensional ultrasound assessment of fetal liver volume in normal pregnancy: a comparison of reproducibility with two-dimensional ultrasound and a search for a volume constant," *Ultrasound in Medicine & Biology*, vol. 23, no. 3, pp. 381–389, 1997.
- [17] A. T. Papageorghiou, E. O. Ohuma, D. G. Altman et al., "International standards for fetal growth based on serial ultrasound measurements: the Fetal Growth Longitudinal Study of the INTERGROWTH-21st Project," *The Lancet*, vol. 384, no. 9946, pp. 869–879, 2014.
- [18] M. Paruszevska-Achtel, *Morphometric study of the liver in human foetuses [Ph.D. thesis]*, Nicolaus Copernicus University, Bydgoszcz, Poland, 2014.
- [19] M. Szpinda, W. Siedlaczek, A. Szpinda, A. Woźniak, C. Mila-Kierzenkowska, and M. Wiśniewski, "Volumetric growth of the lungs in human fetuses: an anatomical, hydrostatic and statistical study," *Surgical and Radiologic Anatomy*, vol. 36, no. 8, pp. 813–820, 2014.
- [20] A. M. Guihard-Costa, F. Ménez, and A. L. Delezoide, "Organ weights in human fetuses after formalin fixation: standards by gestational age and body weight," *Pediatric and Developmental Pathology*, vol. 5, no. 6, pp. 559–578, 2002.
- [21] A. C. G. Breeze, F. A. Gallagher, D. J. Lomas, G. C. S. Smith, and C. C. Lees, "Postmortem fetal organ volumetry using magnetic resonance imaging and comparison to organ weights at conventional autopsy," *Ultrasound in Obstetrics & Gynecology*, vol. 31, no. 2, pp. 187–193, 2008.
- [22] S. Albay, M. A. Malas, E. Cetin, N. Cankara, and N. Karahan, "Development of the liver during the fetal period," *Saudi Medical Journal*, vol. 26, no. 11, pp. 1710–1715, 2005.
- [23] S. M. Boito, P. C. Struijk, N. T. C. Ursem, L. Fedele, and J. W. Wladimiroff, "Fetal brain/liver volume ratio and umbilical volume flow parameters relative to normal and abnormal human development," *Ultrasound in Obstetrics & Gynecology*, vol. 21, no. 3, pp. 256–261, 2003.
- [24] A. Hirose, T. Nakashima, S. Yamada, C. Uwabe, K. Kose, and T. Takakuwa, "Embryonic liver morphology and morphometry by magnetic resonance microscopic imaging," *The Anatomical Record*, vol. 295, no. 1, pp. 51–59, 2012.
- [25] C. Ioannou, I. Sarris, L. J. Salomon, and A. T. Papageorghiou, "A review of fetal volumetry: the need for standardization and definitions in measurement methodology," *Ultrasound in Obstetrics & Gynecology*, vol. 38, no. 6, pp. 613–619, 2011.
- [26] M. C. D. S. Rizzi, E. A. Júnior, L. M. M. Nardoza, A. L. D. Diniz, L. C. Rolo, and A. F. Moron, "Nomogram of fetal liver volume by three-dimensional ultrasonography at 27 to 38 weeks of pregnancy using a new multiplanar technique," *American Journal of Perinatology*, vol. 27, no. 8, pp. 641–647, 2010.
- [27] A. B. Roberts, J. M. Mitchell, L. M. McCowan, and S. Barker, "Ultrasonographic measurement of liver length in the small-for-gestational-age fetus," *The American Journal of Obstetrics and Gynecology*, vol. 180, no. 3, pp. 634–638, 1999.

## Research Article

# Morphometric Evaluation of Korean Femurs by Geometric Computation: Comparisons of the Sex and the Population

**Ho-Jung Cho, Dai-Soon Kwak, and In-Beom Kim**

*Department of Anatomy, Catholic Institute for Applied Anatomy, The Catholic University of Korea,  
222 Banpo-Daero, Seocho-gu, Seoul 137-701, Republic of Korea*

Correspondence should be addressed to Dai-Soon Kwak; [daisoon@catholic.ac.kr](mailto:daisoon@catholic.ac.kr) and In-Beom Kim; [ibkimmd@catholic.ac.kr](mailto:ibkimmd@catholic.ac.kr)

Received 26 February 2015; Revised 14 May 2015; Accepted 21 May 2015

Academic Editor: Gulsum Ozyigit

Copyright © 2015 Ho-Jung Cho et al. This is an open access article distributed under the Creative Commons Attribution License, which permits unrestricted use, distribution, and reproduction in any medium, provided the original work is properly cited.

We measured 28 parameters of 202 femurs from Koreans by an automated geometric computation program using 3D models generated from computed tomography images. The measurement parameters were selected with reference to physical and forensic anthropology studies as well as orthopedic implant design studies. All measurements were calculated using 3D reconstructions on a computer using scientific computation language. We also analyzed sex and population differences by comparison with data from previous studies. Most parameters were larger in males than in females. The height, head diameter, head center offset, and chord length of the diaphysis, most parameters in the distal femur, and the isthmic width of the medullary canal were smaller in Koreans than in other populations. However, the neck-shaft angle, subtense, and width of the intercondylar notch in the distal femur were larger than those in other populations. The results of this study will be useful as a reference for physical and forensic anthropology as well as the design of medical devices suitable for Koreans.

## 1. Introduction

The femur is the largest bone in the human body. Its proximal part and the pelvis constitute the hip joint, and its distal part constitutes part of the knee joint. Therefore, the femur is widely researched in fields such as physical and forensic anthropology, human kinematics, and orthopedics. Physical and forensic anthropology research involves using metric or nonmetric methods to determine differences in the femur with respect to populations, sex, and age [1–10]. In addition, orthopedics research involves analysis of the femoral head, neck, and the proximal part of the medullary canal for hip joint studies [11–33] as well as the shape of the distal part of the femur for knee joint studies [34–47]. Furthermore, some studies have investigated the shape of the medullary canal and femoral curvature to design intramedullary fixators and investigated the axes for orthopedic surgery [23, 48–51].

Most of those studies used bones from cadavers or patients who underwent surgery. Moreover, efforts have been made to reduce inter- and intraobserver measurement errors when using dry bone, radiography, and 3D models. Although some studies have used digital methods [21, 30, 52], they have focused only on portions of the femur.

Therefore, this study morphometrically evaluated 28 parameters of 202 femurs from Koreans by an automated geometric computation program using 3D models generated from computed tomography (CT) images. Furthermore, we calculated the size of the medullary canal for implant stem and intramedullary device design. Finally, we analyzed sex and population differences by comparison with data from previous studies.

## 2. Materials and Methods

The study included 202 femurs from Koreans from the Catholic Digital Human Library (November 2003 to present), which was established from CT images from the whole bodies of cadavers. CT images had a slice thickness of 0.75 or 1.0 mm and a pixel dimension from 0.431 to 0.832 mm. CT scans of cadavers alongside a plastic ball of known size (diameter: 2.25 inches) for calibration were used to construct 3D skeleton models. The images obtained were reconstructed in 3D skeleton models created by a 3D reconstruction program (Mimics, version 16, Materialise, Belgium). The gray-level threshold value at the time of the 3D reconstruction was determined

by comparing the actual and three-dimensional volumes of the plastic ball. Thus, the size of the 3D reconstructed bone models was not different from that of the real bones ( $P = 0.74$ ).

We selected femurs with no congenital anomalies or pathological deformities as determined by a radiologist and anatomist. Demographic information including sex, age, and height was available for each sample. The mean age and height of male samples ( $n = 88$ ) were 50 years and 167 cm, respectively; those of female samples ( $n = 114$ ) were 54 years and 156.4 cm, respectively. We examined 102 and 100 left and right femurs, respectively. All measurements and calculations were conducted using 3D reconstructions on a computer using Matlab (version R2011, MathWorks, MA, USA).

Prior to measurement, we aligned the femurs by using 3 different methods. In the first method, we aligned the mechanical axis of the femur in the sagittal and coronal planes as described by Seo et al. [53]; the mechanical axis was defined as the line connecting the center of the femoral head to the apex of the intercondylar notch (Figure 1(a)). In the second method, we aligned the anatomical axis of the femur in the sagittal and coronal planes; the anatomical axis was defined as a least-square-fitting line calculated from the diaphysis (Figure 1(b)). The third method was osteometric board alignment. The most inferior points of both condyles were aligned in a transverse plane. In all methods, the extreme posterior points of the medial and lateral condyles were aligned in the coronal plane (Figure 1(c)).

After the alignment procedure, we exported the 3D femur models to stereolithography format file for geometric computation. The geometric computation software, which was programmed in Matlab, had 3 basic functions. The first function was finding extreme points: the most superior, inferior, anterior, and posterior points were located, and the distances between them were calculated. The second function was least square primitive geometric fitting by line, sphere, and cylinder; the anatomical and mechanical axes of the femur were located, and the angle between them was calculated. The third function was section reconstruction, in which arbitrary sectional images of 3D objects were created and used to calculate sectional parameters. Our in-house coding program was verified using simple solid primitives (i.e., a sphere, hexahedron, and cylinder). Then, we randomly chose 10 samples to compare the measurement results of our program with those of commercial stereo lithography computer-aided design software (3-matic version 8.0, Materialise, Belgium). There were no differences in any parameter between programs ( $P = 0.71$ ).

Measurement parameters were selected with reference to physical and forensic anthropology studies as well as orthopedic implant design studies. A total of 28 variables were measured by using the models: the whole femur, including the length and axes of the whole femur; proximal femur, including the sizes and angles of the head and neck; diaphysis, including the length, curvature, and angle of the femoral shaft; distal femur, including the sizes of the condyle and intercondylar notch; and medullary part, including the isthmic position and the size of the cross sections of the medullary canal (Table 1 and Figure 2).

TABLE 1: Definitions of femur parameters.

Group	Abbreviation	Measurement
Whole	HMA	Height after mechanical axis alignment
	HAA	Height after anatomical axis alignment
	HOB	Height measured by osteometric board
	AMAC	Angle between mechanical axis and anatomical axis in coronal plane
	AMAS	Angle between mechanical axis and anatomical axis in sagittal plane
Proximal	HSD	Sphere diameter fit to head
	HCO	Head center offset
	NA2D	Neck angle on coronal plane
	NA3D	Neck angle in 3D vector
	VAAP	Version angle on axial plane
Diaphysis	PDA	Proximal diaphysis (1/3) angle on sagittal plane
	CDA	Central diaphysis (2/3) angle on sagittal plane
	DDA	Distal diaphysis (3/3) angle on sagittal plane
	ACC	Anterior cortex curvature on sagittal plane
	PCC	Posterior cortex curvature on sagittal plane
	CL	Chord length
	ST	Subtense
Distal	DLC	Depth of lateral condyle
	WLC	Width of lateral condyle
	DMC	Depth of medial condyle
	WMC	Width of medial condyle
	DIN	Depth of intercondylar notch
	WIN	Width of intercondylar notch
Medullary canal	IPDE	Isthmic position from distal end
	MLWI	Mediolateral width at isthmus
	APWI	Anteroposterior width at isthmus
	APWM	Anteroposterior width at mid center

Data were analyzed using SPSS (version 17.0; SPSS Inc., Chicago, IL, USA). Independent  $t$ -tests were performed to assess differences in the means of variables between sexes and population by comparison with data from previous studies after the data were tested for normality of distribution by the Kolmogorov-Smirnov test. Variables that did not exhibit a normal distribution were analyzed by the Mann-Whitney  $U$  test. The level of significance was set at  $P < 0.05$ .

### 3. Results and Discussion

**3.1. Comparison of Femur Parameters between Sexes.** The results of the automatic geometric calculations are shown in Table 2. The height of the whole femur was calculated after applying the 3 alignment methods mentioned above.

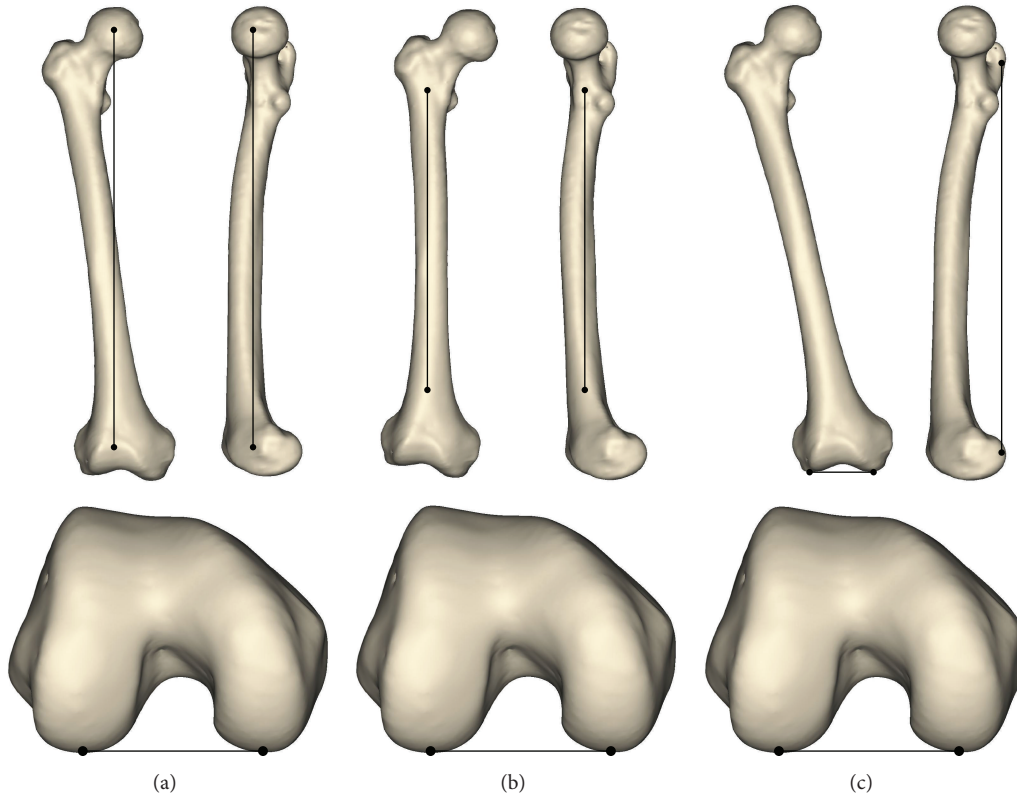


FIGURE 1: Three alignment methods. (a) Mechanical axis alignment; (b) anatomical axis alignment; (c) alignment by osteometric board.

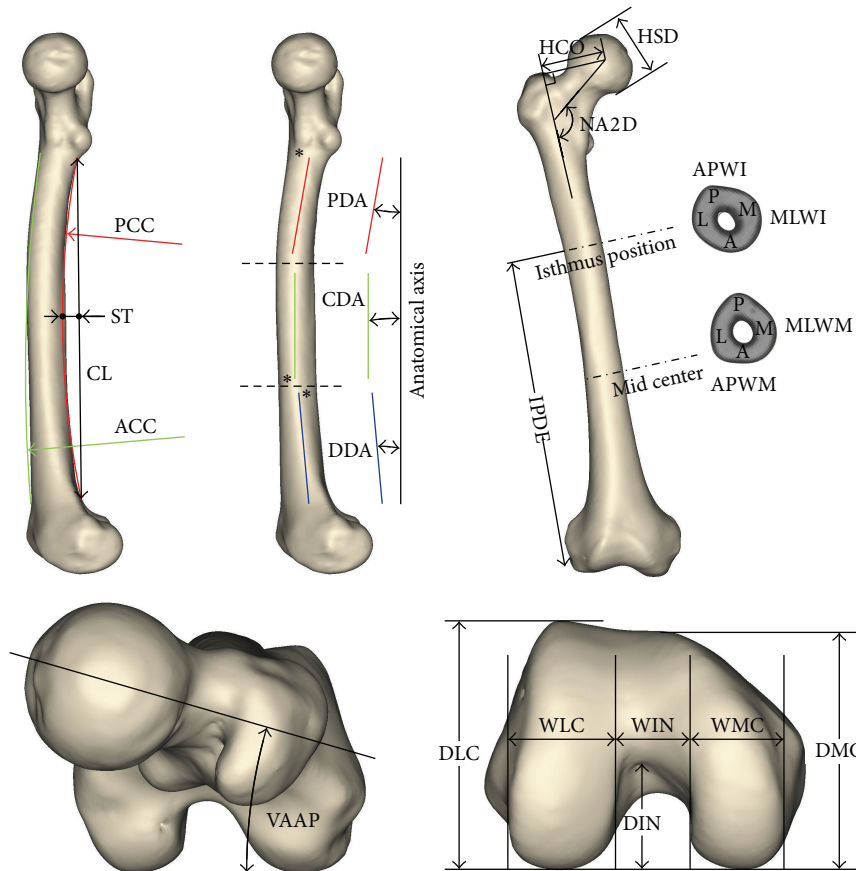


FIGURE 2: Measurement parameters (see Table 1 for definitions).

TABLE 2: Comparison of femur parameters by sex.

Group	Abbreviation	Female		Male		Combined		<i>P</i>
		Mean	SD	Mean	SD	Mean	SD	
Whole	HMA (mm)	404.65	18.11	434.43	19.29	417.41	23.73	<0.01
	HAA (mm)	403.97	18.10	434.19	23.90	416.96	23.90	<0.01
	HOB (mm)	401.71	17.87	431.62	23.66	414.52	23.66	<0.01
	AMAC (deg.)	5.49	0.89	5.42	0.82	5.46	0.86	0.57
	AMAS (deg.)	3.80	0.88	3.07	1.03	3.49	1.02	<0.01
Proximal	HSD (mm)	43.25	2.12	48.50	2.23	45.50	3.39	<0.01
	HCO (mm)	37.26	5.40	38.69	5.29	37.88	5.39	0.72
	NA2D (deg.)	130.80	6.34	129.56	6.09	130.27	6.25	0.18
	NA3D (deg.)	127.70	5.80	128.16	6.35	127.90	6.06	0.60
	VAAP (deg.)	20.34	10.54	14.61	10.30	17.89	10.79	<0.01
Diaphysis	PDA (deg.)	7.31	1.60	7.90	1.42	7.56	1.55	<0.01
	CDA (deg.)	-0.08	0.47	-0.43	0.52	-0.23	0.52	<0.01
	DDA (deg.)	-7.22	1.85	-6.89	1.49	-7.08	1.71	0.18
	ACC (mm)	1350.98	741.17	1381.04	473.02	1364.16	636.25	0.06*
	PCC (mm)	755.65	160.78	889.69	188.15	814.43	185.25	<0.01
	CL (mm)	274.47	14.95	289.61	16.56	281.11	17.35	<0.01
	ST (mm)	13.82	2.83	13.43	2.87	13.65	2.85	0.35
Distal	DLC (mm)	58.39	2.76	64.63	3.65	60.11	4.43	<0.01
	WLC (mm)	24.05	2.00	27.96	1.91	25.76	2.76	<0.01
	DMC (mm)	55.25	3.02	61.22	3.06	57.85	4.24	<0.01
	WMC (mm)	23.46	2.39	25.78	1.85	24.47	2.45	<0.01
	DIN (mm)	27.16	1.85	30.50	2.05	28.61	2.25	<0.01
	WIN (mm)	18.97	2.75	21.66	2.66	20.14	3.02	<0.01
Medullary canal	IPDE (mm)	403.97	18.10	434.19	23.90	416.96	23.90	<0.01
	MLWI (mm)	9.59	1.93	9.60	1.94	9.60	1.93	0.98
	APWI (mm)	10.97	2.60	11.51	2.35	11.24	2.49	0.22
	MLWM (mm)	10.24	1.82	11.48	1.96	10.77	1.97	<0.01
	APWM (mm)	12.41	2.08	13.71	2.19	12.97	2.22	<0.01

\*The result of nonparametric test by Mann-Whitney *U* test.

HMA: height after mechanical axis alignment, HAA: height after anatomical axis alignment, HOB: height measured by osteometric board, AMAC: angle between mechanical axis and anatomical axis in coronal plane, AMAS: angle between mechanical axis and anatomical axis in sagittal plane, HSD: sphere diameter fit to head, HCO: head center offset, NA2D: neck angle on coronal plane, NA3D: neck angle in 3D vector, VAAP: version angle on axial plane, PDA: proximal diaphysis (1/3) angle on sagittal plane, CDA: central diaphysis (2/3) angle on sagittal plane, DDA: distal diaphysis (3/3) angle on sagittal plane, ACC: anterior cortex curvature on sagittal plane, PCC: posterior cortex curvature on sagittal plane, CL: chord length, ST: subtense, DLC: depth of lateral condyle, WLC: width of lateral condyle, DMC: depth of medial condyle, WMC: width of medial condyle, DIN: depth of intercondylar notch, WIN: width of intercondylar notch, IPDE: isthmic position from distal end, MLWI: mediolateral width at isthmus, APWI: anteroposterior width at isthmus, MLWM: mediolateral width at mid center, and APWM: anteroposterior width at mid center.

The greatest height was aligned by using the mechanical axis (HMA,  $417.41 \pm 23.73$  mm), followed by the anatomical axis (HAA,  $416.96 \pm 23.90$  mm) and the osteometric board (HOB,  $414.52 \pm 23.66$  mm). There were statistical differences among alignment methods ( $P < 0.01$ ), and all results were significantly greater in male samples than in female samples ( $P < 0.01$ ). The mean angle between mechanical and anatomical axes in the coronal plane (AMAC) did not differ statistically between sexes ( $P = 0.57$ ). In the sagittal plane, the angle between mechanical and anatomical axes (AMAS) in females ( $3.80 \pm 0.88^\circ$ ) was more posteriorly inclined than that in males ( $3.07 \pm 1.03^\circ$ ) ( $P < 0.01$ ).

At the proximal part of the femur, the femoral head diameter (HSD) was significantly greater in males ( $48.50 \pm 2.23$  mm) than in females ( $43.25 \pm 2.12$  mm) ( $P < 0.01$ ). The femoral head center offset (HCO), which is the distance between the femoral head center and anatomical axis, was not statistically different between sexes ( $P = 0.72$ ). The femoral neck-shaft angle in the coronal plane as projected in 2D and 3D planes (NA2D and NA3D, resp.) was not statistically different between sexes ( $P = 0.18$  and  $P = 0.60$ , resp.). However, there were statistical differences between the 2D and 3D angles ( $P < 0.01$ ). The version angle on axial plane (VAAP) was significantly greater in females ( $20.34 \pm 10.54^\circ$ )

TABLE 3: Comparison of parameters of the whole and proximal femur among populations.

Group	Measurement		Population	Female	Male	Combined	
	Abbreviation						
Whole	HOB (mm)		Korean (this study)	401.71	431.62	414.52	
			Inuit [9]	405.6	430		
			North American Indian I [9]	399.3	445.2		
			North American Indian II [9]	419.2	443.4		
			European American I [9]	433.8	448.6		
			African American II [9]	427.4	464.0		
			British (Aberdeen, UK)* [2]	428	459	448	
			African American I [9]	434.5	471.0		
Proximal	HSD (mm)		French* [28]			43	
			Korean (this study)	43.25	48.50	45.50	
			French* [22]			45.6	
			Turkish [11]			45.8	
			American (Texas, USA)* [23]			46.1	
			Pakistani [31]			50.1	
			Korean (this study)	37.26	38.69	37.88	
	HCO (mm)		Swiss, French (Caucasian) [27]			40.5	
			French* [22]			41.0	
			Pakistani [31]			41.9	
			Turkish [11]			42.7	
			American (Texas, USA)* [23]			43	
			French* [28]			47.0	
			French* [28]			122.9	
			French* [22]			123.1	
		NA2D (deg.)		American (Texas, USA)* [23]			124.7
				Turkish [11]			128.4
	Swiss, French (Caucasian) [27]				129.2		
	Korean (this study)		130.80	129.56	130.27		
	Pakistani [31]				130.3		

\*Specific population not mentioned; samples were considered to be from the country of the authors' institute.

HOB: height measured by osteometric board, HSD: sphere diameter fit to head, HCO: head center offset, and NA2D: neck angle on coronal plane.

than in males ( $14.61 \pm 10.30^\circ$ ) ( $P < 0.01$ ); also, 94.74% of samples exhibited anteroversion.

We divided the diaphysis into 3 equal parts. The angles between the proximal, central, and distal diaphysis and the anatomical axis in the sagittal plane (PDA, CDA, and DDA, resp.) were  $7.56 \pm 1.55^\circ$ ,  $-0.23 \pm 0.52^\circ$ , and  $-7.08 \pm 1.71^\circ$ , respectively. The angles of the proximal and central parts of the diaphysis differed statistically between sexes (both  $P < 0.01$ ). The anterior cortex curvature in the sagittal plane (ACC) tended to be greater in males ( $1381.04 \pm 473.02$  mm) than in females ( $1350.98 \pm 741.17$  mm), although the difference was not significant ( $P = 0.06$ ). The posterior cortex curvature in the sagittal plane (PCC) was significantly greater in males ( $889.69 \pm 188.15$  mm) than in females ( $755.65 \pm 160.78$  mm) ( $P < 0.01$ ). The chord length (CL) of the diaphysis was statistically longer in males ( $289.61 \pm 16.56$  mm) than in females ( $274.47 \pm 14.95$  mm) ( $P < 0.01$ ). There was no statistic difference in subtense (ST) length between females and males ( $P = 0.35$ ).

At the distal part of the femur, the depth and width of the lateral condyle (DLC and WLC, resp.), depth and width of the medial condyle (DMC and WMC, resp.), and depth and width of the intercondylar notch (DIN and WIN, resp.) were statistically smaller in females than in males (all  $P < 0.01$ ).

Regarding the medullary canal, the isthmic position of the medullary canal (IPDE) from the distal end of the femur was significantly greater in males ( $434.19 \pm 23.90$  mm) than in females ( $403.97 \pm 18.10$  mm) ( $P < 0.01$ ). The mediolateral and anteroposterior widths of the isthmus (MLWI and APWI, resp.) did not differ statistically between sexes ( $P = 0.98$  and  $P = 0.22$ , resp.). In the medullary canal at the mid center of the femoral shaft, the mediolateral anteroposterior widths (MLWM and APWM, resp.) were statistically larger in males than in females ( $11.48 \pm 1.96$  versus  $10.24 \pm 1.82$  mm and  $13.71 \pm 2.19$  versus  $12.41 \pm 2.08$  mm, resp.; both  $P < 0.01$ ).

*3.2. Comparison of Femur Parameters between Koreans and Other Populations.* We compared the results of the present

TABLE 4: Comparison of parameters of the diaphysis among populations.

Group	Measurement Abbreviation	Population	Female	Male	Combined
Diaphysis	CL (mm)	Japanese III [51]	254.0	273.5	265.7
		Japanese II [51]	268.5	293.5	280.4
		Korean (this study)	274.47	289.61	281.11
		Japanese I [51]	293.2	311.4	285.3
		North American Indian III [51]	299.3	316.7	308.2
		Inuit [9]	305.5	318.4	312.1
		North American Indian I [9]	302.6	329.6	319.1
		North American Indian II [9]	313.8	327.7	320.9
		African American II [9]	318.4	339.6	329.0
		European American I [9]	322.5	330.6	329.4
		European American II [51]	317.3	343.2	330.2
		African American I [9]	319.6	342.7	332.1
		African American I [9]	8.4	8.6	8.5
		European American II [51]	8.4	9.3	8.8
	African American II [9]	9.2	9.0	9.1	
	ST (mm)	Japanese III [51]	9.2	9.1	9.1
		European American I [9]	9.4	9.8	9.7
		Inuit [9]	9.7	11.0	10.3
		Japanese I [51]	9.6	11.6	10.5
		North American Indian II [9]	9.8	11.6	10.7
		North American Indian III [51]	11.0	11.0	11.0
		Japanese II [51]	10.7	12.5	11.6
		North American Indian I [9]	10.9	12.2	11.7
		Korean (this study)	13.82	13.43	13.65

CL: chord length; ST: subtense.

study with those of previous studies using adult femurs. We also compared sex differences between the present and previous studies that contained relevant data. The parameters of the whole and proximal femur by population are shown in Table 3. The height of the whole femur was measured by 3 methods. It should be noted that there were statistic differences among all 3 methods ( $P < 0.01$ ). Whole femur height measured by HOB in Koreans was significantly shorter than that in African American populations I and II, British, European Americans, male North American Indians I, and North American Indians II (all  $P < 0.05$ ), but not statistically different from that in Inuit and female North American Indians I [2, 9]. We were unable to compare our data with those of Americans, French, or Germans, because the measurement axis was unspecified or different from that used in the present study [22, 23, 28, 36].

Regarding the proximal part of the femur, the HSD of Koreans was not statistically different from those of the French, Turks, or Americans [11, 22, 23]. However, the HSD of Pakistanis and the French was statistically larger and smaller than that of Koreans (both  $P < 0.01$ ) [28, 31]. HCO was statistically smaller in Koreans than in the Swiss French, the French, Pakistanis, Turks, and Americans (all  $P < 0.01$ ) [11, 22, 23, 27, 28, 31]. NA2D was statistically larger in Koreans

than in the French, Americans, and Turks (all  $P < 0.01$ ) [11, 22, 23, 28]; however, there was no difference compared to that of the Swiss French or Pakistanis [27, 31]. At the proximal part of the femur, the HSD of Koreans was similar to that of other populations. However HCO was smaller and NA2D was larger in Koreans compared to those of other populations (Table 3).

At the diaphysis (Table 4), CL was statistically longer in Koreans than in Japanese populations II and III ( $P < 0.05$ ) [51]. CL was statistically shorter in Koreans than African American populations I and II, European American populations I and II, North American Indian populations I–III, Inuit, and Japanese population I (all  $P < 0.01$ ) [9, 51]. ST was statistically larger in Koreans than in all other populations ( $P < 0.01$ ), except that of male North American Indian population I [9]. This indicates Korean femurs generally have a greater sagittal curve. In most previous studies, ST was larger in males than in females. However, ST was larger in females in the Korean population, African American population II [9], and Japanese population III than in males [51]. In addition, there was no sex difference in ST in North American Indian population III [51].

At the distal part of the femur (Table 5), DLC was statistically smaller in Koreans than in Germans in both

TABLE 5: Comparison of parameters of the distal femur and medullary canal among populations.

Group	Measurement Abbreviation	Population	Female	Male	Combined
Distal	DLC (mm)	Korean (this study)	58.39	64.63	60.11
		German* [36]	63.1	69.3	
		Japanese* [40]			24.8
	WLC (mm)	Taiwanese* [38]			25.3
		Korean (this study)	24.05	27.96	25.76
		German* [36]	26.0	30.6	
	DMC (mm)	Korean (this study)	55.25	61.22	57.85
		German* [36]	62.3	69.3	
		Korean (this study)	23.46	25.78	24.47
	WMC (mm)	Taiwanese* [38]			26.7
		Japanese* [40]			30.1
		German* [36]	28.4	32.3	
	DIN (mm)	Korean (this study)	27.16	30.50	28.61
		German* [36]	30.3	32.5	
Taiwanese* [38]				18.2	
WIN (mm)	German* [36]	19.0	19.3		
	Korean (this study)	18.97	21.66	20.14	
	Korean (this study)	9.59	9.6	9.6	
Medullary canal	MLWI (mm)	Turkish [11]			10.7
		American (Texas, USA)* [23]			12.3
		Korean (this study)	10.97	11.51	11.24
	APWI (mm)	Turkish [11]			13.7
		American (Texas, USA)* [23]			16.9

\*Specific population not mentioned; samples were considered to be from the country of the authors' institute.

DLC: depth of lateral condyle, WLC: width of lateral condyle, DMC: depth of medial condyle, WMC: width of medial condyle, DIN: depth of intercondylar notch, WIN: width of intercondylar notch, MLWI: mediolateral width at isthmus, and APWI: anteroposterior width at isthmus.

sexes (both  $P < 0.01$ ) [36]. WLC was statistically smaller in Koreans than in Germans in both sexes (both  $P < 0.01$ ) [36]. Moreover, WLC tended to be larger than that in the Japanese and the Taiwanese, although not statistically [38, 40]. DMC was statistically smaller in Koreans than in Germans in both sexes (both  $P < 0.01$ ) [36]. WMC was statistically smaller in Koreans than in Germans, the Japanese, and the Taiwanese (all  $P < 0.01$ ) [36, 38, 40]. DIN was statistically smaller in Koreans than in Germans in both sexes (both  $P < 0.01$ ) [36]. WIN was statistically larger in Koreans than in Germans and the Taiwanese (both  $P < 0.01$ ), except for German females [36, 38]. Thus, the WLC of Koreans was similar to that of most other populations except Germans, and WIN was larger than that in other populations; meanwhile, all other parameters in the distal femur were smaller in Koreans.

At the medullary canal (Table 5), both MLWI and APWI were statistically smaller in Koreans than in Turks and Americans (both  $P < 0.01$ ) [11, 23].

#### 4. Conclusion

We calculated the 28 morphometric parameters of femurs from Koreans by using a geometric computation program. The results show that most parameters were larger in males

than in females. Moreover, 14 variables differed statistically between Koreans and other populations.

These data can be used for studies in physical and forensic anthropology as well as orthopedic implant design. Many previous studies only measured specific regions of the femur, such as the proximal and distal parts for the hip and knee joints, respectively. However, data of the whole femur are more useful for the aforementioned purposes. Traditional direct measurement methods require many times whole femur study. On the other hand, automated software can rapidly analyze the whole femur as well as other bones. Also, automated computation methods have lower inter- and intraobserver variations than traditional direct measurement methods.

We expect that the Korean data and comparisons with other populations will be useful references for physical and forensic anthropology as well as orthopedic device design. In addition, this computational measurement method may be useful for surgical navigation systems.

#### Conflict of Interests

The authors declare that there is no conflict of interests regarding the publication of this paper.

## Acknowledgment

This research was partially supported by the Basic Science Research Program through the National Research Foundation of Korea (NRF) funded by the Ministry of Education, Science and Technology (NRF-2013R1A1A1009600).

## References

- [1] M. B. Trudell, "Anterior femoral curvature revisited: race assessment from the femur," *Journal of Forensic Sciences*, vol. 44, no. 4, pp. 700–707, 1999.
- [2] W. Bruns, M. Bruce, G. Prescott, and N. Maffulli, "Temporal trends in femoral curvature and length in medieval and modern Scotland," *American Journal of Physical Anthropology*, vol. 119, no. 3, pp. 224–230, 2002.
- [3] I. De Groote, "Femoral curvature in Neanderthals and modern humans: a 3D geometric morphometric analysis," *Journal of Human Evolution*, vol. 60, no. 5, pp. 540–548, 2011.
- [4] B. M. Gilbert, "Anterior femoral curvature: its probable basis and utility as a criterion of racial assessment," *American Journal of Physical Anthropology*, vol. 45, no. 3, pp. 601–604, 1976.
- [5] A. Harma and H. M. Karakas, "Determination of sex from the femur in Anatolian Caucasians: a digital radiological study," *Journal of Forensic and Legal Medicine*, vol. 14, no. 4, pp. 190–194, 2007.
- [6] H. M. Karakaş and A. Harma, "Femoral shaft bowing with age: a digital radiological study of Anatolian Caucasian adults," *Diagnostic and Interventional Radiology*, vol. 14, no. 1, pp. 29–32, 2008.
- [7] S. P. Singh and S. Singh, "A study of anterior femoral curvature in Indian subjects," *Acta Anatomica*, vol. 83, no. 3, pp. 416–425, 1972.
- [8] T. D. Stewart, "Anterior femoral curvature: its utility for race identification," *Human Biology*, vol. 34, pp. 49–62, 1962.
- [9] N. A. Walensky, "A study of anterior femoral curvature in man," *The Anatomical Record*, vol. 151, pp. 559–570, 1965.
- [10] D.-I. Kim, D.-S. Kwak, and S.-H. Han, "Sex determination using discriminant analysis of the medial and lateral condyles of the femur in Koreans," *Forensic Science International*, vol. 233, no. 1–3, pp. 121–125, 2013.
- [11] B. Atilla, A. Oznur, O. Caglar, M. Tokgözoglu, and M. Alpaslan, "Osteometry of the femora in Turkish individuals: a morphometric study in 114 cadaveric femora as an anatomic basis of femoral component design," *Acta Orthopaedica et Traumatologica Turcica*, vol. 41, no. 1, pp. 64–68, 2007.
- [12] K. Haraguchi, N. Sugano, T. Nishii et al., "Comparison of fit and fill between anatomic stem and straight tapered stem using virtual implantation on the ORTHODOC workstation," *Computer Aided Surgery*, vol. 6, no. 5, pp. 290–296, 2001.
- [13] K. L. Hermann and N. Egund, "CT measurement of anteversion in the femoral neck: the influence of femur positioning," *Acta Radiologica*, vol. 38, no. 4, pp. 527–532, 1997.
- [14] M. Ito, N. Wakao, T. Hida et al., "Analysis of hip geometry by clinical CT for the assessment of hip fracture risk in elderly Japanese women," *Bone*, vol. 46, no. 2, pp. 453–457, 2010.
- [15] A. Kaneuji, T. Matsumoto, M. Nishino, T. Miura, T. Sugimori, and K. Tomita, "Three-dimensional morphological analysis of the proximal femoral canal, using computer-aided design system, in Japanese patients with osteoarthritis of the hip," *Journal of Orthopaedic Science*, vol. 5, no. 4, pp. 361–368, 2000.
- [16] E. Khmel'nitskaya, P. Mohandas, P. S. Walker, and S. K. Muirhead-Allwood, "Optimizing for head height, head offset, and canal fit in a set of uncemented stemmed femoral components," *HIP International*, vol. 18, no. 4, pp. 286–293, 2008.
- [17] K. M. Kim, J. K. Brown, K. J. Kim et al., "Differences in femoral neck geometry associated with age and ethnicity," *Osteoporosis International*, vol. 22, no. 7, pp. 2165–2174, 2011.
- [18] H.-J. Laine, M. U. K. Lehto, and T. Moilanen, "Diversity of proximal femoral medullary canal," *The Journal of Arthroplasty*, vol. 15, no. 1, pp. 86–92, 2000.
- [19] G. S. Lausten, F. Jorgensen, and J. Boesen, "Measurement of anteversion of the femoral neck. Ultrasound and computerised tomography compared," *The Journal of Bone and Joint Surgery—British Volume*, vol. 71, no. 2, pp. 237–239, 1989.
- [20] G. Lecerf, M. H. Fessy, R. Philippot et al., "Femoral offset: anatomical concept, definition, assessment, implications for preoperative templating and hip arthroplasty," *Orthopaedics & Traumatology: Surgery & Research*, vol. 95, no. 3, pp. 210–219, 2009.
- [21] B. Mahaisavariya, K. Sittthiseripratip, T. Tongdee, E. L. J. Bohez, J. Vander Sloten, and P. Oris, "Morphological study of the proximal femur: a new method of geometrical assessment using 3-dimensional reverse engineering," *Medical Engineering & Physics*, vol. 24, no. 9, pp. 617–622, 2002.
- [22] P. Massin, L. Geais, E. Astoin, M. Simondi, and F. Lavaste, "The anatomic basis for the concept of lateralized femoral stems: a frontal plane radiographic study of the proximal femur," *The Journal of Arthroplasty*, vol. 15, no. 1, pp. 93–101, 2000.
- [23] P. C. Noble, J. W. Alexander, L. J. Lindahl, D. T. Yew, W. M. Granberry, and H. S. Tullos, "The anatomic basis of femoral component design," *Clinical Orthopaedics and Related Research*, no. 235, pp. 148–165, 1988.
- [24] A. Unnanuntana, P. Toogood, D. Hart, D. Cooperman, and R. E. Grant, "Evaluation of proximal femoral geometry using digital photographs," *Journal of Orthopaedic Research*, vol. 28, no. 11, pp. 1399–1404, 2010.
- [25] D. S. Casper, G. K. Kim, J. Parvizi, and T. A. Freeman, "Morphology of the proximal femur differs widely with age and sex: relevance to design and selection of femoral prostheses," *Journal of Orthopaedic Research*, vol. 30, no. 7, pp. 1162–1166, 2012.
- [26] B. D. Ferris, C. Kennedy, M. Bhamra, and W. Muirhead-Allwood, "Morphology of the femur in proximal femoral fractures," *The Journal of Bone & Joint Surgery—British Volume*, vol. 71, no. 3, pp. 475–477, 1989.
- [27] O. Husmann, P. J. Rubin, P.-F. Leyvraz, B. De Roguin, and J.-N. Argenson, "Three-dimensional morphology of the proximal femur," *The Journal of Arthroplasty*, vol. 12, no. 4, pp. 444–450, 1997.
- [28] P. J. Rubin, P. F. Leyvraz, J. M. Aubaniac, J. N. Argenson, P. Esteve, and B. de Roguin, "The morphology of the proximal femur: a three-dimensional radiographic analysis," *The Journal of Bone & Joint Surgery—British Volume*, vol. 74, no. 1, pp. 28–32, 1992.
- [29] S. Schumann, M. Tannast, L.-P. Nolte, and G. Zheng, "Validation of statistical shape model based reconstruction of the proximal femur—a morphology study," *Medical Engineering and Physics*, vol. 32, no. 6, pp. 638–644, 2010.
- [30] N. Sugano, P. C. Noble, and E. Kamaric, "A comparison of alternative methods of measuring femoral anteversion," *Journal of Computer Assisted Tomography*, vol. 22, no. 4, pp. 610–614, 1998.

- [31] M. Umer, Y. J. Sepah, A. Khan, A. Wazir, M. Ahmed, and M. U. Jawad, "Morphology of the proximal femur in a Pakistani population," *Journal of Orthopaedic Surgery*, vol. 18, no. 3, pp. 279–281, 2010.
- [32] X. Cheng, J. Li, Y. Lu, J. Keyak, and T. Lang, "Proximal femoral density and geometry measurements by quantitative computed tomography: association with hip fracture," *Bone*, vol. 40, no. 1, pp. 169–174, 2007.
- [33] G. Khang, K. Choi, C.-S. Kim, J. S. Yang, and T.-S. Bae, "A study of Korean femoral geometry," *Clinical Orthopaedics and Related Research*, no. 406, pp. 116–122, 2003.
- [34] C. Chaichankul, A. Tanavalee, and P. Itiravivong, "Anthropometric measurements of knee joints in Thai population: correlation to the sizing of current knee prostheses," *The Knee*, vol. 18, no. 1, pp. 5–10, 2011.
- [35] F. B. Cheng, X. F. Ji, Y. Lai et al., "Three dimensional morphometry of the knee to design the total knee arthroplasty for Chinese population," *The Knee*, vol. 16, no. 5, pp. 341–347, 2009.
- [36] J. Dargel, J. W. P. Michael, J. Feiser, R. Ivo, and J. Koeke, "Human knee joint anatomy revisited: morphometry in the light of sex-specific total knee arthroplasty," *The Journal of Arthroplasty*, vol. 26, no. 3, pp. 346–353, 2011.
- [37] K. Hitt, J. R. Shurman II, K. Greene et al., "Anthropometric measurements of the human knee: correlation to the sizing of current knee arthroplasty systems," *The Journal of Bone & Joint Surgery Series A*, vol. 85, no. 4, pp. 115–122, 2003.
- [38] W.-P. Ho, C.-K. Cheng, and J.-J. Liao, "Morphometrical measurements of resected surface of femurs in Chinese knees: correlation to the sizing of current femoral implants," *The Knee*, vol. 13, no. 1, pp. 12–14, 2006.
- [39] K. A. Murshed, A. E. Çiçekcibaşı, A. Karabacakoglu, M. Şeker, and T. Ziyilan, "Distal femur morphometry: a gender and bilateral comparative study using magnetic resonance imaging," *Surgical and Radiologic Anatomy*, vol. 27, no. 2, pp. 108–112, 2005.
- [40] K. Urabe, H. Miura, T. Kuwano et al., "Comparison between the shape of resected femoral sections and femoral prostheses used in total knee arthroplasty in Japanese patients: simulation using three-dimensional computed tomography," *The Journal of Knee Surgery*, vol. 16, no. 1, pp. 27–33, 2003.
- [41] J. Victor, "Rotational alignment of the distal femur: a literature review," *Orthopaedics & Traumatology: Surgery & Research*, vol. 95, no. 5, pp. 365–372, 2009.
- [42] H.-C. Lim, J.-H. Bae, J.-Y. Yoon, S.-J. Kim, J.-G. Kim, and J.-M. Lee, "Gender differences of the morphology of the distal femur and proximal tibia in a Korean population," *The Knee*, vol. 20, no. 1, pp. 26–30, 2013.
- [43] P. L. Poilvache, J. N. Insall, G. R. Scuderi, and D. E. Font-Rodriguez, "Rotational landmarks and sizing of the distal femur in total knee arthroplasty," *Clinical Orthopaedics and Related Research*, no. 331, pp. 35–46, 1996.
- [44] W. P. H. Charlton, T. A. St. John, M. G. Ciccotti, N. Harrison, and M. Schweitzer, "Differences in femoral notch anatomy between men and women: a magnetic resonance imaging study," *The American Journal of Sports Medicine*, vol. 30, no. 3, pp. 329–333, 2002.
- [45] M. D. Tillman, K. R. Smith, J. A. Bauer, J. H. Cauraugh, A. B. Falsetti, and J. L. Pattishall, "Differences in three intercondylar notch geometry indices between males and females: a cadaver study," *The Knee*, vol. 9, no. 1, pp. 41–46, 2002.
- [46] D. Kwak, S. Han, and C. W. Han, "Resected femoral anthropometry for design of the femoral component of the total knee prosthesis in a Korean population," *Anatomy & Cell Biology*, vol. 43, no. 3, pp. 252–259, 2010.
- [47] D. S. Kwak, Q. B. Tao, M. Todo, and I. Jeon, "Determination of representative dimension parameter values of Korean knee joints for knee joint implant design," *Proceedings of the Institution of Mechanical Engineers, Part H: Journal of Engineering in Medicine*, vol. 226, no. 5, pp. 368–376, 2012.
- [48] P. C. Noble, G. G. Box, E. Kamaric, M. J. Fink, J. W. Alexander, and H. S. Tullos, "The effect of aging on the shape of the proximal femur," *Clinical Orthopaedics and Related Research*, no. 316, pp. 31–44, 1995.
- [49] S. A. Feik, C. D. L. Thomas, R. Bruns, and J. G. Clement, "Regional variations in cortical modeling in the femoral mid-shaft: sex and age differences," *American Journal of Physical Anthropology*, vol. 112, no. 2, pp. 191–205, 2000.
- [50] R. B. Martin and P. J. Atkinson, "Age and sex-related changes in the structure and strength of the human femoral shaft," *Journal of Biomechanics*, vol. 10, no. 4, pp. 223–231, 1977.
- [51] L. L. Shackelford and E. Trinkaus, "Late Pleistocene human femoral diaphyseal curvature," *American Journal of Physical Anthropology*, vol. 118, no. 4, pp. 359–370, 2002.
- [52] J. S. Kim, T. S. Park, S. B. Park, and S. I. Kim, "Measurement of femoral neck anteversion in 3D. Part 2: 3D modelling method," *Medical & Biological Engineering and Computing*, vol. 38, no. 6, pp. 610–616, 2000.
- [53] J.-G. Seo, B.-K. Kim, Y.-W. Moon et al., "Bony landmarks for determining the mechanical axis of the femur in the sagittal plane during total knee arthroplasty," *Clinics in Orthopedic Surgery*, vol. 1, no. 3, pp. 128–131, 2009.

## Research Article

# Change in the Pathologic Supraspinatus: A Three-Dimensional Model of Fiber Bundle Architecture within Anterior and Posterior Regions

Soo Y. Kim,<sup>1</sup> Rohit Sachdeva,<sup>1</sup> Zi Li,<sup>2</sup> Dongwoon Lee,<sup>3</sup> and Benjamin W. C. Rosser<sup>4</sup>

<sup>1</sup>School of Physical Therapy, College of Medicine, University of Saskatchewan, Saskatoon, SK, Canada S7N 0W3

<sup>2</sup>Department of Surgery, University of Toronto, Toronto, ON, Canada M5T 1P5

<sup>3</sup>Department of Computer Science, University of Toronto, Toronto, ON, Canada M5S 3G4

<sup>4</sup>Department of Anatomy and Cell Biology, College of Medicine, University of Saskatchewan, Saskatoon, SK, Canada S7N 5E5

Correspondence should be addressed to Soo Y. Kim; [soo.kim@usask.ca](mailto:soo.kim@usask.ca)

Received 18 February 2015; Revised 2 April 2015; Accepted 3 April 2015

Academic Editor: Heather F. Smith

Copyright © 2015 Soo Y. Kim et al. This is an open access article distributed under the Creative Commons Attribution License, which permits unrestricted use, distribution, and reproduction in any medium, provided the original work is properly cited.

Supraspinatus tendon tears are common and lead to changes in the muscle architecture. To date, these changes have not been investigated for the distinct regions and parts of the pathologic supraspinatus. The purpose of this study was to create a novel three-dimensional (3D) model of the muscle architecture throughout the supraspinatus and to compare the architecture between muscle regions and parts in relation to tear severity. Twelve cadaveric specimens with varying degrees of tendon tears were used. Three-dimensional coordinates of fiber bundles were collected *in situ* using serial dissection and digitization. Data were reconstructed and modeled in 3D using Maya. Fiber bundle length (FBL) and pennation angle (PA) were computed and analyzed. FBL was significantly shorter in specimens with large retracted tears compared to smaller tears, with the deeper fibers being significantly shorter than other parts in the anterior region. PA was significantly greater in specimens with large retracted tears, with the superficial fibers often demonstrating the largest PA. The posterior region was absent in two specimens with extensive tears. Architectural changes associated with tendon tears affect the regions and varying depths of supraspinatus differently. The results provide important insights on residual function of the pathologic muscle, and the 3D model includes detailed data that can be used in future modeling studies.

## 1. Introduction

Supraspinatus tendon tears of the rotator cuff are associated with changes in both the tendon and muscle. Fraying and thinning of the lateral aspect of the tendon occur with full-thickness tears [1, 2]. Muscular inhibition and disuse due to pain can lead to changes in the muscle. A decrease in muscle volume and fat infiltration can occur with large tendon tears [3–5]. The musculotendinous unit of the supraspinatus can also retract medially altering the length of fiber bundles [6, 7]. The alignment of fiber bundles relative to the axis of pull or line of force which is known as the pennation angle (PA) can also change as a result of retraction [8].

The function of a muscle is directly correlated with its architecture. Among the architectural parameters of skeletal muscles, fiber bundle length (FBL) is known to be the most

important as it is proportional to muscle excursion and the velocity of contraction [9, 10]. A direct linear relationship has been found between muscle length and force of isometric contraction [11]. Thus, a change in FBL can affect the optimal range and speed at which a muscle contracts [12]. In pennated muscles, only a component of the muscle fibers' force is projected onto the line of force; thus a change in PA will also impact the force-producing capabilities [13].

The muscle and tendon architecture of the supraspinatus is complex. The normal muscle has two main regions, anterior and posterior [14–18], which have been found to be functionally distinct [19–21]. The anterior region accounts for 75–86% of the muscle volume and its pennated fiber bundles attach laterally to the anterior tendon [14, 16]. It produces the majority of force for the muscle [14, 16]. The posterior region is substantially smaller in volume and partially lies

deep to the anterior. The parallel fiber bundles attach laterally to the posterior tendon [14, 16]. Based on its architecture, dynamic FBL changes with shoulder movements [19], fiber type composition [20], and innervation pattern [21], the posterior region is thought to play an important role in adjusting tension on the rotator cuff. Within each region there are three distinct parts, superficial, middle, and deep, based on the lateral attachment sites onto the tendon and fiber bundle orientation [16].

To date, the fiber bundle architecture of the pathologic supraspinatus has not been investigated throughout the muscle volume. In previous investigations, fiber bundle measurements were taken from the superficial surface of the muscle, not accounting for the different regions and parts of the muscle [6, 7]. Since the length of fiber bundles and PA are directly related to skeletal muscle function [22], it is important to quantify these parameters for both the anterior and posterior regions of the pathologic supraspinatus. In addition, given that architectural changes are considered to be the most important pathophysiological consequence of tendon tears and a critical factor in the success of tendon repair surgery, a thorough understanding of these parameters is needed [23].

A robust fiber bundle architecture database of the pathologic supraspinatus can be used to advance three-dimensional (3D) musculoskeletal computer models of the shoulder. 3D modeling is a powerful tool for analyzing the biomechanics underlying normal and pathological movements, particularly in complex systems such as the shoulder [24, 25]. Finite-element muscle models can provide detailed information about the distribution of strain within a muscle and the transmission of force [24]. These models, which are dependent on accurate fiber bundle data, can be used to make clinically relevant predictions about the functional deficits caused by rotator cuff tendon tears and the functional outcomes following surgery and rehabilitation [26, 27].

The purpose of this study was to investigate and model the muscle architecture throughout the volume of the supraspinatus using cadaveric specimens with varying degrees of tendon tears. It was hypothesized that fiber bundle architecture would differ between the anterior and posterior regions and their respective parts, superficial, middle, and deep, and that the architectural changes would be associated with the degree of tendon pathology.

## 2. Materials and Methods

**2.1. Specimens.** Twelve formalin embalmed cadaveric shoulder specimens (3 males, 9 females) with evidence of supraspinatus tendon pathology, that is, partial thickness or full-thickness tears, were used. Mean age was  $82.1 \pm 10.8$  years with a range of 64–95. Ethics approval was obtained from the Biomedical Research Ethics Board, University of Saskatchewan (Bio#11-77).

To expose the muscle and determine the presence of supraspinatus tendon pathology all overlying soft tissues (skin, fascia, trapezius, and deltoid) were removed. The clavicle and lateral aspect of the acromion were also removed to

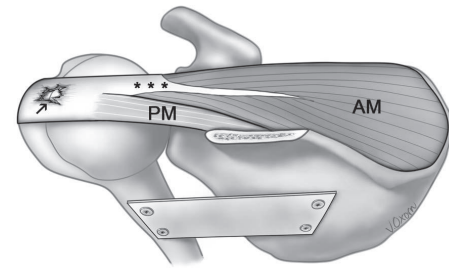


FIGURE 1: Supraspinatus with full-thickness tendon tear with no retraction (specimen representative of category B). Superior view of the middle part of the muscle belly with acromion removed. Fiber bundles of the superficial parts of anterior and posterior regions have been removed. Specimen stabilized with metal plate. Anterior part of supraspinatus tendon represented by \*\*\*; middle part of anterior region (AM); middle part of posterior region (PM). Fiber bundles of deep parts lie deep to the AM and PM. Arrow (↑) points to a full-thickness tear illustrated on the supraspinatus tendon.

allow full visualization of the rotator cuff tendons. Specimens with evidence of shoulder surgery or gross bony deformities were not used.

Specimens were placed into one of three categories based on the degree of tendon tear of the supraspinatus: (A) partial thickness tear; (B) full-thickness tear with no tendon retraction; (C) full-thickness tear with tendon retraction. A tear was deemed as having tendon retraction when the tear involved the entire extent (width) of the supraspinatus tendon in the sagittal plane. In specimens with full-thickness tendon tears (“B” and “C”), coronal and sagittal dimensions of the tear were measured using a digital caliper (Traceable ISO 17025 Calibrated, Fisher Scientific, Nepean, ON, Canada) and recorded.

**2.2. Dissection and Digitization.** Each of the 12 specimens was digitized. Previously developed digitization protocols for human skeletal muscles were adapted for this study [16, 28]. The glenohumeral joint was stabilized in  $0^\circ$  of abduction, flexion, and lateral rotation with a metal plate screwed to the humerus and scapula (Figure 1). The lateral aspect of the scapular spine, coracoid process, and greater tubercle were selected as reference points and demarcated with screws. These reference points were used in the modeling process and assisted in reconstructing the specimen in 3D. Specimens were then clamped into a securely mounted vice.

The periphery of the supraspinatus tendon was outlined with small dots 2 mm apart using a paint pen. Next, each point was digitized using a Microscribe G2X Digitizer (Immersion Corporation, San Jose, CA, USA). Following this, the division between the anterior and posterior regions on the superficial surface of the muscle as defined by Kim et al. [16] was identified and marked with small pins (3 mm in length). The anterior region of the supraspinatus muscle belly was serially dissected and digitized *in situ* first. Starting with the most superficial layer, 10–60 fiber bundles were identified. Each fiber bundle was then digitized using 10–20 sequential sites, beginning at the medial attachment site and ending at

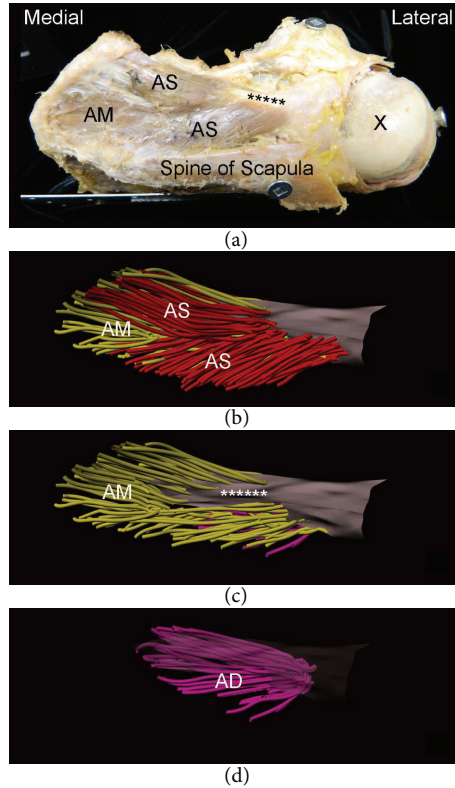


FIGURE 2: Retracted full-thickness tendon tear of supraspinatus without a distinguishable posterior region modelled throughout its volume in 3D (specimen from category C). (a) Superior view of specimen with lateral aspect of spine of scapula removed; superficial part of anterior region (AS); middle part of anterior region (AM); \* \* \* intramuscular portion of anterior supraspinatus tendon. Metal plate (bottom left) was used to stabilize the specimen and screws (scapular spine, coracoid process, and greater tubercle) were used in modeling process. (b) Computer model of anterior region including AS (red fibers) and AM (yellow fibers). (c) AM; AS not shown; (d) deep part of anterior region (AD) (pink fibers); AS, AM, and tendon are not shown.

the lateral. Once the entire layer had been digitized, fiber bundles were carefully removed to expose the underlying fascicles about 1-2 mm deeper. The periphery of the tendon was digitized whenever the tendon shape was found to change which was approximately at every 3–5 mm of the muscle’s depth. Once the entire anterior region had been digitized, the posterior region was serially dissected and digitized as outlined above.

2.3. *Modeling.* Digitized data were exported to Autodesk Maya 2009 (Autodesk, San Jose, CA, USA) and reconstructed in 3D using plug-ins developed in the laboratory. Fiber bundles and their attachment onto the tendon could be clearly visualized volumetrically using the model. Architecturally distinct regions and parts as defined by Kim et al. [16] were identified and color coded (Figure 2).

2.4. *Data Analysis.* Fiber bundle lengths and PA were computed with algorithms used in previously published work [16, 29, 30]. For a detailed description of computational methods the reader is referred to Lee et al. [29, 30]. Digitized fiber bundles were first reconstructed into an interpolating

cubic Catmull-Rom spline. Using arc-length parameterisation, digitized points were then resampled to make the curve representation uniform. FBL was approximated as an entire arc-length of the curve [29]. In the present study, PA is defined as an angle between the fiber bundle orientation and the line of force. The fiber bundle orientation was estimated by a tangent vector along the curve. The tangent vectors at the lateral and medial attachment sites were calculated as average derivatives of the curve over the lateral and medial regions, respectively [29, 30]. Hence, two angles were computed, lateral PA and medial PA. The line of force was determined as a vector best approximating the axis of the intramuscular tendon.

Statistical analysis was carried out using SPSS (version 18.0, Chicago, IL, USA). All architectural parameters for the anterior and posterior regions and their distinct parts were characterized with descriptive statistics (median and minimum-maximum values). Mann-Whitney *U* tests were used to compare median tear dimensions between specimen categories B and C and architectural parameters between categories of A and B of the posterior region. The Kruskal-Wallis test followed by pairwise comparisons (Mann-Whitney *U* tests) was used to compare median age of specimens and

TABLE 1: Summary of specimens.

Specimen #	Side	Sex	Age	Tear category	RCT location	Coronal plane (cm)	Sagittal plane (cm)
1460	R	F	67	A	SP	—	—
1463	R	F	95	A	SP	—	—
1429	R	F	64	A	SP	—	—
1425	R	M	89	A	SP	—	—
1458	R	F	73	B	SP	1.88	1.63
1450	R	F	77	B	SP	1.04	2.08
1447	R	F	94	B	SP	1.47	1.52
1447	L	F	94	B	SP	1.40	1.17
1455*	R	F	82	C	SP, SSC, ISP	3.33	3.84
1427*	R	M	76	C	SP, SSC, ISP	5.0	3.00
1444	R	M	83	C	SP, SSC, ISP	2.59	3.76
1445	L	F	91	C	SP, SSC, ISP	2.59	3.67

\*Specimens with no posterior region. R: right; L: left; F: female; M: male; RCT: rotator cuff tear; A: partial thickness tear; B: full-thickness tear with no retraction; C: full-thickness tear with retraction of the tendon; SP: supraspinatus; SCC: subscapularis; ISP: infraspinatus; —: not measured.

architectural parameters between the three tear categories and between superficial, middle, and deep parts. Significance was accepted at  $P < 0.05$  with Bonferroni adjustments made where appropriate ( $0.05/3 = 0.0167$ ).

### 3. Results

**3.1. Tendon Morphology.** Within each of the three tendon tear categories, there were four specimens. The largest diameters of the tear in the coronal and sagittal planes, measured in specimens of categories B and C, are presented in Table 1. The median tear dimensions in category C (2.96 cm for coronal plane; 3.72 cm for sagittal plane) were significantly larger than those in category B (1.58 cm for coronal plane; 1.44 cm for sagittal plane) for both planes ( $P = 0.020$  for coronal and  $P = 0.021$  for sagittal). All specimens in category C also had a tear of the infraspinatus and subscapularis tendons. There was no difference in the median age of specimens between categories.

#### 3.2. Muscle Morphology

**3.2.1. Anterior Region.** Table 2 provides a summary of the architectural parameters of the anterior region as a whole. In all specimens an anterior region was present (Figure 1). Median FBL significantly differed between the three tear categories ( $P < 0.001$ ). Specimens of category C had the shortest fibers. Median lateral PA in category C was significantly larger than categories A and B ( $P < 0.001$ ). Median medial PA significantly differed between all tear categories ( $P < 0.001$ ), with the largest PA found in category C.

Table 3 provides a summary of median FBL values of the superficial, middle, and deep parts within the anterior region. Median FBL was significantly different between all the parts in each tear category. The significance level was  $P < 0.001$  except between the superficial and deep in category B and the middle and deep in category C, which was  $P = 0.001$ .

The middle and deep parts were shorter than the superficial in all categories.

Tables 4 and 5 provide a summary of median lateral and medial PA values of the superficial, middle, and deep parts within the anterior region. Median lateral PA of the superficial part was significantly larger than the middle ( $P < 0.001$ ) in category B. No statistical difference was found between the superficial and deep ( $P = 0.022$ ) and middle and deep ( $P = 0.071$ ). No statistical difference was found between parts in category A ( $P = 0.167$ ) or category C ( $P = 0.274$ ). Median medial PA of the superficial part was significantly larger than the middle and deep ( $P < 0.001$ ) in all tear categories. No statistical difference was found between the middle and deep ( $P = 0.163$ ) in category A. In categories B and C, median medial PA was significantly different between all parts ( $P < 0.001$ ).

**3.2.2. Posterior Region.** Architectural parameters for the posterior region as a whole are summarized in Table 2. In two specimens of category C a distinct posterior region was absent (Figure 2). Due to the reduced sample size in category C, statistical analysis of these specimens was not carried out. Median FBL significantly differed between categories A and B ( $P < 0.001$ ). Median lateral PA significantly differed between categories A and B ( $P = 0.013$ ). Median lateral PA in category A was larger than category B ( $P = 0.013$ ). Median medial PA in category A was significantly larger than that of category B ( $P < 0.001$ ).

Median FBL values for the superficial, middle, and deep parts within the posterior region are summarized in Table 3. In category A, median FBL of the middle part was significantly longer than that of the superficial and deep ( $P < 0.001$ ). No statistical difference was found between the superficial and deep ( $P = 0.699$ ). In category B, no difference was found between parts ( $P = 0.114$ ).

A summary of median lateral and medial PAs of the superficial, middle, and deep parts within the posterior region can be found in Tables 4 and 5. Median lateral PA

TABLE 2: Median values of architectural parameters for anterior and posterior regions.

Region of muscle and tear category	<i>n</i>	FBL (cm)	PA lat. (degree)	PA med. (degree)
<b>Anterior</b>				
A	4	6.76 <sup>a</sup> (3.21–10.26)	14.95 <sup>a*</sup> (2.04–45.24)	13.81 <sup>a</sup> (2.17–45.11)
B	4	4.97 <sup>b</sup> (2.59–9.86)	13.91 <sup>a*</sup> (2.01–46.37)	14.77 <sup>b</sup> (2.02–46.63)
C	4	2.65 <sup>c</sup> (0.54–8.98)	23.02 <sup>b</sup> (2.06–80.38)	24.34 <sup>c</sup> (2.01–89.20)
<b>Posterior</b>				
A	4	5.89 <sup>a</sup> (2.12–8.52)	24.14 <sup>a***</sup> (2.04–38.81)	15.94 <sup>a</sup> (3.78–34.52)
B	4	4.81 <sup>b</sup> (1.48–8.92)	20.61 <sup>b***</sup> (4.42–47.55)	11.98 <sup>b</sup> (2.10–34.68)
C	2	3.02 <sup>†</sup> (1.59–4.76)	31.95 <sup>†</sup> (2.42–55.23)	14.29 <sup>†</sup> (4.83–33.15)

A: partial thickness tendon tear; B: full-thickness tear with no retraction of tendon; C: full-thickness tendon tear with retraction; FBL: fiber bundle length; PA lat.: lateral pennation angle; PA med.: medial pennation angle; ( ) minimum and maximum values. If superscript letters are different, it indicates statistically significant difference of  $P < 0.001$  of parameter between tear categories within the same region. \*  $P = 0.100$ ; \*\*  $P = 0.013$ ; † statistical analysis was not conducted due to sample size.

TABLE 3: Median FBL values for the superficial, middle, and deep parts of the anterior and posterior regions.

Region of muscle and tear category	<i>n</i>	FBL (cm)		
		Superficial	Middle	Deep
<b>Anterior</b>				
A	4	7.56 <sup>a</sup> (5.36–10.26)	6.71 <sup>b</sup> (3.21–10.01)	6.24 <sup>c</sup> (3.38–8.68)
B	4	5.58 <sup>a*</sup> (2.97–9.68)	4.71 <sup>b</sup> (2.59–9.86)	5.16 <sup>c*</sup> (2.70–9.05)
C	4	2.95 <sup>a</sup> (1.45–8.98)	2.57 <sup>b*</sup> (1.04–7.19)	2.50 <sup>c*</sup> (0.54–5.41)
<b>Posterior</b>				
A	4	5.89 <sup>a***</sup> (2.12–8.47)	6.42 <sup>b</sup> (2.79–7.91)	5.85 <sup>a***</sup> (3.19–8.52)
B	4	4.88 <sup>a***</sup> (2.13–7.82)	4.98 <sup>a***</sup> (1.50–8.92)	4.65 <sup>a***</sup> (1.48–8.54)
C	2	2.96 <sup>†</sup> (1.90–4.47)	3.48 <sup>†</sup> (1.93–4.76)	2.80 <sup>†</sup> (1.59–4.59)

A: partial thickness tendon tear; B: full-thickness tear with no retraction of tendon; C: full-thickness tendon tear with retraction; FBL: fiber bundle length; median with ( ) minimum and maximum values. If superscript letters are different, it indicates statistically significant ( $P < 0.001$ ) difference between the superficial, middle, and deep parts of specimens within the same tear category. \*  $P = 0.001$ ; \*\*  $P = 0.699$ ; \*\*\*  $P = 0.114$ ; † statistical analysis was not conducted due to sample size.

TABLE 4: Median lateral PA values for the superficial, middle, and deep parts of the anterior and posterior regions.

Region of muscle and tear category	<i>n</i>	PA lat. (degree)		
		Superficial	Middle	Deep
<b>Anterior</b>				
A	4	14.26 <sup>a*</sup> (2.62–45.24)	15.71 <sup>a*</sup> (2.04–40.86)	14.15 <sup>a*</sup> (2.37–35.39)
B	4	15.59 <sup>a***</sup> (2.27–46.37)	12.73 <sup>b***</sup> (2.01–42.70)	14.15 <sup>ab***</sup> (2.89–40.38)
C	4	25.16 <sup>a****</sup> (2.06–64.58)	22.92 <sup>a****</sup> (2.18–80.38)	21.80 <sup>a****</sup> (3.15–74.67)
<b>Posterior</b>				
A	4	26.39 <sup>a****</sup> (2.04–38.81)	25.60 <sup>a****</sup> (2.19–36.34)	18.79 <sup>b</sup> (3.92–36.57)
B	4	27.17 <sup>a</sup> (9.86–41.02)	23.43 <sup>b</sup> (4.42–47.55)	17.71 <sup>c</sup> (6.32–32.00)
C	2	38.46 <sup>†</sup> (7.82–55.23)	35.25 <sup>†</sup> (2.42–51.13)	25.17 <sup>†</sup> (2.55–46.18)

A: partial thickness tendon tear; B: full-thickness tear with no retraction of tendon; C: full-thickness tendon tear with retraction; PA lat.: lateral pennation angle; median with ( ) minimum and maximum values. If superscript letters are different, it indicates statistically significant ( $P < 0.001$ ) difference between the superficial, middle, and deep parts of specimens within the same tear category. \*  $P = 0.167$ ; \*\*  $P = 0.022$  superficial and deep,  $P = 0.071$  middle and deep; \*\*\*  $P = 0.274$ ; \*\*\*\*  $P = 0.238$ ; † statistical analysis was not conducted due to sample size.

of the superficial and middle parts was significantly larger than the deep ( $P < 0.001$ ) in category A. No statistical difference was found between the superficial and middle ( $P = 0.238$ ). In category B, median lateral PA significantly differed between all parts ( $P < 0.001$ ) with the largest being

in the superficial part. Median medial PA of the superficial part was significantly larger than the middle ( $P < 0.001$ ) in category A. No statistical difference was found between the deep and middle ( $P = 0.021$ ) or superficial ( $P = 0.026$ ). In category B, median medial PA of the superficial part was

TABLE 5: Median medial PA values for the superficial, middle, and deep parts of the anterior and posterior regions.

Region of muscle and tear category	n	PA med. (degree)		
		Superficial	Middle	Deep
<b>Anterior</b>				
A	4	15.58 <sup>a</sup> (2.19–29.78)	12.97 <sup>b</sup> (2.20–45.11)	13.87 <sup>b*</sup> (2.17–30.51)
B	4	19.22 <sup>a</sup> (3.88–44.64)	15.95 <sup>b</sup> (2.02–46.63)	11.52 <sup>c</sup> (2.34–27.95)
C	4	28.40 <sup>a</sup> (2.37–89.20)	22.96 <sup>b</sup> (2.01–85.95)	19.99 <sup>c</sup> (2.17–89.11)
<b>Posterior</b>				
A	4	17.85 <sup>a</sup> (7.14–34.52)	14.46 <sup>b***</sup> (4.52–31.42)	16.54 <sup>ab***</sup> (3.78–32.19)
B	4	14.06 <sup>a***</sup> (2.96–34.68)	13.55 <sup>ab***</sup> (2.10–23.96)	10.71 <sup>b***</sup> (2.20–33.36)
C	2	19.40 <sup>†</sup> (4.83–33.15)	12.58 <sup>†</sup> (5.29–23.38)	13.89 <sup>†</sup> (5.39–26.37)

A: partial thickness tendon tear; B: full-thickness tear with no retraction of tendon; C: full-thickness tendon tear with retraction; PA med.: medial pennation angle; median with ( ) minimum and maximum values. If superscript letters are different, it indicates statistically significant ( $P < 0.001$ ) difference between the superficial, middle, and deep parts of specimens within the same tear category. \* $P = 0.163$  middle and deep; \*\* $P = 0.026$  superficial and deep,  $P = 0.021$  middle and deep; \*\*\* $P = 0.047$  superficial and middle,  $P = 0.002$  superficial and deep, and  $P = 0.419$  middle and deep;  $P = 0.208$  middle and deep. †Statistical analysis was not conducted due to sample size.

significantly larger than that of the deep ( $P = 0.002$ ). No statistical difference was found between the middle and deep ( $P = 0.419$ ) or superficial ( $P = 0.047$ ).

#### 4. Discussion

This is the first study to investigate and model the fiber bundle architecture of the pathologic supraspinatus throughout the muscle volume including the anterior and posterior regions and their respective parts. We demonstrate that significant changes in architecture occur with rotator cuff tendon pathology and these changes are not uniform for the anterior and posterior regions of supraspinatus.

Median FBL of the anterior and posterior regions significantly differed between the tear categories, with a gradual decrease in FBL occurring as the size of the tear increased. Significant shortening of FBL with tendon tears has been reported in two previous studies [6, 7]. In both studies, however, only the anterior region was investigated as per reported lateral attachment of fiber bundles onto the intramuscular tendon. In addition, length measurements were taken from just two to three fibers from superficial surface of the anterior region of each specimen. Based on our model, we know that both anterior and posterior regions undergo significant shortening with tendon tears. Shortening of muscle fibers and tendon retraction are barriers for structural healing following open and arthroscopic tendon repair [31]. When structural healing is not achieved, recovery of strength has been poorer and the glenohumeral joint may be more prone to degenerative changes [31, 32].

In the normal supraspinatus, FBLs within the superficial, middle, and deep parts of the anterior region were found to be uniform [16]. In the present study of the pathologic muscle, however, in general as the severity of the tear increased a progressive shortening of FBLs from the superficial to deep parts was observed. This pattern of FBL change within the volume of the anterior region could be of clinical importance. First, tears on the articular surface of the supraspinatus

tendon are two to three times more frequent than bursal-sided tears [33, 34]. Our findings further support this prevalence and suggest tears involving the anterior portion of the supraspinatus tendon propagate from the articular surface toward the bursal surface. Secondly, as a consequence of this progressive shortening starting in the deep part of the muscle, the deeper fibers may undergo greater stretching during tendon repair. To achieve tendon to bone repair, the torn and often retracted musculotendinous unit is mobilized laterally. Overstretching, particularly of the shortened deep fibers, can cause damage and lead to proliferation of non-contractile tissue [33]. Furthermore, the articular side of the supraspinatus tendon has been found to experience more strain compared to the bursal surface under uniaxial loading [35]. These tendon strain patterns may be correlated with the pattern of FBL changes observed in this study.

In the posterior region, the pattern of progressive shortening of FBLs from the superficial to deep parts was not observed. The differences found between the anterior and posterior regions may be related in part to the differences in muscle architecture. For example, the fibers of the anterior region are in a penniform configuration, while in the posterior region they are fusiform.

A decrease in FBL will decrease the absolute active muscle range and maximum contraction velocity [36]. In the torn supraspinatus, sarcomeres have been found to maintain their optimal operating length [7]. Tomioka et al. [7] found no significant difference in sarcomere length of the supraspinatus between the intact and torn tendon specimens examined. Despite this maintenance, a recent study investigating the contractility of muscle fibers sampled from patients with chronic full-thickness tears found a 30% reduction in the maximum isometric force production [37]. The normalized force production was found to be negatively correlated with tear size [37]. The architectural changes documented in our study will compound these force production deficits reported by Mendias et al. [37]. Our data on FBL along with insights of sarcomere lengths changes [7] and muscle fiber contractility [37] can be used in future computer modeling studies to

predict the changes in active range and contraction velocity of the pathologic muscle and to simulate the biomechanical effects on the shoulder complex.

An increase in PA with rotator cuff tendon tears has been previously reported with larger and retracted tears being correlated with larger angles [8, 17]. Although direct comparison of our PA values with those from other cadaveric and imaging studies is difficult due to differences in measurement methods, our findings support the general trends reported in these previous studies. In the present study, median lateral and medial PAs of the anterior region were significantly larger in specimens with a retracted tendon. In contrast, the median lateral and medial PAs of the posterior region were significantly larger in specimens with partial tears compared to full-thickness tears. Again, these regional differences may be attributed to differences in muscle architecture and possibly the location of the tendon pathology, that is, articular versus bursal sided and/or anterior versus posterior.

The posterior region of the supraspinatus was present in all normal specimens examined by Kim et al. [16] and Roh et al. [14]. The absence of a distinguishable posterior region in half of the specimens with large retracted tendon tears in the present study raises important clinical questions given the broad lateral attachment of fibers onto the supraspinatus tendon and its distinct function [18–21]. First, what is the functional impact of not having a posterior region in both the unrepaired and repaired tendon states? Since the posterior region is thought to quickly adjust tension on the rotator cuff, preventing buckling of the tendon with dynamic movement [20, 21], the loss of this region can have a significant functional impact. The residual function of the pathological muscle thus needs to be better understood. Expectations and approaches for rehabilitation and surgical repair may also need to be altered when there is loss of the posterior region. Secondly, is loss of the posterior region an eventual change that occurs with chronic tendon tears? It is known that chronicity of the tendon tear is positively related to rotator cuff muscle atrophy [38, 39]. As the volume of the posterior region is significantly smaller than that of the anterior region in the normal muscle [14, 16] even a small amount of atrophy could considerably impact the posterior region. If atrophy or complete loss is indeed found to be an eventual consequence of chronic tears, it would further underscore the importance of early detection of the tear and repair of the tendon. Delayed detection of tears is associated with surgical complications and inferior outcomes [40] and extensive changes to the posterior region may play a role in these problems.

## 5. Conclusions

The fiber bundle architecture of both anterior and posterior regions was investigated and distinct patterns of change were found. Fiber bundle length shortening is associated with the degree of tendon tear with the fibers of the deep part showing the greatest degree of shortening. Pennation angle changes are also related to the degree of tendon tear, with the superficial fibers possibly undergoing greater changes than other parts of the muscle. The posterior region

was completely absent in specimens with extensive tendon tears raising several clinically relevant questions that need to be further explored. Since the supraspinatus muscle is an important dynamic stabilizer of the glenohumeral joint and most commonly involved with rotator cuff pathology, a thorough understanding of the muscle changes is essential. It is expected that the model created in this study will be used to advance computer models that can simulate different surgical techniques and rehabilitation protocols. Furthermore, the model can be incorporated with existing shoulder models to be used for biomechanical analysis in different patient populations with supraspinatus tendon pathologies.

## Conflict of Interests

The authors declare that there is no conflict of interests regarding the publication of this paper.

## Acknowledgments

The authors would like to acknowledge the Saskatchewan Health Research Foundation (SHRF) for funding this project. They would like to express gratitude to the families who participated in the Body Bequeathal Program of the Department of Anatomy and Cell Biology, College of Medicine, University of Saskatchewan. They also thank Corrie Willfong and David Shewchuk, technical staff of the Department of Anatomy and Cell Biology, Autodesk Inc., for providing the research/educational license for Autodesk Maya 2009 (Autodesk Inc., San Rafael, CA, USA), Valerie Oxorn, B.A., M.A., M.S., B.M.C., Medical Illustrator, for illustrating Figure 1, and the College of Medicine, University of Saskatchewan.

## References

- [1] C. J. Petersson, "Ruptures of the supraspinatus tendon. Cadaver dissection," *Acta Orthopaedica Scandinavica*, vol. 55, no. 1, pp. 52–56, 1984.
- [2] X. Liu, D. Laron, K. Natsuhara, G. Manzano, H. T. Kim, and B. T. Feeley, "A mouse model of massive rotator cuff tears," *The Journal of Bone & Joint Surgery—American Volume*, vol. 94, no. 7, article e41, 2012.
- [3] D. Goutallier, J.-M. Postel, J. Bernageau, L. Lavau, and M.-C. Voisin, "Fatty muscle degeneration in cuff ruptures: pre- and postoperative evaluation by CT scan," *Clinical Orthopaedics and Related Research*, no. 304, pp. 78–83, 1994.
- [4] D. Goutallier, J.-M. Postel, P. Gleyze, P. Leguilloux, and S. Van Driessche, "Influence of cuff muscle fatty degeneration on anatomic and functional outcomes after simple suture of full-thickness tears," *Journal of Shoulder and Elbow Surgery*, vol. 12, no. 6, pp. 550–554, 2003.
- [5] C. Gerber, D. C. Meyer, E. Frey et al., "Neer Award 2007: reversion of structural muscle changes caused by chronic rotator cuff tears using continuous musculotendinous traction. An experimental study in sheep," *Journal of Shoulder and Elbow Surgery*, vol. 18, no. 2, pp. 163–171, 2009.
- [6] E. Itoi, H.-C. Hsu, S. W. Carmichael, B. F. Morrey, and K.-N. An, "Morphology of the torn rotator cuff," *Journal of Anatomy*, vol. 186, no. 2, pp. 429–434, 1995.

- [7] T. Tomioka, H. Minagawa, H. Kijima et al., "Sarcomere length of torn rotator cuff muscle," *Journal of Shoulder and Elbow Surgery*, vol. 18, no. 6, pp. 955–959, 2009.
- [8] J. Zuo, H. Sano, and E. Itoi, "Changes in pennation angle in rotator cuff muscles with torn tendons," *Journal of Orthopaedic Science*, vol. 17, no. 1, pp. 58–63, 2012.
- [9] R. L. Lieber and S. R. Ward, "Skeletal muscle design to meet functional demands," *Philosophical Transactions of the Royal Society B: Biological Sciences*, vol. 366, no. 1570, pp. 1466–1476, 2011.
- [10] R. L. Lieber and J. Fridén, "Clinical significance of skeletal muscle architecture," *Clinical Orthopaedics and Related Research*, no. 383, pp. 140–151, 2001.
- [11] J. B. Morrison, "The mechanics of muscle function in locomotion," *Journal of Biomechanics*, vol. 3, no. 4, pp. 431–451, 1970.
- [12] R. L. Lieber and S. C. Bodine-Fowler, "Skeletal muscle mechanics: implications for rehabilitation," *Physical Therapy*, vol. 73, no. 12, pp. 844–856, 1993.
- [13] C. Gans and A. S. Gaunt, "Muscle architecture in relation to function," *Journal of Biomechanics*, vol. 24, no. 1, pp. 53–65, 1991.
- [14] M. S. Roh, V. M. Wang, E. W. April, R. G. Pollock, L. U. Bigliani, and E. L. Flatow, "Anterior and posterior musculotendinous anatomy of the supraspinatus," *Journal of Shoulder and Elbow Surgery*, vol. 9, no. 5, pp. 436–440, 2000.
- [15] A. D. Ward, G. Hamarneh, R. Ashry, and M. E. Schweitzer, "3D shape analysis of the supraspinatus muscle: a clinical study of the relationship between shape and pathology," *Academic Radiology*, vol. 14, no. 10, pp. 1229–1241, 2007.
- [16] S. Y. Kim, E. L. Boynton, K. Ravichandiran, L. Y. Fung, R. Bleakney, and A. M. Agur, "Three-dimensional study of the musculotendinous architecture of supraspinatus and its functional correlations," *Clinical Anatomy*, vol. 20, no. 6, pp. 648–655, 2007.
- [17] S. M. Thompson, P. Reilly, R. J. Emery, and A. M. J. Bull, "An anatomical description of the pennation angles and central tendon angle of the supraspinatus both in its normal configuration and with full thickness tears," *Journal of Shoulder and Elbow Surgery*, vol. 20, no. 6, pp. 899–903, 2011.
- [18] V. Karas, V. M. Wang, A. Dhawan, and B. J. Cole, "Biomechanical factors in rotator cuff pathology," *Sports Medicine and Arthroscopy Review*, vol. 19, no. 3, pp. 202–206, 2011.
- [19] S. Kim, R. Bleakney, E. Boynton et al., "Investigation of the static and dynamic musculotendinous architecture of supraspinatus," *Clinical Anatomy*, vol. 23, no. 1, pp. 48–55, 2010.
- [20] S. Y. Kim, D. D. Lunn, R. J. Dyck, L. J. Kirkpatrick, and B. W. C. Rosser, "Fiber type composition of the architecturally distinct regions of human supraspinatus muscle: a cadaveric study," *Histology and Histopathology*, vol. 28, no. 8, pp. 1021–1028, 2013.
- [21] J. A. Hermenegildo, S. L. Roberts, and S. Y. Kim, "Innervation pattern of the suprascapular nerve within supraspinatus: a three-dimensional computer modeling study," *Clinical Anatomy*, vol. 27, no. 4, pp. 622–630, 2014.
- [22] P. L. Powell, R. R. Roy, P. Kanim, M. A. Bello, and V. R. Edgerton, "Predictability of skeletal muscle tension from architectural determinations in guinea pig hindlimbs," *Journal of Applied Physiology*, vol. 57, no. 6, pp. 1715–1721, 1984.
- [23] D. C. Meyer, K. Wieser, M. Farshad, and C. Gerber, "Retraction of supraspinatus muscle and tendon as predictors of success of rotator cuff repair," *American Journal of Sports Medicine*, vol. 40, no. 10, pp. 2242–2247, 2012.
- [24] S. L. Delp, F. C. Anderson, A. S. Arnold et al., "OpenSim: open-source software to create and analyze dynamic simulations of movement," *IEEE Transactions on Biomedical Engineering*, vol. 54, no. 11, pp. 1940–1950, 2007.
- [25] K. R. Saul, X. Hu, C. M. Goehler et al., "Benchmarking of dynamic simulation predictions in two software platforms using an upper limb musculoskeletal model," *Computer Methods in Biomechanics and Biomedical Engineering*, vol. 18, no. 13, pp. 1445–1458, 2014.
- [26] S. L. Delp, A. S. Arnold, R. A. Speers, and C. A. Moore, "Hamstrings and psoas lengths during normal and crouch gait: implications for muscle-tendon surgery," *Journal of Orthopaedic Research*, vol. 14, no. 1, pp. 144–151, 1996.
- [27] A. G. Hannam, I. K. Stavness, J. E. Lloyd, S. S. Fels, A. J. Miller, and D. A. Curtis, "A comparison of simulated jaw dynamics in models of segmental mandibular resection versus resection with alloplastic reconstruction," *The Journal of Prosthetic Dentistry*, vol. 104, no. 3, pp. 191–198, 2010.
- [28] A. M. Agur, V. Ng-Thow-Hing, K. A. Ball, E. Fiume, and N. H. McKee, "Documentation and three-dimensional modelling of human soleus muscle architecture," *Clinical Anatomy*, vol. 16, no. 4, pp. 285–293, 2003.
- [29] D. Lee, K. Ravichandiran, K. Jackson, E. Fiume, and A. Agur, "Robust estimation of physiological cross-sectional area and geometric reconstruction for human skeletal muscle," *Journal of Biomechanics*, vol. 45, no. 8, pp. 1507–1513, 2012.
- [30] D. Lee, Z. Li, Q. Z. Sohail, K. Jackson, E. Fiume, and A. Agur, "A three-dimensional approach to pennation angle estimation for human skeletal muscle," *Computer Methods in Biomechanics and Biomedical Engineering*, vol. 18, no. 13, pp. 1474–1484, 2015.
- [31] H. Ellman, "Diagnosis and treatment of incomplete rotator cuff tears," *Clinical Orthopaedics and Related Research*, no. 254, pp. 64–74, 1990.
- [32] D. C. Meyer, M. Farshad, N. A. Amacker, C. Gerber, and K. Wieser, "Quantitative analysis of muscle and tendon retraction in chronic rotator cuff tears," *American Journal of Sports Medicine*, vol. 40, no. 3, pp. 606–610, 2012.
- [33] M. A. Zumstein, J. B. Hempel, J. Hodler, and C. Gerber, "The clinical and structural long-term results of open repair of massive tears of the rotator cuff," *The Journal of Bone and Joint Surgery—American Volume*, vol. 90, no. 11, pp. 2423–2431, 2008.
- [34] G. M. Gartsman and J. C. Milne, "Articular surface partial-thickness rotator cuff tears," *Journal of Shoulder and Elbow Surgery*, vol. 4, no. 6, pp. 409–415, 1995.
- [35] C.-Y. Huang, V. M. Wang, R. J. Pawluk et al., "Inhomogeneous mechanical behavior of the human supraspinatus tendon under uniaxial loading," *Journal of Orthopaedic Research*, vol. 23, no. 4, pp. 924–930, 2005.
- [36] R. L. Lieber, *Skeletal Muscle Structure, Function, and Plasticity: The Physiological Basis of Rehabilitation*, Lippincott Williams & Wilkins, Baltimore, Md, USA, 3rd edition, 2010.
- [37] C. L. Mendias, S. M. Roche, J. A. Harning et al., "Reduced muscle fiber force production and disrupted myofibrillar architecture in patients with chronic rotator cuff tears," *Journal of Shoulder and Elbow Surgery*, vol. 24, no. 1, pp. 111–119, 2015.
- [38] C. Gerber, D. C. Meyer, A. G. Schneeberger, H. Hoppeler, and B. von Rechenberg, "Effect of tendon release and delayed repair on the structure of the muscles of the rotator cuff: an experimental study in sheep," *The Journal of Bone & Joint Surgery—American Volume*, vol. 86, no. 9, pp. 1973–1982, 2004.
- [39] J. N. Gladstone, J. Y. Bishop, I. K. Y. Lo, and E. L. Flatow, "Fatty infiltration and atrophy of the rotator cuff do not improve after

rotator cuff repair and correlate with poor functional outcome,” *The American Journal of Sports Medicine*, vol. 35, no. 5, pp. 719–728, 2007.

- [40] M. E. Hantes, G. K. Karidakis, M. Vlychou, S. Varitimidis, Z. Dailiana, and K. N. Malizos, “A comparison of early versus delayed repair of traumatic rotator cuff tears,” *Knee Surgery, Sports Traumatology, Arthroscopy*, vol. 19, no. 10, pp. 1766–1770, 2011.

## Research Article

# How to Quantify Penile Corpus Cavernosum Structures with Histomorphometry: Comparison of Two Methods

**Bruno Felix-Patricio,<sup>1,2</sup> Diogo Benchimol De Souza,<sup>1</sup> Bianca Martins Gregório,<sup>1</sup> Waldemar Silva Costa,<sup>1</sup> and Francisco José Sampaio<sup>1</sup>**

<sup>1</sup>*Urogenital Research Unit, State University of Rio de Janeiro, Boulevard 28 de Setembro, 87 Fundos, Vila Isabel, 20551-030 Rio de Janeiro, RJ, Brazil*

<sup>2</sup>*Institute for Humanities and Health, Federal Fluminense University, Rua Recife, s/n, Jardim Bela Vista, Rio das Ostras, RJ, Brazil*

Correspondence should be addressed to Diogo Benchimol De Souza; [diogobenchimol@gmail.com](mailto:diogobenchimol@gmail.com)

Received 4 February 2015; Revised 31 March 2015; Accepted 7 April 2015

Academic Editor: Tuncay Peker

Copyright © 2015 Bruno Felix-Patricio et al. This is an open access article distributed under the Creative Commons Attribution License, which permits unrestricted use, distribution, and reproduction in any medium, provided the original work is properly cited.

The use of morphometrical tools in biomedical research permits the accurate comparison of specimens subjected to different conditions, and the surface density of structures is commonly used for this purpose. The traditional point-counting method is reliable but time-consuming, with computer-aided methods being proposed as an alternative. The aim of this study was to compare the surface density data of penile corpus cavernosum trabecular smooth muscle in different groups of rats, measured by two observers using the point-counting or color-based segmentation method. Ten normotensive and 10 hypertensive male rats were used in this study. Rat penises were processed to obtain smooth muscle immunostained histological slices and photomicrographs captured for analysis. The smooth muscle surface density was measured in both groups by two different observers by the point-counting method and by the color-based segmentation method. Hypertensive rats showed an increase in smooth muscle surface density by the two methods, and no difference was found between the results of the two observers. However, surface density values were higher by the point-counting method. The use of either method did not influence the final interpretation of the results, and both proved to have adequate reproducibility. However, as differences were found between the two methods, results obtained by either method should not be compared.

## 1. Introduction

Cell and tissue morphological alterations are highly associated with functional and developmental changes and thus are the focus of scientific research [1]. Traditionally, tissue or cell morphology is studied by describing normal and/or pathological findings of the organ of interest.

Although the description of morphological changes is valid in some specific circumstances, for most situations, scientific data gain value when expressed numerically [2, 3], and this is the premise supporting the use of morphometry for medical research. Commonly, it is possible to quantify morphological changes in disease-affected structures or after medical or surgical treatments [4]. Macroscopic or microscopic quantification of a structure increases accuracy by

generating numerical data that can be used for statistical comparisons, thus giving credibility to the study [5, 6].

Score quantification based on observer's interpretation has been previously reported, but as the result depends directly on experience, the method is less reliable and reproducible. Thus, the use of objective morphometric analytical methods is preferable, as observer's experience will have little impact on the outcome of the results [5, 6].

The quantification of structure surface density of an organ, tissue, or cell allows their characterization and comparison in different pathological conditions. For example, Bertoni-Freddari et al. [7] measured synaptic surface density in different areas of the cerebral cortex of monkeys at different ages to study the effects of aging on the brain, while Romek et al. [8] used this methodology to study inner mitochondrial

membrane surface density in relation to the preimplantation development and metabolic alterations of the porcine embryo. Therefore, these methods provide important information to enable comparisons between groups of patients or animals subjected to different conditions.

The surface density of a structure of interest is traditionally calculated using the point-counting method, whereby the number of points that intercepts the structure is divided by the total number of points superimposed to the field of interest. Although this method is considerably reliable, as long as its premises (i.e., randomization, repetition, and blind measurements) are respected [5, 6, 9–11], the time spent counting the points of each analyzed image is a major disadvantage.

Computer-aided quantification of structures based on the area occupied by certain colors has emerged as an alternative [12–14]. This method, called color-based segmentation, requires less time for its execution, accelerating the achievement of scientific results. According to this method, the structure to be quantified must have a color distinguishable from the other structures in the image, so that the computer can measure the percentage of the area occupied by that color, and consequently of the structure of interest.

Although both methods are considered reliable and reproducible for surface density determination, they have not been objectively compared under the same biological conditions. In principle, comparable structure surface density results should be obtained using the point-counting or color-based segmentation method in the same group of individual samples.

The aim of this study is to compare the results of surface density analysis of penile corpus cavernosum smooth muscle in different groups of rats, measured by the point-counting and color-based segmentation method and by two different observers.

## 2. Materials and Methods

**2.1. Experimental Design.** Twenty 120-day-old male rats were used in this experiment. Rats were maintained in an animal facility room at a temperature of  $21 \pm 1^\circ\text{C}$ , with a controlled 12-hour light/dark cycle (artificial light, 7:00 am to 7:00 pm), and received commercial food and water *ad libitum*. All procedures were carried out in conformity with the conventional guidelines on animal experimentation. Experimental protocols were approved by the Institutional Animal Experimentation Ethics Committee (Protocol no. CEUA/051/2012).

The animals were divided into two groups: a normotensive Wistar Kyoto strain (WKY) group and a spontaneously hypertensive strain (SHR) group, containing 10 rats each. Systolic blood pressure was measured weekly to validate the experimental models used [15].

**2.2. Euthanasia and Histological Procedures.** Rats were euthanized at 160 days of age with an anesthetic overdose and their penises were dissected and fixed in 4% buffered formalin. Because of the presence of a distal bone in the rat penis, the midshaft of each organ was used for morphological analyses.

This tissue was processed for paraffin embedding and  $5\ \mu\text{m}$  thick sections were prepared. Immunolabeling was performed using a primary antibody antismooth muscle  $\alpha$ -actin (Zymed Laboratories, Carlsbad, California) (Figure 1(a)).

All morphometrical analyses were carried out from photomicrographs captured under  $\times 400$  magnification, using a digital camera (DP70, Olympus, Tokyo, Japan) coupled to a microscope (BX51, Olympus, Tokyo, Japan). For each animal, 25 histological fields of cavernous tissue were photographed. In these photomicrographs, the trabecular smooth muscle surface density was quantified by the two different methods described below. All morphometrical analyses were performed by two different researchers.

**2.3. Counting-Point Method [4, 9, 16–18].** For this analysis, the Image J software (version 1.45s, National Institutes of Health, Bethesda, USA) was used. A 99-point grid was superimposed over the images using the grid tool of Image J software, and the points touching the trabecular smooth muscle were marked and counted with the cell counter tool. The number of points touching the smooth muscle was multiplied by 100 and divided by 99 to correct for the 99 points used as test system (Figure 1(b)). This result was considered the surface density and expressed as a percentage. The mean of 25 analyzed photomicrographs was considered as the smooth muscle surface density for each animal.

**2.4. Color-Based Segmentation [13, 19, 20].** For this analysis, the Image-Pro Plus software (version 4.5.0.29z, Media Cybernetics, Rockville, USA) was used. The smooth muscle surface area was calculated using the histogram tool after a color segmentation of the image, based on automatic counting of the percentage of pixels with the same color (brown in our immunohistochemistry images).

First, the brown colored pixels in the image were marked with the perform segmentation tool, selecting different positive stained areas, and a mask created with the new mask tool. All selected areas of the images were transformed into white colored pixels while the remaining pixels appeared in black (Figure 1(c)). Then, the “histogram” tool was opened and moving the bar to the right, the percentage of white pixels was determined by the software (Figure 1(d)). This percentage represents the surface density of brown colored areas, previously selected, and, thus, the smooth muscle surface density. The mean of 25 analyzed photomicrographs was considered as the smooth muscle surface density for each animal.

**2.5. Statistical Analysis.** The data were first tested for normality using the Shapiro-Wilk normality test. All data passed the normality test and were considered to be parametric ( $P > 0.05$ ). The means of the WKY versus SHR group, obtained by each observer and analyzed by the counting-point and color-based segmentation methods, were compared using an unpaired Student's *t*-test. Finally, to test the reproducibility of each method, the results obtained by observers A and B were compared with the paired Student's *t*-test. All analyses were performed using the GraphPad Prism 5.0 software

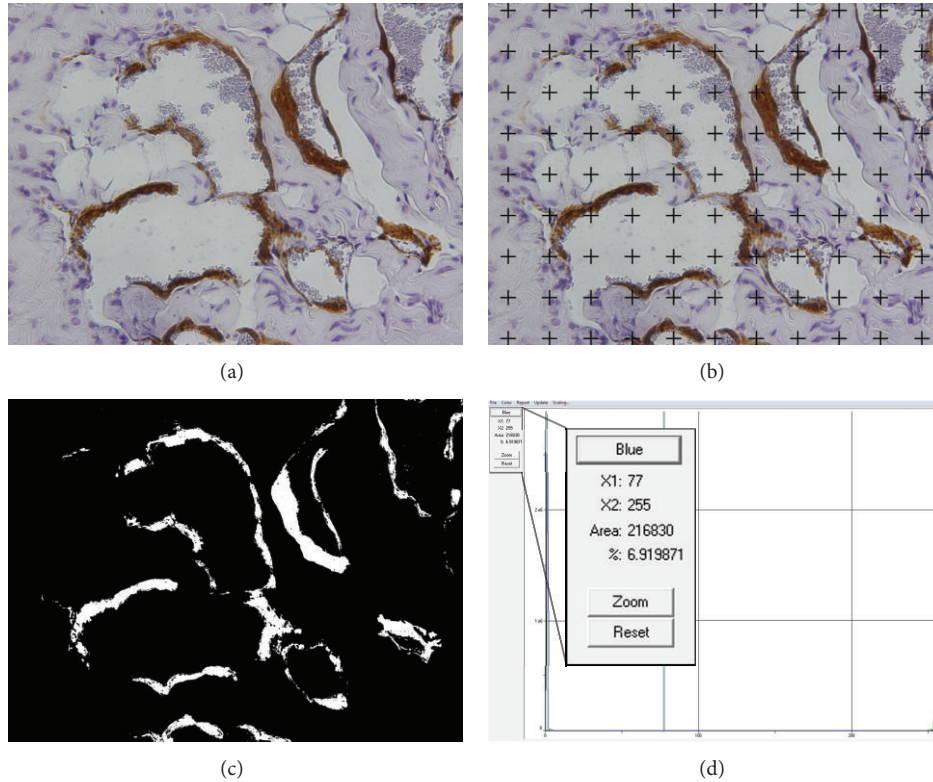


FIGURE 1: (a) Example of a histological field of a rat’s corpus cavernosum immunostained with antismooth muscle  $\alpha$ -actin and captured under a  $\times 400$  magnification field. (b) The same field after superimposition of the 99-point grid. The points touching the smooth muscle were counted. (c) The same field after all smooth muscle areas was transformed into white colored pixels while the remaining pixels of the images appear in black. (d) Histogram data of image (c) showing that 6.9% of the image is composed by white pixels, that is, smooth muscle.

TABLE 1: Smooth muscle surface density of corpus cavernosum of Wistar Kyoto normotensive animals (WKY) and spontaneously hypertensive rats (H) as measured by two different morphometrical methods.

Observer	WKY	H	<i>P</i> value
<b>A</b>			
Point-counting method (%)	10.30 $\pm$ 3.08	13.28 $\pm$ 1.33	0.012
Color-based segmentation method (%)	09.18 $\pm$ 2.72	11.48 $\pm$ 1.76	0.038
<i>P</i> value	0.119	0.001	
<b>B</b>			
Point-counting method (%)	11.08 $\pm$ 2.27	13.94 $\pm$ 1.45	0.003
Color-based segmentation method (%)	07.85 $\pm$ 0.93	10.83 $\pm$ 2.34	0.002
<i>P</i> value	0.001	0.002	

Data are shown as mean  $\pm$  standard deviation. Means were considered significantly different if  $P < 0.05$ .

(GraphPad Software, San Diego, USA). Mean differences were considered significant if  $P < 0.05$ . All results are presented as the mean  $\pm$  standard deviation.

### 3. Results

The smooth muscle surface density analyzed by the point-counting and color-based segmentation method was 26–29% (observer A  $P = 0.035$ ; observer B  $P = 0.012$ ) and 25–32% (observer A  $P = 0.038$ ; observer B  $P = 0.002$ ) higher, respectively, in hypertensive (SHR) than in normotensive (WKY) animals (Figure 2 and Table 1).

Comparison of smooth muscle surface density between the two methods in normotensive (WKY) animals showed no difference between the means obtained by observer A ( $P = 0.119$ ), but the means obtained by observer B were significantly different ( $P = 0.001$ ). Moreover, when smooth muscle surface density between the two methods was compared in the hypertensive (SHR) animals, the means obtained by the point-counting method were higher than that obtained by the color-based segmentation method, for both observers (observer A  $P = 0.001$ ; observer B 0.002).

Finally, when comparing the results obtained by observer A and observer B, for each group of animals and type of

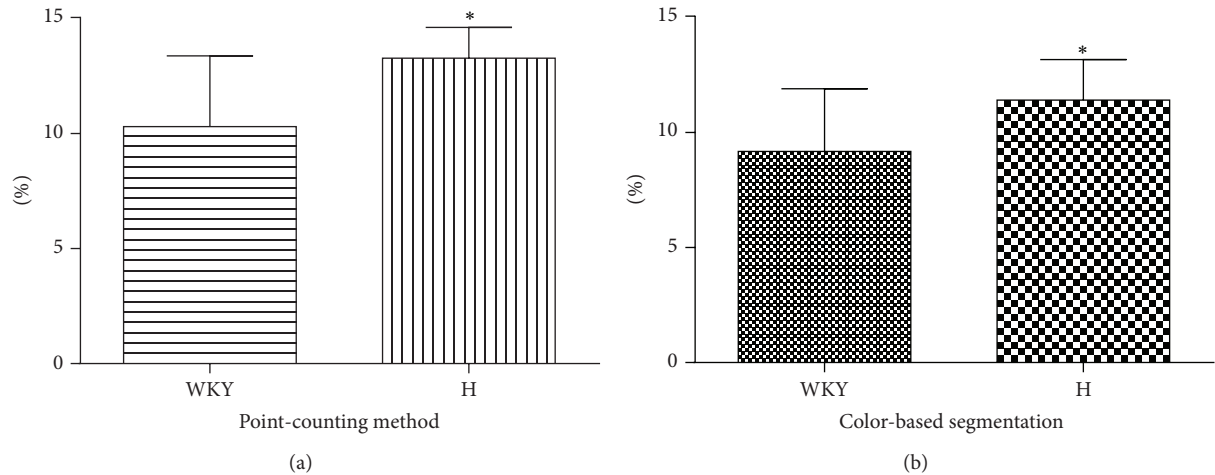


FIGURE 2: (a) Smooth muscle surface density measured by the point-counting method in the corpus cavernosum of normotensive and hypertensive rats ( $*P = 0.012$ ). (b) Smooth muscle surface density measured by the color-based segmentation method, in corpus cavernosum of normotensive and hypertensive rats ( $*P = 0.038$ ) (columns and error bars represent the mean and standard deviation, resp.). Results shown are those of observer A.

method, no statistical differences were found (point-counting method, WKY  $P = 0.437$ ; SHR  $P = 0.323$ ; color-based segmentation method, WKY  $P = 0.180$ ; SHR  $P = 0.518$ ).

#### 4. Discussion

The quantification of morphological structures is highly recommended for studying biological alterations in tissues, cells, or intracellular organelles. Translating the morphology in numbers is useful as it improves the understanding of changes in the specimens under examination [6, 11]. In addition, numerical data allows statistical comparisons with other specimens, subjected to different conditions or at different developmental stages. Based on these premises, morphometry has been extensively used in different biomedical research fields, and important scientific knowledge has been generated from morphometrical analyses [21–24].

Surface density is one of the most commonly used morphometrical tools. It represents the percentage of area occupied by the measured structure, which according to the Delesse principle, allows its quantity estimation [5, 9]. Given the importance of surface density measurement, we decided to study this tool more thoroughly.

However, as intra- and interobserver variability (the normal biological variation) in the quantification of the same structure occur, the number of measurements necessary for the adequate estimation of surface density needs to be taken into account. One principle used for the determination of the number of measurements is that the structure being measured by the point-counting method should be touched by 200 points for each individual [11]. Accordingly, it is thought that 20 fields in which 99 points are counted in each should be sufficient to measure the smooth muscle rat's corpus cavernosum. In our studies of cavernous tissue in different species, surface density measurements are commonly performed by counting 99 or 100 points per field, in 25 fields.

In this study, we used our standard laboratory protocol and analyzed 25 fields per animal. Considering that 10 animals were studied per group, we analyzed 250 fields or 24,750 points.

However, calculating surface density by the point-counting method is time-consuming, as the analysis of the structure of interest requires the full observer's attention to avoid overcounting or missing points that touch the studied structure. To overcome these issues, the color-based segmentation method is increasingly being used in several laboratories (as used in this study or with some variations) [13, 14, 19]. This method is based on the principle of differential color staining of structures, after which the percentage of pixels of one color can be measured in the field using different image editing software. This measurement can be performed in a few steps and the final results are rapidly obtained. Moreover, compared to the point-counting method whereby only some samples of the images (where the superimposed points are located) are analyzed, the color-based segmentation method allows the analysis of the whole field. These features highly increase precision and favor the use of the color-based segmentation over the point-counting method.

However, the great advantage of the so-called automated methods is the absence of observer's interference. As mentioned above, a distraction may result in a researcher missing or overcounting the points touching the structure of interest, leading to underestimation or overestimation of surface density when the point-counting method is used. In principle, these types of error should not occur with automated methods as the analysis is not interpreted by an individual. Nevertheless, discrepancies between different tones of the same color may not be automatically adjusted by the software, resulting in a lack of color uniformity within the same image and in different images. For example, the immunohistochemical preparations shown in this study appeared to have different tones of brown, most of them

corresponding to smooth muscle. Thus, to reduce color variation, manual adjustment by the observer is required. However, this not only adds bias due to systematic over- or underestimation of surface density structure but also increases the time it takes for the researcher to perform the analysis. Thus, special attention should be taken when using this color adjustment tool.

In this study, the interpretation of results was not affected by the method used to measure cavernous smooth muscle surface density. This parameter showed a statistically significant increase in hypertensive animals, comparable between the two methods (25% versus 29%). Also, it was found that the results obtained with both methods were reproducible as no differences were observed between observers. This is a very important aspect to consider, since reproducibility is one of the pillars of morphometric evaluation of biologic structures.

It is possible that when the point-counting method was used, some points that did not touch the smooth muscle were counted as such, leading to count overestimation. However, it is more acceptable that when the color-based segmentation method was used a common mistake has occurred. When setting the software to interpret what tones should be considered brown, some dark or light brown shades could be missed, resulting in count underestimation.

However, as color standardization in all fields is challenging, color tone differences are common in histological images. These issues hinder the application of the color-based segmentation method to histological specimens and should be taken into consideration when choosing the method. This study showed that, although the interpretation of results was not affected, differences between methods were observed. Compared to the systematic errors to which the color-based segmentation method is prone regardless of researcher's experience, we favor the use of the point-counting method, despite being time-consuming, as a well-trained researcher is less likely to make counting errors.

## 5. Conclusion

The use of the point-counting or color-based segmentation method did not influence the final interpretation of results, and both proved to be reproducible between different researchers. However, as differences were found between the two methods, results obtained by either method should not be compared.

## Conflict of Interests

The authors declare no competing financial interests.

## Acknowledgments

This study was funded by grants from the National Council of Scientific and Technological Development (CNPq; <http://www.cnpq.br/>), Foundation for Research Support of Rio de Janeiro (FAPERJ; <http://www.faperj.br/>), and Coordination for the Improvement of Higher Education Personnel (CAPES; <http://www.capes.gov.br/>), Brazil. This work was

conducted at the Urogenital Research Unit, State University of Rio de Janeiro.

## References

- [1] K. Perica, A. K. Kosmides, and J. P. Schneck, "Linking form to function: biophysical aspects of artificial antigen presenting cell design," *Biochimica et Biophysica Acta—Molecular Cell Research*, vol. 1853, no. 4, pp. 781–790, 2015.
- [2] M. Flisinski, A. Brymora, G. Elminowska-Wenda et al., "Morphometric analysis of muscle fibre types in rat locomotor and postural skeletal muscles in different stages of chronic kidney disease," *Journal of Physiology and Pharmacology*, vol. 65, no. 4, pp. 567–576, 2014.
- [3] B. Kundalić, S. Ugrenović, I. Jovanović et al., "Morphometric analysis of connective tissue sheaths of sural nerve in diabetic and nondiabetic patients," *BioMed Research International*, vol. 2014, Article ID 870930, 7 pages, 2014.
- [4] W. S. Costa, F. B. Carrerete, W. G. Horta, and F. J. B. Sampaio, "Comparative analysis of the penis corpora cavernosa in controls and patients with erectile dysfunction," *BJU International*, vol. 97, no. 3, pp. 567–569, 2006.
- [5] H. R. Anderson, A. W. Stitt, T. A. Gardiner, and D. B. Archer, "Estimation of the surface area and volume of the retinal capillary basement membrane using the stereologic method of vertical sections," *Analytical and Quantitative Cytology and Histology*, vol. 16, no. 4, pp. 253–260, 1994.
- [6] C. A. Mandarim-de-Lacerda, "Stereological tools in biomedical research," *Anais da Academia Brasileira de Ciências*, vol. 75, no. 4, pp. 469–486, 2003.
- [7] C. Bertoni-Freddari, P. Fattoretti, B. Giorgetti et al., "Synaptic and mitochondrial morphometry provides structural correlates of successful brain aging," *Annals of the New York Academy of Sciences*, vol. 1097, pp. 51–53, 2007.
- [8] M. Romek, B. Gajda, M. Rolka, and Z. Smorag, "Mitochondrial activity and morphology in developing porcine oocytes and pre-implantation non-cultured and cultured embryos," *Reproduction in Domestic Animals*, vol. 46, no. 3, pp. 471–480, 2011.
- [9] A. J. Baddeley, H. J. Gundersen, and L. M. Cruz-Orive, "Estimation of surface area from vertical sections," *Journal of Microscopy*, vol. 142, pp. 259–276, 1986.
- [10] C. Bertoni-Freddari, P. Fattoretti, B. Giorgetti et al., "Alterations of synaptic turnover rate in aging may trigger senile plaque formation and neurodegeneration," *Annals of the New York Academy of Sciences*, vol. 1096, pp. 128–137, 2007.
- [11] L. M. Cruz-Orive and E. R. Weibel, "Recent stereological methods for cell biology: a brief survey," *The American Journal of Physiology—Lung Cellular and Molecular Physiology*, vol. 258, no. 3, pp. L148–L156, 1990.
- [12] Y.-C. Liu, H.-C. Chen, H.-H. Shih et al., "Computer aided quantification of pathological features for flexor tendon pulleys on microscopic images," *Computational and Mathematical Methods in Medicine*, vol. 2013, Article ID 914124, 9 pages, 2013.
- [13] Y.-N. Sun, Y.-Y. Wang, S.-C. Chang, L.-W. Wu, and S.-T. Tsai, "Color-based tumor tissue segmentation for the automated estimation of oral cancer parameters," *Microscopy Research and Technique*, vol. 73, no. 1, pp. 5–13, 2010.
- [14] T. H. Yang, H. C. Chen, Y. C. Liu et al., "Clinical and pathological correlates of severity classifications in trigger fingers based on computer-aided image analysis," *BioMedical Engineering OnLine*, vol. 13, article 100, 2014.

- [15] B. Felix-Patricio, J. L. Medeiros, D. B. De Souza, W. S. Costa, and F. J. Sampaio, "Penile histomorphometrical evaluation in hypertensive rats treated with sildenafil or enalapril alone or in combination: a comparison with normotensive and untreated hypertensive rats," *The Journal of Sexual Medicine*, vol. 12, no. 1, pp. 39–47, 2015.
- [16] D. B. de Souza, L. L. de Oliveira, M. C. da Cruz et al., "Laparoscopic partial nephrectomy under warm ischemia reduces the glomerular density in a pig model," *Journal of Endourology*, vol. 26, no. 6, pp. 706–710, 2012.
- [17] D. B. de Souza, D. Silva, C. M. Cortez, W. S. Costa, and F. J. B. Sampaio, "Effects of chronic stress on penile corpus cavernosum of rats," *Journal of Andrology*, vol. 33, no. 4, pp. 735–739, 2012.
- [18] C. T. Ribeiro, D. B. D. Souza, J. L. Medeiros Jr., W. S. Costa, M. A. Pereira-Sampaio, and F. J. B. Sampaio, "Pneumoperitoneum induces morphological alterations in the rat testicle," *Acta Cirurgica Brasileira*, vol. 28, no. 6, pp. 419–422, 2013.
- [19] C. B. Gallo, W. S. Costa, A. Furriel, A. L. Bastos, F. J. Sampaio, and M. S. Kellermayer, "Modifications of erectile tissue components in the penis during the fetal period," *PLoS ONE*, vol. 9, no. 8, Article ID e106409, 2014.
- [20] A. F. Miranda, C. B. M. Gallo, D. B. de Souza, W. S. Costa, and F. J. B. Sampaio, "Effects of castration and late hormonal replacement in the structure of rat corpora cavernosa," *Journal of Andrology*, vol. 33, no. 6, pp. 1224–1232, 2012.
- [21] N. Barbuto, J. R. Almeida, L. M. M. Pereira, and C. A. Mandarim-De-Lacerda, "Renal cortex remodeling in nitric oxide deficient rats treated with enalapril," *Journal of Cellular and Molecular Medicine*, vol. 8, no. 1, pp. 102–108, 2004.
- [22] J. Chen, S. Toghi Eshghi, G. Bova, Q. Li, X. Li, and H. Zhang, "Epithelium percentage estimation facilitates epithelial quantitative protein measurement in tissue specimens," *Clinical Proteomics*, vol. 10, no. 1, p. 18, 2013.
- [23] W. S. Costa, M. N. Ribeiro, L. E. M. Cardoso et al., "Nutritional supplementation with l-arginine prevents pelvic radiation-induced changes in morphology, density, and regulating factors of blood vessels in the wall of rat bladder," *World Journal of Urology*, vol. 31, no. 3, pp. 653–658, 2013.
- [24] O. T. Da Costa, A. C. Pedretti, A. Schmitz, S. F. Perry, and M. N. Fernandes, "Stereological estimation of surface area and barrier thickness of fish gills in vertical sections," *Journal of Microscopy*, vol. 225, no. 1, pp. 1–9, 2007.

## Research Article

# Dentin Morphology of Root Canal Surface: A Quantitative Evaluation Based on a Scanning Electronic Microscopy Study

Giuseppe Lo Giudice,<sup>1</sup> Giuseppina Cutroneo,<sup>2,3</sup> Antonio Centofanti,<sup>2,3</sup>  
Alessandro Artemisia,<sup>1</sup> Ennio Bramanti,<sup>1</sup> Angela Militi,<sup>1</sup> Giuseppina Rizzo,<sup>2,3</sup>  
Angelo Favaloro,<sup>2,3</sup> Alessia Irrera,<sup>4</sup> Roberto Lo Giudice,<sup>1</sup> and Marco Cicciù<sup>5</sup>

<sup>1</sup>Department of Medical-Surgery and Odontostomatologic Experimental Sciences, University of Messina, Italy

<sup>2</sup>Department of Biomedical Sciences and Morpho-Functional Imaging, University of Messina, Italy

<sup>3</sup>IRCCS Centro Neurolesi "Bonino-Pulejo", Messina, Italy

<sup>4</sup>IPCF-CNR Viale Stagno D'Alcontres, 98100 Messina, Italy

<sup>5</sup>Department of Human Pathology, University of Messina, Via Consolare Valeria, 98100 Messina, Italy

Correspondence should be addressed to Marco Cicciù; [acromarco@yahoo.it](mailto:acromarco@yahoo.it)

Received 14 February 2015; Revised 25 March 2015; Accepted 13 April 2015

Academic Editor: Levent Sarikcioglu

Copyright © 2015 Giuseppe Lo Giudice et al. This is an open access article distributed under the Creative Commons Attribution License, which permits unrestricted use, distribution, and reproduction in any medium, provided the original work is properly cited.

Dentin is a vital, hydrated composite tissue with structural components and properties that vary in the different topographic portions of the teeth. These variations have a significant implication for biomechanical teeth properties and for the adhesive systems utilized in conservative dentistry. The aim of this study is to analyse the root canal dentin going from coronal to apical zone to find the ratio between the intertubular dentin area and the surface occupied by dentin tubules varies. Observations were conducted on 30 healthy premolar teeth extracted for orthodontic reasons in patients aged between 10 and 14. A SEM analysis of the data obtained in different canal portions showed that, in the coronal zone, dentinal tubules had a greater diameter ( $4.32\ \mu\text{m}$ ) than the middle zone ( $3.74\ \mu\text{m}$ ) and the apical zone ( $1.73\ \mu\text{m}$ ). The average number of dentinal tubules (in an area of  $1\ \text{mm}^2$ ) was similar in coronal zone ( $46,798 \pm 10,644$ ) and apical zone ( $45,192 \pm 10,888$ ), while in the middle zone they were lower in number ( $30,940 \pm 7,651$ ). However, intertubular dentin area was bigger going from apical to coronal portion. The differences between the analysed areas must be considered for the choice of the adhesive system.

## 1. Introduction

Dentin is the calcified tissue that forms the major part of the tooth. It is composed mainly by type I collagen fibrils (and a small amount of types III, IV collagen, noncollagen proteins, and proteoglycans) and by hydroxylapatite [1–3].

Anatomic dentin microstructure shows dentinal tubules, cylindrical canals of  $1\text{--}2\ \mu\text{m}$  in diameter, running from the pulp to the dentinoenamel junction (DEJ) in the crown, and the cementodentinal junction (CEJ) in the root. An intertubular dentin layer individually surrounds these tubules. Calcified collagen fibrils are  $50\text{--}100\ \mu$  of average diameter and constitute the dentin basic structure; they are orthogonal to

the tubules and form an intertubular dentin matrix network [1, 4].

In order to evaluate dentin ultrastructure several studies [5, 6] and many different techniques have been performed immunofluorescence, microradiography, scanning electron microscopy (SEM), and transmission electron microscopy (TEM).

A detailed knowledge of dentin structure is essential in order to understand its physiology and the mechanism by which different adhesive systems work in restorative dentistry. In the total etching technique we use the exposed intertubular collagen fibrils together with resin tubular tags to obtain a  $>20\ \text{MPa}$  adhesion force [5–8].

The majority of teeth anatomical studies analyse the coronal dentinal substratum. Cagidiaco and Ferrari [6] demonstrated how the anatomy of the coronal dentin is characterized by different density, diameter, and orientation of dentinal tubules in different cavity preparation cutting planes.

From the literature analysis, observing the coronal part of the dentin layer close to the pulp, the dentinal tubules number was 65,000–45,000/mm<sup>2</sup>; this number was higher if compared to the outer dentin areas (15,000–20,000/mm<sup>2</sup>) [9, 10].

The tubular diameter is larger near to the pulp (3–4  $\mu$ ) and smaller in the peripheral area near to the DEJ (average diameter 1.7  $\mu$ ). Casually large dentinal tubules have been observed [11].

Age determines variations of the tubular lumen diameter due to a physiological sclerosis of the dentinal tubules; indeed, in advanced age, the tubules located in the most superficial dentin layer may measure even 0.2  $\mu$  [12].

Dentinal tubules have very thin collateral ramifications (1  $\mu$  diameter). These secondary tubules are right-angled, divided, and connected to closer tubules through intertubular dentin forming a three-dimensional network [11, 13].

We can state that tubule morphology and intertubular substance differences were found in coronal and root dentin as well as a wide variation among different areas of the root canal [14, 15].

This micromorphological study is aimed to evaluate, in vitro, dentinal tubules size and tubular distribution in coronal, middle, and apical root portions. This anatomical condition, related to the intertubular dentin area and the surface occupied by dentinal tubules (determined by their number and diameter), may influence the adhesives efficiency in endocanal cementation of composite reinforced posts.

## 2. Materials and Methods

Observations were conducted on 30 healthy premolars extracted for orthodontic reasons, in patients aged between 10 and 14 (mean age: 11.4 years, STD 1.26) and preserved in saline solution (0.9%) at 4°C. Informed consent was obtained from all patients and all the procedures were performed according to the Helsinki Declaration of 1975.

The preparation procedure of specimens consisted in a preliminary tooth crown and a root pulp tissue removal.

Pulp removal was performed using manual endodontic files under irrigation of 5% NaOCl (Nicolor 5; OGNA Lab S.r.l Muggiò, MB, IT) at 50°C, alternating with 17% EDTA (OGNA Lab S.r.l Muggiò, MB, IT) for 20 min followed by a wash with 5% NaOCl for 1 min and a saline solution (OGNA Lab S.r.l Muggiò, MB, IT).

Preliminary to the observation we proceeded by etching the canal lumen with 37% orthophosphoric acid (Universal Etchant Scotchbond; 3M ESPE, St. Paul, USA) for 15 sec., washing with saline solution and metallizing [16]. Afterwards, all specimens were divided along the longitudinal axis using a coronal-apical groove such as a fracture guide.

All specimens were analysed with Gemini Field Emission SEM (FE-SEM) SUPRA 25 (Carl Zeiss NTS GmbH, Oberkochen, Germany), with an EDAX EDX detector.

Surface was analysed with a 1.7  $\mu$ m resolution (15 kV) at a 3072  $\times$  2304 pixels resolution. A 2,500x was used to quantify dentinal tubules density and intertubular surface, while a 23,000x was used to evaluate tubule morphology. Three different areas (coronal, middle, and apical) of the root canal of each specimen were examined [16, 17]. Within the same area of the canal, measurement was conducted by taking random references from three default areas that were 400  $\mu$ m<sup>2</sup>. According to anatomical observations, the number of tubules in the three measurement areas was quantified and the tubules average number was calculated in each area (Table 1). On 9 tubules randomly selected within each area (3 for each area) the diameter was measured (Table 1).

According to these data, quantification of the dentinal surface area occupied by the tubular lumens (in absolute value and percentage) and intertubular dentin surface area was made.

The aforementioned quantification was carried out as follows.

- (1) Identification of the number of dentinal tubules per mm<sup>2</sup>: this parameter was calculated by the Schellenberg formula ( $X = n10^6/z$ ), where  $n$  is the number of tubules observed in each analysed area and  $z$  is the global surface of observation (Table 2).
- (2) Identification of tubular lumen average surface: considering the tubule section is roughly circular, and the area was obtained through its average diameter (Table 2).
- (3) Calculation of area occupied by all tubules: this datum was obtained by multiplying tubules number in one mm<sup>2</sup> to tubules average area (Table 2).
- (4) The intertubular dentin surface area was obtained by subtraction of the area occupied by the tubules (Table 2).

A further datum was obtained by calculating the percentage ratio between the observation area and the tubular lumen area (Table 2).

A two-way ANOVA test is a way for investigating the effect of two nominal predictor variables on a continuous outcome variable. For this reason two-way analysis of variance (ANOVA) was performed to verify statistically significant difference among the tested groups. A  $P$  value < 0.05 was considered as significant. Then we considered the post hoc doc accordingly with LSD Fisher' test:  $LSD = t_{\alpha/2,df} \sqrt{2S_e^2/n}$  in order to have the significance values [18].

## 3. Results

The analysis of the data obtained from the microphotographs taken in various canal portions is summarised in Tables 1 and 2 and Graphs (Figures 1(a) and 1(b)).

Table 1 shows averages, found in each specimen, and standard deviation of the number of tubules identified in the three random areas, carried out in the coronal, middle, and apical root canal portions.

TABLE 1: Average and St. Dev. of tubular number and tubular diameter (three observations/areas of 400  $\mu\text{m}^2$ ).

	Sample 1	Sample 2	Sample 3	Sample 4	Sample 5	Sample 6	Sample 7	Sample 8	Sample 9	Sample 10	
Portion	Tubular number										
Apical	17	6	21	23	11	13	19.33	23	25	22	
Middle	12	13.66	12.66	11.33	11	7.66	16.6	14	18	7.12	
Coronal	14.66	17.33	23.33	12	14.33	15	23	21	26	22	
Portion	Tubular diameter										
Apical	0.69	3.36	0.62	0.56	2.21	1.93	2.17	2.34	2.28	2.1	
Middle	6.11	2.32	2.72	3.12	2.6	4.69	6.64	6.35	5.97	6.03	
Coronal	3.36	3.08	3.38	5.38	4.05	5.8	5.9	5.05	3.69	6.43	
	Sample 11	Sample 12	Sample 13	Sample 14	Sample 15	Sample 16	Sample 17	Sample 18	Sample 19	Sample 20	
Portion	Tubular number										
Apical	15	20	18	14	22	24	14.33	22	17	14	
Middle	12.33	5.33	15.66	8.66	15.33	12	14.66	16.33	15.33	13.33	
Coronal	20.66	12.33	16.33	13	15	13.66	24	23.66	18.33	23	
Portion	Tubular diameter										
Apical	0.67	0.58	2.11	3.2	2.15	2.33	2.56	2.54	0.54	0.66	
Middle	1.7	3.13	3.08	3.17	2.41	2.64	2.36	2.98	3.48	3.27	
Coronal	2.44	4.38	4.2	3.97	2.57	3.57	4.25	5.7	3.33	5.76	
	Sample 21	Sample 22	Sample 23	Sample 24	Sample 25	Sample 26	Sample 27	Sample 28	Sample 29	Sample 30	
Portion	Tubular number										
Apical	21	20.33	14	15	23	22	17	16	14.66	18.66	
Middle	13.66	11.66	12.66	11.33	7.33	15	14.66	7.33	11.33	13.33	
Coronal	21.33	18.33	14.66	19.66	15.33	24	24.66	16.33	11.33	23.33	
Portion	Tubular diameter										
Apical	2.26	2.73	0.55	2.44	2.23	2.72	0.41	1.97	0.46	0.56	
Middle	2.42	2.86	4.79	3.21	6.23	2.46	3.47	6.12	2.7	3.44	
Coronal	5.27	3.9	3.54	4.2	4.67	5.37	4.21	4.1	3.76	4.41	
			Tubular number						Tubular diameter		
			Portion	Average	St. Dev.				Portion	Average	St. Dev.
			Apical	18.077	4.35				Apical	1.731	0.93
			Middle	12.376	3.10				Middle	3.749	1.48
			Coronal	18.586	4.25				Coronal	4.324	1.00

TABLE 2: Observation data ( $\text{mm}^2$  and %) for each root portion.

Portion	Tubular number ( $\text{mm}^2$ )	Tubular lumen area ( $\mu\text{m}^2$ )	Surface occupied by tubules ( $1\text{mm}^2$ )	Intertubular area ( $\text{mm}^2$ )	Tubular lumen area/dentinal surface (%)
Apical	45,192 $\pm$ 10,888	3.033 $\pm$ 2.43	0.14	0.86	13.71%
Middle	30,940 $\pm$ 7,651	12.77 $\pm$ 10.23	0.40	0.60	39.53%
Coronal	46,798 $\pm$ 10,644	15.47 $\pm$ 7.06	0.72	0.28	72.42%

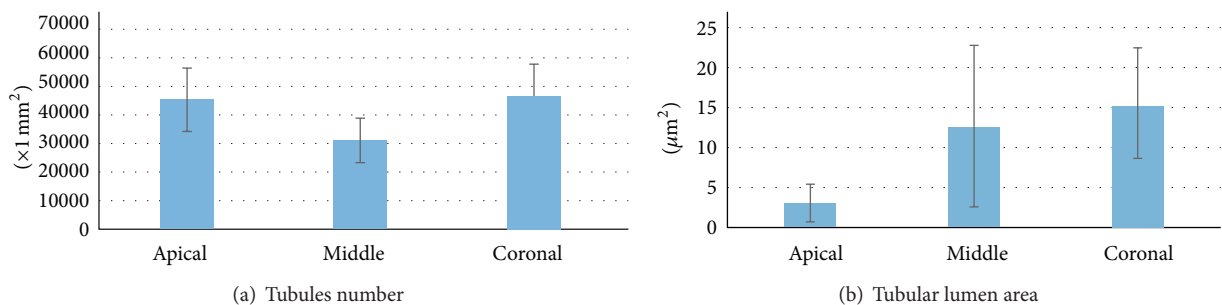


FIGURE 1: Dentinal tubules number (in  $1\text{mm}^2$ ) (a) and tubular lumen area ( $\mu\text{m}^2$ ) (b) in each root portion.

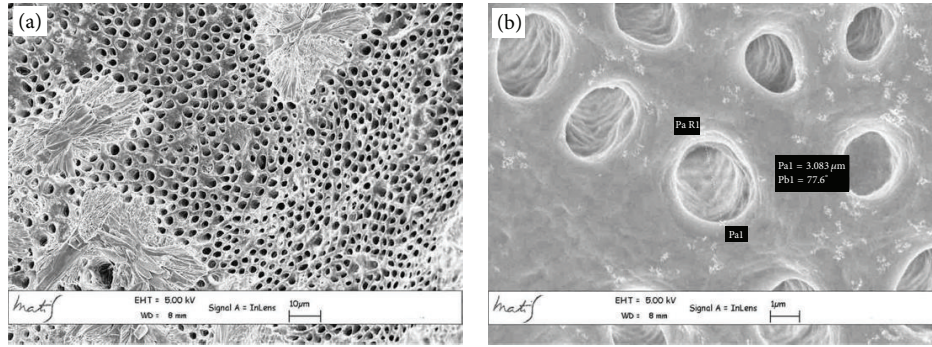


FIGURE 2: Coronal area metallised dentin specimens analysed with Gemini Field Emission SEM (FEM-SEM) at  $1.7 \mu\text{m}$  and  $3072 \times 2304$  pixel resolution 2500x (a) and 23000x (b) magnification: presence of calcospherites (Figure 3(a)).

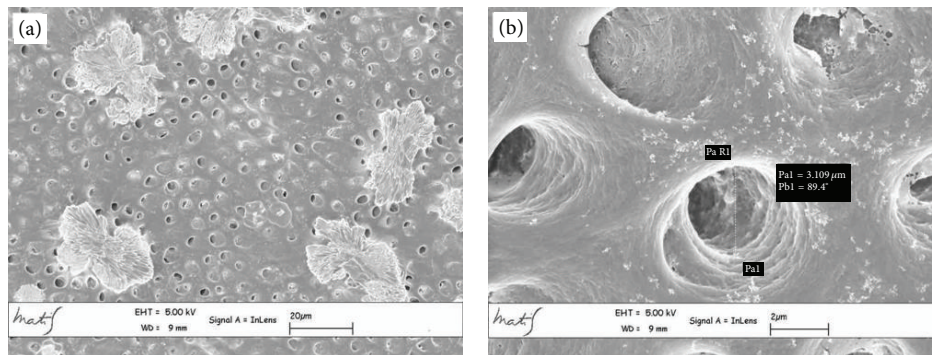


FIGURE 3: Middle area metallised dentin specimens analysed with Gemini Field Emission SEM (FEM-SEM) at  $1.7 \mu\text{m}$  and  $3072 \times 2304$  pixel resolution 2500x (a) and 23000x (b) magnification: presence of calcospherites (Figure 4(a)).

The average linear values of the dentinal tubules diameters evaluated in 9 areas, expressed in  $\mu\text{m}$ , are listed in Table 2. The average diameter within the various areas has a variation range between  $6.43$  and  $2.44 \mu\text{m}$  (coronal area Figures 2(a) and 2(b)),  $6.64$  and  $1.7 \mu\text{m}$  (middle area Figures 3(a) and 3(b)), and  $3.36$  and  $0.41 \mu\text{m}$  (apical area Figures 4(a) and 4(b)).

General averages calculated in  $\text{mm}^2$  show that the coronal third of the canal has a higher tubular density than the middle third ( $46,798 \pm 10,644 \text{mm}^2$  versus  $30,940 \pm 7,651 \text{mm}^2$ ). In the same areas the tubules average diameter decreases ( $4.324 \mu\text{m}$  versus  $3.749 \mu\text{m}$ ). The apical third shows an average tubular density of  $45,192 \pm 10,888 \text{mm}^2$  that is similar to the coronal third, but with smaller tubular diameter ( $1.731 \mu\text{m}$ ) (Table 1).

The ANOVA analysis shows that differences between tubular diameter and number observed among the three canal areas (apical versus middle, middle versus coronal) and the ones evaluated by post hoc Fisher's test ( $\text{LSD} = t_{\alpha/2,df} \sqrt{2S_e^2/n}$ ) result significant ( $P < 0.05$ ).

As shown in Table 2 and Figure 2, the ratio between tubular lumen area and dentinal surface, moving from coronal to apical areas, decreases from  $72.42\%$  to  $39.53\%$  and  $13.71\%$ .

Furthermore, analysing individually high-magnification microphotographs, the secondary tubules appear to be more common inside the dentinal tubule wall in the coronal

portion than those observed in the middle and apical portions (Figures 5(a), 5(b), and 5(c)).

#### 4. Discussion

The restoration of teeth treated with endodontic therapy frequently requires the use of endocanal post cemented with adhesive resin, in order to provide the retention of the coronal restoration and to achieve a better homogeneity between the composite inlay, the build-up, the fiber posts, and the luting agents, reinforcing the residual dental structure [19, 20].

Ferrari et al. [21] report that the anatomical variations that are present between different dentin portions of the root canal can influence the efficiency of the adhesive system used; therefore, the knowledge of details related to canal dentinal structure as well as its tubules and their ramifications is essential to develop efficacious resinous build-ups, adhesives, and endodontic cements [5].

Several authors [21–24] described anatomical variations of both number and size of dentinal tubules, when moving from the coronal to the apical portion of the root canal.

Data retrieved from our research show a substantial morphological variability among the dentin that forms the different endocanal regions; this variability is seen in tubular number differences and diameter differences. Moving

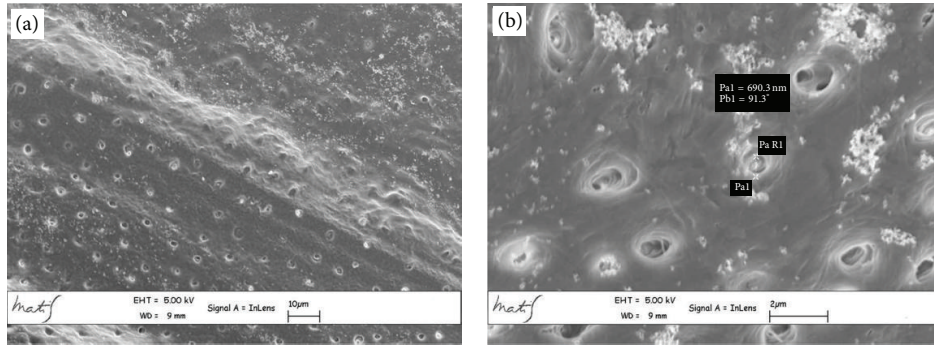


FIGURE 4: Apical area metallised dentin specimens analysed with Gemini Field Emission SEM (FEM-SEM) at 1.7  $\mu\text{m}$  and 3072  $\times$  2304 pixel resolution 2500x (a) and 23000x (b) magnification.

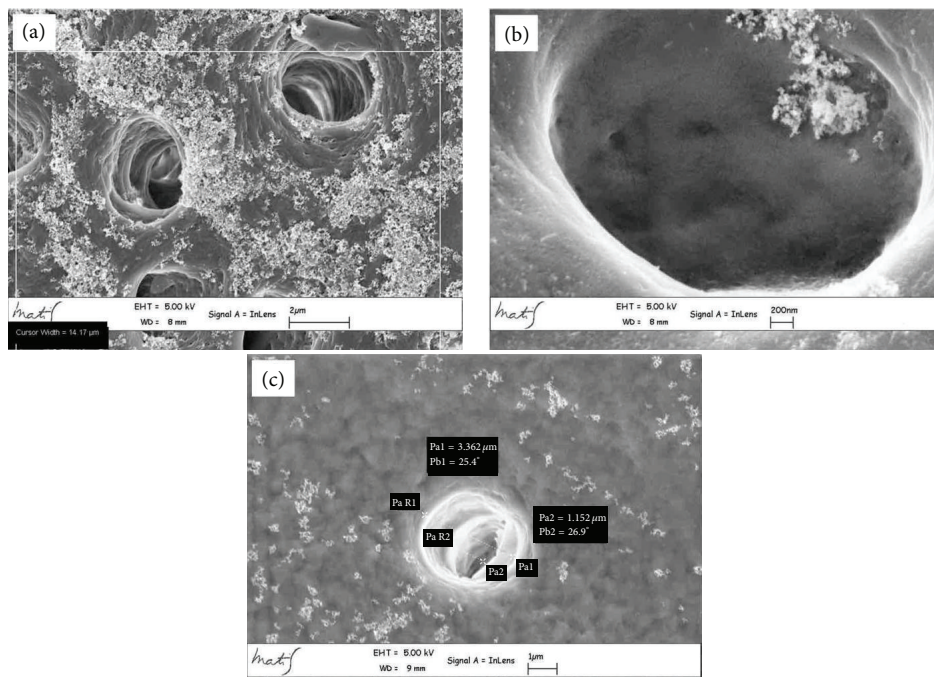


FIGURE 5: High magnification microphotograph analysis shows a higher number of secondary tubules access cavities in coronal zone than (a) in the middle (b) and apical (c) ones. In Figure (c) the Pa1 is 3.362  $\mu\text{m}$  and it represents the external diameter while the Pa2 is 1.152  $\mu\text{m}$  and it represents the diameter of the internal portion of the tubule.

forward from coronal to apical zone our study shows how the tubular lumen area progressively decreases from 15.47  $\pm$  7.06  $\mu\text{m}^2$  of the coronal zone to 12.77  $\pm$  10.23  $\mu\text{m}^2$  of the middle zone, reaching his minimum of 3.033  $\pm$  2.43  $\mu\text{m}^2$  in the apical zone.

Tubular distribution does not seem to be regular moving from 46,798  $\pm$  10,644  $\text{mm}^2$  to 30,940  $\pm$  7,651  $\text{mm}^2$  and to 45,192  $\pm$  10,888  $\text{mm}^2$ , respectively, in the coronal, middle, and apical zones.

From the crossed analysis of this data it is evident how the surface occupied by the intertubular dentin, calculated by difference, progressively increases moving from coronal to apical while the ratio between tubular lumen area and dentinal surface progressively decreases (Table 2, Figure 2).

The endocanal structural differences resulted from our data analysis appear to be substantially influenced by the diameter instead of the tubular number.

Although some authors consider that the endocanal zone does not affect adhesion, further studies have revealed differences [25, 26].

According to the authors, the push-out test shows higher bond strength values in the apical third than those in other parts of the root canal [27–30].

Differences, in the endocanal regions, regarding the efficiency of various adhesive systems (total-etch and self-etching adhesive systems) are reported in the literature.

A study by Perdigão et al. [24] showed higher bond strength values in the coronal region using total-etch system. This kind of adhesive exploits both a resin-collagen hybrid

layer formation and a micromechanical retention with resin tags inside the dentinal tubules.

The presence of numerous tubules with big diameter and secondary tubule access cavities, identified in our research, can promote this mechanism [31].

Instead in the apical region, the self-etching adhesives that exploit all the dentinal surface show better performances, because the adhesion with these systems is obtained modifying the collagen fibers present in the intertubular dentin area [25, 28, 30].

Our observations agree with this thesis and explain their inner mechanisms, showing the presence of numerous small diameter tubules and a wide intertubular area surface.

Considering this observation, the dentin, as interface of endocanal adhesion, has to be studied not only considering its tubular number but also considering its diameter and consequently the intertubular dentin characteristics that, biologically, are strictly linked to the odontoblast activities that induce and regulate the mineralization [32].

These cells are involved in type I collagen synthesis and the secretion of proteoglycans and noncollagenous proteins, increasing the level of mineralization of secondary dentin.

The secondary dentin deposition is associated with odontoblasts reorganization in a single layer and determines the decrease in the number of odontoblasts [9].

Bjørndal and Thylstrup demonstrated a low frequency of disjunctions between the odontoblast layer and the predentin in the undermineralized tooth [33].

In presence of carious lesions further mineralization and dentinal anatomy modifications are evident, along with the tertiary dentin formation from the odontoblast-like cells and partially from fibroblasts. Considering that tooth maturation and bacteria invasion can cause intratubular and peritubular ex novo dentin formation, dentinal surface does not have to be considered constant in time [32, 34, 35].

Our research has been conducted on premolars in paediatric-aged patients, extracted for orthodontic reasons, in order not to include excessive variables in the research data.

The results of our research showed that dentinal structure varied in the different root canal portions. This anatomic peculiarity can explain the differences identified in the adhesive efficiency in the different endocanal regions.

The dentinal microscopic structure is an important topic in conservative dentistry for the choice of different adhesive technologies and for a correct clinical approach.

## Conflict of Interests

The authors declare that there is no conflict of interests regarding the publication of this paper.

## References

- [1] A. Linde and M. Goldberg, "Dentinogenesis," *Critical Reviews in Oral Biology & Medicine*, vol. 45, pp. 679–728, 1993.
- [2] A. Nanci, *Oral Histology. Development, Structure and Function*, Mosby, St. Louis, Mo, USA, 2003.
- [3] R. K. Nalla, A. E. Porter, C. Daraio et al., "Ultrastructural examination of dentin using focused ion-beam cross-sectioning and transmission electron microscopy," *Micron*, vol. 36, no. 7-8, pp. 672–680, 2005.
- [4] S. J. Jones and A. Boyde, "Ultrastructure of dentin and dentinogenesis," in *Dentin and Dentinogenesis*, pp. 81–134, CRC Press, Linde, Boca Raton, Fla, USA, 1984.
- [5] I. A. Mjör, M. R. Smith, M. Ferrari, and F. Mannocci, "The structure of dentine in the apical region of human teeth," *International Endodontic Journal*, vol. 34, no. 5, pp. 346–353, 2001.
- [6] M. C. Cagidiaco and M. Ferrari, *Bonding to dentin. Mechanism, morphology and efficacy of bonding resin composites to dentin in vitro and in vivo [Ph.D. thesis]*, University of Amsterdam, Amsterdam, The Netherlands, 1995.
- [7] A. J. Gwinnett, F. R. Tay, K. M. Pang, and S. H. Y. Wei, "Quantitative contribution of the collagen network in dentin hybridization," *American Journal of Dentistry*, vol. 9, no. 4, pp. 140–144, 1996.
- [8] J. Perdigão, G. Gomes, and V. Augusto, "The effect of dowel space on the bond strengths of fiber posts," *Journal of Prosthodontics*, vol. 16, no. 3, pp. 154–164, 2007.
- [9] J.-C. Franquin, M. Remusat, I. A. Hashieh, and J. Dejou, "Immunocytochemical detection of apoptosis in human odontoblasts," *European Journal of Oral Sciences*, vol. 106, no. 1, pp. 384–387, 1998.
- [10] L. Vermelin, S. Lécolle, D. Septier, J.-J. Lasfargues, and M. Goldberg, "Apoptosis in human and rat dental pulp," *European Journal of Oral Sciences*, vol. 104, no. 5-6, pp. 547–553, 1996.
- [11] H. Agematsu, H. Watanabe, H. Yamamoto, M. Fukayama, T. Kanazawa, and K. Miake, "Scanning electron microscopic observations of microcanals and continuous zones of interglobular dentin in human deciduous incisal dentin," *The Bulletin of Tokyo Dental College*, vol. 31, no. 2, pp. 163–173, 1990.
- [12] L. Schroeder and R. M. Frank, "High-resolution transmission electron microscopy of adult human peritubular dentine," *Cell and Tissue Research*, vol. 242, no. 2, pp. 449–451, 1985.
- [13] T. Dyngeland, G. Fosse, and N. P. Berg Justesen, "Histochemical study of giant tubule content in dentin of unerupted cow incisors," *Scandinavian Journal of Dental Research*, vol. 92, no. 3, pp. 177–182, 1984.
- [14] G. R. Holland, "Morphological features of dentine and pulp related to dentine sensitivity," *Archives of Oral Biology*, vol. 39, pp. 3s–11s, 1994.
- [15] W. Grayson and J. Marshall, "Dentina: microestructura y caracterización," *Quintessence*, vol. 8, pp. 160–170, 1995.
- [16] R. A. Pimenta, C. V. D. S. R. Penido, R. D. A. Cruz, and J. B. Alves, "Morphology of the dentin on primary molars after the application of phosphoric acid under different conditions," *Brazilian Oral Research*, vol. 24, no. 3, pp. 323–328, 2010.
- [17] M. B. Lopes, M. A. C. Sinhoreti, A. G. Júnior, S. Consani, and J. F. McCabe, "Comparative study of tubular diameter and quantity for human and bovine dentin at different depths," *Brazilian Dental Journal*, vol. 20, no. 4, pp. 279–283, 2009.
- [18] C. R. Rao, "Diversity: its measurement, decomposition, apportionment and analysis," *Sankhyā: The Indian Journal of Statistics Series A*, vol. 44, part 1, pp. 1–12, 1982.
- [19] M.-A. Kahnouei, N. Mohammadi, E.-J. Navimipour, and M. Shakerifar, "Push-out bond strength of quartz fibre posts to root canal dentin using total-etch and self-adhesive resin cements," *Medicina Oral, Patologia Oral y Cirugia Bucal*, vol. 17, no. 2, pp. 337–344, 2012.

- [20] G. lo Giudice, F. Lipari, A. Lizio, G. Cervino, and M. Cicciù, "Indirect composite restorations in the posterior region—case reports," *International Journal of Clinical Dentistry*, vol. 1, article 1, 2008.
- [21] M. Ferrari, F. Mannocci, A. Vichi, M. C. Cagidiaco, and I. A. Mjör, "Bonding to root canal: structural characteristics of the substrate," *American Journal of Dentistry*, vol. 13, no. 5, pp. 255–260, 2000.
- [22] L. Boschian Pest, G. Cavalli, P. Bertani, and M. Gagliani, "Adhesive post-endodontic restorations with fiber posts: push-out tests and SEM observations," *Dental Materials*, vol. 18, no. 8, pp. 596–602, 2002.
- [23] C. Goracci, F. T. Sadek, A. Fabianelli, F. R. Tay, and M. Ferrari, "Evaluation of the adhesion of fiber posts to intraradicular dentin," *Operative Dentistry*, vol. 30, no. 5, pp. 627–635, 2005.
- [24] J. Perdigão, S. Geraldeli, and I. K. Lee, "Push-out bond strengths of tooth-colored posts bonded with different adhesive systems," *American Journal of Dentistry*, vol. 17, no. 6, pp. 422–426, 2004.
- [25] R. M. Foxton, M. Nakajima, J. Tagami, and H. Miura, "Adhesion to root canal dentine using one and two-step adhesives with dual-cure composite core materials," *Journal of Oral Rehabilitation*, vol. 32, no. 2, pp. 97–104, 2005.
- [26] C. Goracci, A. U. Tavares, A. Fabianelli et al., "The adhesion between fiber posts and root canal walls: comparison between microtensile and push-out bond strength measurements," *European Journal of Oral Sciences*, vol. 112, no. 4, pp. 353–361, 2004.
- [27] B. H. Kivanç, H. D. Arisu, M. B. Üçtaşı, and T. C. Okay, "The effect of different adhesive system applications on push-out bond strengths of glass fiber posts," *Journal of Advanced Prosthodontics*, vol. 5, no. 3, pp. 305–311, 2013.
- [28] K. Bitter, H. Meyer-Lueckel, K. Priehn, J. P. Kanjuparambil, K. Neumann, and A. M. Kielbassa, "Effects of luting agent and thermocycling on bond strengths to root canal dentine," *International Endodontic Journal*, vol. 39, no. 10, pp. 809–818, 2006.
- [29] L. Muniz and P. Mathias, "The influence of sodium hypochlorite and root canal sealers on post retention in different dentin regions," *Operative Dentistry*, vol. 30, no. 4, pp. 533–539, 2005.
- [30] B. A. Gaston, L. A. West, F. R. Liewehr, C. Fernandes, and D. H. Pashley, "Evaluation of regional bond strength of resin cement to endodontic surfaces," *Journal of Endodontics*, vol. 27, pp. 321–324, 2001.
- [31] M.-A. Kahnamousi, N. Mohammadi, E.-J. Navimipour, and M. Shakerifar, "Push-out bond strength of quartz fibre posts to root canal dentin using total-etch and self-adhesive resin cements," *Medicina Oral, Patologia Oral y Cirugia Bucal*, vol. 17, no. 2, pp. e337–e344, 2012.
- [32] F. Bleicher, "Odontoblast physiology," *Experimental Cell Research*, vol. 325, no. 2, pp. 65–71, 2014.
- [33] L. Bjørndal and A. Thylstrup, "A comparative histologic study of the pulp-dentinal interface in undemineralized and demineralized tooth sections," *Acta Odontologica Scandinavica*, vol. 52, no. 4, pp. 198–202, 1994.
- [34] M. T. Mamaladze and M. G. Ustiashvili, "Theoretical and practical principles of dentinogenesis: hypotheses and confirmed clinically reality," *Georgian Medical News*, vol. 186, pp. 22–28, 2010.
- [35] W. H. Arnold, S. Konopka, and P. Gaengler, "Qualitative and quantitative assessment of intratubular dentin formation in human natural carious lesions," *Calcified Tissue International*, vol. 69, no. 5, pp. 268–273, 2001.

## Research Article

# Functional and Structural Details about the Fabella: What the Important Stabilizer Looks Like in the Central European Population

**Nicole Helene Hauser, Sebastian Hoechel, Mireille Toranelli, Joerg Klaws, and Magdalena Müller-Gerbl**

*Department of Biomedicine, Musculoskeletal Research, University of Basel, Pestalozzistrasse 20, 4056 Basel, Switzerland*

Correspondence should be addressed to Sebastian Hoechel; [sebastian.hoechel@unibas.ch](mailto:sebastian.hoechel@unibas.ch)

Received 18 January 2015; Accepted 5 March 2015

Academic Editor: Ilker Ercan

Copyright © 2015 Nicole Helene Hauser et al. This is an open access article distributed under the Creative Commons Attribution License, which permits unrestricted use, distribution, and reproduction in any medium, provided the original work is properly cited.

The posterolateral corner of the knee accommodating the fabella complex is of importance in orthopaedic surgery. Unfortunately, there is a lack of data in literature for clinical routine. Therefore, we investigated the fabella's characteristics, biomechanical nature, and present histologic details. Of special interest were the fabella's occurrence and position, calcium concentration as long-term load intake indicator, and the histology. Within our analysis, fabellae were found in 30.0% of all datasets, located on the upper part of the posterolateral femoral condyle. The region of fabella contact on this condyle showed a significantly lower calcium concentration than its surroundings. Histologically, the fabella showed no articular cartilage but a clearly distinguishable fabellofibular ligament that consisted of two bundles: one, as already described in literature inserted at the fibular tip, and another part newly described on the top of the lateral meniscus. In its role of stabilizing the soft tissue structures of the posterolateral knee, the fabella seems to serve as suspension for the ligaments evolving from its base. Even though a joint formation of any kind is unlikely, the presence of a fabella needs to be kept in mind during knee examination and any surgical procedures.

## 1. Introduction

The occurrences of patients with knee injuries are constantly rising. Though injuries of the medial compartment are more frequent, the consequence of a traumatic distress on the lateral side is more disabling, since the lateral compartment is subjected to greater force during gait [1, 2]. In addition, possible posterolateral pathology may remain unrecognized if injuries of the cruciate ligaments mask secondary findings due to their extensive symptoms [3, 4]. In its stabilizing function, the posterolateral corner with its complex arrangement of muscles, tendons, and ligaments is of crucial importance for the physiological function of the knee. It is suggested that untreated damage and therefore insufficient support of the posterior knee not only prolong the healing process, but also cause postsurgical failure after cruciate ligament reconstruction [5, 6]. Since the injury occurs following direct varus force in external rotation of the tibia as well as sudden hyperextension of the knee, various case reports describe

traumata after car accidents with frontal impact not only to the ligamentous structures, but also to the occasional fabella present [7–11]. To understand the possible injuries and repair mechanisms of the posterolateral corner, the arrangement and variation of anatomical structures must be considered. A literature review of the fabella is confusing, since information about the fabella complex is obtained by many different research methods. Unfortunately, the derived results are still compared to each other which results in a mix of data which is difficult to handle. Despite the fact that information about the central European population is negligible [12], various numbers of Chinese and Japanese studies report the occurrences of the fabella positioned in the lateral head of the gastrocnemius muscle and the possible structure of the fabellofibular ligament (FFL) [13, 14].

Tabira et al. report in 2013 the prevalence of the fabella to be 68.6 percent (%) per knee in the elderly Japanese population. Included were bony and cartilaginous findings evaluated

by inspection and palpation within the lateral head of the gastrocnemius muscle [15]. On the contrary, Kawashima et al. report their results of 66% bony and cartilaginous fabellae present in a similar Japanese study per gastrocnemius head and not per knee [14]. In addition, some studies conduct their focus on clinical radiographs which mainly take into consideration the prevalence of osseous fabellae [16]. The main confusion arises, when these findings are compared with each other and the methods of examination are not clearly stated [17].

Despite the differences in these data, the description of the endochondral ossification and the occurrence and structure of the FFL is consistent. Running from the base of the fabella to the styloid process of the fibular head, it serves as a static stabilizer of the knee, which tenses in full extension [18]. It can be found in up to 80% of humans with a fabella present [16, 19, 20].

For the orthopaedic surgeon, this information provides ideas about the posterolateral knee complex and helps to tackle arising symptoms like pain and swelling in this area, especially if the interaction of the fabella and the posterolateral femoral condyle (PLFC) is taken into account. Many researchers favour the idea of a fabellofemoral joint with typically associated joint diseases like chondromalacia and osteoarthritis, which can be found in many case reports [7, 11, 21]. In progressive stages, the cartilage of the fabella is described as softened and fibrillated or even completely absent. In this case, the bare subchondral bone plate of the fabella comes into contact with the femoral condyle and leads to increasing posterolateral pain [22]. The gross anatomy of the proclaimed joint in a healthy state and the formation of the interacting surfaces are difficult to retrieve from literature. The description of the joint cavity was done by gelatine-injection, which was not characterized any further and documented in black and white pictures in which the markings hide the important areas. What can clearly be identified is the distinctive impression on the PLFC caused by the fabella [14, 17]. Histologic images of the fabella and the surrounding formation lack representation in literature. Most of the presentations are very small and reveal only fractions of the posterolateral aspect of the knee. In addition, the images available are mainly printed in black and white and are not connected to an overview presentation [17, 20, 23, 24]. In these studies, the cartilage formation and the interaction with the femoral condyle are not sufficiently described and do not provide conclusive information about the anatomical arrangement in order to evaluate and understand patient cases better.

Our goal was to (1) determine the incidence and position of the fabella in a central European population and to better estimate clinical appearances. (2) Furthermore, we describe the biomechanical impact of the little sesamoid bone on its interaction with the femur in order to determine a possible pressure distribution. (3) Histologic demonstration will define the anatomical structures with special attention to the ligamentous tissue and clarify the formation of the existing cartilage in order to determine any possible joint formation. The arrangement of the structures of the posterolateral knee will be shown in its entirety including all bony

surroundings. A stained overview presentation is not yet available in literature, since deficient bone decalcification has hampered the production of cuttings that include materials with different rigidity.

## 2. Materials and Methods

*2.1. Sample Collection.* Four hundred knees of 200 Europeans were included (cadaveric study group—corpses donated to science and research, 99 men, 101 women; conventional datasets generated by computed tomography (CT), extended knee position). The data was acquired during investigations at the Institute of Anatomy, University of Basel. The sample age ranged from 20 to 104 years (mean: 75.8, SD: 19.43). Histologic procedures were carried out selectively on five of the most prominent and representative bony fabella samples.

*2.2. Descriptive Quantitative Analysis.* We evaluated CT-studies (SOMATOM 16, Siemens, Erlangen, Germany, 120-kilovolt, 180-milliampere-second, axial slices) with a slice thickness of 0.6 millimetres (mm) (only the bony fabella could be registered with the CT-method). Three-dimensional (3D) reconstructions (ANALYZE 11.0, Biomedical Imaging Resource, Mayo Foundation, Rochester, USA; VGStudio Max 2.2, Heidelberg, Germany) were orientated in coronal posterior view for determination of the location of the fabella. To gain comparable data, a size-independent measurement grid system was applied on the PLFC to allocate the corresponding coordinates to the centre of the fabella (Figures 1(a)–1(c)). The determined location coordinates of every fabella were superimposed on one reconstructed 3D-sample of the PLFC with respect to the anatomical orientation for final evaluation.

To determine the size of the fabella, the largest diameter ( $x$ ) was measured (SOMATOM 16, Siemens, Erlangen, Germany) in coronal posterior view, regardless of the anatomical knee-axes. For the second dimension, the largest diameter of the corresponding perpendicular orientation ( $y$ ) was used.

*2.3. Joint Impact Analysis.* The method of CT-osteodensitometry (CT-OAM) for assessment of the density distribution was used on the same 3D reconstructions of the conventional datasets from the descriptive analysis described above. The 3D reconstructions of the knee were divided into datasets of the fabella and the femoral component. The subchondral bone plate (SBP) of the PLFC and of the fabella as the region of interest was arranged in a way to be in coronal frontal view. Using a “maximum intensity projection” the software (ANALYZE 11.0, Biomedical Imaging Resource, Mayo Foundation, Rochester, USA) projected the most dense voxels onto the surface and assigned them colours, where the highest density values (>1200 Hounsfield units) were represented in black and lower values in red, yellow, green, and blue (in descending order) [25, 26]. In accordance with the density values displayed, phantom measurements led to the calculation of the corresponding mineral content as an indication of the long-term load intake [27].

For statistical analysis, the mean concentration of calcium hydroxyapatite/ $\text{Ca}_5(\text{PO}_4)_3(\text{OH})$  (subsequently abbreviated

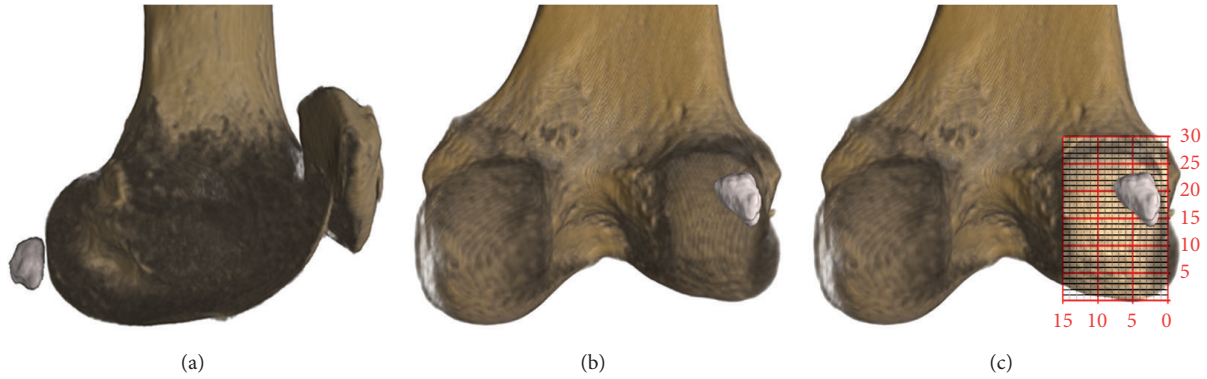


FIGURE 1: 3D reconstructions for descriptive quantitative analysis. (a) 3D reconstruction of the distal femur, patella, and fabella in sagittal view. (b) 3D reconstruction of (a) positioned in posterior view. (c) Applied coordinate-grid system on the posterolateral femoral condyle for determination of fabellar position.

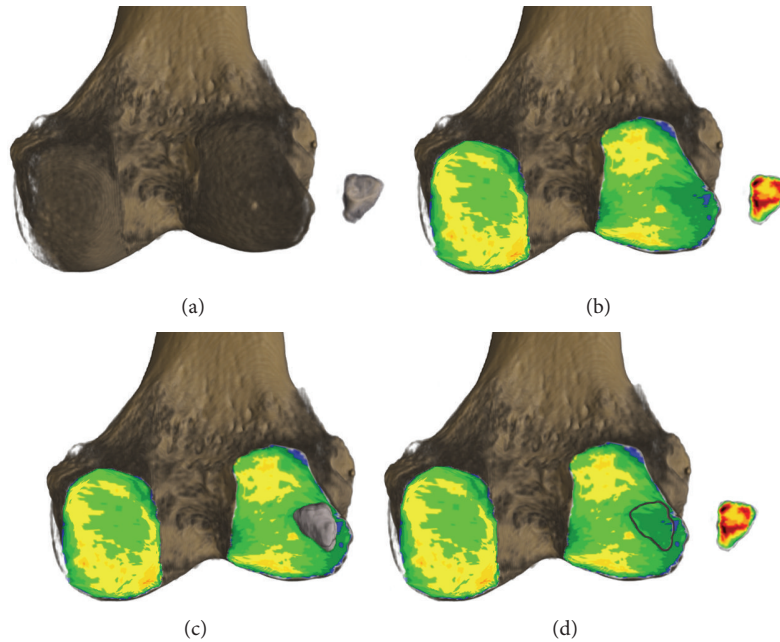


FIGURE 2: Method of CT-osteodensitometry on 3D reconstructions to determine density distribution within the subchondral bone plate. (a) Distal femur in posterior view with fabella arranged in anterior view (subchondral bone plate of articular surface shown). (b) Subchondral bone plates shown with colour-coded density distribution (black, red, yellow, green, and blue = Hounsfield units in descending order in 200 unit steps). (c) Fabella in original position on density distribution pattern. (d) Density distribution with marked region of fabella contact on the posterolateral femoral condyle.

as CAHA) within the SBP of the fabella and the corresponding area of contact on the PLFC was evaluated. In addition, the mineral content of the SBP of both posterior femoral condyles was measured for reference (Figures 2(a)–2(d)).

**2.4. Histologic Imaging.** For sectioning and staining, the five largest fabella samples were dissected and removed with the attached soft tissue structures as well as the corresponding PLFC.

The dissected tissue was treated to dehydration in ethanol starting with 40% increasing to 100% over a time period of 25 days. Afterwards, the initial defatting process was increased

using isopropyl alcohol and chloroform. After completion, the next step included methyl methacrylate (MMA) infiltration for 3 days at a storage temperature of 4° Celsius. Following this step of infiltration and mixing of chemicals, the resulting solution was exchanged for pure MMA again for the final embedding at 4° Celsius. The time of polymerization was in accordance with the size of the sample and lasted approximately one month. For all further steps, the hardened MMA blocks embedding the bone samples were used.

The sectioning in sagittal anatomical orientation was performed using a diamond wheel saw with 400-micrometre ( $\mu\text{m}$ ) saw band thickness. The resulting slices (thickness:

TABLE 1: Fabella occurrence in accordance with selected age groups.

Age group	<i>n</i> *	Distribution of fabella occurrence						
		Male	Female	Number of knees	Fabellae present	Bilat./Unilat. per <i>N</i> **	Percentage per age group (%)	Relative distribution
20–29	5	3	2	10	0	0	0.00	0.00
30–39	5	4	1	10	2	B-1	1.90	0.38
40–49	17	11	6	34	9	B-4; U-1	8.57	0.50
50–59	8	4	4	16	2	B-1	1.90	0.24
60–69	14	10	4	28	6	B-3	5.71	0.41
70–79	38	20	18	76	17	B-8; U-1	16.19	0.43
80–89	65	30	35	130	41	B-17; U-7	39.05	0.60
90–99	45	17	28	90	28	B-11; U-6	26.67	0.59
100–109	3	0	3	6	0	0	0.00	0.00
Sum	200	99	101	400	105	B-45; U-15	100.00	

\*CT-studies of both knees.

\*\*B: bilateral; U: unilateral.

600  $\mu\text{m}$ ) were fixed on white, light-transmissive object holders for further processing. To accomplish optimal staining conditions, the slides were ground down to 200  $\mu\text{m}$  and polished. Staining methods obtained the following.

- (i) Toluidine blue epoxy staining of 3  $\mu\text{m}$  [28], for basophil structures to acquire different shades of blue where calcified cartilage shows the darkest shade,
- (ii) Trichrome Masson-Goldner surface staining of 3  $\mu\text{m}$  [29], where mineralized bone and collagen are stained green, calcified cartilage is stained light green, and muscle tissue and cytoplasm are stained in different shades of red. The resulting histologic slices were documented for inspection (20.5:1 Zoom and FusionOptics Technology Leica M205 C; Canon EOS 40D).

**2.5. Statistical Analysis.** Continuous variables were expressed with mean, standard deviation, and minimum-maximum values where categorical variables were reported as frequency and related percentage. Independent samples *t*-test was performed between group comparisons. Linear regression analysis was performed for modelling the relationship between PLFC, FAS, and ROFC. All age group data were tested for normalcy and homogeneity using Kolmogorov-Smirnov tests. For the gender distribution analysis, the unpaired two-sample *t*-test was used.

All statistical analyses were done using RStudio (RStudio: integrated development environment for R, Version 0.96.122, Boston, MA, USA). The significance level for all statistical tests was set a priori to  $<0.001$ .

### 3. Results

**3.1. Descriptive Quantitative Analysis.** 30.0% of all CT-studies (each CT-study of one human included the left and right knee) presented with 105 bony fabellae overall where the bilateral to unilateral occurrence ratio was 3:1 (bilateral: 45; unilateral: 15). The relative occurrence showed no significant



FIGURE 3: Results of descriptive quantitative analysis. Colour-coded fabella positions on posterolateral femoral condyle (red, yellow, and green; in descending order).

( $P > 0.001$ ) difference between the assigned age groups, where fabellae were present (mean occurrence: 23.63%; min: 12.5%; max: 31.54%; SD: 6.71%). The data did not reveal any difference in gender distribution (fabellae in male versus fabellae in female: 1:1;  $P = 0.453$ ) (Table 1). The fabella was positioned invariably over the PLFC and in close relation to its lateral border (Figure 3). The measured sizes of the analysed fabellae ranged from (*x*) 4.84 mm, (*y*) 3.63 mm to (*x*) 13.12 mm, (*y*) 11.71 mm.

**3.2. Joint Impact Analysis.** The CAHA concentration of the posteromedial femoral condyle (mean: 461.14 mg/mL; min: 282.66 mg/mL; max: 656.63 mg/mL; SD: 112.93 mg/mL) was significantly ( $P < 0.001$ ) higher compared to the PLFC (mean: 402.59 mg/mL; min: 260.16 mg/mL; max: 577.28 mg/mL; SD: 92.82 mg/mL), hosting the fabella. The measured concentration of the region of fabella contact (ROFC) on the PLFC was significantly ( $P < 0.001$ ) lower (mean: 336.77 mg/mL; min: 198.23 mg/mL; max: 521.98 mg/mL; SD: 91.20 mg/mL) than the mean value measured over the whole PLFC itself. The mineral content of the ROFC, in comparison

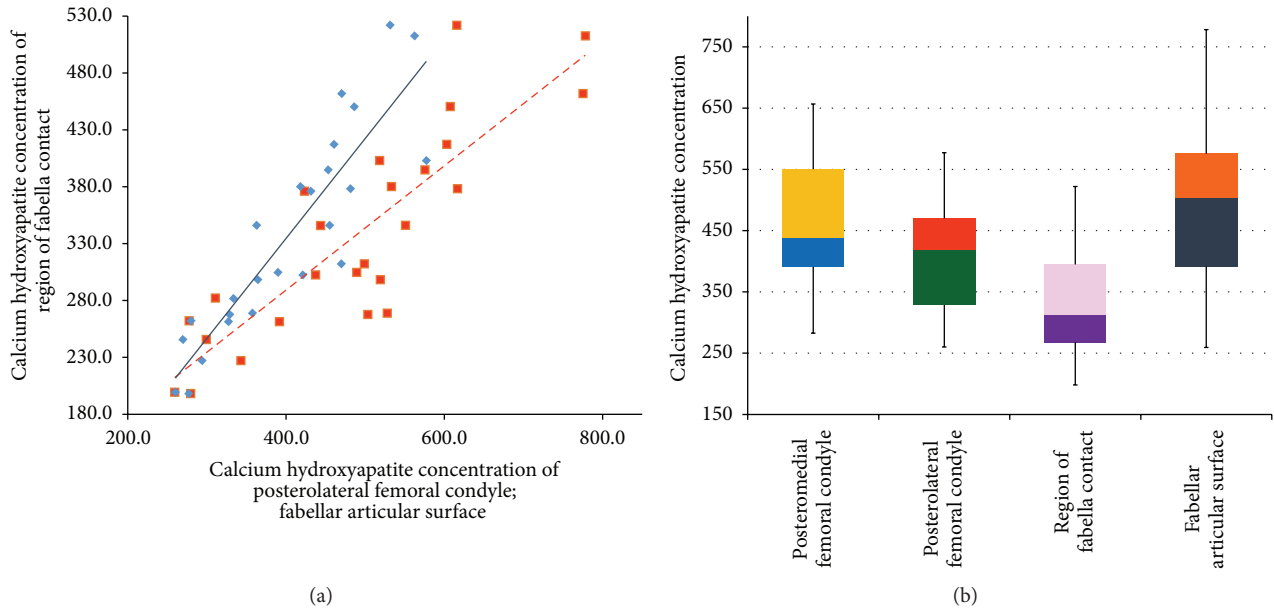


FIGURE 4: Results of calcium hydroxyapatite analysis of the subchondral bone plates. (a) Level of calcium hydroxyapatite (mg/mL) of the subchondral bone plates of the articular surfaces of interest. (b) Dependency of the evaluated data of the region of fabella contact on the posterolateral femoral condyle ( $y$ ; mg/mL) to the concentration on the mean posterolateral femoral condyle and the fabellar articular surface ( $x$ ; mg/mL).

to the mineral content on the whole PLFC, showed a mean difference of  $-16.59\%$  (min:  $-1.77\%$ ; max:  $-33.53\%$ ).

The fabellar articular surface (FAS) had the highest CAHA concentration (mean:  $487.09$  mg/mL; min:  $259.29$  mg/mL; max:  $778.15$  mg/mL; SD:  $142.99$  mg/mL) which was on the same level as seen in other joints of the human body (Figure 4(a)).

The linear regression (of CAHA concentration) of the ROFC is dependent on the PLFC and can be interpreted as

$$(i) \text{ROFC} = 0.878 \times \text{PLFC} - 16.843 \quad (R^2 = 0.80; P < 0.001).$$

As for the CAHA concentration of the ROFC which is dependent on the FAS:

$$(i) \text{ROFC} = 0.546 \times \text{FAS} + 70.79 \quad (R^2 = 0.73; P < 0.001) \quad (\text{Figure 4(b)}).$$

**3.3. Histologic Imaging.** Represented on the sagittal sections of the posterolateral corner of the knee, the macroscopic images involve all corresponding bones (Figures 5(A) and 5(B)). The fabella was located within the lateral gastrocnemius tendon. The collagen fibres can be found along the anterior and posterior sides of the fabella, joining again to form the muscle-tendon junction at its base. The concave imprint on the articular cartilage of the femur induced by the fabella is formed in the topmost region of the articular cartilage of the PLFC (Figure 5; arrow). The FFL originating from the base of the fabella crosses over the popliteal tendon and is inserted at the styloid process at the tip of the fibula. A second bundle of the FFL can be identified which separates from the main bundle and is inserted at the topmost rim of the lateral meniscus.

The magnified image (Figure 6) demonstrated different zones of the femoral articular cartilage with its subsequent tidemark, calcified cartilage, and the SBP. The corresponding surface of the fabella is composed of collagen fibres originating from the gastrocnemius tendon. Just below these longitudinal structures, an unmineralized fibrocartilage followed by tidemark and mineralized fibrocartilage is distinguishable. The medullary cavity within the fabella consists of a clearly defined trabecular network including osteocytes. The accumulation of unmineralized and mineralized fibrocartilage in the middle part of the anterior side of the fabella demonstrates the beginning of pathologic thickening.

#### 4. Discussion

The frequency of occurrence of the fabella is discussed in different ways in literature. While Kawashima et al. [14] report cartilage and bony fabellae to be present in  $66\%$  of 150 gastrocnemius heads, the comparing paper of Tabira et al. [15] calculated their  $68.6\%$  per knee. Another paper, referring to Kawashima et al., quoted them with  $92\%$ , a number which does not appear in the paper at all [17]. The confusion arises from different mathematic procedures, calculated either per person, per knee, or per gastrocnemius head. The interpretation of the described differences is mainly based on the state and formation of the fabella, classified as either bony and cartilaginous or soft and hard [14–17, 20, 24]. CT-data will only show bony samples, whereas dissection may derive both and enlarge the number of findings [4]. The so-called commonly known fact that a fabella ossifies at 3 years of age confronts the idea of an induced ossification with aging [6, 14]. Following the data of Minowa et al. who found

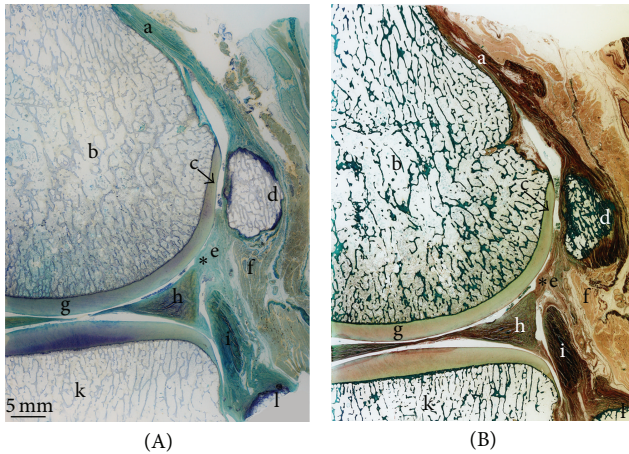


FIGURE 5: Histologic imaging of posterolateral corner of the knee (sagittal section). (A) Toluidine blue staining. (B) Trichrome Masson-Goldner staining. On both (A) and (B): a: gastrocnemius tendon; b: posterolateral femoral condyle; c: femur condyle impression; d: bony fabella; e: collagen fibres of fabellofibular ligament; f: muscle cells of lateral gastrocnemius head; g: femoral articular cartilage; h: lateral meniscus; i: popliteus muscle; k: lateral condyle of tibial plateau; l: fibular head; \*second bundle of the FFL.

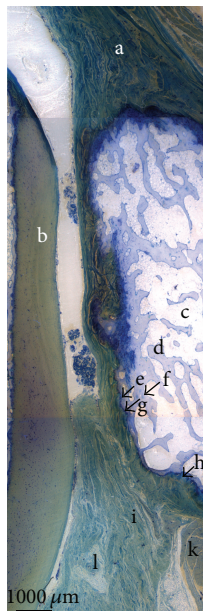


FIGURE 6: Fusion of magnified histological sections (1000  $\mu\text{m}$ ; Toluidine blue staining). a: gastrocnemius tendon; b: femoral articular cartilage; c: medullary cavity of fabella; d: trabecular bone; e: mineralized fibrocartilage; f: osteocytes; g: tidemark; h: unmineralized fibrocartilage; i: collagen fibres of the fabellofibular ligament; k: muscle cells with nuclei; l: fibrocyte.

bony fabellae in fetuses already, one has to rethink about the ossification timeframe mentioned above. To provide reliable data of the central European population that adds to the present state in literature and describes details of the fabella for clinicians, we limited our study to CT-recognizable, bony appearances as they will be the ones discovered in clinical

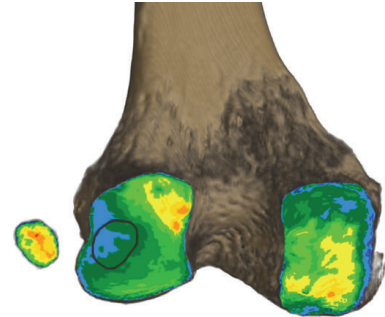


FIGURE 7: Density distribution of subchondral bone plates of the fabella and femur. Distribution pattern with marked region of fabella contact on the posterolateral femoral condyle.

routine. Our findings are in accordance with the commonly understood 30% of fabellae present [16]. Within our study, the distribution of occurrence proved to be quite consistent regarding the patients' age. It is for sure that intrinsic genetic factors as well as extrinsic epigenetic stimuli trigger the ossification of this sesamoid bone. One interpretation that it is due to the aging process is not supported by our data. Reasons for the absence of fabellae in the age groups 20–29 and 100–109 will presumably be the limited number of CT-datasets.

All evaluated bony fabella samples were situated within the tendon of the lateral gastrocnemius muscle and in close relation to the lateral border of the PLFC. In contrast to the literature, we observed the majority located within the superior lateral area. Despite the previous reported main location of the fabella the inferior lateral area of the PLFC [14, 15], we only found about 30% of all fabellae located there.

The data of the long-term loading history evaluated with the method of CT-OAM revealed surprising results. Since the mineralization distribution of the SBP changes in adaptation to the long-term load intake of a joint by CAHA integration and degradation and correlates directly with its mechanical strength, the distribution of the mineral content within a joint surface can be regarded as a reflection of the load intake over time and represents the loading history [25, 30–32]. Due to the fact that the interacting parts of the femoral condyle and the fabella are described as a joint, we expected joint-loading to be represented in the density distribution pattern [14]. The PLFC, however, showed to be less mineralized in the ROFC than the rest of the evaluated area. The contour of the fabella itself is even recognizable as it is coded in a different colour resembling a lower mineral content (Figures 7 and 2(d)). A joint formation between the corresponding bones does not seem to exist here. In addition, the histologic pictures support these findings with the absence of articular cartilage and a cover of collagen fibres on the fabella. The SBP of the fabella meanwhile shows a mineral content that is on a comparable level to other joints [27]. The fact of the lower load uptake of the ROFC leads us to take the knee-biomechanics into account for explanation. Within its fabella complex, the sesamoid bone serves as the combined origin of the oblique popliteal ligament, arcuate ligament, and the FFL as well as the plantaris muscle. All these structures fix the

sesamoid bone in its position within the gastrocnemius head. Due to the rollback of the lateral femoral condyle during knee flexion, the PLFC moves on the tibial plateau over a greater distance than the medial one. From 120° of flexion, the lateral femoral condyle moves 23 mm in anterior direction until -5° of extension. On the medial side, the contact point only moves 3 mm [19]. This kinematic condition produces more tensile stress on the lateral head than on the medial one which might serve as an extrinsic epigenetic stimulus to trigger the calcification but surely separates the PLFC from the fabella and reduces the impact as shown.

The histologic images in their representation of the posterolateral knee complex add to the current available data in literature, since they include a stained overview, as well as detailed information about the structural composition of the bony components as well as soft tissue. In addition to the already described imprint of the fabella onto the femoral articular cartilage, the tendon of the gastrocnemius muscle can clearly be identified surrounding the fabella and embedding it. Articular cartilage on the fabella is missing. In addition to the already in literature described FFL (originating from the base of the fabella and being inserted at the styloid process of the fibula), a second bundle of collagen fibres is present. Also originating at the base, it separates from the main FFL and is inserted at the topmost corner of the lateral meniscus (Figures 5(A) and 5(B)) [18]. A posterior fixation of the lateral meniscus is therefore possible through this ligamentous bundle. This constellation, however, forms a capsule-like surrounding of the fabella which might be the explanation for the observed articular cavity described by Kawashima et al. [14].

Possible limitations to this study are seen in the pathologic alterations of the histologic samples. An osteoarthritic process can be found in the middle part of the fabella. Since the continuity of the collagen fibres is clearly visible in its full extent, we nevertheless regard this information to be representative.

## 5. Concluding Remarks

A fabella is present within the posterolateral knee complex in 30.0% of the European population and needs to be distinguished from any fracture parts suspected within this area. In its function of supporting the soft tissue structures, it imprints on the articular cartilage of the PLFC in close relation to its lateral border where it is constantly found in CT-datasets if present. Although this close relation created an imprint on the femoral articular cartilage that proves interaction between the fabella and the PLFC, the SBP of the femoral part does not reveal any signs of long-term loading from the fabella in this area. The fabella itself shows no sign of articular cartilage. Instead, it is isolated from the femur, just being surrounded by fixating collagen fibres originating from the lateral head of the gastrocnemius muscle. In its role of stabilizing soft tissue structures, it seems to serve as suspension for the ligament evolving from its base. Despite previous descriptions of this FFL running distally and being inserted at the styloid process, we clearly identified a second

bundle inserted into the top rim of the lateral meniscus, which we assume provides mechanical support and a possible back-tracking of the lateral meniscus during its sliding movement on the lateral tibial condyle. Certainly, within the complex field of traumatic knee injuries, a distortion with damage to the lateral meniscus is bound to damage this ligamentous structure as well. Next to the described fabella, the FFL with its second, meniscal attached bundle needs to be kept in mind during knee examination.

## Conflict of Interests

The authors declare that they have no conflict of interests. Furthermore, the authors received no grant or sources of financial support related to the topic or topics of this paper.

## Authors' Contribution

Nicole Helene Hauser and Magdalena Müller-Gerbl designed the study and collected the data. Joerg Klawns and Sebastian Hoechel developed the methodology. Mireille Toranelli contributed the histology work. Nicole Helene Hauser and Sebastian Hoechel wrote the paper. Nicole Helene Hauser and Sebastian Hoechel contributed equally to this work.

## Acknowledgments

The authors would like to thank Mrs. Christine Müller-Thompson for the linguistic correction and final proof. Furthermore, they appreciate the help of Mr. Peter Zimmermann and his kind contribution of ideas towards the histologic staining as well as Mr. Roger Kurz for his support with the required preparation.

## References

- [1] J. A. Nicholas, "Acute and chronic lateral instabilities of the knee: diagnosis, characteristics, and treatment," in *Proceedings of the AAOS Symposium on Reconstructive Surgery of the Knee*, Mosby, St. Louis, Mo, USA, May 1978.
- [2] W. Muller, R. Biedert, F. Hefti, R. P. Jakob, U. Munzinger, and H. U. Staubli, "OAK knee evaluation. A new way to assess knee ligament injuries," *Clinical Orthopaedics and Related Research*, no. 232, pp. 37–50, 1988.
- [3] D. M. Veltri and R. F. Warren, "Posterolateral instability of the knee," *The Journal of Bone and Joint Surgery—American Volume*, vol. 76, no. 3, pp. 460–472, 1994.
- [4] R. F. LaPrade, C. J. Griffith, B. R. Coobs, A. G. Geeslin, S. Johansen, and L. Engebretsen, "Improving outcomes for posterolateral knee injuries," *Journal of Orthopaedic Research*, vol. 32, no. 4, pp. 485–491, 2014.
- [5] S. J. O'Brien, R. F. Warren, H. Pavlov, R. Panariello, and T. L. Wickiewicz, "Reconstruction of the chronically insufficient anterior cruciate ligament with the central third of the patellar ligament," *The Journal of Bone & Joint Surgery—American Volume*, vol. 73, no. 2, pp. 278–286, 1991.
- [6] R. F. LaPrade, S. Johansen, J. Agel, M. A. Risberg, H. Moksnes, and L. Engebretsen, "Outcomes of an anatomic posterolateral knee reconstruction," *The Journal of Bone and Joint Surgery Series A*, vol. 92, no. 1, pp. 16–22, 2010.

- [7] A. Robertson, S. C. E. Jones, R. Paes, and G. Chakrabarty, "The fabella: a forgotten source of knee pain?" *The Knee*, vol. 11, no. 3, pp. 243–245, 2004.
- [8] F. Franceschi, U. G. Longo, L. Ruzzini et al., "Dislocation of an enlarged fabella as uncommon cause of knee pain: a case report," *The Knee*, vol. 14, no. 4, pp. 330–332, 2007.
- [9] J. Y. Tang, H. Mulcahy, and F. Chew, "High-energy fracture of the fabella," *Radiology Case Reports*, vol. 5, no. 4, 2010.
- [10] G. M. Heideman, K. E. Baynes, A. P. Mautz, M. S. DuBois, and J. W. Roberts, "Fabella fracture with CT imaging: a case report," *Emergency Radiology*, vol. 18, no. 4, pp. 357–361, 2011.
- [11] A. R. F. Barreto, F. A. Chagas-Neto, M. D. Crema et al., "Fracture of the fabella: a rare injury in knee trauma," *Case Reports in Radiology*, vol. 2012, Article ID 390150, 3 pages, 2012.
- [12] O. Raheem, J. Philpott, W. Ryan, and M. O'Brien, "Anatomical variations in the anatomy of the posterolateral corner of the knee," *Knee Surgery, Sports Traumatology, Arthroscopy*, vol. 15, no. 7, pp. 895–900, 2007.
- [13] Z. Dannawi, V. Khanduja, K. K. Vemulapalli, J. Zammit, and M. El-Zebdeh, "Arthroscopic excision of the fabella," *The Journal of Knee Surgery*, vol. 20, no. 4, pp. 299–301, 2007.
- [14] T. Kawashima, H. Takeishi, S. Yoshitomi, M. Ito, and H. Sasaki, "Anatomical study of the fabella, fabellar complex and its clinical implications," *Surgical and Radiologic Anatomy*, vol. 29, no. 8, pp. 611–616, 2007.
- [15] Y. Tabira, T. Saga, N. Takahashi, K. Watanabe, M. Nakamura, and K.-I. Yamaki, "Influence of a fabella in the gastrocnemius muscle on the common fibular nerve in Japanese subjects," *Clinical Anatomy*, vol. 26, no. 7, pp. 893–902, 2013.
- [16] G. C. Terry and R. F. LaPrade, "The posterolateral aspect of the knee: anatomy and surgical approach," *The American Journal of Sports Medicine*, vol. 24, no. 6, pp. 732–739, 1996.
- [17] S.-X. Zeng, X.-L. Dong, R.-S. Dang et al., "Anatomic study of fabella and its surrounding structures in a Chinese population," *Surgical and Radiologic Anatomy*, vol. 34, no. 1, pp. 65–71, 2012.
- [18] P. Tyler, A. Datir, and A. Saifuddin, "Magnetic resonance imaging of anatomical variations in the knee. Part I: ligamentous and musculotendinous," *Skeletal Radiology*, vol. 39, no. 12, pp. 1161–1173, 2010.
- [19] Y. C. Kim, I. H. Chung, W. K. Yoo, J.-S. Suh, S. J. Kim, and C. I. Park, "Anatomy and magnetic resonance imaging of the posterolateral structures of the knee," *Clinical Anatomy*, vol. 10, no. 6, pp. 397–404, 1997.
- [20] T. Minowa, G. Murakami, H. Kura, D. Suzuki, S. H. Han, and T. Yamashita, "Does the fabella contribute to the reinforcement of the posterolateral corner of the knee by inducing the development of associated ligaments?" *Journal of Orthopaedic Science*, vol. 9, no. 1, pp. 59–65, 2004.
- [21] R. Goldenberg and E. L. Wild, "Chondromalacia fabellae," *The Journal of Bone and Joint Surgery (American Volume)*, vol. 24, no. 3, pp. 688–690, 1952.
- [22] D. S. Weiner and I. Macnab, "The 'fabella syndrome': an update," *Journal of Pediatric Orthopaedics*, vol. 2, no. 4, pp. 405–408, 1982.
- [23] J. G. Silva, C. A. A. Chagas, D. F. M. Torres, L. Servidio, A. C. Vilela, and W. A. Chagas, "Morphological analysis of the fabella in Brazilians," *International Journal of Morphology*, vol. 28, no. 1, pp. 105–110, 2010.
- [24] P. Phukubye and O. Oyedele, "The incidence and structure of the fabella in a South African cadaver sample," *Clinical Anatomy*, vol. 24, no. 1, pp. 84–90, 2011.
- [25] M. Muller-Gerbl, R. Putz, N. Hodapp, E. Schulte, and B. Wimmer, "Computed tomography-osteodensitometry for assessing the density distribution of subchondral bone as a measure of long-term mechanical adaptation in individual joints," *Skeletal Radiology*, vol. 18, no. 7, pp. 507–512, 1989.
- [26] M. Muller-Gerbl, R. Putz, N. Hodapp, E. Schulte, and B. Wimmer, "Demonstration of subchondral density patterns by CT osteodensitometry (CT-OAM) for in vivo assessment of individual stresses in joints," *Zeitschrift für Orthopädie und ihre Grenzgebiete*, vol. 128, no. 2, pp. 128–133, 1990.
- [27] M. Müller-Gerbl, "The subchondral bone plate," *Advances in Anatomy, Embryology, and Cell Biology*, vol. 141, pp. 1–134, 1998.
- [28] B. F. Trump, E. A. Smuckler, and E. P. Benditt, "A method for staining epoxy sections for light microscopy," *Journal of Ultrastructure Research*, vol. 5, no. 4, pp. 343–348, 1961.
- [29] J. Goldner, "A modification of the masson trichrome technique for routine laboratory purposes," *The American Journal of Pathology*, vol. 14, no. 2, pp. 237–243, 1938.
- [30] F. Pauwels, *Gesammelte Abhandlungen zur funktionellen Anatomie des Bewegungsapparates*, Springer, Berlin, Germany, 1965.
- [31] D. R. Carter, T. E. Orr, and D. P. Fyhrie, "Relationships between loading history and femoral cancellous bone architecture," *Journal of Biomechanics*, vol. 22, no. 3, pp. 231–244, 1989.
- [32] S. Hoechel, D. Wirz, and M. Müller-Gerbl, "Density and strength distribution in the human subchondral bone plate of the patella," *International Orthopaedics*, vol. 36, no. 9, pp. 1827–1834, 2012.

## Research Article

# Quantitative Anatomy of the Growing Lungs in the Human Fetus

Michał Szpinda,<sup>1</sup> Waldemar Siedlaczek,<sup>1</sup> Anna Szpinda,<sup>1</sup> Alina Woźniak,<sup>2</sup>  
Celestyna Mila-Kierzenkowska,<sup>2</sup> and Mateusz Badura<sup>1</sup>

<sup>1</sup>Department of Normal Anatomy, Collegium Medicum of Nicolaus Copernicus University, Łukasiewicza 1 Street, 85-821 Bydgoszcz, Poland

<sup>2</sup>Department of Medical Biology, Collegium Medicum of Nicolaus Copernicus University, Karłowicza 24 Street, 85-092 Bydgoszcz, Poland

Correspondence should be addressed to Michał Szpinda; [kizanat@cm.umk.pl](mailto:kizanat@cm.umk.pl)

Received 18 February 2015; Revised 7 April 2015; Accepted 20 April 2015

Academic Editor: Gulsum Ozyigit

Copyright © 2015 Michał Szpinda et al. This is an open access article distributed under the Creative Commons Attribution License, which permits unrestricted use, distribution, and reproduction in any medium, provided the original work is properly cited.

Using anatomical, digital, and statistical methods we examined the three-dimensional growth of the lungs in 67 human fetuses aged 16–25 weeks. The lung dimensions revealed no sex differences. The transverse and sagittal diameters and the base circumference were greater in the right lungs while the lengths of anterior and posterior margins and the lung height were greater in the left lungs. The best-fit curves for all the lung parameters were natural logarithmic models. The transverse-to-sagittal diameter ratio remained stable and averaged  $0.56 \pm 0.08$  and  $0.52 \pm 0.08$  for the right and left lungs, respectively. For the right and left lungs, the transverse diameter-to-height ratio significantly increased from  $0.74 \pm 0.09$  to  $0.92 \pm 0.08$  and from  $0.56 \pm 0.07$  to  $0.79 \pm 0.09$ , respectively. The sagittal diameter-to-height ratio significantly increased from  $1.41 \pm 0.23$  to  $1.66 \pm 0.18$  in the right lung, and from  $1.27 \pm 0.17$  to  $1.48 \pm 0.22$  in the left lung. In the fetal lungs, their proportionate increase in transverse and sagittal diameters considerably accelerates with relation to the lung height. The lung dimensions in the fetus are relevant in the evaluation of the normative pulmonary growth and the diagnosis of pulmonary hypoplasia.

## 1. Introduction

Lung growth determination indubitably comprises the most life-threatening constituent of the prenatal assessment [1]. Modern *in utero* diagnostic imaging (three-dimensional ultrasound, ultrafast MRI) enables clinicians to reliably detect congenital respiratory malformations [2, 3] and evaluate both maturation and well-being of the fetus [4, 5]. Antenatal lung growth and maturation are becoming increasingly relevant in determining survival and outcomes in both preterm newborns and neonates affected by pulmonary hypoplasia. Pulmonary hypoplasia appears secondary to many pathological conditions that hamper normal development of the fetal lungs [6–8]. It is noteworthy that apposite assessment of fetal development is mainly grounded in morphologic analysis and biometric measurements [9, 10].

To date however, apart from pulmonary volumetric patterns [6, 9–14], no nomograms on other lung dimensions

in the human fetus have been computed. Therefore, in the present study we aimed to focus on the following:

- (i) reference intervals for lung dimensions (transverse and sagittal diameters, base circumference, height, lengths of anterior, and posterior margins) at successive gestational ages (age-specific reference intervals),
- (ii) possible sex and laterality differences,
- (iii) the optimal growth curves against gestational age for the six aforementioned parameters,
- (iv) the relative growth of either lung (transverse-to-sagittal diameter ratio, transverse diameter-to-height ratio, and sagittal diameter-to-height ratio).

TABLE 1: Distribution of the fetuses studied.

Fetal age [weeks]*	Crown-rump length [mm]				n	Sex	
	Mean	SD	Min	Max		Male	Female
16	111.0	4.2	108.0	114.0	2	1	1
17	122.1	3.7	115.0	126.0	8	4	4
18	136.7	4.3	130.0	142.0	10	5	5
19	153.3	2.0	150.0	155.0	6	4	2
20	161.6	3.3	156.0	166.0	14	7	7
21	174.4	3.8	170.0	180.0	7	2	5
22	188.2	2.5	185.0	190.0	5	3	2
23	195.8	1.8	193.0	198.0	6	4	2
24	208.3	2.9	205.0	212.0	6	4	2
25	220.0	0.0	220.0	220.0	3	1	2
Total					67	35	32

\*Note: for anatomists the most objective information for estimating fetal ages is the crown-rump length, when compared to amenorrhea and ultrasound ages.

## 2. Materials and Methods

The present study was performed in Department of Anatomy of the Ludwik Rydygier Collegium Medicum in Bydgoszcz. The sample encompassed 67 autopsied human fetuses, comprising 35 males and 32 females of White racial origin, derived from spontaneous abortions or stillbirths in the years 1989–1999. First of all, the sample was constructed by elimination of fetuses from diabetic or multiple gravidities and specimens affected by innate and chromosomal abnormalities or intrauterine growth restriction. Legitimate and ethical dilemmas were sanctioned by the University Research Ethics Committee (KB 190/2011). After evaluating the fetal crown-rump length (gestational age), known date of the beginning of the last maternal menstrual period (amenorrhea age), and the five fetal anthropometric measurements (head circumference, biparietal diameter, occipitofrontal diameter, abdominal circumference, and femur length) assessed by early second-trimester ultrasound scan (ultrasound age), the fetal age of 16–25 weeks (Table 1) was fine-tuned [9, 15].

**2.1. Anatomical Method.** After having been submerged in 10% neutral buffered formalin solution for 12–24 months, the fetuses through sternotomy were anatomically dissected; then the lungs were cut off at their hila and removed out of the thoracic cavity. Since no lung malformations were macroscopically perceived in the individuals studied, the sample could rightly be considered normal.

**2.2. Digital Image Analysis.** Every isolated lung with a millimeter scale was positioned perpendicularly to the optical lens axis, recorded in superior, inferior (diaphragmatic), medial (mediastinal), and lateral (sternocostal) projections using NIKON D200 camera (with Micro-Nikkor AF-S 60 mm f/2.8 G ED lens), digitalized to TIFF images, and quantitatively assessed (Figure 1) with the use of digital image analysis. In the present study a valid objective automatic software package, that is, NIS Elements AR (Advanced Research) 3.0 (Nikon) was used for measuring the selected pulmonary

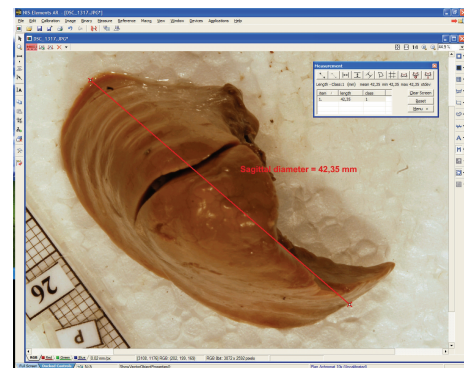


FIGURE 1: A screen of digital image analysis of NIS Elements AR 3.0 (Nikon) while assessing the sagittal diameter of the right lung.

dimensions in the fetus, with the greatest accuracy to the nearest 0.01 mm. As an optimized digital-image analysis system for advanced research applications, NIS-Elements AR 3.0 offers, among other things, flawlessly automatic six-dimensional ( $X$ ,  $Y$ ,  $Z$ , wavelength,  $T$ , multistage points) image acquisition, sophisticated image processing, peripheral device control, and data analysis.

In every fetus for the right and left lungs the following six (Figure 2) independent measurements (1–6) in mm and three calculations (7–9) were done:

- (1) transverse diameter of the lung, corresponding to the greatest horizontal distance of the lung from lateral to medial surface, measured in its superior projection,
- (2) sagittal diameter of the lung, corresponding to the greatest horizontal distance of the lung from anterior to posterior margin, measured in its superior projection,
- (3) height of the lung, measured in its mediastinal projection,
- (4) base circumference, measured in its diaphragmatic projection,

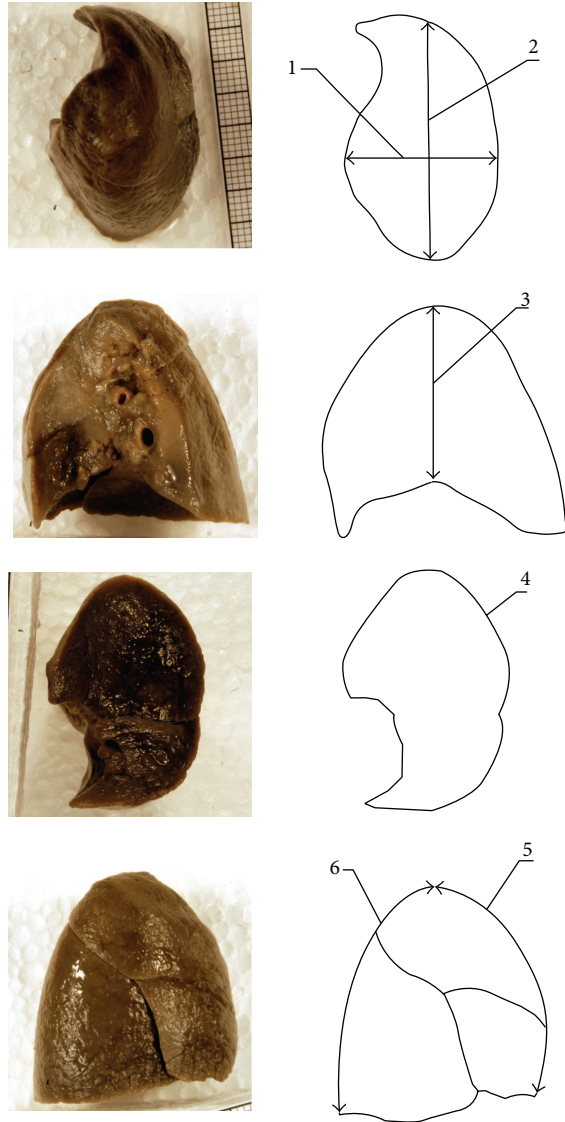


FIGURE 2: Measurements of the pulmonary parameters studied (with relation to the right lung): (1) transverse diameter, (2) sagittal diameter, (3) height, (4) base circumference, (5) length of the anterior margin, and (6) length of the posterior margin.

- (5) length of the lung anterior margin, measured from the lung top to its base in its sternocostal projection,
- (6) length of the lung posterior margin, measured from the lung top to its base in its sternocostal projection,
- (7) transverse-to-sagittal diameter ratio,
- (8) transverse diameter-to-height ratio,
- (9) sagittal diameter-to height ratio.

2.3. *Statistical Analysis.* In a constant effort to minimize measurement and observer bias, all measurements were performed by one researcher (W.S.). Each measurement was done three times under the same settings but at diverse times and then averaged. The intraobserver variation between the reiterated measurements was evaluated by ANOVA for

repeated measurements and post hoc RIR Tukey test. The numerical data were verified for normality of distribution (the Kolmogorov-Smirnov test) and homogeneity of variance (Levene’s test). The fetuses studied were collected into 10 one-week intervals inadequately dispersed with fetal age. Since 3 fetuses were included in the gestational age of 25 weeks and even 2 fetuses in the gestational age of 16 weeks, which clearly did not represent adequate samples for statistical analysis, the first three intervals of 16–18 weeks ( $n = 20$ ), the consecutive three intervals of 19–21 weeks ( $n = 27$ ), and the last four intervals of 22–25 weeks ( $n = 20$ ) were aggregated. The statistical analysis was started by assessing the probability of appearance of statistically significant differences in values with relation to sex (Student  $t$ -test for unpaired variables) and laterality (Student  $t$ -test for paired variables). In order to examine sex differences, at first we tested differences between the following three age groups, 16–18, 19–21, and 22–25 weeks, and after that for the whole sample, without considering fetal ages. To examine whether or not significant differences existed with age, the one-way ANOVA test for unpaired data and then post hoc Bonferroni comparisons were used. The algebraic data for every parameter studied was correlated to fetal age, and linear and nonlinear regression analysis was used to compute the best-fit curve for each parameter considered *versus* gestational age, supported by particular coefficients of determination ( $R^2$ ). The relative growth of either lung was expressed as the transverse-to-sagittal diameter ratio, transverse diameter-to-height ratio, and sagittal diameter-to height ratio. Differences were deliberated significant at  $p < 0.05$ .

### 3. Results

No statistically significant differences ( $p > 0.05$ ) in evaluating intraobserver reproducibility of pulmonary measures were found. The morphometric values obtained were characterized by normality of distribution and homogeneity of variance. As a result, quantitative variables have been expressed as the mean  $\pm$  standard deviation. Without any significant differences in pulmonary measures with relation to sex ( $p > 0.05$ ), the quantitative data for the right (Table 2) and left (Table 3) lungs for both sexes have been aggregated. On the contrary, there were some laterality differences observed, as follows. Firstly, in the right lungs, their transverse and sagittal diameters and the base circumference were significantly greater ( $p < 0.01$ ) than those in the left ones. Secondly, on the left the anterior and posterior margins and the lung height were significantly ( $p < 0.01$ ) greater than particular parameters on the right. Of note, a statistically significant logarithmic increase in values of all the six measures for the right (Figure 3) and left (Figure 4) lungs was found when related to advancing fetal age. In the right lung, the means for all the pulmonary parameters studied differed significantly at  $p < 0.001$  between the three age groups of 16–18, 19–21, and 22–25 weeks. In the left lung, the means for most of the pulmonary parameters studied differed significantly at  $p < 0.001$  between the three forenamed age groups, except for the height and length of posterior margin between 16–18 and 19–21 weeks that differed significantly at  $p < 0.01$ .

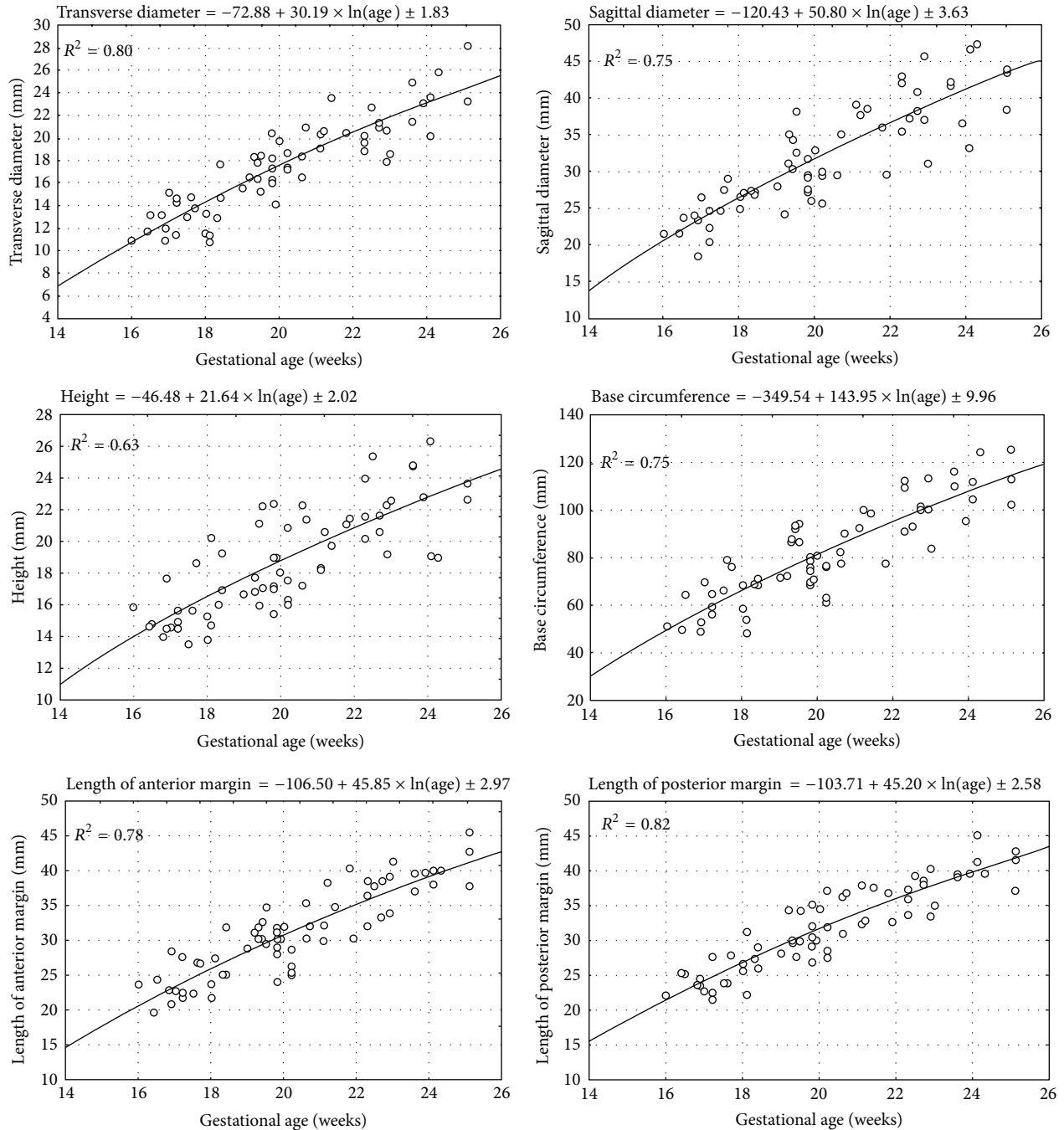


FIGURE 3: The growth dynamics of the parameters studied of the right lung.

The growth dynamics of every parameter studied has been displayed in Table 4, including the regression formula of best fit and coefficient of determination ( $R^2$ ).

The relative growth of either lung was expressed by the following three indexes: transverse-to-sagittal diameter ratio, transverse diameter-to-height ratio, and sagittal diameter-to-height ratio. The transverse-to-sagittal diameter ratio was stable throughout the analyzed period and averaged  $0.56 \pm$

$0.08$  and  $0.52 \pm 0.08$  for the right and left lungs, respectively. For the right and left lungs, the transverse diameter-to-height ratio significantly increased from  $0.74 \pm 0.09$  to  $0.92 \pm 0.08$  ( $p < 0.01$ ) and from  $0.56 \pm 0.07$  to  $0.79 \pm 0.09$  ( $p < 0.05$ ), respectively. During the study period, the sagittal diameter-to-height ratio was found to gradually increase from  $1.41 \pm 0.23$  to  $1.66 \pm 0.18$  ( $p < 0.05$ ) in the right lung and from  $1.27 \pm 0.17$  to  $1.48 \pm 0.22$  ( $p < 0.05$ ) in the left lung.

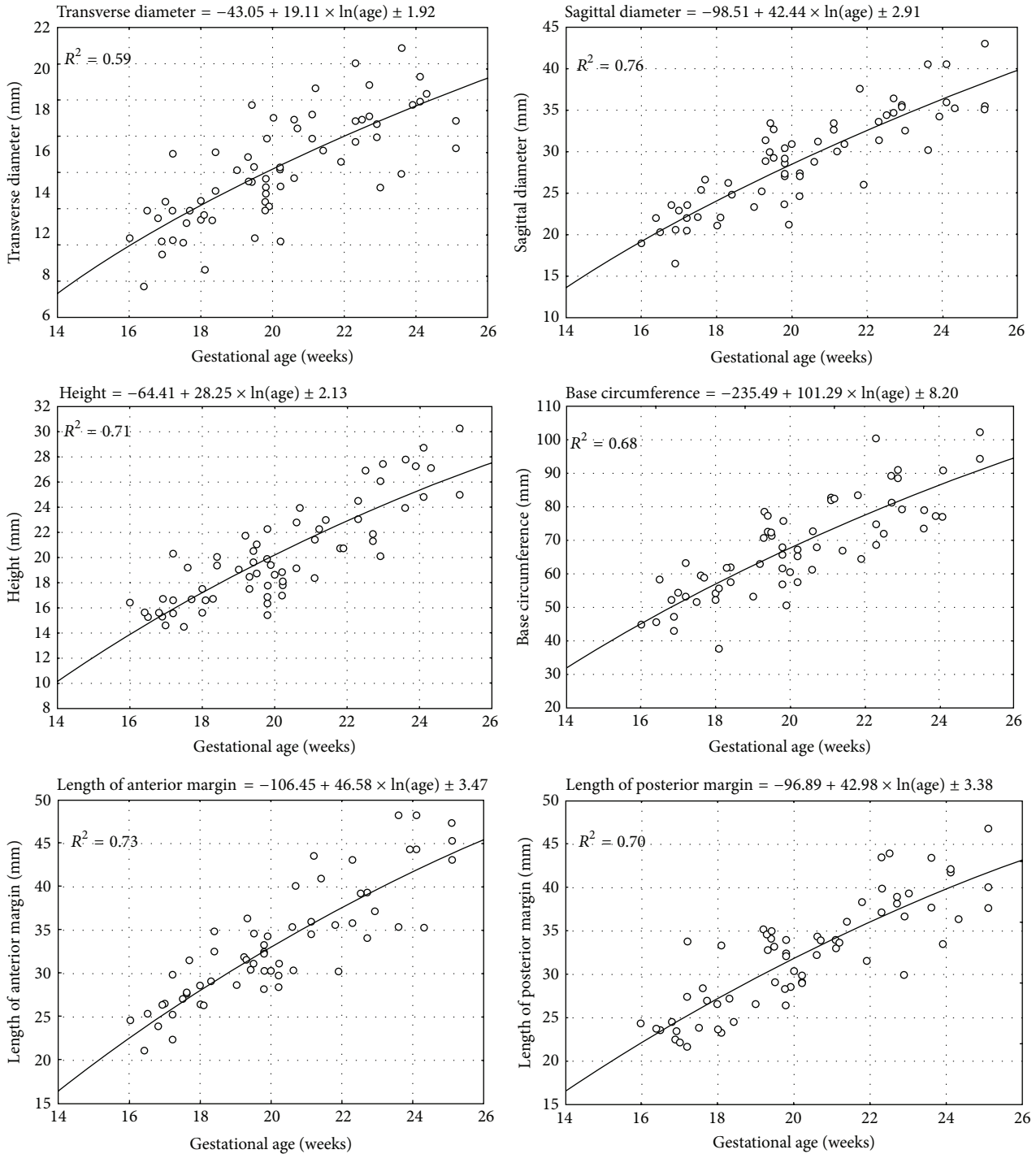


FIGURE 4: The growth dynamics of the parameters studied of the left lung.

#### 4. Discussion

Advances in perinatal medicine result in the early recognition and prompt implementation of corrective procedures in the fetus with life-threatening congenital malformations of the respiratory system [16]. As a prerequisite, a widespread understanding of fetal quantitative anatomy is clearly required so as to produce both normative and pathological criteria adapted to fetal and neonatal respiratory

structures [9, 17]. Thus, the current research refers to morphometric analysis of the fetal lungs, providing the existing medical literature with innovative quantitative data. Notwithstanding our findings have been based on 67 human fetuses aged 16–25 weeks; they imitate an age-related sequence in one fetus at the aforementioned age range.

In our opinion, the results achieved in the present study are both normative and factual due to the following three reasons. Firstly, the fetuses studied could be considered normal,

TABLE 2: Numerical data of the growing right lung.

Age [weeks]	n	Right lung (all parameters are expressed in millimeters [mm])											
		Transverse diameter		Sagittal diameter		Height		Base circumference		Anterior margin length		Posterior margin length	
		Mean	SD	Mean	SD	Mean	SD	Mean	SD	Mean	SD	Mean	SD
16	2	11.35	0.62	21.56	0.02	15.28	0.86	50.48	1.08	21.59	2.88	23.79	2.35
17	8	13.14	1.56	22.94	2.53	15.12	1.15	54.77	14.84	23.89	2.75	23.94	1.92
18	10	13.43	2.01	25.57	4.05	16.43	2.31	66.02	9.64	24.64	4.36	26.42	2.67
16-18	20	13.10 <sup>(a)</sup>	1.79	24.12 <sup>(a)</sup>	3.54	15.79 <sup>(a)</sup>	1.87	59.97 <sup>(a)</sup>	12.86	24.03 <sup>(a)</sup>	3.61	25.17 <sup>(a)</sup>	2.59
19	6	17.21	1.17	30.46	4.06	18.62	2.90	84.09	9.71	30.83	1.35	31.32	4.01
20	14	16.90	2.46	29.51	3.98	17.95	2.62	75.50	8.84	29.01	3.05	30.91	3.55
21	7	19.96	2.23	33.89	7.64	19.72	1.86	94.02	12.55	33.33	3.03	34.99	2.83
19-21	27	17.76 <sup>(b)</sup>	2.49	31.50 <sup>(b)</sup>	4.76	19.18 <sup>(b)</sup>	2.78	82.21 <sup>(b)</sup>	10.49	30.53 <sup>(b)</sup>	2.24	32.06 <sup>(b)</sup>	3.79
22	5	18.51	2.99	37.16	5.43	21.70	1.40	92.08	19.42	35.58	4.27	35.36	2.04
23	6	20.37	1.79	38.35	4.81	22.00	2.07	98.93	9.78	37.42	3.14	37.50	2.65
24	6	23.23	2.12	41.23	5.56	22.82	3.11	110.66	9.95	39.14	1.28	40.76	2.26
25	3	23.36	4.80	41.94	3.03	25.22	3.57	113.80	11.68	42.13	3.94	40.55	2.97
22-25	20	21.21 <sup>(c)</sup>	3.24	39.45 <sup>(c)</sup>	5.02	22.66 <sup>(c)</sup>	2.62	102.97 <sup>(c)</sup>	14.78	38.19 <sup>(c)</sup>	3.63	38.40 <sup>(c)</sup>	2.69

Note: between the three age groups of 16-18, 19-21, and 22-25 weeks, the means for all the pulmonary parameters studied marked by letters (a), (b), and (c) in every column differ significantly: (a) versus (b)  $p < 0.001$ , (a) versus (c)  $p < 0.001$ , and (b) versus (c)  $p < 0.001$ .

TABLE 3: Numerical data of the growing left lung.

Age [weeks]	n	Left lung (all parameters are expressed in millimeters [mm])											
		Transverse diameter		Sagittal diameter		Height		Base circumference		Anterior margin length		Posterior margin length	
		Mean	SD	Mean	SD	Mean	SD	Mean	SD	Mean	SD	Mean	SD
16	2	9.06	1.88	20.45	2.26	16.07	0.56	45.23	0.49	22.90	2.50	24.12	0.50
17	8	11.60	1.74	21.24	2.35	16.27	1.80	48.83	13.75	25.78	2.18	24.95	4.06
18	10	11.71	1.70	22.84	3.74	17.91	2.40	55.30	7.08	28.08	4.91	28.76	7.80
16-18	20	11.40 <sup>(a)</sup>	1.82	21.96 <sup>(a)</sup>	3.13	17.07 <sup>(a)</sup>	2.16	51.71 <sup>(a)</sup>	10.40	26.64 <sup>(a)</sup>	4.05	26.77 <sup>(a)</sup>	6.26
19	6	15.56	2.52	28.73	3.80	19.54	1.52	69.38	9.61	33.26	4.42	33.09	3.28
20	14	13.28	1.87	27.20	3.47	18.47	1.82	64.75	7.02	30.93	2.23	30.02	2.16
21	7	16.31	1.57	29.80	3.88	21.60	2.09	73.91	8.74	37.26	4.52	33.90	1.20
19-21	27	14.57 <sup>(b)</sup>	2.34	28.22 <sup>(b)</sup>	3.68	19.52 <sup>(b)</sup>	2.21	68.29 <sup>(b)</sup>	8.72	33.09 <sup>(b)</sup>	4.26	31.71 <sup>(b)</sup>	2.83
22	5	17.96	3.25	33.83	5.56	23.59	3.28	78.48	14.38	36.16	4.56	38.09	4.37
23	6	16.46	1.86	34.84	1.31	24.02	3.23	83.78	7.28	37.08	8.10	37.85	4.56
24	6	18.05	2.32	36.14	3.94	26.67	1.84	85.94	16.17	42.64	5.92	39.16	3.87
25	3	20.10	6.94	37.89	4.47	25.37	4.87	78.10	35.32	45.27	2.17	41.54	4.75
22-25	20	17.86 <sup>(c)</sup>	3.32	35.44 <sup>(c)</sup>	3.88	24.91 <sup>(c)</sup>	3.18	82.25 <sup>(c)</sup>	16.40	39.75 <sup>(c)</sup>	6.67	38.86 <sup>(c)</sup>	4.49

Note: between the three age groups of 16-18, 19-21, and 22-25 weeks, the means marked by letters (a), (b), and (c) in every column differ significantly: for transverse diameter: (a) versus (b)  $p < 0.001$ , (a) versus (c)  $p < 0.001$ , and (b) versus (c)  $p < 0.001$ ; for sagittal diameter: (a) versus (b)  $p < 0.001$ , (a) versus (c)  $p < 0.001$ , and (b) versus (c)  $p < 0.001$ ; for height: (a) versus (b)  $p < 0.01$ , (a) versus (c)  $p < 0.001$ , and (b) versus (c)  $p < 0.001$ ; for base circumference: (a) versus (b)  $p < 0.001$ , (a) versus (c)  $p < 0.001$ , and (b) versus (c)  $p < 0.001$ ; for length of anterior margin: (a) versus (b)  $p < 0.001$ , (a) versus (c)  $p < 0.001$ , and (b) versus (c)  $p < 0.001$ ; for length of posterior margin: (a) versus (b)  $p < 0.01$ , (a) versus (c)  $p < 0.001$ , and (b) versus (c)  $p < 0.001$ .

TABLE 4: The best-fit regression formulae for the growing lungs in the fetus.

Parameter	Right lung		Left lung	
	Regression formula	$R^2$ value	Regression formula	$R^2$ value
Transverse diameter	$y = -72.88 + 30.19 \times \ln(\text{age}) \pm 1.83$	0.80	$y = -43.05 + 19.11 \times \ln(\text{age}) \pm 1.92$	0.59
Sagittal diameter	$y = -120.43 + 50.80 \times \ln(\text{age}) \pm 3.63$	0.75	$y = -98.51 + 42.44 \times \ln(\text{age}) \pm 2.91$	0.76
Height	$y = -46.48 + 21.64 \times \ln(\text{age}) \pm 2.02$	0.63	$y = -64.41 + 28.25 \times \ln(\text{age}) \pm 2.13$	0.71
Base circumference	$y = -349.54 + 143.95 \times \ln(\text{age}) \pm 9.96$	0.75	$y = -235.49 + 101.29 \times \ln(\text{age}) \pm 8.20$	0.68
Length of anterior margin	$y = -106.50 + 45.85 \times \ln(\text{age}) \pm 2.97$	0.78	$y = -106.45 + 46.58 \times \ln(\text{age}) \pm 3.47$	0.73
Length of posterior margin	$y = -103.71 + 45.20 \times \ln(\text{age}) \pm 2.58$	0.82	$y = -96.89 + 42.98 \times \ln(\text{age}) \pm 3.38$	0.70

because they lacked both external and internal conspicuous anomalies. Besides, they could not suffer from intrauterine growth restriction, since the gestational, amenorrhea, and ultrasound ages proved to be harmonious ( $r = 0.99$ ;  $p < 0.001$ ) [18]. Secondly, since completely degassed fetal lungs perfectly fitted the sealed thoracic cavity, the influence of formalin fixation on lung shrinkage was minimized to roughly 0.5–1.0% [9, 18]. Thirdly, an optimized reliable and objective digital-image analysis system (NIS Elements AR 3.0, Nikon) used in the current study for measuring the clearly defined pulmonary parameters in a direct manner offered real numerical data, instead of deduced, extrapolated through a series of indirect measurements. Of note, digital image analysis proved to be an excellent method of determining the quantitative anatomy of the growing lungs, because all the parameters studied, including the anterior and posterior pulmonary margins and the base circumference, could be perfectly traced using a cursor.

In the material under examination the evidence material covered 12 measurements and 6 calculations for every fetus, resulting in 1206 individual algebraic data for the entire sample. On the other hand, disadvantages of this study may result from both a relatively narrow fetal age (16–25 weeks) and a lack of interobserver variability. Furthermore, it is typical of anatomical research to include only retrospective analysis without prospective ultrasound quality control.

No significant difference in the pulmonary dimensions between two sexes was corroborated in our series. In fact, this remains consistent with all authors, Gerards et al. [19] being excepted, who reported fetal lung volume to be unfettered by sex [20–23]. As reported by Gerards et al. [19], the fetal lung volumes were greater in males by approximately 4.3%. After reviewing the existing literature on laterality differences of the lungs, we managed to find only pulmonary volumetric data, with greater values on the right [9, 12, 19, 21, 23, 24]. It is noteworthy that we found the right-left differences with relation to all the six pulmonary parameters in question. As proved, the transverse and sagittal diameters and the base circumference of the right lungs predominated over the same parameters of the left lungs. In our opinion, these three smaller pulmonary parameters on the left could be restricted by the heart. Furthermore, the three pulmonary features, that is, lengths of anterior and posterior margins, and lung height were considerably smaller on the right, being probably limited by the liver.

In order to choose the best-fit models for the growing lungs, we verified disparate regression formulae from linear to fourth-degree polynomial, taking into account the following three criteria: the greatest  $R^2$  value, all coefficients different from 0, and the lowest SD of regression [9, 15]. Regrettably, in the estimated second-degree, third-degree, and fourth-degree polynomial models, their parameters were found to be statistically insignificant ( $p > 0.05$ ). Both the linear and logarithmic models were statistically significant ( $p < 0.05$  and  $p < 0.001$ , resp.), but the latter demonstrated greater  $R^2$  values at the range of 0.59–0.82. Besides, when compared to the linear regressions, the logarithmic models were characterized by the lowest values of both standard deviation for parameters and the standard error of the estimate for the complete model. It is noteworthy that residual value analysis showed normality of distribution for both linear and logarithmic models. In the linear and logarithmic models there were four and two extremal values, respectively, for which standardized residuals were beyond the range of  $(-2, +2)$ . Finally, the logarithmic models were of best-fit for our empirical data throughout the analyzed fetal period. We substantiated that the growth curves of best-fit for each parameter studied versus gestational ages were natural logarithmic functions, as presented in Table 4. Of note, the greatest  $R^2$  values referred to the lengths of posterior ( $R^2 = 0.82$ ) and anterior ( $R^2 = 0.78$ ) margins and transverse diameter ( $R^2 = 0.80$ ) of the right lung. The intermediate values of  $R^2$  were typical of the sagittal diameter and base circumference ( $R^2 = 0.75$ ) of the right lung and the sagittal diameter ( $R^2 = 0.76$ ), the lengths of anterior ( $R^2 = 0.73$ ) and posterior ( $R^2 = 0.70$ ) margins, and the height ( $R^2 = 0.71$ ) of the left lung. Finally, the lowest  $R^2$  values characterized the height of the right lung ( $R^2 = 0.63$ ) and the remaining two features of the left lung, that is, transverse diameter ( $R^2 = 0.59$ ) and base circumference ( $R^2 = 0.68$ ). In terms of mathematics, a logarithmic relationship is always one-to-one, continuous, and increasing with a declining rate of change, clearly presented as a concave down graph [15, 17]. This means that an increase in length of the six pulmonary parameters studied gradually decelerated, inexorably deviating downwards from an imaginary axis ( $y = x$ ).

Apart from absolute values of the lung dimensions, some novel information on the topic of their relative growth has been addressed by this study. As ascertained, in both lungs the transverse and sagittal diameters evolved proportionately,

because the transverse-to-sagittal diameter ratio remained constant for the duration of the study period and attained the values of  $0.56 \pm 0.08$  for the right lung and  $0.52 \pm 0.08$  for the left lung. However, both the transverse and sagittal diameters of either lung grew much faster than the lung height. This fact was meticulously unveiled by the two lung indexes: transverse diameter-to-height ratio and sagittal diameter-to-height ratio. The former considerably increased from  $0.74 \pm 0.09$  to  $0.92 \pm 0.08$  in the right lung and from  $0.56 \pm 0.07$  to  $0.79 \pm 0.09$  in the left lung. The latter gained in values from  $1.41 \pm 0.23$  to  $1.66 \pm 0.18$  and from  $1.27 \pm 0.17$  to  $1.48 \pm 0.22$  for the right and left lungs, respectively.

To the best of our knowledge, the present paper is the first in the medical literature to quantitatively evaluate pulmonary dimensions in question. The complete lack of information in the professional literature relating to the lung parameters studied evidently limits a debate on this subject. The novel growth patterns improve our understanding of pulmonary quantitative morphology and allow calculating the mean of pulmonary parameters according to gestational age. This may particularly be of potential relevance in fetuses suffering from pulmonary hypoplasia, as a result of the following disorders: renal malformations, oligohydramnios, fetal hydrops, skeletal dysplasias, congenital diaphragmatic hernia, intrathoracic masses, congenital adenomatoid malformation, bronchopulmonary sequestration, and cervical and sacrococcygeal teratomata [6, 7]. The medical diagnosis or exclusion of pulmonary hypoplasia may use both prenatal ultrasound and MRI (2–4). In doing so, our quantitative data obtained in this study, as relevant fetal age-specific references for pulmonary parameters, may reliably be conducive. We believe that the normative data for the lung dimensions in the fetus obtained in this study will offer the indispensable background for future autopsy and *in utero* studies.

## 5. Conclusions

The lung dimensions in the fetus divulge no sex differences. The transverse and sagittal diameters and the base circumference are greater in the right lungs, while the lengths of anterior and posterior margins and the lung height are greater in the left lungs. The three-dimensional growth of the fetal lungs follows natural logarithmic functions. In the fetal lungs, their proportionate increase in transverse and sagittal diameters considerably accelerates with relation to the lung height. The lung dimensions in the fetus are relevant in the evaluation of the normative pulmonary growth and the diagnosis of pulmonary hypoplasia.

## Conflict of Interests

The authors declare that they have no conflict of interests.

## References

- [1] M. E. de Paepe, S. R. Carr, and J. A. Cassese, “Postmortem validation of imaging-derived formulas for prediction of fetal lung volume,” *Fetal Diagnosis and Therapy*, vol. 18, no. 5, pp. 353–359, 2003.
- [2] S. Mayer, P. Klaritsch, S. Petersen et al., “The correlation between lung volume and liver herniation measurements by fetal MRI in isolated congenital diaphragmatic hernia: a systematic review and meta-analysis of observational studies,” *Prenatal Diagnosis*, vol. 31, no. 11, pp. 1086–1096, 2011.
- [3] I. Sandaite, F. Claus, F. de Keyzer et al., “Examining the relationship between the lung-to-head ratio measured on ultrasound and lung volumetry by magnetic resonance in fetuses with isolated congenital diaphragmatic hernia,” *Fetal Diagnosis and Therapy*, vol. 29, no. 1, pp. 80–87, 2011.
- [4] M. Cannie, J. Jani, F. de Keyzer, I. Roebben, L. Breysem, and J. Deprest, “T2 quantifications of fetal lungs at MRI-normal ranges,” *Prenatal Diagnosis*, vol. 31, no. 7, pp. 705–711, 2011.
- [5] A. C. G. Breeze, F. A. Jessop, P. A. K. Set et al., “Minimally-invasive fetal autopsy using magnetic resonance imaging and percutaneous organ biopsies: clinical value and comparison to conventional autopsy,” *Ultrasound in Obstetrics & Gynecology*, vol. 37, no. 3, pp. 317–323, 2011.
- [6] E. A. Junior, P. S. de Oliveira, L. M. M. Nardoza et al., “Fetal lung volume in fetuses with urinary tract malformations: comparison by 2D-, 3D-sonography and magnetic resonance imaging,” *The Journal of Maternal-Fetal & Neonatal Medicine*, vol. 23, no. 1, pp. 60–68, 2010.
- [7] M. Cannie, J. C. Jani, F. de Keyzer et al., “Fetal body volume: use at MR imaging to quantify relative lung volume in fetuses suspected of having pulmonary hypoplasia,” *Radiology*, vol. 241, no. 3, pp. 847–853, 2006.
- [8] J. C. Jani, M. Cannie, C. F. A. Peralta, J. A. Deprest, K. H. Nicolaides, and S. Dymarkowski, “Lung volumes in fetuses with congenital diaphragmatic hernia: comparison of 3D US and MR imaging assessments,” *Radiology*, vol. 244, no. 2, pp. 575–582, 2007.
- [9] M. Szpinda, W. Siedlaczek, A. Szpinda, A. Woźniak, C. Mila-Kierzenkowska, and M. Wiśniewski, “Volumetric growth of the lungs in human fetuses: an anatomical, hydrostatic and statistical study,” *Surgical and Radiologic Anatomy*, vol. 36, no. 8, pp. 813–820, 2014.
- [10] F. Rypens, T. Metens, N. Rocourt et al., “Fetal lung volume: estimation at MR imaging—initial results,” *Radiology*, vol. 219, no. 1, pp. 236–241, 2001.
- [11] F. V. Coakley, J. B. Lopoo, Y. Lu et al., “Normal and hypoplastic fetal lungs: volumetric assessment with prenatal single-shot rapid acquisition with relaxation enhancement MR imaging,” *Radiology*, vol. 216, no. 1, pp. 107–111, 2000.
- [12] D. Moeglin, C. Talmant, M. Duyme et al., “Fetal lung volumetry using two- and three-dimensional ultrasound,” *Ultrasound in Obstetrics & Gynecology*, vol. 25, no. 2, pp. 119–127, 2005.
- [13] C. F. A. Peralta, P. Cavoretto, B. Csapo, O. Falcon, and K. H. Nicolaides, “Lung and heart volumes by three-dimensional ultrasound in normal fetuses at 12–32 weeks’ gestation,” *Ultrasound in Obstetrics & Gynecology*, vol. 27, no. 2, pp. 128–133, 2006.
- [14] J. R. Thompson, D. C. Wood, and S. Weiner, “Fetal pulmonary development and ultrasound,” *Ultrasonografia*, vol. 28, no. 28, pp. 51–57, 2007.
- [15] A. T. Papageorghiou, E. O. Ohuma, D. G. Altman et al., “International standards for fetal growth based on serial ultrasound measurements: the fetal growth longitudinal study of the INTERGROWTH-21st project,” *The Lancet*, vol. 384, no. 9946, pp. 869–879, 2014.

- [16] W. Wagner and M. R. Harrison, "Fetal operations in the head and neck area: current state," *Head and Neck*, vol. 24, no. 5, pp. 482–490, 2002.
- [17] M. Szpinda, M. Daroszewski, A. Woźniak et al., "Novel patterns for the growing main bronchi in the human fetus: an anatomical, digital and statistical study," *Surgical and Radiologic Anatomy*, vol. 36, no. 1, pp. 55–65, 2014.
- [18] W. Siedlaczek, *Morphometric study of the lungs in the human fetus [Doctoral thesis]*, Nicolaus Copernicus University, Bydgoszcz, Poland, 2012.
- [19] F. A. Gerards, M. A. J. Engels, J. W. R. Twisk, and J. M. G. van Vugt, "Normal fetal lung volume measured with three-dimensional ultrasound," *Ultrasound in Obstetrics & Gynecology*, vol. 27, no. 2, pp. 134–144, 2006.
- [20] A. Bahmaie, S. W. Hughes, T. Clark et al., "Serial fetal lung volume measurement using three-dimensional ultrasound," *Ultrasound in Obstetrics & Gynecology*, vol. 16, no. 2, pp. 154–158, 2000.
- [21] C.-H. Chang, C.-H. Yu, F.-M. Chang, H.-C. Ko, and H.-Y. Chen, "Volumetric assessment of normal fetal lungs using three-dimensional ultrasound," *Ultrasound in Medicine and Biology*, vol. 29, no. 7, pp. 935–942, 2003.
- [22] G. Kasprian, C. Balassy, P. C. Brugger, and D. Prayer, "MRI of normal and pathological fetal lung development," *European Journal of Radiology*, vol. 57, no. 2, pp. 261–270, 2006.
- [23] I. S. W. Britto, L. C. de Silva Bussamra, E. A. Júnior et al., "Fetal lung volume: comparison by 2D- and 3D-sonography in normal fetuses," *Archives of Gynecology and Obstetrics*, vol. 280, no. 3, pp. 363–368, 2009.
- [24] R. Ruano, L. Joubin, M.-C. Aubry et al., "A nomogram of fetal lung volumes estimated by 3-dimensional ultrasonography using the rotational technique (Virtual organ computer-aided analysis)," *Journal of Ultrasound in Medicine*, vol. 25, no. 6, pp. 701–709, 2006.